Innovating a human adipocyte spheroid platform to explore the role of metabolite-sensing GPCRs in metabolic disease

Elaine Margaret Duncan

BA (Hons), MA (Cantab)

Submitted in fulfilment of the requirements for the degree of

Doctor of Philosophy

School of Molecular Biosciences

College of Medical, Veterinary & Life Sciences

University of Glasgow

December 2025

Abstract

Metabolic diseases such as obesity and type 2 diabetes are a global healthcare and economic burden affecting over 1 billion individuals worldwide. These diseases are characterised by excessive accumulation and dysfunction of adipose tissue, leading to impaired metabolic regulation and severe downstream consequences for patients. Low level chronic inflammation of adipose tissue is an important hallmark of metabolic disease, and there is growing evidence that metabolite-sensing G Protein-Coupled Receptors (m-GPCRs) can regulate metabolic function through autocrine and paracrine signalling loops. However, it has been challenging to dissect these complex signalling networks using traditional 2D cell culture or *in vivo* experimental models. This thesis aimed to address this gap by engineering and validating an innovative 3D *in vitro* model of adipose tissue suitable for investigating the role of m-GPCRs in metabolic disease.

First, a series of novel genetically encoded NanoBiT biosensors were designed and optimised to quantify real time signalling of unmodified GPCRs in live cells. Next, spheroids were generated by seeding human Simpson Golabi Behmel Syndrome (SGBS) preadipocytes in ultra-low adhesion plates and differentiating them into adipocytes. Comprehensive morphological, transcriptional and protein-level characterisation demonstrated that spheroids accumulate lipid droplets and upregulate key markers of adipogenesis during differentiation. Critically, the differentiated spheroids show characteristic adipocyte functions, including ß-adrenergic-stimulated lipolysis, and insulin-stimulated glucose uptake. To mimic a metabolic disease-relevant phenotype, spheroids were treated with Tumor Necrosis Factor which induced a pro-inflammatory, insulin resistant microenvironment, and revealed upregulation of the FFA4 receptor in disease-relevant conditions. Finally, the role of m-GPCRs in adipogenesis and lipolysis could be defined by treating adipocyte spheroids with pharmacological tool compounds, and genetically encoded biosensors were incorporated to directly measure receptor signalling in adipocytes.

Overall, a novel human adipocyte spheroid platform has been developed which has allowed the investigation of m-GPCR function within a physiologically- and disease-relevant context. This therefore provides a strong foundation to

interrogate the complex metabolic-immune signalling networks within adipose tissue, and may ultimately lead to new GPCR-focused therapeutic strategies for metabolic disease.

Table of Contents

List of Tables

List of Figures

List of Publications

Abstracts

Duncan, E. M., Lucianno, O., Dibnah, B., Moniz e Castro, A. & Hudson, B. D. (2026). Glowing science: Illuminating drug discovery with table-top engagement activities. *British Journal of Pharmacology,* 183(3), 717-718

Moniz e Castro, A., Duncan, E. M. & Hudson, B. D. (2026). Novel BRET-based GPCR-Gα subtype biosensors to measure plasma membrane GPCR activation in real time. *British Journal of Pharmacology,* 183(3), 737-738

Duncan, E. M., Berry, C. C., Dalby, M. J. & Hudson, B. D. (2025). A 3D adipocyte spheroid model to investigate the role of metabolite-sensing GPCRs in metabolic disorders. *British Journal of Pharmacology,* 182(3), 778-779

Duncan, E. M., Dow, E. & Hudson, B. D. (2023). NanoBiT biosensors to investigate FFA4 signalling in adipocyte spheroids. *British Journal of Pharmacology,* 180(S1), 696-697

Publications

Valentini, A., Dibnah, B., Ciba, M., Duncan, E. M., Manandhar, A., Strellis, B., Vita, L., Lucianno, O., Massey, C., Coe, S., Ulven, T., Hudson, B. D. & Rexen Ulven, E. (2025). Multicolored sequential resonance energy transfer for detection of simultaneous ligand binding at G protein-coupled receptors. *Nature Communications* 16:6413. doi: 10.1038/s41467-025-61690-5

Alshammari, W. S., Duncan, E. M., Vita L., Kenawy, M., Dibnah, B., Wabitsch, M., Gould, G. W. & Hudson, B. D. (2025). Inverse agonism of the FFA4 free fatty acid receptor controls both adipogenesis and mature adipocyte function. *Cellular Signalling,* 131:111714. doi: 10.1016/j.cellsig.2025.111714

Duncan, E. M.*, Vita L.*, Dibnah, B. & Hudson, B. D. (2023). Metabolite-sensing GPCRs controlling interactions between adipose tissue and inflammation. *Frontiers in Endocrinology,* 14:1197102. doi: 10.3389/fendo.2023.1197102 *(*shared first authorship)*

Acknowledgements

Firstly, I would like to thank my supervisors Dr Brian Hudson, Dr Catherine Berry and Prof Matt Dalby for their support throughout the project. Matt and Catherine, thank you for guiding us as we took our tentative first steps with spheroids. Brian, you have been a fantastic supervisor since before I even started in the lab. Thank you for teaching me everything I know about molecular pharmacology, for pushing and supporting when needed but also giving space for me to learn for myself. You have made me into a better scientist, and I will carry that with me for the rest of my career.

Being part of the LifETIME CDT has been an utter joy. I'd like to thank the academics, support staff, and students (especially the 2021 cohort) for the core memories. I'd also like to mention my friends and former colleagues who encouraged me to start a PhD in the first place and have continued to support me from a distance – thank you.

A cross-disciplinary project like this has given me the best opportunity to work with so many different people. Thank you to the staff and students across the university who have provided technical support, especially Frazer Bell, Margaret Mullen and Tyler Shaw (imaging), Dr Giuseppe Ciccone (nanoindentation), Dr Gillian Higgins (ADSCs) and of course the members of Translational Pharmacology and CeMi. A special mention goes to my thesis mentor Arianna for her encouragement through the writing process.

I am so grateful for my friends and family for cheering me on throughout this journey. To the past, present and future members of Lab 441/Sports Chat, especially Kat, Dom, Euan, Alex, Olivia and Andreia, thank you for the lunchtime chats, TC therapy sessions, and general good vibes. Claire, thank you for guiding me towards the light at the end of the thesis tunnel. You knew exactly what to say (and what not to say!) to help me through the tough times. To Mum and Dad, you have always encouraged me to work hard, and the fact that I've merged your medical and engineering backgrounds with a PhD in Cell Engineering shows how much you both have inspired my career. I hope to pay this forward by championing future scientists who haven't grown up with the same

opportunities. Thank you for offering meals, breaks and support to get me through the difficult times.

To the original Slackers, your friendship has absolutely been the highlight of this experience for me. Luca, I am so grateful that we could share the pain of spheroids – working together has been a lot more fun. Beth and Beth, we have shared so many big life moments in the past 4 years that it feels like it should be much longer – thank you for your scientific help but more importantly for the crafternoons. You have all been the best cheerleaders.

Finally, to my fiancé Ryden. You asked me once whether you would get an acknowledgement for teaching me the basics of materials science. While that's true (thank you!), you made a much greater contribution by looking after our lives outside the PhD, and making sure I was fed, watered, and loved through all the ups and downs of this journey. I absolutely could not have done this without you, and for that I will be forever grateful.

Author's Declaration

"I declare that, except where explicit reference is made to the contribution of others, this dissertation is the result of my own work and has not been submitted for any other degree at the University of Glasgow or any other institution."

December 2025

Elaine Duncan

Abbreviations

2DG	2-deoxyglucose
α-LA	α-Linolenic Acid
ADSC	Adipose Derived Stromal Cell
ANOVA	Analysis Of Variance
AQUA	Advanced Quick Assembly
ATGL	Adipocyte Triglyceride Lipase
ATP	Adenosine Triphosphate
AUC	Area Under Curve
BAT	Brown Adipose Tissue
BERKY	BRET Biosensor with ER/K Linker and YFP
bFGF	Basic Fibroblast Growth Factor
BHB	B-Hydroxybutyrate
BRET	Bioluminescent Resonance Energy Transfer
BSA	Bovine Serum Albumin
cAMP	Cyclic Adenosine Monophosphate
cDNA	Complementary deoxyribonucleic acid
CeNL	Cyan eNL
CMV	Cytomegalovirus
CpFP	Circularly Permutated Fluorescent Protein
CVD	Cardiovascular Disease
DAB	3,3'-Diaminobenzidine
DAG	Diacylglycerol
DMEM	Dulbecco's Modified Eagle Medium
DMSO	Dimethyl sulfoxide
DNA	Deoxyribonucleic Acid
EC50	Half Maximal Effective Concentration
ECM	Extracellular Matrix
EGF	Epidermal Growth Factor
eNL	Enhanced NanoLantern
FABP4	Fatty Acid Binding Protein 4
FBS	Fetal Bovine Serum
FFA	Free Fatty Acid
FL	Flexible Linker
FP	Fluorescent Protein
FRET	Förster Resonance Energy Transfer
GDP	Guanosine Diphosphate
GEF	Guanine Nucleotide Exchange Factors

GEMTA	G Protein Effector Membrane Translocation Assays
GeNL	Green eNL
GLP-1	Glucagon-Like Peptide-1
GPCR	G Protein-Coupled Receptor
GRK	G-Protein Receptor Kinases
GTP	Guanosine Triphosphate
H&E	Haematoxylin & Eosin
HA	Hemagglutinin
HBSS(-H)	Hanks' Balanced Salt Solution (with HEPES)
HEK293-T	Human Embryonic Kidney 293-T
HI	Heat-Inactivated
HIF-1α	Hypoxia-Inducible Factor 1-Alpha
hMADS	Human Multipotent Adipose Derived Stem
hPL	Human Platelet Lysate
HRP	Horseradish Peroxidase
HS	Human Serum
HSL	Hormone Sensitive Lipase
IBMX	Isobutyl-1-methylxanthine
ICC	Immunocytochemistry
ICL	Intracellular Loop
ICW	In Cell Western
IHC	Immunohistochemistry
IL	Interleukin
IP_1	Inositol monophosphate
IP_3	Inositol 1,4,5-trisphosphate
IR	Insulin Resistance
IRES	Internal Ribosome Entry Site
KRP(-H)	Krebs-Ringer-Phosphate (with HEPES)
LB	Lysogeny Broth
LgBiT	Large BiT
LPL	Lipoprotein Lipase
LPS	Lipopolysaccharide
m-GPCR	Metabolite-Sensing G Protein-Coupled Receptor
M-MLV	Moloney Murine Leukemia Virus
MASH	Metabolic Dysfunction-Associated Steatohepatitis
MASLD	Metabolic Dysfunction-Associated Steatotic Liver Disease
MCP1	Monocyte Chemoattractant Protein 1
MEM	Minimal Essential Medium
mG	MiniG

MGL	Monoacylglycerol Lipase
mNG	mNeonGreen
mRNA	Messenger RNA
MSC	Mesenchymal Stem Cell
NAFLD	Non-Alcoholic Fatty Liver Disease
NASH	Non-Alcoholic Steatohepatitis
NBA	NanoBiT Arrestin Recruitment
NLuc	NanoLuciferase
OD	Optical Density
ONE-GO	One Vector G-Protein Optical
ORO	Oil Red O
P2A	Self-cleaving 2A peptide from porcine teschovirus-1
PBS	Phosphate Buffered Saline
PCR	Polymerase Chain Reaction
PDE3B	Phosphodiesterase 3B
PDL	Poly-D-lysine
PEI	Polyethyleneimine
PFA	Paraformaldehyde
PIP_2	Phosphatidylinositol 4,5-bisphosphate
PKA	Protein Kinase A
PKC	Protein Kinase C
PLA_2	Phospholipase A2
PLC	Phospholipase C
qPCR	Quantitative PCR
RET	Resonance Energy Transfer
RLU	Relative Luminescence Units
RNA	Ribonucleic Acid
ROS	Reactive Oxygen Species
SEM	Scanning Electron Microscopy
SEM	Standard Error of the Mean
SGBS	Simpson Golabi Behmel Syndrome
siRNA	Short Interfering RNA
SmBiT	Small BiT
SPASM	Systematic Protein Affinity Strength Modulation
SpNB	SPASM NanoBiT
SVF	Stromal Vascular Fraction
T2D	Type 2 Diabetes
TAE	Tris-Acetate-EDTA
TBS	Tris Buffered Saline

TEM	Transmission Electron Microscopy
TGs	Triglycerides
TM	Transmembrane
TNF	Tumor Necrosis Factor
UCP-1	Uncoupling Protein 1
WAT	White Adipose Tissue
YeNL	Yellow eNL
YFP	Yellow Fluorescent Protein

1 Introduction

1.1 Metabolic Diseases

1.1.1 Overview

Metabolic diseases such as obesity and type 2 diabetes (T2D) represent one of the biggest current global healthcare and economic challenges. Over 1 billion individuals worldwide are currently living with obesity, and over 530 million living with T2D, with the prevalence of both continuing to rise (International Diabetes Federation, 2025; World Obesity Federation, 2025). Metabolic diseases are life limiting conditions characterised by excessive accumulation of adipose tissue leading to impaired metabolic regulation, and are highly associated with an increased risk of serious health conditions including cardiovascular disease, some cancers and metabolic dysfunction-associated steatotic liver disease (MASLD) (Guh et al., 2009; Institute for Health Metrics and Evaluation, 2024; World Health Organisation, 2025). Furthermore, it is thought that obesity and associated conditions cost the UK economy £126 billion per year through both direct healthcare costs and indirect costs of reduced productivity and quality of life (Bone et al., 2025).

Although treatments for metabolic diseases are available, these typically act indirectly through e.g. suppression of appetite or reduction of blood glucose levels rather than directly addressing metabolic dysfunction in adipose tissue (Gupta and Chen, 2023; Peri and Eisenberg, 2024a). There is therefore a pressing need to better understand the molecular and cellular mechanisms of these diseases in order to develop more effective treatment options and reduce their burden on global populations.

1.1.2 Pathophysiology

Metabolic diseases are typically driven by an imbalance between an individual's energy intake and expenditure, leading to excess accumulation of adipose tissue and downstream functional impairment (Peri and Eisenberg, 2024b). This imbalance is often caused by dietary overconsumption of foods high in fat and sugar but can also be influenced by a person's genetics (Loos and Yeo, 2022) as well as environmental and lifestyle factors (Nicolaidis, 2019). Obesity and related conditions are therefore complex and multifactorial, highlighting challenges to their successful treatment (Peri and Eisenberg, 2024b). A failure of

the body to effectively regulate this chronic energy surplus ultimately leads to systemic metabolic consequences.

In normal physiological conditions, energy homeostasis is maintained by a complex interplay of hormonal factors between metabolic and endocrine tissues including the pancreas, adipose tissue, the liver and skeletal muscle (Persaud and Jones, 2022). When blood glucose levels increase, insulin is released by pancreatic ß-cells, which promotes glucose uptake to adipose and muscle tissues through a signalling cascade resulting in translocation of the insulin-regulated glucose transporter, GLUT4, to the cell surface (Klip et al., 2019). Excess glucose can then be stored as triglycerides in adipocytes or glycogen in liver and muscle. In periods of fasting, the process is largely reversed by the production of glucagon from pancreatic α-cells, stimulating the breakdown of glycogen in the liver and increased blood glucose (Persaud and Jones, 2022). In metabolic disease, energy homeostasis is disrupted, leading to elevated blood glucose levels primarily caused by the body becoming resistant to circulating insulin (Petersen and Shulman, 2018).

Insulin Resistance (IR) is defined as a pathophysiological state of abnormal insulin response, whereby insulin-dependent cells become less able to take up glucose from the circulation, leading to elevated blood glucose levels (Yaribeygi et al., 2019). During obesity, the expansion of adipose tissue leads to cellular stress, ectopic lipid accumulation, and recruitment of inflammatory cells leading to release of pro-inflammatory cytokines, which have all been reported to contribute to the generation of IR (Goedeke et al., 2016; Yaribeygi et al., 2019). Beyond the local impacts of these stresses in adipose tissue (discussed later), insulin resistance in adipose can have a systemic impact on other tissues (Petersen and Shulman, 2018). For example, insulin suppresses lipolysis in adipose tissue, and dysregulation of this process leads to elevated circulating lipid levels (Petersen and Shulman, 2018). This can lead to ectopic fat deposition, or deposition of lipid in normally lean tissues such as liver and muscle, contributing to increased cardiovascular risk and lipotoxicity (Lim and Meigs, 2014; Neeland et al., 2018, 2019). Furthermore, higher circulating insulin levels add strain to pancreatic ß-cells resulting in their dysfunction and eventual death (Eizirik et al., 2020). If uncontrolled, this global metabolic dysfunction results in prolonged hyperglycaemia and the clinical manifestation of T2D.

1.1.3 Clinical Outcomes

Clinically, obesity and T2D are major risk factors for the development of other comorbidities including cardiovascular disease (CVD), liver disease, and some cancers (Institute for Health Metrics and Evaluation, 2024). Overall, the life expectancy of obese individuals is reduced by up to 14 years compared to healthy weight individuals (Kitahara et al., 2014; Lung et al., 2019).

Obesity drives the development of CVD through multiple mechanisms causing structural, functional, and haemodynamic changes to cardiac tissues (Lopez-Jimenez et al., 2022). Obesity accelerates the development of atherosclerotic plaques in the vasculature, leading to an increased incidence of coronary artery disease and myocardial infarction (Henning, 2021). Furthermore, elevated blood glucose levels driven by insulin resistance causes damage to the vasculature, leading to retinopathy and nephropathy causing blindness and kidney disease respectively (Rask-Madsen and King, 2013). Additionally, total blood volume and cardiac output are increased in obese individuals, driving an increase in blood pressure and ultimately can cause heart failure (Powell-Wiley et al., 2021). Together, over two thirds of obesity-related deaths are attributed to CVD, making CVD the most common cause of death for people with metabolic disease (The GBD 2015 Obesity Collaborators, 2017; Powell-Wiley et al., 2021).

Metabolic dysfunction-associated steatotic liver disease (MASLD) and the more severe form, metabolic dysfunction-associated steatohepatitis (MASH), describe a spectrum of liver conditions formerly termed non-alcoholic fatty liver disease (NAFLD) and non-alcoholic steatohepatitis (NASH) (Syed-Abdul, 2023). These conditions affect ~30% of the global population, with prevalence increasing in line with similar trends in metabolic disease (Fazel et al., 2016; Younossi et al., 2023). MASLD is thought to be primarily caused by ectopic lipid accumulation in hepatocytes, and its progression to MASH driven by lipotoxicity and altered lipid metabolism causing inflammation and ultimately leading to irreversible fibrosis and development of hepatocarcinoma (Syed-Abdul, 2023). Consequently, MASLD/MASH is a leading indication for liver transplantation and contributes significant socioeconomic costs of over £4 billion per year in the UK (Morgan et al., 2021; Younossi et al., 2024; Le et al., 2025).

Patients with T2D have increased risk of developing several long-term complications (International Diabetes Federation, 2025). As mentioned, hyperglycaemia can cause damage to systemic blood vessels, leading to CVD, blindness and kidney failure (Rask-Madsen and King, 2013; Diabetes UK, 2025). A further consequence is the development of diabetic neuropathies, when the vasculature surrounding nerves becomes damaged leading to dysfunction in peripheral nerves and loss of sensation (Boulton et al., 2005). Diabetic neuropathies are the most common cause of diabetic foot ulcers which can progress to severe infections requiring amputation (Kim, 2023; Rashki et al., 2025).

Overall, these clinical outcomes highlight the systemic nature of metabolic disease, leading to a high incidence of comorbidities in patients. There is therefore a pressing need to improve our understanding of these conditions and develop more effective therapeutics to address this severe healthcare burden.

1.1.4 Current Treatments

The initial management of metabolic diseases is through lifestyle and behavioural interventions such as dietary caloric restriction and increased physical exercise to reduce weight and improve metabolic health (Gupta and Chen, 2023; Peri and Eisenberg, 2024a; National Institute for Health and Care Excellence, 2025). Pharmacological intervention is recommended to treat obesity in patients who have been unsuccessful in reaching a sufficient weight loss target, typically >5% body weight within 6 months (Gupta and Chen, 2023; Tchang et al., 2024). In T2D, first line medications are offered when a target level of glycated haemoglobin (HbA1c) is not achieved through lifestyle and diet alone (National Institute of Health and Care Excellence, 2022). Examples of current approved pharmacological agents for treatment of obesity and T2D in the UK are described in **Table 1.1.**

Table 1.1 - Current approved pharmacological agents for treatment of obesity and T2D in the UK. Adapted from National Institute of Health and Care Excellence guidelines.

Disease	Drug Class	Examples (Trade Names)	Mechanism of Action
Obesity	Orlistat	(Xenical)	Pancreatic lipase inhibitor reduces fat absorption
Obesity & T2D	GLP-1 Receptor Agonists	Liraglutide (Saxenda), Semaglutide (Wegovy/Ozempic)	Stimulates insulin secretion, inhibits glucagon secretion, and promotes satiety
	GIP/GLP-1 Receptor Agonists	Tirzepatide (Mounjaro/Zepbound)	Stimulates insulin secretion, inhibits glucagon secretion, and promotes satiety
	SGLT2 inhibitors	Canagliflozin (Invokana), Dapagliflozin (Forxiga), Empagliflozin (Jardiance), Ertugliflozin (Steglatro)	Inhibit glucose reabsorption by the kidney, resulting in glucosuria
T2D	Metformin	N/A	Inhibits gluconeogenesis in the liver, resulting in reduced blood glucose
	Sulfonylureas	Gliclazide (Diamicron), Glimepiride (Amaryl), Glipizide (Glucotrol), Tolbutamide (Orinase)	Insulin secretagogues, increase insulin release by pancreas by inducing closure of ATP-sensitive potassium channels
	DPP-4 Inhibitors	Alogliptin (Vipidia), Linagliptin (Trajenta), Saxagliptin (Onglyza), Sitagliptin (Januvia), Vildagliptin (Galvus)	Inhibits degradation of incretins GLP-1 and GIP, resulting in increased insulin release
	Thiazolidinediones	Pioglitazone (Actos)	PPAR agonists, increases fatty acid storage in adipocytes and improves insulin sensitivity

Many of the treatments for obesity and T2D listed in **Table 1.1** do not directly address metabolic dysfunction in adipose tissue, but rather act indirectly to reduce appetite, stimulate insulin secretion or reduce blood glucose levels

(Gupta and Chen, 2023). The notable exceptions to this are the thiazolidinediones, which act on adipocytes to increase adipogenesis and improve insulin sensitivity (Soccio et al., 2014). Unfortunately, many thiazolidinediones are associated with safety concerns, with rosiglitazone withdrawn from the European market for cardiovascular risk and pioglitazone suspended in France and Germany due to increased bladder cancer risk (Marín-Peñalver et al., 2016). Furthermore, thiazolidinediones are associated with weight gain, although insulin resistance is reduced even in patients gaining weight (Wilding, 2006). These drugs continue to be approved in the USA, and pioglitazone is in use in the UK. However, there is a clear opportunity for novel therapeutics for metabolic disease which address the underlying pathology of these disorders and therefore may provide a more curative treatment.

In summary, metabolic diseases are a major healthcare and economic burden and existing treatment options do not address their underlying pathologies. Adipose tissue plays a central role in metabolic regulation, and its dysfunction is central to the development and progression of metabolic disease. Therefore, improving our understanding of the physiology and mechanistic signalling of adipose tissue may uncover new therapeutic strategies to address this global challenge.

1.2 Adipose Tissue as a Metabolic Organ

1.2.1 Normal structure and function of adipose tissue

1.2.1.1 Adipose tissue structure

Adipose is a large and dynamic organ comprising 10-30% of the total body weight of healthy individuals and may increase to over 70% of total body mass in obese individuals (Sakers et al., 2022). Historically, adipose was often considered an inert energy store, however in the past 50 years it has become known as a major endocrine organ with crucial roles in the physiology of energy homeostasis (Rosen and Spiegelman, 2014). Dysfunction of adipose tissue is highly associated with the development of IR and metabolic disease (Trayhurn, 2013). Adipose tissue can be broadly categorised into two main types – white adipose tissue (WAT) and brown adipose tissue (BAT) – which differ in their cellular composition, body distribution, and physiological functions.

WAT forms the majority of mammalian adipose tissue, and functions primarily to store excess energy as triglycerides and regulate energy homeostasis. Most of the tissue volume of white adipose tissue is made up of white adipocytes, which have a unilocular appearance containing a single large lipid droplet which pushes the nucleus and other organelles towards the plasma membrane **(Figure 1.1)**. In humans, WAT is predominantly located in two main regions: subcutaneous fat, located around the body in the hypodermis region under the skin; and visceral fat, which surrounds the internal organs (Lee et al., 2013b). Higher levels of visceral fat are highly associated with the incidence of metabolic disease (Shah et al., 2014). Rodent models are extensively used for *in vivo* studies of adipose tissue function, however rodents have different adipose tissue deposits, with inguinal and anterior fat pads typically used as a representative subcutaneous tissue, and mesenteric and gonadal deposits representing visceral fat (Börgeson et al., 2022) **(Figure 1.2)**.

BAT is critical for temperature homeostasis as the site of non-shivering thermogenesis in mammals, stimulated through ß-adrenergic activation following cold exposure, for example postnatally and following hibernation (Cannon and Nedergaard, 2004). In contrast to white adipocytes, brown adipocytes contain multiple, smaller lipid droplets and receive their colour from their high density

of mitochondria **(Figure 1.1)**. Brown adipocytes express uncoupling protein 1 (UCP-1) which drives thermogenic activity by generating a proton 'leak' through the mitochondrial inner membrane, thus dissipating the proton gradient set up by the electron transport chain as heat while bypassing the generation of ATP (Fedorenko et al., 2012). In humans, historically BAT was thought to only be present in infants, however a series of studies within the past 20 years confirmed its presence in adult humans and its presence inversely correlates with incidence of obesity (Saito et al., 2020). Subsequently, research interest in BAT has increased exponentially as a potential therapeutic avenue for obesity and metabolic disease (Singh et al., 2021). BAT is primarily located in the interscapular region of mice and supraclavicular region of humans, but deposits can also be found in perirenal, paravertebral, periaortic and axillary areas **(Figure 1.2).** The differences in adipose tissue distribution between mice and humans may have significant consequences for their biology and highlights the importance of human-relevant models in adipose tissue and metabolic disease research (Börgeson et al., 2022).

More recently, beige (or brite) adipocytes have been described which have features of both white and brown adipocytes, including a mixture of small and large lipid droplets, a moderate number of mitochondria and measurable expression of UCP-1 (Wu et al., 2012) **(Figure 1.1)**. These are thought to develop predominantly in subcutaneous WAT through the transdifferentiation - or 'beiging' – of white adipocytes in response to external cues including cold exposure, diet or pharmacological agents (Richard et al., 2020). Beige adipocytes are of particular interest for the treatment of metabolic disease, as it is thought that inducing and activating beige adipocytes can increase metabolic activity and promote glucose uptake and lipolysis, improving insulin sensitivity and glucose homeostasis and therefore the clinical outcomes of obesity and T2D (Cheng et al., 2021).

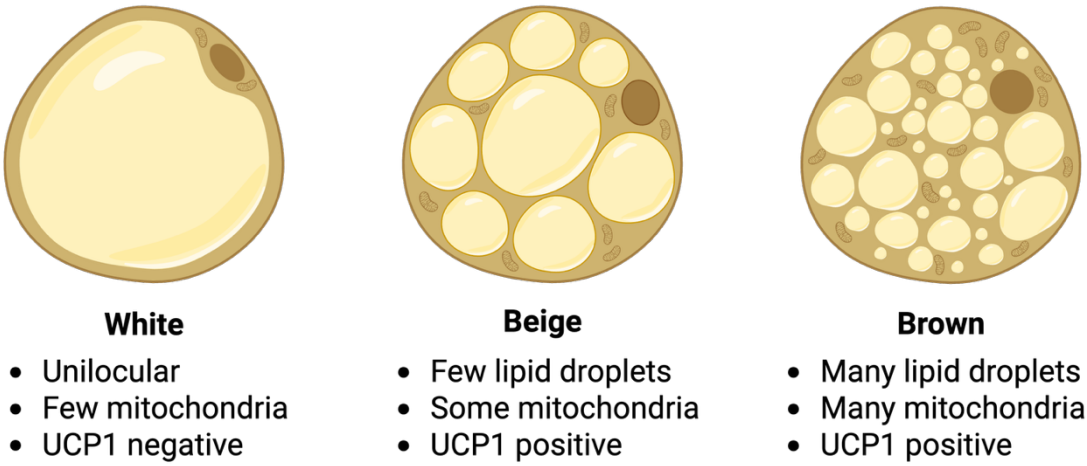

Figure 1.1 - Adipocytes are classed according to their hue. White, beige, and brown adipocytes show distinct structural and functional differences.

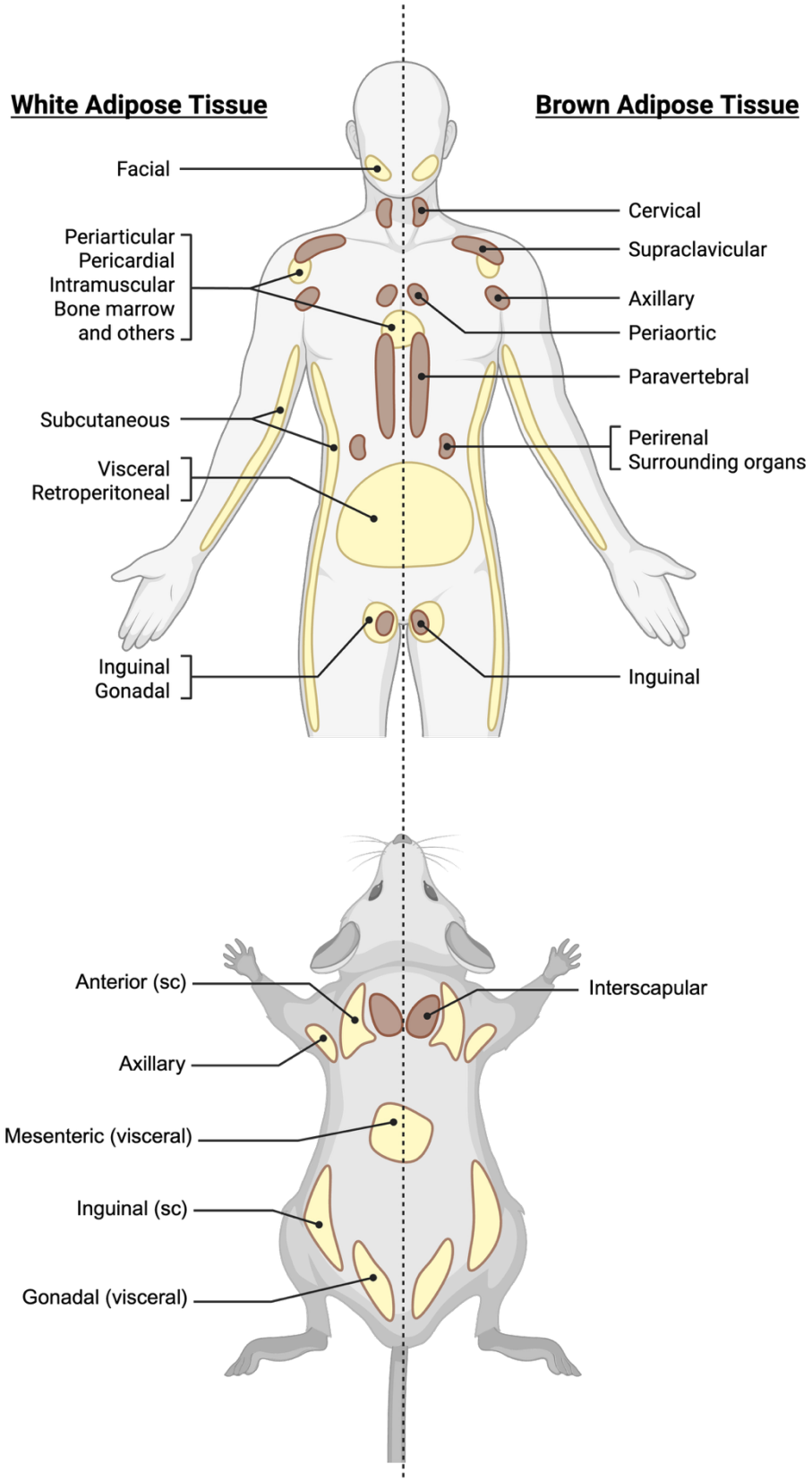

Figure 1.2 - Schematic diagram illustrating White and Brown Adipose Tissue deposits in human (top) and mouse (bottom). Adapted from Börgeson et al., 2022; Torres Irizarry et al., 2022 and BioRender templates.

In addition to adipocytes, adipose tissue contains a heterogenous mixture of other cell types including preadipocytes, fibroblasts, endothelial and immune cells, as well as extensive extracellular matrix (ECM) which can be isolated from

adipose tissue as the stromal vascular fraction (SVF) (Lee et al., 2013b; Ramakrishnan and Boyd, 2018). These SVF cells outnumber the total number of adipocytes, although white adipocytes comprise most of the tissue volume, and are responsible for the support and regeneration of adipocyte populations though vascularisation and innervation of the tissue (Rosen and Spiegelman, 2014). SVF cells can be easily isolated through low-speed centrifugation of primary lipoaspirates and contain several multipotent cell types including adipose-derived stromal cells (ADSCs) and endothelial precursor cells which have been shown to self-assemble *in vitro* to form complex vascular networks (Koh et al., 2011; Ramakrishnan and Boyd, 2018). Therefore, ADSCs and SVF have been researched extensively for tissue engineering approaches (Ramakrishnan and Boyd, 2018). Finally, adipose tissue also comprises a dynamic ECM of collagens, fibronectin and laminin which can be remodelled and reorganised in response to adipocyte expansion (Mariman and Wang, 2010; Ruiz-Ojeda et al., 2019).

Overall, the complex structure and cellular heterogeneity of adipose tissue facilitate its crucial roles in energy storage and maintenance of homeostasis. However, species-specific differences in adipose tissue deposits between humans and rodents illustrate the need for human-relevant experimental models to research human disease.

1.2.1.2 Metabolic roles of adipose tissue

Free fatty acids (FFAs) are crucial biomolecules with high oxidative potential generating high energy yield, in addition to their vital roles in membrane composition and as signalling molecules (Grabner et al., 2021). However, high concentrations of FFAs, particularly saturated FFAs such as palmitic acid, can exert cellular lipotoxicity by triggering an ER stress response and reducing membrane fluidity (Obaseki et al., 2024). Consequently, FFAs are typically stored esterified as neutral triglycerides (TGs), which can then be hydrolysed to release FFAs for use in other organs when nutrient availability is low or energy demand is high (Trayhurn and Beattie, 2001; Richard et al., 2020). This process can occur in most cell types, but in mammals predominantly occurs in the adipocytes of WAT (Grabner et al., 2021). Adipocytes can therefore respond to nutritional and hormonal cues to maintain energy homeostasis through lipogenesis or lipolysis to achieve energy storage or release respectively.

Lipogenesis is the process by which cells, primarily adipocytes and hepatocytes, convert carbohydrate substrates into fatty acids, and the subsequent esterification of fatty acids and glycerol to form TGs for storage in lipid droplets (Jeon et al., 2023). Fatty acids can either be synthesised *de novo* - through repeated reduction of acetyl CoA by Fatty Acid Synthase to increase the length of the carbon chain - or can be taken up the bloodstream following hydrolysis of circulatory triglycerides from dietary or hepatic sources in lipoproteins by the enzyme lipoprotein lipase (LPL) (Richard et al., 2020). The enzyme diacylglycerol acyltransferase then catalyses the esterification of fatty acids and glycerol, produced from glucose by glycolysis, allowing their storage as neutral TGs (Richard et al., 2020) **(Figure 1.3)**.

Conversely, lipolysis is the process by which adipocytes can mobilise stored TG stocks as FFAs for use by peripheral tissues. TGs are sequentially hydrolysed to diacylglycerols, then monoacylglycerols and finally to glycerol, releasing a single FFA at each step. These reactions are catalysed by lipases, specifically adipocyte triglyceride lipase (ATGL), hormone sensitive lipase (HSL) then monoacylglycerol lipase (MGL) (Schweiger et al., 2006). The resulting glycerol and FFAs can either be re-esterified in the adipocytes themselves or released to the circulation for use in tissues such as the liver for gluconeogenesis or the muscles for oxidative phosphorylation (Richard et al., 2020; Grabner et al., 2021) **(Figure 1.3)**.

These processes are tightly regulated by nutritional and hormonal cues to maintain energy homeostasis (Kersten, 2001). In the fed state, insulin is secreted by the pancreas and promotes glucose uptake by triggering translocation of the GLUT4 glucose transporter to the cell membrane, activates LPL to facilitate hydrolysis of circulatory lipoproteins and increases transcription of lipogenic enzymes through the transcriptional regulators SREBP1 and ChREBP (Czech et al., 2013; Jeon et al., 2023) **(Figure 1.3)**. Lipolysis can be stimulated by several factors including hormones, neurotransmitters and cytokines, but is classically driven by activation of ß-adrenoceptors by noradrenaline and adrenaline which leads to increased cellular cyclic AMP (cAMP) levels, activation of protein kinase A (PKA), and subsequent activation of the lipolytic enzymes ATGL and HSL (Richard et al., 2020; Grabner et al., 2021). Consequently, in the fed state, insulin can inhibit lipolysis through activation of phosphodiesterase 3b (PDE3B) which hydrolyses and reduces cAMP levels (Grabner et al., 2021) **(Figure 1.3)**.

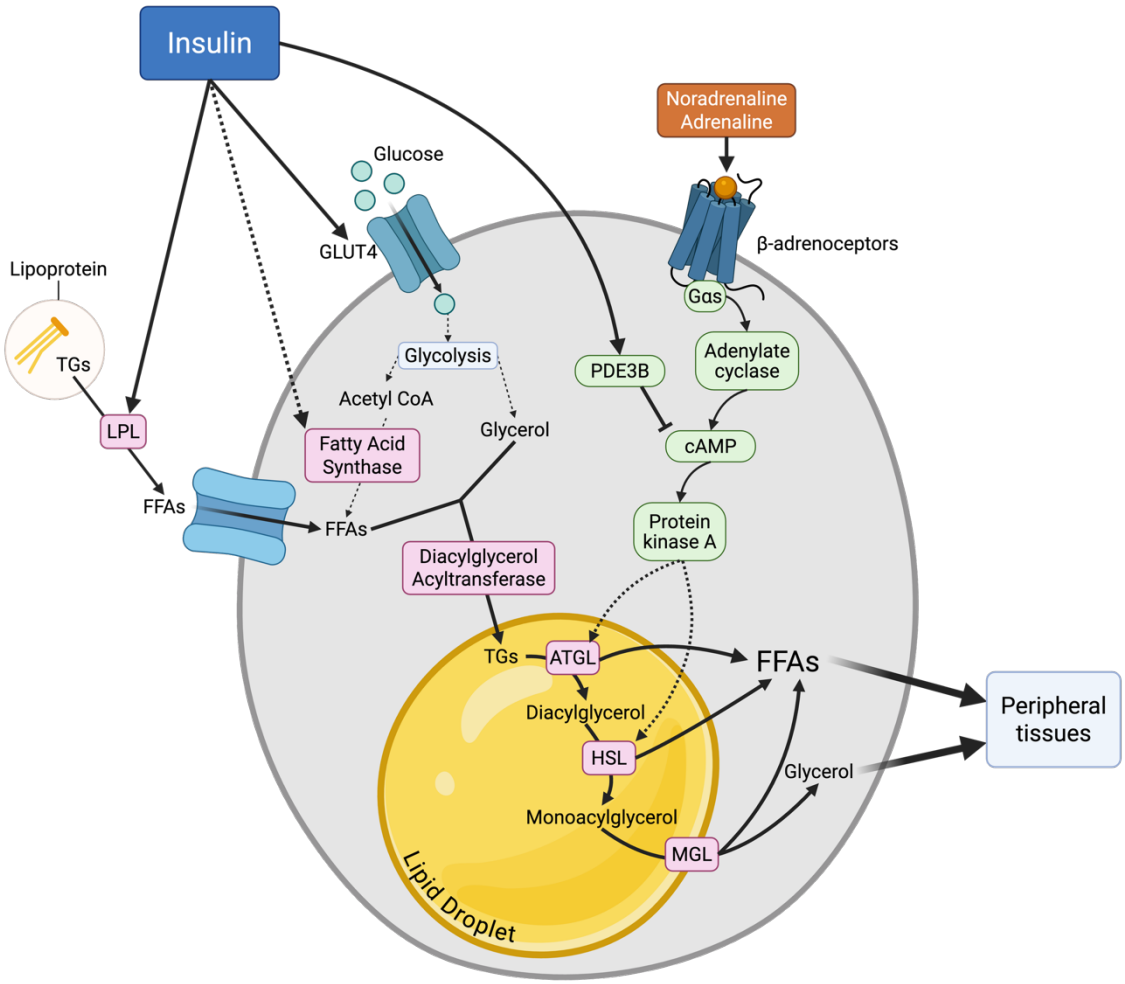

Figure 1.3 - Lipogenesis and lipolysis are tightly regulated in adipocytes to maintain energy homeostasis. Free fatty acids (FFAs) can be synthesised *de novo* or taken up from the circulation and are esterified with glycerol by diacylglycerol acetyltransferase to be stored as neutral triglycerides (TGs). Lipolysis is stimulated by noradrenaline and adrenaline activating a β-adrenoceptor signalling cascade, culminating in activation of protein kinase A activating lipolytic enzymes. TGs are sequentially hydrolysed by adipocyte triglyceride lipase (ATGL), hormone sensitive lipase (HSL) and monoacylglycerol lipase (MGL) to release FFAs and glycerol for use in peripheral tissues. These processes can be regulated by insulin signalling, which promotes lipogenesis by activating lipoprotein lipase (LPL), stimulating GLUT4 translocation, and upregulating lipogenic enzymes, and inhibits lipolysis by activating phosphodiesterase 3B (PDE3B) to reduce cAMP levels. Adapted from Richard et al., 2020.

Furthermore, adipose tissue has a critical role in thermal homeostasis. While WAT acts as an insulating layer to prevent excessive heat loss (Gregory, 1989; Trayhurn and Beattie, 2001), BAT is the major site of non-shivering thermogenesis, providing a means for mammals to generate heat from stored chemical energy in cold environments (Rosen and Spiegelman, 2014). It is therefore clear that adipose tissue plays varied and essential metabolic roles in the maintenance of energy homeostasis.

1.2.1.3 Endocrine roles of adipose tissue

In addition to its metabolic roles, in recent years it has become clear that adipose is a dynamic endocrine organ which plays an active role in the regulation of energy homeostasis. Adipose tissue can express and secrete a number of protein factors, termed adipokines, which are vital in the coordination of metabolic responses through autocrine, paracrine, and endocrine communication with distant tissues including the immune system and central nervous system (Kershaw and Flier, 2004; Clemente-Suárez et al., 2023). To date, hundreds of adipokines have been discovered through proteomic analysis of the adipose tissue 'secretome', with several adipokines being investigated as biomarkers for metabolic disease phenotypes (Lehr et al., 2012).

Leptin was the first adipocyte-secreted hormone to be identified with mutations in its gene leading to obesity in *ob*/*ob* 'obese' mouse strains, and parabiosis (whole blood transfer) experiments concluding that this effect was due to a circulating factor (Zhang et al., 1994; Richard et al., 2020). Similarly, mutations in the leptin receptor, expressed predominantly in the central nervous system but also peripherally in hepatocytes and pancreatic ß-cells, were identified as the main driver for obesity in the *db*/*db* 'diabetes' mouse strain (Tartaglia et al., 1995; Richard et al., 2020). Circulating leptin levels are strongly correlated with body fat mass in both mice and humans, thus highlighting its role as a sensor of available energy stores and allowing the regulation of appetite, metabolism, and energy homeostasis (Frederich et al., 1995; Maffei et al., 1995). The expression and secretion of leptin is tightly regulated, and leptin signalling is responsible for decreasing body weight by reducing appetite and increasing energy expenditure through behavioural and metabolic effects as well as promoting inflammation (Rosen and Spiegelman, 2014).

Adiponectin is another highly expressed adipokine, with incredibly high circulating concentrations of 2-20 µg/mL (Turer and Scherer, 2012). However, unlike leptin, adiponectin secretion is inversely correlated with body fat, meaning that lean individuals have higher circulating adiponectin than obese individuals (Hu et al., 1996). Adiponectin receptors are widely expressed throughout the body, including in the liver, immune cells, pancreas, and peripheral tissues, and adiponectin consequently has a range of insulin

sensitising, anti-inflammatory and anti-apoptotic effects (Kershaw and Flier, 2004; Turer and Scherer, 2012; Rosen and Spiegelman, 2014).

Additionally, cytokines including interleukin 6 (IL-6) and tumor necrosis factor (TNF) and the chemokine monocyte chemoattractant protein 1 (MCP1) are also expressed and secreted by adipose tissue, allowing them to be considered as adipokines (Kershaw and Flier, 2004). These immune factors are likely secreted by a combination of adipocytes and immune cells such as macrophages, and their expression is positively correlated with obesity (Clemente-Suárez et al., 2023). The role of inflammation in the development of insulin resistance and metabolic disease will be discussed in subsequent sections.

These adipose-secreted factors, as well as several others including resistin, visfatin and the lipocalin carrier proteins, have diverse functional effects throughout the body and therefore confirm the importance of adipose as an endocrine organ (Rosen and Spiegelman, 2014). The disruption of endocrine function during obesity and metabolic disease highlights the significance of these roles in metabolic regulation (Kershaw and Flier, 2004).

1.2.2 Dysfunction of adipose tissue in metabolic disease

Adipose tissue has a high degree of plasticity which is essential for it to achieve its primary metabolic and endocrine functions (Sakers et al., 2022). When there is an energy surplus, adipose tissue can expand through an increase in adipocyte size - hypertrophy – or through an increase in adipocyte number – hyperplasia – as well as associated structural changes in the ECM to accommodate lipid storage (Richard et al., 2020), with hyperplasia suggested to be the most metabolically favourable mechanism. However, when the capacity of the tissue to expand is exceeded, further energy surplus can become pathological, leading to cellular stress and impaired adipokine signalling (Sakers et al., 2022).

As adipose tissue expands, the distance between hypertrophic adipocytes and the vasculature increases, leading to hypoxia. Furthermore, hypertrophic adipocytes themselves can be larger than the typical distance limit for oxygen diffusion (Mirabelli et al., 2024). Consequently, this hypoxic environment can activate the oxygen-sensitive transcription factor hypoxia-inducible factor 1α

(HIF-1α) driving pro-inflammatory stress responses and metabolic dysfunction, as well as increased adipocyte death (Rosen and Spiegelman, 2014). Despite the demand for oxygen, angiogenesis is impaired in dysfunctional adipose tissue, although the mechanisms for this are not fully understood (Crewe et al., 2017).

In addition, adipocyte expansion requires remodelling of the ECM, however in obesity, excessive accumulation of ECM components including collagens and fibronectin can lead to fibrosis (Marcelin et al., 2022). Fibrosis can then drive adipocyte dysfunction through physical constraint to tissue expansion as well as driving differentiation of ADSCs towards fibroblast-like phenotypes rather than adipocytes (Sakers et al., 2022) and increasing adipose tissue inflammation (Richard et al., 2020). Together, these mechanisms impair the capacity of adipocytes to take up and store lipid appropriately, leading to elevated circulating lipid levels and ectopic accumulation in tissues such as the liver and skeletal muscle, known to be a significant driver of systemic insulin resistance (Heilbronn et al., 2004).

The endocrine activity of adipose tissue is also disrupted during metabolic disease, with altered adipokine signalling contributing to insulin resistance and further metabolic dysfunction. Elevated leptin levels are observed in obese individuals, although leptin resistance can develop which hinders its ability to regulate food intake and energy expenditure (Kershaw and Flier, 2004). Conversely, adiponectin levels are reduced in obese individuals, leading to a reduction in its anti-inflammatory and insulin-sensitising properties (Clemente-Suárez et al., 2023). Finally, the release of pro-inflammatory adipokines including TNF, IL-6 and MCP1 by immune cells and adipocytes in adipose tissue is elevated in obesity, leading to a state of chronic adipose tissue inflammation (Sewter et al., 1999; Chouchani and Kajimura, 2019; Rohm et al., 2022).

Together, the combination of these disturbances can drive the development of insulin resistance and associated metabolic consequences, as well as wider endocrine complications at a systemic level. However, the molecular basis of adipose tissue dysfunction remains unclear, particularly when considering the complex interactions and temporal organisation between the pathologies discussed. It is therefore clear that additional insight is required to fully understand adipose tissue in pathophysiological contexts.

1.2.3 Role of inflammation in metabolic disease

In dysfunctional adipose tissue, a combination of the above factors can lead to a pro-inflammatory response in adipose tissue, and this low-level chronic inflammation is thought to be an important driver for the development of insulin resistance (Olefsky and Glass, 2010; Crewe et al., 2017).

Resident immune cells are essential to the normal function of adipose tissue, however during metabolic disease there is elevated infiltration of monocyte-derived macrophages which become activated in response to tissue hypoxia, adipocyte death, and fibrosis (Li et al., 2023b). This critical discovery was initially shown in murine models of genetic and diet induced obesity (Weisberg et al., 2003; Xu et al., 2003) and later confirmed in humans (Harman-Boehm et al., 2007). It is thought that extreme adipocyte expansion and hypoxia cause increased adipocyte cell death through apoptosis and necrosis, triggering a wound healing response which promotes further macrophage recruitment into 'crown-like structures' surrounding dying cells (Crewe et al., 2017). Furthermore, resident adipose tissue macrophages undergo a phenotypic switch from the anti-inflammatory M2 state to an activated pro-inflammatory M1 state (Sakers et al., 2022). M1-type cells release pro-inflammatory cytokines such as TNF, IL-1 and IL-6 as well as generating reactive oxygen species (ROS) which can cause oxidative damage to neighbouring cells, resulting in further inflammatory and fibrotic activity (Crewe et al., 2017).

The importance of pro-inflammatory cytokines in the development of insulin resistance was elucidated in the early 1990s, where it was shown that TNF was upregulated in obese rodents, and that inhibition of TNF using a neutralising antibody was able to improve the insulin sensitivity of these animals (Hotamisligil et al., 1993). Subsequently, several studies have supported the finding that cytokines produced by both recruited immune cells and hypertrophic adipocytes themselves can drive metabolic effects in local and systemic tissues (de Luca and Olefsky, 2008; Olefsky and Glass, 2010; Gasmi et al., 2020). For example, TNF induces downregulation of GLUT4 in adipocytes but also in liver, as well as impairing insulin signalling both directly through insulin receptor substrate phosphorylation, and indirectly by increasing the concentration of circulating FFAs (Kershaw and Flier, 2004). Crucially, in obesity, this pro-

inflammatory response fails to resolve, resulting in low level chronic inflammation which impairs insulin and adipokine signalling and driving further adipose tissue dysfunction (Richard et al., 2020; Kawai et al., 2021).

The clinical relationship between low level chronic inflammation and obesity, T2D and CVD is well-established, with pro-inflammatory biomarkers closely associated with the incidence and outcomes of metabolic disease (Pradhan et al., 2001; Tsalamandris et al., 2019; Wu and Ballantyne, 2020). The interaction between metabolism and inflammation may therefore be a promising direction towards new therapeutic intervention for metabolic disease (Tsalamandris et al., 2019; Li et al., 2023b). However, despite significant advancement in this area, much of the mechanistic detail of these complex metabolic-immune interactions remains to be elucidated. Therefore, it is essential to improve our understanding of the molecular mechanisms regulating adipose tissue inflammation in order to address the burden of metabolic disease.

1.3 G Protein-Coupled Receptors

1.3.1 Overview

G Protein-Coupled Receptors (GPCRs) are the largest family of transmembrane receptors in the mammalian genome, and act to transduce extracellular signals including hormones, odours and neurotransmitters into diverse biological effects through a variety of intracellular signalling pathways (Pierce et al., 2002; Odoemelam et al., 2020; Yang et al., 2021). Over 800 members of the GPCR superfamily have been identified in humans and share a common structure featuring seven transmembrane (TM) helical domains separated by extracellular and intracellular loop domains, with extracellular N-terminal and cytosolic C-terminal regions differing in size and function according to the specific receptor class **(Figure 1.4)** (Herrera et al., 2025).

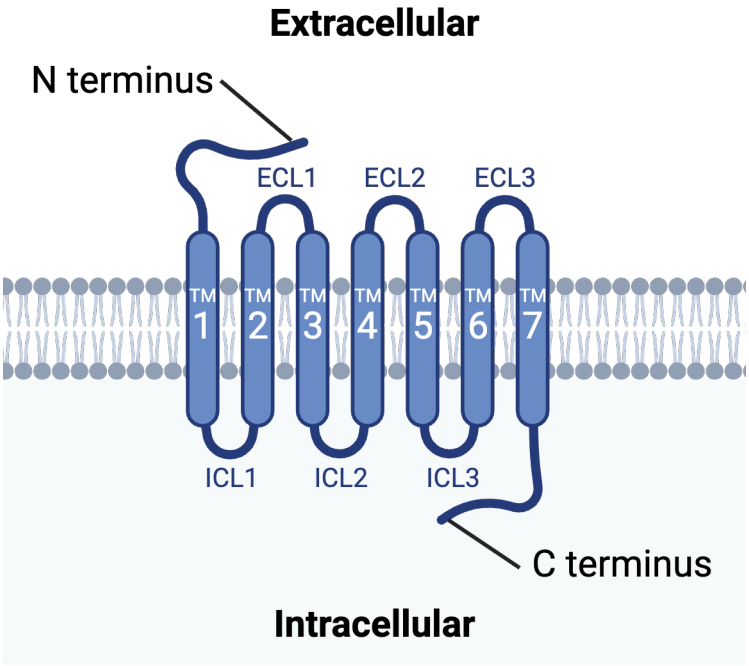

Figure 1.4 - Schematic diagram of a typical GPCR with transmembrane (TM), extracellular loop (ECL) and intracellular loop (ICL) domains indicated.

Following the completion of the human genome project, a complete list of potential GPCRs was compiled and classed according to phylogenetic similarity to the rhodopsin (class A), secretin (class B), metabotropic glutamate (class C) or frizzled (class F) receptors (Fredriksson et al., 2003; Foord et al., 2005). Receptors are then grouped into subfamilies based on their common ligands and given a specific name often according to their endogenous ligand, but occasionally after drugs which act on them (e.g. cannabinoid and opioid

receptors) (Alexander et al., 2023). Orphan receptors are those for which the endogenous ligand is unknown, and receptors can be ‘deorphanised’ and renamed when two independent publications confirm ligand binding and receptor activity at a suitable potency for biological activity (Davenport et al., 2013; Alexander et al., 2023).

Historically, GPCRs have been incredibly successful drug targets, with ~35% of currently FDA-approved therapeutics acting either directly or indirectly through GPCRs (Hauser et al., 2017; Lorente et al., 2025), including the Glucagon-like Peptide-1 (GLP-1) receptor agonists now routinely used for the treatment of metabolic disease. Given this therapeutic success, it is important to continue improving our understanding of the complex signalling and regulatory pathways that control the behaviour of GPCRs in pathological contexts.

1.3.2 GPCR Signalling

In addition to their conserved structures, the superfamily of GPCRs share a conserved activation mechanism leading to a set of downstream signalling cascades **(Figure 1.5)**. Recent advances in X-ray crystallography and cryogenic electron microscopy (cryo-EM) techniques have allowed the rapid generation of high-quality structures of GPCRs in complex with various binding partners, with molecular dynamics stimulations further enhancing our understanding of GPCR molecular mechanisms including interactions with ligands, conformational changes, and downstream signalling (Conflitti et al., 2025). GPCR signalling is activated by the binding of a (typically) extracellular ligand, which induces a conformational change in the receptor involving an outward movement of TM6 (Rasmussen et al., 2011). This exposes an intracellular pocket between TM5 and TM6 which allows interaction with a heterotrimeric G protein, consisting of α, ß and γ subunits, driven predominantly by the C-terminal α5-helix of the Gα-subunit (Rasmussen et al., 2011). The binding of the G protein to the receptor facilitates the exchange of GDP on the Gα subunit to GTP, leading to the dissociation of the Gα from the Gßγ subunits and allowing these to activate further downstream signals (Ibay and Gilchrist, 2021). The intrinsic GTPase activity of the Gα subunit allows hydrolysis of the bound GTP to GDP and reassociation of the Gα and Gßγ subunits to return to a resting state **(Figure 1.5)**. The Gα subunit is typically considered to be the driver of downstream

signalling, however the Gβγ complex can also trigger its own independent signalling cascades primarily through ion channels and activation of phospholipase C (PLC) (Lin and Smrcka, 2011; Tennakoon et al., 2021).

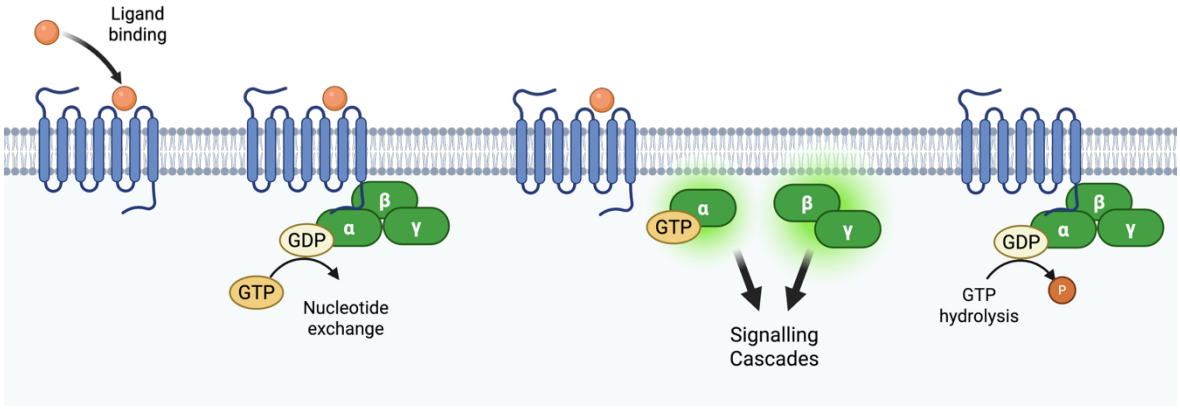

Figure 1.5 – Schematic diagram of the canonical G protein activation mechanism. Ligand binding induces a conformational change in the receptor which facilitates the recruitment of a heterotrimeric G protein complex. GDP is exchanged for GTP, leading to dissociation of the Gα from the Gβγ subunits and downstream signalling. The intrinsic GTPase activity of the Gα subunit allows hydrolysis of GTP back to GDP and reassociation of the G protein heterotrimer.

There are 16 Gα genes identified in humans which are divided into 4 families – Gs, Gi/o, Gq/11 and G12/13 – based on their subsequent downstream signalling cascades **(Figure 1.6)**. The Gs family, comprising $G\alpha_s$ and $G\alpha_{olf}$, activate adenylyl cyclase leading to an increase in the second messenger cAMP and activation of PKA which can activate further downstream targets. Conversely, the Gi/o family, comprising $G\alpha_{i1\text{-}3}$, $G\alpha_o$, $G\alpha_z$, $G\alpha_{t1\text{-}2}$ and $G\alpha_{gust}$, inhibits adenylyl cyclase and consequently reduces cAMP levels. The Gq/11 family of $G\alpha_q$, $G\alpha_{11}$, $G\alpha_{14}$ and $G\alpha_{15}$ activates PLC at the plasma membrane, which cleaves phosphatidylinositol 4,5-bisphosphate (PIP_2) into inositol trisphosphate (IP_3), which drives intracellular calcium release from the endoplasmic reticulum, and diacylglycerol (DAG), which along with the increased intracellular calcium, activates protein kinase C (PKC) driving further downstream responses. Finally, the G12/13 family of $G\alpha_{12}$ and $G\alpha_{13}$ activate guanine nucleotide exchange factors (GEFs) for the Rho small GTPases, leading to cytoskeletal rearrangements.

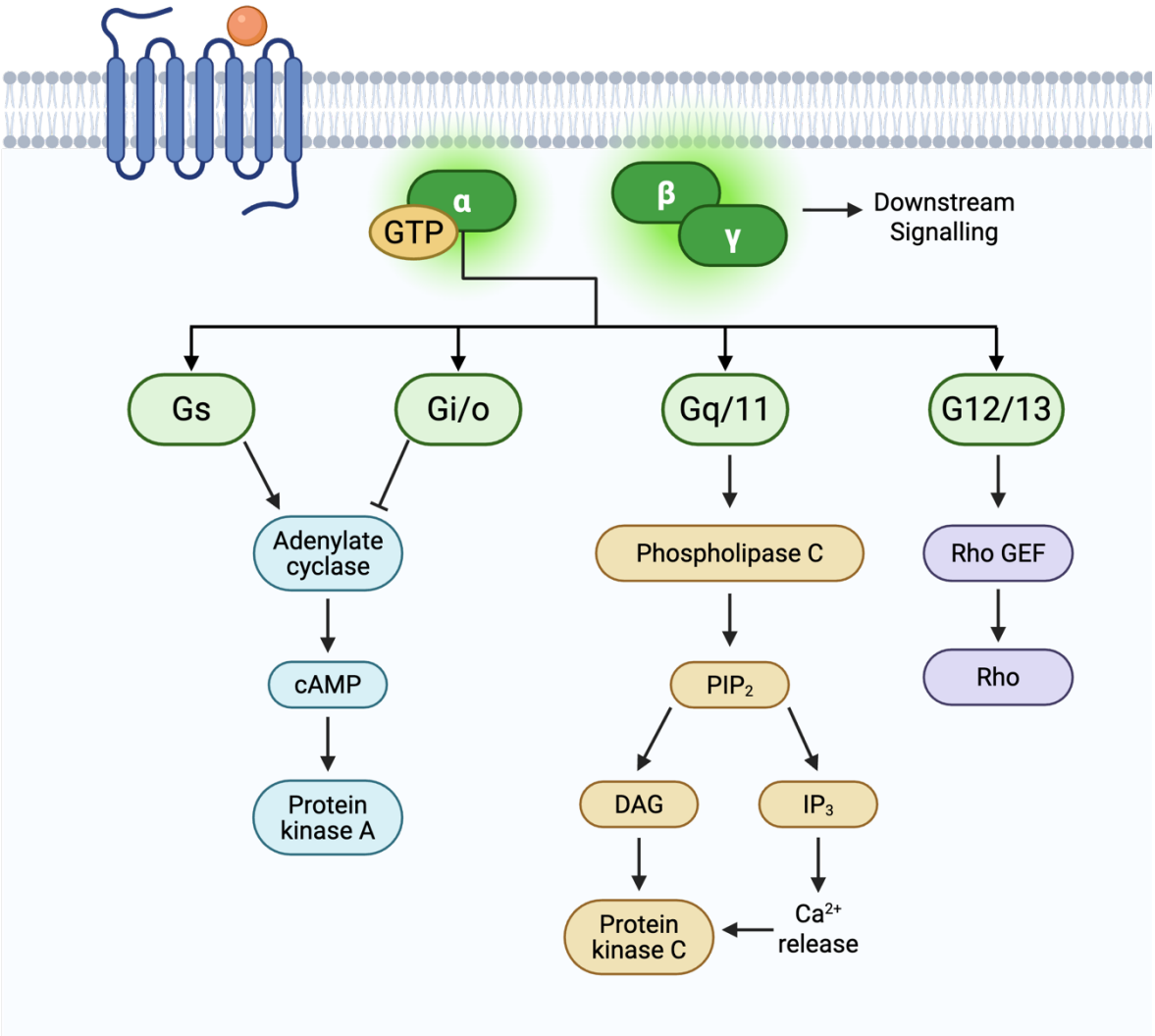

Figure 1.6 – The Gα subunit is the primary determinant of downstream signalling cascades. The 16 members of the Gα family can be grouped according to their coupling to secondary messengers and downstream signalling effectors. The Gβγ complex can also trigger its own independent signalling cascades.

Although some GPCRs will have a coupling preference to a single G protein family, many receptors are now known to be more promiscuous and are able to couple to several different G proteins. The dominant coupling can change based on factors including receptor localisation, posttranslational modifications and the specific conformational change induced by any given ligand (Vaidehi et al., 2021). Biased agonism describes the ability of a ligand to differentially activate GPCR signalling through a specific pathway (Kolb et al., 2022). Development of compounds which exhibit biased signalling among G protein families is emerging as a novel therapeutic strategy to preferentially activate specific downstream effects (Caroli et al., 2023; Lorente et al., 2025).

Termination of GPCR signalling occurs by the phosphorylation of the GPCR intracellular loops or C-terminal tail by G-protein receptor kinases (GRKs) which facilitates the interaction with arrestin proteins **(Figure 1.7)**. Arrestin-1 (visual arrestin) and arrestin-4 (cone arrestin) are only expressed in the retina and will not be discussed further, whereas arrestins-2 and -3, also known as ß-arrestin-1 and -2, are expressed ubiquitously. Following receptor phosphorylation, ß-arrestin is recruited where its N domain can interact with the negatively charged phosphorylated residues on the GPCR, with the arrestin finger loop structure interacting with the receptor core and the arrestin C domain associating predominantly with the plasma membrane (Gurevich and Gurevich, 2019; Gomes et al., 2025). Arrestin recruitment both occludes further G protein binding and can provide a scaffold for receptor internalisation via clathrin-mediated endocytosis (Barreto et al., 2021). If internalised, arrestin is released and the receptor is dephosphorylated for recycling to the plasma membrane or degradation (Ibay and Gilchrist, 2021). The arrestin proteins themselves can also act as signal transducers independently of G protein signalling, often through scaffolding interactions activating kinase cascades (Jean-Charles et al., 2017). Biased ligands therefore also exist which can direct GPCR activation through either G protein or arrestin pathways, with arrestin vs G protein bias being extensively explored in the drug discovery industry to develop therapeutics with reduced side effects (Kolb et al., 2022; Lorente et al., 2025). These layers of signalling complexity allow GPCRs to tightly regulate the cellular response to a diverse range of cues and highlights the need for advanced methodologies to fully understand these networks.

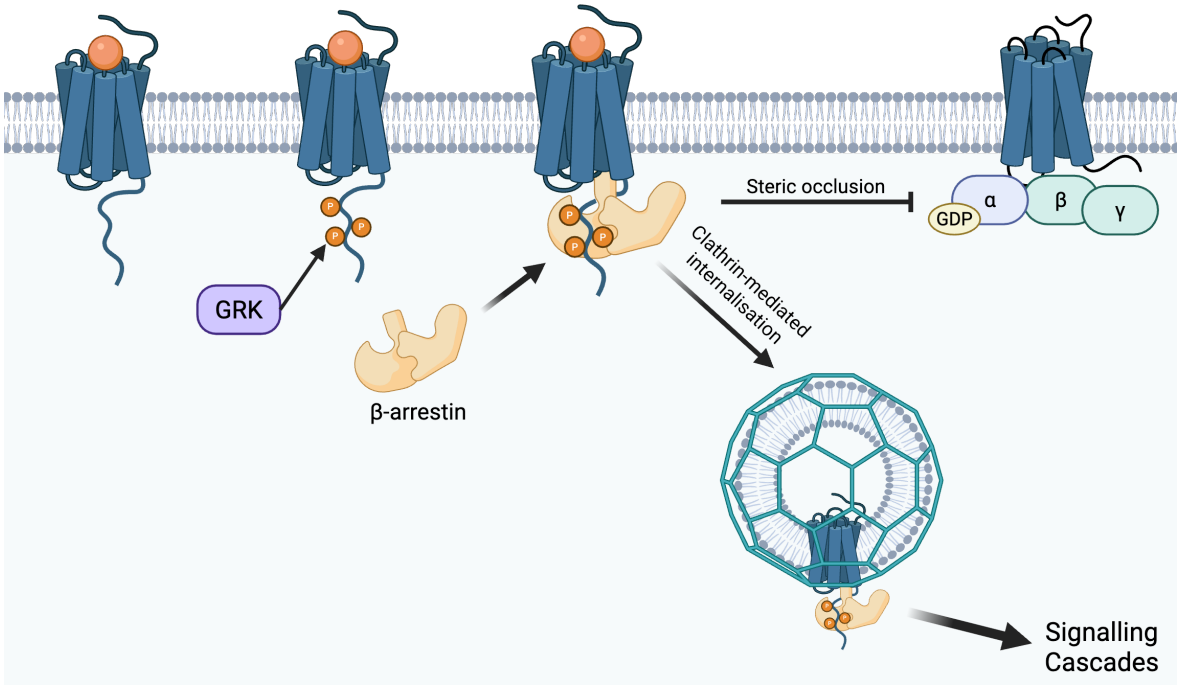

Figure 1.7 – β-arrestin is recruited to GPCRs following phosphorylation by GRKs. β-arrestin recruitment occludes binding of heterotrimeric G proteins as well as facilitating clathrin-mediated receptor internalisation and driving further signalling cascades.

1.3.3 Metabolite-sensing GPCRs and their role in metabolic disease

In addition to typical hormonal, neurotransmitter and odorant signalling, there are several GPCRs which are activated by endogenous ligands perhaps better known for their roles as metabolic intermediates. These metabolite-sensing GPCRs (m-GPCRs) respond to molecules such as amino acids, short carboxylic acid metabolites, and triglyceride metabolites which are obtained from nutrients, the gut microbiota or released by endocrine and metabolic tissues (Blad et al., 2012; Husted et al., 2017). m-GPCRs can therefore respond to these signals of metabolic activity and energy levels to further regulate energy metabolism, for example by modulating lipolysis, hormone secretion, and interactions with the immune system (Blad et al., 2012). It is therefore unsurprising that many of these receptors have been recognised as key mediators of metabolic diseases, and have been investigated for their therapeutic potential in the treatment of obesity and T2D but also other inflammatory disorders including cancer, chronic pain and rheumatoid arthritis (Cosín-Roger et al., 2020; Duncan et al., 2023; Yang et al., 2024; Pușcașu et al., 2025).

m-GPCRs include receptors for free fatty acids (FFA1-4 and GPR84) and hydroxycarboxylic acids (HCA_{1-3}) as well as the succinate receptor (SUCNR1). These receptors are highly expressed in enteroendocrine cells within the gastrointestinal tract and pancreatic cells where they can regulate secretion of key metabolic hormones including GLP-1 and insulin. For example, the long chain fatty acid receptors FFA1 and FFA4 have been reported to increase secretion of GLP-1 through a Gq (and possibly Gs) pathway (Hirasawa et al., 2005; Hauge et al., 2015), with FFA1 also enhancing glucose dependent insulin secretion directly in pancreatic ß-cells (Itoh et al., 2003).

In adipose tissue, several Gi coupled m-GPCRs are expressed which likely act as negative regulators of lipolysis driven by Gs-coupled ß-adrenoceptor activation (Husted et al., 2017). These receptors include a short-chain fatty acid receptor (FFA2), SUCNR1, and the HCA receptors activated by lactate (HCA_1), ß-hydroxybutyrate (BHB) (HCA_2) and 3-hydroxyoctanoate (HCA_3) (Brown et al., 2003; Taggart et al., 2005; Regard et al., 2008). The ligands for these receptors are likely released in response to metabolic stress; short-chain fatty acids are typically derived through digestion of dietary fibre by the gut microbiota but may also be produced by the liver during alcohol metabolism (Moffett et al., 2020; Wang et al., 2023) and by pancreatic ß-cells in high glucose conditions (Tang et al., 2015). As an intermediate of the citric acid cycle, succinate is usually localised to the mitochondria, however it can accumulate and be excreted from cells during periods of hypoxia (Ariza et al., 2012; de Castro Fonseca et al., 2016). BHB and 3-hydroxyoctanoate are released by the liver following ß-oxidation of circulating fatty acids during periods of fasting (Newman and Verdin, 2017).

FFA4 is also highly expressed in adipocytes where it has also been shown to inhibit lipolysis through Gi mediated pathways (Satapati et al., 2017; Husted et al., 2020; Alshammari et al., 2025). As the endogenous ligands of FFA4 are long chain fatty acids, it has been proposed that this regulation is through autocrine signalling by adipocytes themselves (Husted et al., 2020). Recently, it has been reported that FFA4 is in fact located intracellularly on the endoplasmic reticulum of adipocytes and can therefore undergo ‘intracrine’ signalling, whereby the fatty acids released from lipid droplets can directly activate FFA4 without requiring extracellular release (O’Brien et al., 2025).

Additionally, FFA4 agonism has been reported to improve adipogenesis, perhaps through a positive feedback loop of FFAs released during differentiation (Gotoh et al., 2007; Song et al., 2016; Alshammari et al., 2025), and improve glucose uptake, likely through a Gq-mediated pathway (Oh et al., 2010; Hudson et al., 2013). FFA4 is a key mediator in the regulation of adipocyte function, and it is therefore unsurprising that FFA4 knockout in high-fat-diet-fed murine models leads to increased body weight, reduced glucose tolerance and development of fatty liver, and a deleterious variant (p.R254H/p.R270H) in human populations associates with an increased risk of obesity (Ichimura et al., 2012).

m-GPCRs have also been reported to play a crucial role in the interaction between adipocytes and immune cells in the development of metabolic disease. In particular, the FFA4, SUCNR1 and HCA_2 receptors are expressed in both adipocytes and infiltrating macrophages, and their respective ligands have been proposed to form paracrine signalling loops which would facilitate communication between these cell types in adipose tissue (Husted et al., 2017; Duncan et al., 2023). FFA4 activation by omega-3 fatty acids or a synthetic agonist can inhibit pro-inflammatory cytokine responses and chemotaxis in macrophages, leading to reduced macrophage infiltration of adipose tissue *in vivo* (Oh et al., 2010, 2014). HCA_2 can also attenuate pro-inflammatory responses in macrophages exposed to lipopolysaccharide (LPS) by reducing production of key cytokines and chemokines (Shi et al., 2017; Mandrika et al., 2018). In contrast, although SUCNR1 is expressed in macrophages, controversial studies have reported both pro- and anti-inflammatory roles of this receptor (Duncan et al., 2023).

However, despite the therapeutic interest around these receptors, it has been challenging to fully understand their complex regulation and mechanistic interactions within the limitations of our existing model systems. The expression of m-GPCRs is highly tissue-specific and often differentially regulated by metabolic state (Husted et al., 2017). Crucially, many experimental set ups do not appropriately consider the source and concentrations of the metabolite ligands, instead exogenously applying artificially high concentrations of synthetic ligands to measure receptor-mediated effects. It is therefore critical to establish novel, physiologically relevant cell models to investigate the signalling,

regulation, and function of m-GPCRs in the development and treatment of metabolic disease.

1.3.4 Methods for studying GPCR signalling

Traditional methods to measure the pharmacology and signalling of GPCRs have typically relied on accumulation of downstream secondary messengers such as cAMP and IP_1, measuring intracellular calcium responses, as well as using radioligand binding assays to determine compound affinity (Pearce et al., 2025). However, these assays can be low-throughput, costly and often only give endpoint measurements, giving no consideration to response kinetics, and are therefore susceptible to interference from interacting signalling pathways and feedback loops (Olsen and English, 2023). Therefore, new approaches were required to facilitate more direct and real time measurement of GPCR activity in living cells.

Genetically encoded biosensors are now widely used to measure almost every aspect of the GPCR signalling cascade including ligand binding, conformational changes, and interactions with G proteins and arrestin **(Figure 1.8)** (Hudson, 2017; Olsen and English, 2023). These technologies are often based on Resonance Energy Transfer (RET) or fragment complementation assays used to measure changes in protein-protein interactions **(Figure 1.9).**

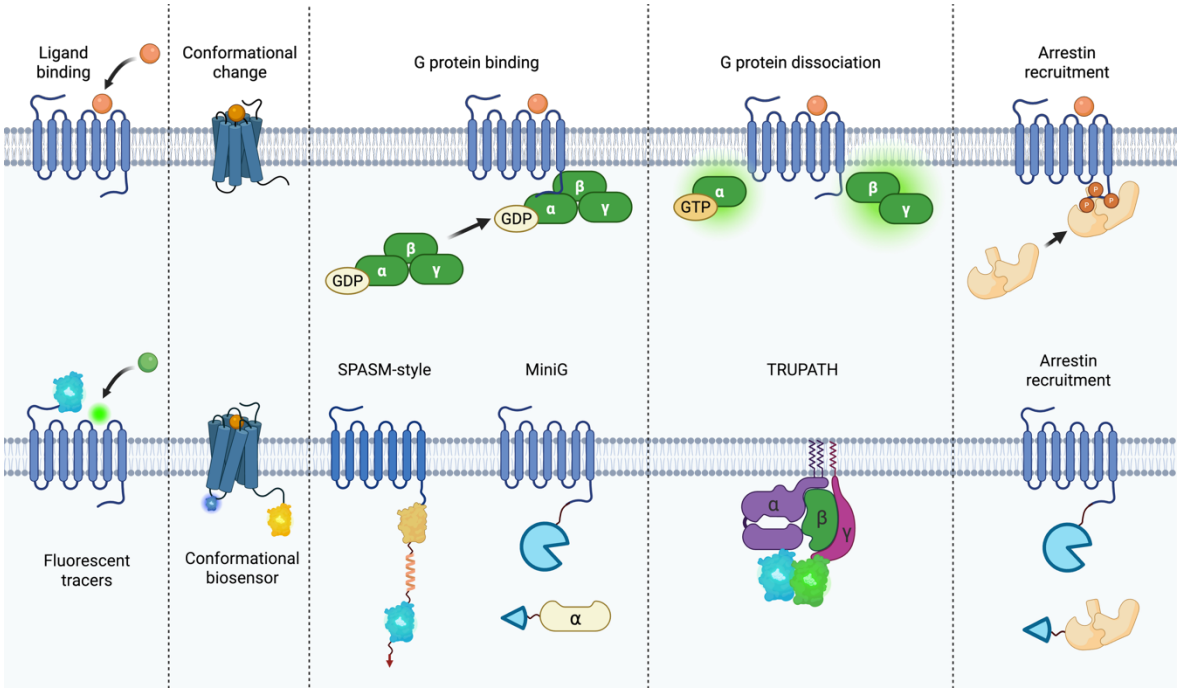

Figure 1.8 – GPCR signalling events (top) can be measured using genetically encoded biosensors (bottom). Examples of biosensors are given which can measure different aspects of the GPCR signalling cascade. GPCR activation is initiated by ligand binding, which can be measured using BRET between fluorescent ligands and luciferase-tagged receptors (Stoddart et al., 2015). GPCR conformational changes can be measured using intramolecular receptor biosensors which measure changes in distance between intracellular loop 3 (ICL3) and the C terminus (Vilardaga et al., 2003). G protein binding can be measured using intramolecular SPASM-style biosensors (Malik et al., 2013) or intermolecular recruitment of miniG proteins (Wan et al., 2018). Dissociation of Gα and Gβγ subunits can be measured as a reduction in BRET using TRUPATH biosensors (Olsen et al., 2020). Recruitment of tagged arrestin can be measured using BRET or NanoBiT to labelled receptors (Bertrand et al., 2002).

Förster RET (FRET) describes a phenomenon whereby if two fluorescent molecules come into close proximity (10-100 Å), nonradiative dipole-dipole energy transfer can occur between an excited donor fluorophore with an emission spectrum which overlaps with the excitation spectrum of an acceptor fluorophore, leading to emission at a lower energy wavelength **(Figure 1.9A)** (Sekar and Periasamy, 2003). Bioluminescent RET (BRET) follows a similar principle however the donor molecule is a bioluminescent protein which generates light by a chemical reaction following oxidation of a substrate **(Figure 1.9B)** (Pfleger and Eidne, 2006). Fragment complementation assays such as the NanoBiT split luciferase system (Dixon et al., 2015) offer an alternative to RET based approaches where a bioluminescent protein is split into two non-functional parts and can recombine to generate a full-length light-emitting reporter **(Figure 1.9C)** (Wehr and Rossner, 2016). With all three of these methodologies, the two components of the biosensor are fused to proteins of interest and changes in the luminescent signal emitted are recorded in response to changes in the distance between the two fusion proteins. However, while the

RET measurements are expressed as a ratio of donor/acceptor wavelengths, split luciferase sensors typically are recorded as raw luminescence reads, resulting in increased sensitivity at low expression levels and a greater dynamic range.

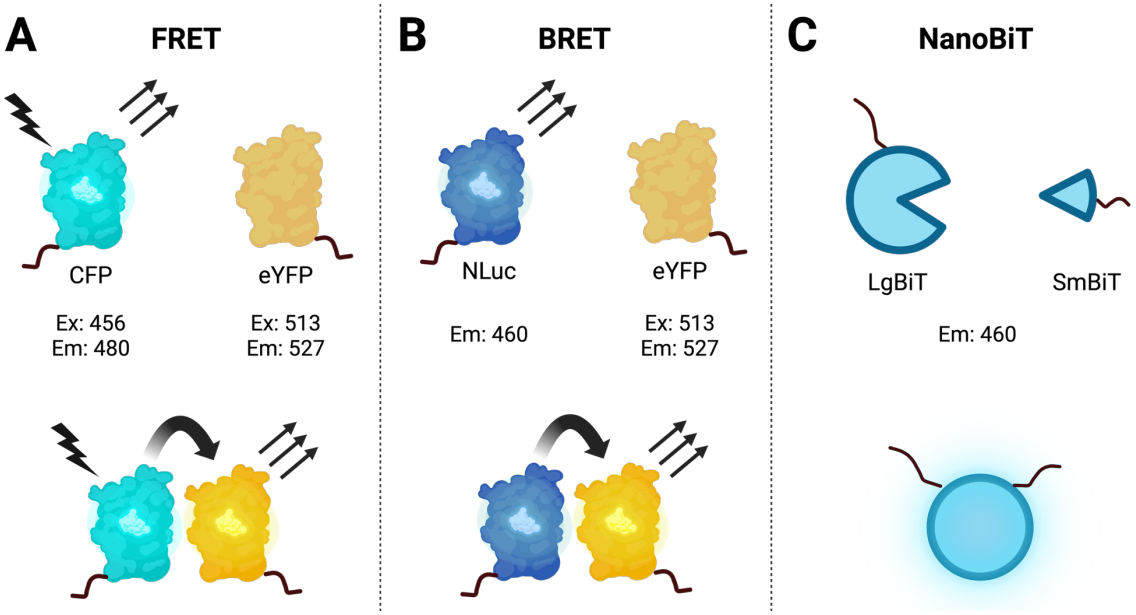

Figure 1.9 - Schematic diagrams indicating the mechanisms of FRET (A), BRET (B) and NanoBiT split luciferase (C). Excitation (Ex) and emission (Em) wavelengths for each fluorescent or bioluminescent protein are indicated in nm.

FRET, BRET and split luciferase biosensors have been reported for several stages of the GPCR signalling cascade and have allowed researchers to gain a deeper mechanistic understanding of signal transduction pathways, including the assessment of biased ligands **(Table 1.2)** (Olsen and English, 2023; Demby and Zaccolo, 2024). Broadly, biosensors can be grouped based on the specific stage of signalling measured (e.g. ligand binding, conformational change, G protein/arrestin recruitment or downstream second messengers) as well as the detection mechanism (BRET, FRET, NanoBiT) and other specific features such as whether the biosensors are intra- or inter-molecular, and whether they measure modified or endogenous receptor activity.

Many of these biosensors require the expression of modified forms of the receptor which may impact their ability to signal through downstream pathways, and constructs are expressed on heterologous promoters, meaning normal transcriptional regulation will not apply (Wright et al., 2024). Several methods have therefore moved to a ‘bystander’ approach which allows measurement of unmodified receptor activation through interactions with biosensor components localised to adjacent cellular compartments. For example, by using fluorescent

proteins (FPs) tagged to different subcellular compartments such as the plasma membrane, endosomes or the golgi with luciferase-tagged G proteins or arrestins, it is possible to follow GPCR activity at intracellular locations (Demby and Zaccolo, 2024).

Table 1.2 - Examples of available genetically encoded biosensors to measure GPCR signalling. Adapted from (Kim et al., 2022; Olsen and English, 2023; Demby and Zaccolo, 2024)

GPCR Signalling Step	Sensor Name	Detection Mechanism	Reference
Ligand binding	Fluorescent tracers	BRET between luciferase-tagged receptor and fluorescent ligand	(Stoddart et al., 2015; Christiansen et al., 2016)
	Ligand binding domains e.g. (i)GluSnFR	FRET between FPs or circularly permutated fluorescent protein (cpFP) flanking a (e.g.) glutamate binding protein on receptor N-terminus	(Tsien, 2006; Hires et al., 2008; Marvin et al., 2013)
Receptor conformational change	Intramolecular receptor sensors	FRET or BRET between receptor C-terminus and intracellular loop 3 (ICL3)	e.g. (Vilardaga et al., 2003; Hoffmann et al., 2005)
		cpFP in ICL3	e.g. (Patriarchi et al., 2018; Sun et al., 2018)
G protein recruitment	SPASM (systematic protein affinity strength modulation)	Receptor tagged with FRET or BRET components separated by an ER/K flexible helix and attached to full length or C-terminal fragments of Gα subunits	(Malik et al., 2013, 2017; Mackenzie et al., 2019)
	MiniG	BRET or NanoBiT between miniG proteins and receptor or plasma membrane	(Carpenter and Tate, 2016; Wan et al., 2018)
G protein activation	BERKY (BRET biosensor with ER/K linker and YFP)	BRET between lipid-anchored donor and acceptor separated by an ER/K flexible	(Maziarz et al., 2020)

		helix, and attached to a peptide which binds GTP-bound Gα subunits	
	GEMTA (G protein effector membrane translocation assays)	BRET between luciferase-tagged downstream effectors and FP targeted to plasma membrane	(Avet et al., 2022)
	ONE-GO (One vector G-protein Optical)	BRET between NLuc-tagged Gα-GTP detector and YFP-tagged Gα	(Janicot et al., 2024)
G protein dissociation	Dissociation between Gα and Gβγ e.g. TRUPATH	FRET, BRET or NanoBiT between tagged Gα and Gβγ subunits	(Janetopoulos et al., 2001; Inoue et al., 2019; Olsen et al., 2020)
	Association between Gβγ and GRKs	FRET or BRET between dissociated Gβγ and GRK3	(Hollins et al., 2009; Masuho et al., 2015b)
ß-arrestin recruitment	Labelled receptor/arrestin constructs	FRET or BRET between labelled receptor and arrestin molecules	(Bertrand et al., 2002)
	Bystander arrestin recruitment	BRET between luciferase-tagged arrestin and FP targeted to plasma membrane	(Donthamsetti et al., 2015; Namkung et al., 2016)
	Arrestin conformational biosensors	Intramolecular BRET between N-terminal luciferase and FP located elsewhere within arrestin molecule to measure conformational dynamics	(Charest et al., 2005; Lee et al., 2016)
Second messengers	Calcium sensors e.g. cameleon or G-CaMP	Intramolecular FRET or cpFP with calmodulin binding domain	(Miyawaki et al., 1997; Nakai et al., 2001)
	cAMP sensors e.g. Epac	Intramolecular FRET, BRET or cpFP with Epac binding domain	e.g. (Nikolaev et al., 2004)

	IP_3 sensors e.g. LIBRA	Intramolecular FRET or BRET with IP_3 binding domain	(Tanimura et al., 2004)
	DAG sensors e.g. Daglas	Intra- or intermolecular FRET or BRET, often using DAG-binding motif to translocate (part of) the biosensor to the plasma membrane	(Violin et al., 2003; Sato et al., 2006)
	PKA or PKC activity sensors e.g. AKAR/CKAR	FRET or BRET components separated by phosphorylatable sequence and phosphoamino acid binding domain	(Zhang et al., 2001; Violin et al., 2003)

Overall, genetically encoded biosensors have allowed researchers to develop a deeper mechanistic understanding of GPCR activity through real-time measurement of signalling events at virtually every stage of the downstream cascade. However, these biosensors still require expression of engineered constructs which may interfere with these signalling cascades, and are typically used in artificial *in vitro* cell systems which have limited physiological relevance to human disease. Therefore, it is crucial to progress methods of expressing these biosensors in complex cell models to allow us to better characterise the role of GPCR signalling in metabolic disease.

1.4 Existing Methods to Study Adipose Tissue

As discussed throughout this chapter, adipose is a dynamic and complex organ comprised of several diverse cell types which contribute to its metabolic and endocrine roles. Therefore, it is essential to develop experimental systems which recapitulate this complexity in order to improve our understanding of adipose tissue function and dysfunction in the context of metabolic disease.

1.4.1 *In vivo* models

Much of our knowledge about adipose tissue and metabolic disease has been obtained from *in vivo* studies. Rodent models have provided an invaluable resource in understanding the systemic metabolic phenotypes associated with obesity as well as downstream disease progression (Suleiman et al., 2019).

Genetically modified mouse strains are available including the commonly used *ob*/*ob* and *db*/*db* lines which develop obesity and show impaired metabolic function due to mutations in the leptin and leptin receptor genes respectively (Suleiman et al., 2019). Furthermore, strains with mutations in the insulin receptor or downstream signalling pathways show impaired insulin sensitivity (Nandi et al., 2004). Diet induced obesity models, where rodents are fed a high-fat diet for several weeks, are also commonly used for studies of obesity and related complications such as diabetes and cardiovascular disease (Wang and Liao, 2012). Finally, the prevalence of obesity means that adipose tissue dysfunction can also be studied directly in humans through large-cohort population studies which use biobank data to link genetic, phenotypic and lifestyle factors to metabolic health (Kivimäki et al., 2022).

The key advantage of *in vivo* approaches is that they allow for investigation of metabolic phenotypes at a systemic level, such as overall body and fat mass accumulation, ectopic lipid accumulation in tissues such as the liver, measurement of biomarkers such as blood glucose and TG concentrations and direct measurement of IR (de Moura e Dias et al., 2021). IR can be determined in humans and rodents using the hyperinsulinemic euglycemic clamp technique. Following a fast period, insulin is infused at a known rate and blood glucose is measured at frequent intervals while glucose or dextrose is given at a flexible

rate to keep levels constant, allowing glucose disposal rate and thus insulin sensitivity to be calculated (Muniyappa et al., 2008). However, these measurements are time consuming, labour intensive and the data can be challenging to interpret, so several other methods such as more straightforward oral or intraperitoneal glucose tolerance and intraperitoneal insulin tolerance tests have been proposed which can provide surrogate measurements if glucose clamp methods are not feasible (Muniyappa et al., 2008, 2009, 2019).

Although information gained from rodent studies is valuable, these approaches are expensive, highly regulated, and low throughput. Alternative *in vivo* approaches have been proposed such as an insulin resistant zebrafish model, which may be more suitable for higher throughput drug screening (Nam et al., 2021). Critically, the species-specific differences in adipose tissue distribution and function mean that findings from animal studies may not be completely relevant to human disease, and the complexity of working with whole organisms makes it challenging to deconvolute specific mechanistic details such as signalling pathways. Therefore, simplified *in vitro* model systems can provide a complementary approach for high-throughput or mechanistic studies.

1.4.2 2D *in vitro* cell culture models

In vitro cell culture models, where adipocytes are grown in monolayer cultures on glass or plastic vessels, have been widely used to study the intricate molecular pathways involved in normal adipocyte function.

Human adipocytes are perhaps one of the most accessible primary cell types to obtain for research purposes, as large quantities of fresh adipose tissue is collected from cosmetic procedures (Dufau et al., 2021). However, the mature adipocytes are fragile, only survive for a short time *ex vivo,* and cannot proliferate or be cryopreserved, making them challenging to manipulate (Dufau et al., 2021; Baganha et al., 2022). Consequently, most adipocyte cell cultures are established from preadipocyte cell types such as adipose-derived stromal cells (ADSCs), which can be isolated from human tissue, expanded *in vitro* and differentiated to an adipocyte-like phenotype (Lee and Fried, 2014). Although use of these patient-derived cells is vital for translational research, the total number of cells obtained is still limiting for higher-throughput studies and cells

typically only retain the capacity to differentiate for a small number of generations following isolation (Mazini et al., 2021). Furthermore, the strict regulatory requirements for human tissue use, lack of standardised protocols and high donor-to-donor variation observed has facilitated the isolation and/or engineering of immortalised cell lines which can be used as an alternative to primary ADSCs (Dufau et al., 2021).

3T3-L1 cells have been the most widely used preadipocyte cell model since their isolation in the 1970s (Green and Meuth, 1974). The native fibroblast phenotype can be differentiated into mature adipocytes using a cocktail of factors including insulin, the synthetic glucocorticoid dexamethasone, and the phosphodiesterase inhibitor 1-methyl-3-isobutylxanthine (IBMX), and adipogenesis can be further enhanced by addition of a PPARG agonist (Zebisch et al., 2012). 3T3-L1 cells have been used to study several aspects of adipocyte function and dysfunction, including the impact of specific compounds, nutrients, and genes on the regulation of adipogenesis and adipocyte function (Wang et al., 2014; Ruiz-Ojeda et al., 2016). Furthermore, IR can be induced in 3T3-L1 cells through treatments such as TNF, hypoxia, or high insulin concentrations (Lo et al., 2013). However, evidence from transcriptomics studies has suggested that each of these methods depict different features of *in vivo* IR, thus indicating that these models cannot fully recapitulate this complex pathophysiological state (Lo et al., 2013). Similarly, as these cells were isolated from Swiss 3T3 mouse embryos, there is significant evidence that they exhibit fundamental differences in cell morphology, gene expression, and phenotypic outcomes to human adipocytes (Soukas et al., 2001; Wang et al., 2014; Morrison and McGee, 2015). Thus, there is a substantial need for human-relevant cell models to improve the translational relevance of adipocyte studies.

Human preadipocyte cell lines have typically been established through transformation and immortalization of primary ADSCs, for example the PAZ6 (Zilberfarb et al., 1997), Chub S7 (Darimont et al., 2003) and TERT-hWA (Markussen et al., 2017) cell lines. Alternatively, cells can be isolated from pathological adipose tissue without further need for immortalization, such as the LiSa-2 cell line isolated from a primary liposarcoma (Wabitsch et al., 2000) or the Simpson-Golabi-Behmel syndrome (SGBS) cell strain isolated from a male infant patient with Simpson-Golabi-Behmel syndrome (Wabitsch et al., 2001).

Finally, human multipotent adipose derived stem (hMADS) cells have been isolated from healthy SVF cells from several infant donors and have been shown to grow and differentiate for up to 200 population doublings, despite not being artificially immortalized (Rodriguez et al., 2004, 2005). As with 3T3-L1 cells, these human preadipocyte cell types are differentiated *in vitro* to mature adipocytes but critically behave more closely to human *in vivo* and primary cell types than murine derived cell models (Rodriguez et al., 2004; Schmidt et al., 2011; Rossi et al., 2020; Dufau et al., 2021).

Although the inherent simplicity of 2D cell culture models makes them compatible with existing plate-based assay technologies and scalable for high-throughput assays, this is also a major disadvantage, as these models cannot recapitulate the full complexity of adipose tissue and are lacking critical features of the cellular microenvironment such as oxygen and nutrient diffusion gradients, interactions with the ECM and neighbouring cells, and the involvement of physical forces **(Figure 1.10)** (Langhans, 2018; Dufau et al., 2021). Use of co-culture models have improved this somewhat by introducing paracrine interactions between the different cell types present in adipose tissue. For example, 3T3-L1 cells have been co-cultured with macrophages such as the murine-derived RAW264.7 cell line, with evidence suggesting the interaction between the cells aggravates the inflammatory response, perhaps leading to increased IR (Suganami et al., 2005). Similarly, SGBS cells have been co-cultured with human THP-1 macrophages, also indicating that pro-inflammatory factors drive insulin resistance and apoptosis (Keuper et al., 2011a). However, these models do not consider other features of the *in vivo* adipose tissue microenvironment.

Overall, 2D adipocyte cell culture systems have provided an invaluable resource to investigate the specific mechanistic details of adipogenesis, adipocyte function, and adipocyte dysfunction in metabolic disease, as well as facilitating high-throughput assays essential for drug screening purposes. However, these artificial systems are limited in their capacity to truly model the complex (patho)physiology of adipose tissue and can thus misrepresent key aspects of metabolic signalling and regulation. There is therefore scope to improve the physiological relevance of *in vitro* adipose tissue models by better representing more aspects of the cellular microenvironment **(Figure 1.10).**

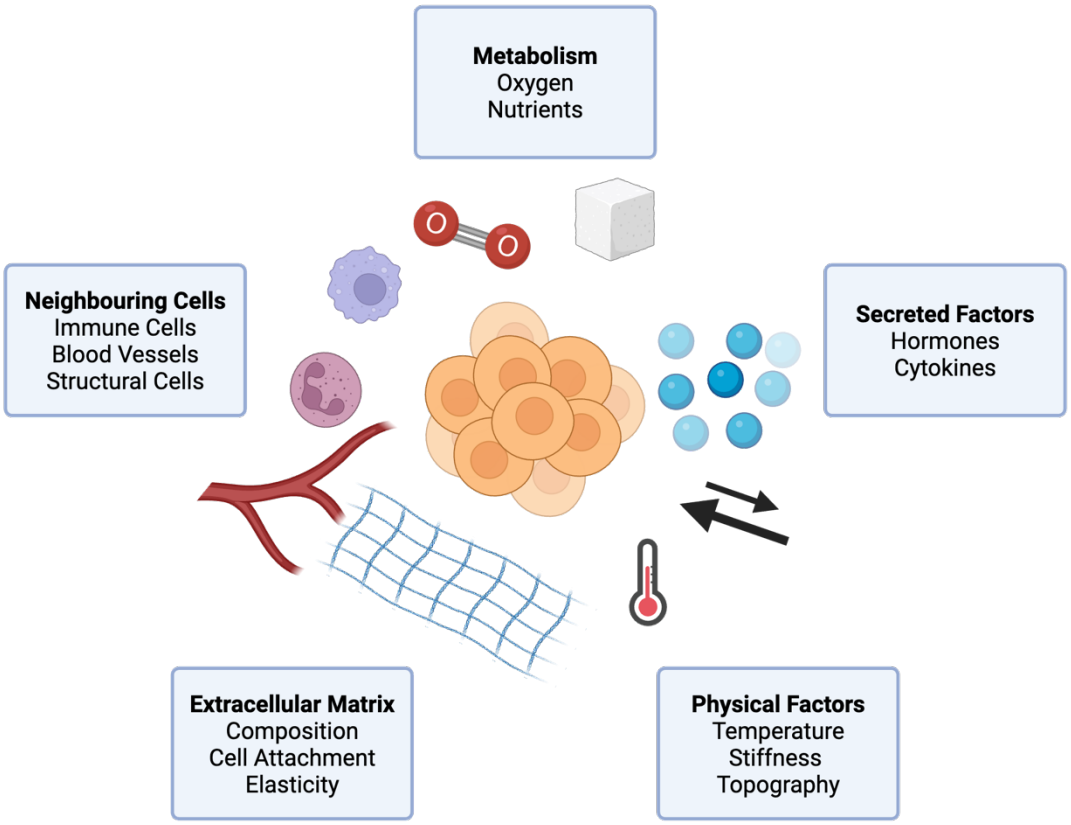

Figure 1.10 – Examples of factors which influence the cellular microenvironment. Adapted from (Lane et al., 2014; Langhans, 2018).

1.4.3 3D *in vitro* cell culture models

The cellular microenvironment, including cell-cell interactions, interactions with the ECM, secreted factors, nutrients and physical forces **(Figure 1.10),** provides essential environmental cues to cells and plays a critical role in the regulation of morphology, metabolism, and proliferation (Dufau et al., 2021). 2D cell culture models typically lack this complexity and as a result can display altered morphology, gene expression, and metabolic function to *in vivo* samples (Shen et al., 2021). 3D cell culture systems can better recapitulate these features *in vitro* than 2D monolayers, thus improving the physiological relevance of *in vitro* models and providing an opportunity to bridge the gap between overly simplistic 2D cell culture and highly complex *in vivo* systems.

The concept of 3D cell culture was initially described in the 1970s as a model of mammary carcinoma, where multicellular spheroids were reported to recapitulate the spatial organisation of tumours including an outer zone of dividing cells, intermediate zone with senescent cells and a necrotic core

(Sutherland et al., 1971). Since the 2000s, 3D cell culture has expanded to include complex stem-cell derived organoids, 3D bioprinting and organ-on-a-chip approaches, and has been widely used in cancer research for tumour modelling, drug discovery, and personalised medicine (Rodrigues et al., 2024). More recently, there has been an increase in development of 3D models for different tissue types including liver, heart and skin for use in drug discovery including toxicity studies, disease modelling, and tissue engineering (Cacciamali et al., 2022). Accordingly, there have now been several reports of 3D adipose cell culture models ranging from adipocyte spheroids to more complex adipose tissue organoids which have been used to study many different aspects of adipose biology (Dufau et al., 2021; Luca et al., 2024).

Adipocyte spheroid cultures can be generated using several available techniques, either with or without the use of a scaffold biomaterial designed to represent the ECM **(Table 1.3)**. Common scaffold-based approaches include the growth of adipocytes in synthetic or natural hydrogels, or bioinks suitable for 3D bioprinting (Celebi et al., 2025). Alternatively, scaffold-free approaches such as hanging drop culture, ultra-low adhesion (ULA) plate coatings, magnetic levitation and spinning bioreactor flasks all ultimately aim to prevent cell adhesion to the culture vessel, thus allowing cells to grow as multicellular spheroids (Di Stefano et al., 2022). The method used to generate spheroids can have a significant impact on their eventual phenotype (Baganha et al., 2022; Lauschke and Hagberg, 2023). For example, the mechanical properties of a scaffold hydrogel can directly affect the morphology and function of the encapsulated cells (Ky et al., 2023), highlighting the importance of biomaterial selection in model development (Contessi Negrini et al., 2025).

Table 1.3 - Example approaches to generate in vitro adipocyte spheroid models

Method	Approach	Description	Example Reference
Scaffold-based	Hydrogels	Cells are encapsulated in a natural or synthetic polymer designed to mimic ECM scaffolds and allow cell culture	(Muller et al., 2019; Ioannidou et al., 2022; Pieters et al., 2022)
	3D bioprinting	Cell-laden bioinks are extruded into desired patterns using 3D printing.	(Louis et al., 2021; Albrecht et al., 2022)
Scaffold-free	Hanging drop	Cell suspensions are seeded in droplets on a solid surface and inverted to allow spheroid formation by gravity.	(Klingelhutz et al., 2018; Mandl et al., 2022)
	Ultra-low adhesion plates	Cells are seeded on low adhesion surface, so cells adhere to each other rather than the plate.	(Shen et al., 2021)
	Magnetic levitation	Cells are loaded with magnetic nanoparticles and a magnetic field applied to aggregate cells into spheroids.	(Daquinag et al., 2013; Wolff et al., 2022)
	Agitation methods	Cell suspensions are constantly agitated using bioreactors such as spinning flasks which prevents adherence to the flask and spheroid formation.	(Hoefner et al., 2020)

Critically, 3D adipocyte culture systems appear to better represent native adipose tissue compared to 2D monolayer culture, with improved differentiation leading to the development of a unilocular morphology, larger lipid droplets and lipid composition and gene expression patterns which more closely resemble *in vivo* samples (Shen et al., 2021). Furthermore, significant differences have been reported between the inflammatory and metabolic responses of otherwise equivalent 2D and 3D cell culture models, suggesting that 3D models may provide a more physiologically relevant platform for translational research purposes (Turner et al., 2018; Wolff et al., 2022; Umetsu et al., 2024). As the field continues to develop, more complex models are becoming available which

mimic specific phenotypes such as inflammation (Turner et al., 2015), fibrosis (Rajangam et al., 2016) and obesity-associated breast cancer (Blyth et al., 2025), as well as anatomical features such as vascularisation (Muller et al., 2019).

Despite these recent advances, 3D cell cultures are not widely used outside of cancer research and tissue engineering applications. In particular, their use in early-stage drug discovery and pharmacological studies has been limited due to the availability of screening assays suitable to measure functional effects of compounds at a suitable throughput, as well as challenges with liquid handling and imaging of 3D structures at scale (Langhans, 2018; Jensen and Teng, 2020). In the GPCR field, only a small number of studies have used 3D models in GPCR signalling or functional studies, with the vast majority investigating some aspect of tumour biology (Uno et al., 2012; Jorand et al., 2016; Van Senten et al., 2019; Azad et al., 2020; De Groof et al., 2021; Mamouni et al., 2021; Barbazán et al., 2022; Yu et al., 2023; Hanif et al., 2025) with one other using brain organoid models to study the reactivity of astrocytes in neural networks (Cvetkovic et al., 2022).

Overall, 3D cell culture models of adipose tissue have the potential to better recapitulate features of the *in vivo* tissue microenvironment, thus providing more physiologically relevant results in studies of adipose tissue function. However, further advances are needed to improve the accessibility of these models in fields outside of cancer research and tissue engineering.

1.4.4 The importance of human relevant systems

As discussed throughout this chapter, there are key species-specific differences in adipose tissue biology between humans and rodent models, from differences in adipose deposits at the anatomic level (Börgeson et al., 2022) to differences in gene expression, adipokine secretion and insulin responsiveness using *in vitro* cell models (Schmidt et al., 2011; Rossi et al., 2020). Furthermore, there are many examples where m-GPCR expression and signalling differ between species (Vassilatis et al., 2003). For example, the HCA_3 receptor gene is only present in hominids with no equivalent in rodent species (Peters et al., 2019), and there are many examples where both endogenous and synthetic ligands for m-GPCRs

show differences in pharmacology between species orthologs (Bolognini et al., 2016; Jenkins et al., 2021; Ciba et al., 2023). It is therefore essential that human relevant systems are used when investigating human disease.

One key difference between human and murine adipocyte cell culture models is that human adipocytes can be differentiated in a chemically defined medium, whereas murine adipocyte protocols typically require serum supplementation (Dufau et al., 2021). This adds an additional layer of complexity, as serum contains an undefined combination of biomolecules and therefore may be influencing adipocyte responses in unknown ways (Gstraunthaler et al., 2013; Valk and Gstraunthaler, 2017). Human-derived systems may therefore result in a more reproducible platform to assess adipocyte function by removing confounding influences from unknown serum components. This rationale could also be extended to eliminate or replace all animal-derived components - including serum, trypsin, and scaffolds such as collagen - from adipocyte culture, to create fully defined, reproducible and ethically sound human-relevant disease models.

1.5 Project Aims

Overall, this thesis aimed to develop a complex *in vitro* model of adipose tissue suitable for exploring the role of m-GPCRs in metabolic diseases. To achieve this, I generated adipocyte spheroids using the human SGBS cell strain and incorporated a genetically encoded biosensor to measure GPCR signalling, as well as features of chronic inflammation to mimic metabolic disease. These objectives have been subdivided as follows:

- The design and optimisation of genetically encoded biosensors which are suitable to measure m-GPCR function in a 3D culture model.

- Development of a 3D spheroid model using SGBS adipocytes, followed by comprehensive characterisation using imaging, transcriptional & protein expression, and functional assay approaches.

- Use of the adipocyte spheroid model to investigate the role of m-GPCRs in metabolic disease through pharmacological modulation and expression of genetically encoded biosensors.

It is hoped that this innovative platform will allow us to better understand m-GPCRs within a physiologically- and disease-relevant microenvironment, therefore deepening our knowledge of adipose tissue biology and ultimately leading to better treatments for metabolic disorders.

2 Materials and Methods

2.1 Materials

Key materials are listed with suppliers and product numbers as appropriate.

2.1.1 General reagents

Ampicillin Sodium Salt - Sigma-Aldrich (A1598)

Bovine Serum Albumin (BSA), fatty-acid free - Roche (03117057001)

Bovine Albumin fraction V- Millipore (81-053-3)

CellTag™ 700 Stain - LI-COR (926-41090)

DAB Substrate Kit, Peroxidase (With Nickel) – Vector Laboratories (SK-4100)

Dimethyl sulfoxide (DMSO) – Fisher (D/4120/PB08)

Eosin Y, Aqueous 1% - Leica (3801590E)

Fast SYBR™ Green Master Mix - Invitrogen (4385612)

Haematoxylin, Harris Acidified – Fisher (12847926)

Hanks' Balanced Salt Solution (HBSS) (10X) – ThermoFisher Scientific (14065-049)

Histo-Clear II – SLS (NAT1334)

Hoechst 33342 - Invitrogen (H3570)

HyperLadder™ 1 kb – Bioline (BIO-33026)

LipidSpot™ 488 – Biotium (70065)

Mounting Medium with DAPI – Abcam (AB104139)

Oil Red O – Sigma-Aldrich (O0625)

Tumor Necrosis Factor (TNF), human recombinant - Sigma-Aldrich (T6674)

2.1.2 Cell culture reagents

Table 2.1 – List of cell culture medium

Medium	Component	Concentration /Volume	Source
HEK293-T complete medium	Dulbecco's Modified Eagle Medium (DMEM), high glucose	-	Gibco (41965-039)
	Heat inactivated Fetal Bovine Serum (FBS)	10% (v/v)	Gibco (10500-064)
	Penicillin/streptomycin	100 U/mL	Gibco (15140-122)
	Normocin	100 µg/mL	InvivoGen (ant-nr)
Flp-In™ T-REx™ 293 selection medium	HEK293-T complete medium	-	As described
	Blasticidin	5 µg/mL	InvivoGen (ant-bl)
	Hygromycin	0.1 mg/mL	InvivoGen (ant-hg)
SGBS 0F medium	DMEM/F-12	500 mL	Gibco (31330-038)
	Penicillin/streptomycin	100 U/mL	Gibco (15140-122)
	D-Pantothenic acid	1.7 mM	Sigma-Aldrich (P5155)
	Biotin	3.3 mM	Sigma-Aldrich (B4639)
SGBS complete medium	SGBS 0F medium	-	As described
	FBS (non-heat inactivated)	10% (v/v)	Gibco (10270-106)
	Normocin	100 µg/mL	InvivoGen (ant-nr)
ADSC complete medium	Minimal Essential Medium (MEM) Alpha	-	Gibco (12571-063)
	Heat inactivated FBS	10% (v/v)	Gibco (10500-064)
	Penicillin/streptomycin	100 U/mL	Gibco (15140-122)

384-well clear polystyrene U-bottom microwell plate with CELLSTAR® Cell-repellent surface – Greiner (787979)

apo-Transferrin – Sigma-Aldrich (T2252)

Collagen from calf skin – Sigma-Aldrich (C8919)

Dexamethasone – Sigma-Aldrich (D1756)

Doxycycline ((4S,4aR,5S,5aR,6R,12aR)-4-(dimethylamino)-1,5,10,11,12a-pentahydroxy-6-methyl-3,12-dioxo-4a,5,5a,6-tetrahydro-4H-tetracene-2-carboxamide) – Sigma-Aldrich (D9891)

Dulbecco's Phosphate Buffered Saline without calcium or magnesium – Gibco (14190-094)

Hydrocortisone – Sigma-Aldrich (H0888)

Insulin, human recombinant, zinc solution – Gibco (12585-014)

3-Isobutyl-1-methylxanthine (IBMX) – Sigma-Aldrich (I5879)

Lipofectamine™ 3000 Transfection Reagent – Invitrogen (L30000015)

Lipofectamine™ MessengerMAX™ Transfection Reagent – Invitrogen (LMRNA001)

MycoStrip® Mycoplasma Detection Kit – InvivoGen (rep-mysnc)

Poly-D-lysine (PDL) hydrobromide – Sigma-Aldrich (P6407)

Polyethylenimine – Polysciences (23966)

Rosiglitazone – Tocris (5325)

3,3',5-Triiodo-L-thyronine sodium salt (T_3) - Sigma-Aldrich (T6397)

Trypan Blue Solution - Gibco (15250061)

TrypLE Express - Gibco (12604-013)

2.1.3 Buffers and solutions

HBSS with HEPES (HBSS-H) – 1X HBSS, 10 mM 4-(2-hydroxyethyl)-1-piperazineethanesulfonic acid (HEPES), 0.035% (v/v) sodium bicarbonate at pH 7.4

Krebs-Ringer-Phosphate buffer with HEPES (KRP-H) – 128 mM NaCl, 4.7 mM KCl, 5 mM NaH_2PO_4, 1.25 mM $MgSO_4$, 1.25 mM $CaCl_2$, 20 mM HEPES at pH 7.4

Lysogeny Broth (LB) & Agar – 1% (w/v) tryptone, 0.5% (w/v) yeast extract, 171 mM NaCl. *Agar only* 1.5% (w/v) agar

Phosphate Buffered Saline (PBS) – 137 mM NaCl, 2.7 mM KCl, 1.8 mM KH_2PO_4, 10 mM Na_2HPO_4 at pH 7.4

Tris-Acetate-EDTA (TAE) buffer – 40 mM Tris-base, 20 mM acetic acid, 1 mM Ethylenediaminetetraacetic acid (EDTA)

Tris Buffered Saline (TBS) – 20 mM Tris, 137 mM NaCl at pH 7.6

2.1.4 Pharmacological compounds

TUG-891 (4-[(4-Fluoro-4'-methyl[1,1'-biphenyl]-2-yl)methoxy]-benzenepropanoic acid) – Tocris (4601) (Shimpukade et al., 2012; Hudson et al., 2013)

AH 7614 (4-Methyl-*N*-9*H*-xanthen-9-yl-benzenesulfonamide) - Tocris (5256) (Sparks et al., 2014)

T-3601386 (T360) (3-cyclopropyl-3-(3-((1-(2-(4,4-dimethylpentyl)-5-methoxyphenyl)piperidin-4-yl)methoxy)phenyl)propanoic acid) – kindly provided by Dr. Elisabeth Rexen Ulven, University of Copenhagen (Ueno et al., 2019)

TUG-1197 (2-(3-fluoro-5-pyridin-2-yloxyphenyl)-3H-1,2-benzothiazole 1,1-dioxide) – kindly provided by Prof. Trond Ulven, University of Copenhagen (Azevedo et al., 2016)

Niacin (Pyridine-3-carboxylic acid) – Merck (PHR1276)

Lodoxamide (2-[[2-chloro-5-cyano-3-(oxaloamino)phenyl]amino]-2-oxoacetic acid) - Sigma-Aldrich (SML2307)

Sodium propionate (C3) – Sigma-Aldrich (P1880)

Disodium succinate – Sigma-Aldrich (W327700)

GSK137647A (4-Methoxy-N-(2,4,6-trimethylphenyl)-benzenesulfonamide) - Tocris (5257) (Sparks et al., 2014)

2-HTP (2-hexylthiopyrimidine-4,6-diol) – Sigma-Aldrich (SML1646)

Isoprenaline (4-[1-hydroxy-2-(propan-2-ylamino)ethyl]benzene-1,2-diol) – Sigma-Aldrich (I2760)

Forskolin ((3R,4aR,5S,6S,6aS,10S,10aR,10bS)-3-ethenyl-6,10,10b-trihydroxy-3,4a,7,7,10a-pentamethyl-1-oxo-dodecahydro-1H-naphtho[2,1-b]pyran-5-yl acetate) - Sigma-Aldrich (93049)

2.1.5 Assay kits

NanoGlo® Luciferase Assay System - Promega (N1130)

Glycerol-Glo™ Assay - Promega (J3150)

CellTiter-Glo® 2.0 Cell Viability Assay - Promega (G9241)

CellTiter-Glo® 3D Cell Viability Assay - Promega (G9681)

Glucose Uptake-Glo™ Assay - Promega (J1341)

QIAquick PCR Purification Kit – QIAGEN (28104)

QIAquick Gel Extraction Kit – QIAGEN (28706)

QIAprep Spin Miniprep Kit – QIAGEN (27106)

QIAGEN Plasmid Maxi Kit – QIAGEN (12162)

RNeasy Mini Kit - QIAGEN (74104)

RNase-Free DNAse Set - QIAGEN (79254)

Herculase II Fusion DNA Polymerase – Agilent (600677)

mMESSAGE mMACHINE T7 kit - ThermoFisher (AM1344)

MEGAclear RNA purification kit - ThermoFisher (AM1908)

M-MLV Reverse Transcriptase - Invitrogen (28025013)

Free Glycerol Reagent – Sigma-Aldrich (F6428)

2.1.6 Lists of antibodies

2.1.6.1 Primary antibodies

Table 2.2 - List of primary antibodies

Antigen	Species	Dilution	Source
Perilipin 1	Mouse	1:500	ThermoFisher (MA5-27861)
Hemagglutinin (HA)	Rat	1:1000	Roche (ROAHAHA)
Fatty Acid Binding Protein 4 (FABP4)	Rabbit	1:250	Abcam (ab92501)
Hypoxia-Inducible Factor 1-alpha (HIF-1α)	Rabbit	1:500	Abcam (ab51608)
IgG control antibody	Rabbit	Equal concentration to primary antibody	Vector Laboratories (I-1000)

2.1.6.2 Secondary antibodies

Table 2.3 - List of secondary antibodies

Antibody	Species	Dilution	Source
AlexaFluor® anti-mouse 594	Goat	1:400	Invitrogen (A-11032)
IRDye® 800CW anti-Rat	Goat	1:1000	LI-COR (926-32219)
ImmPRESS® HRP anti-rabbit IgG polymer kit, peroxidase	Horse	20 µg/mL	Vector Laboratories (MP-7401)

2.1.7 Lists of primers

2.1.7.1 Primers for molecular biology

Table 2.4 - List of primers used for molecular biology

Primer	Sequence
CMV Forward	CGCAAATGGGCGGTAGGCGTG
BGH Reverse	TAGAAGGCACAGTCGAGG
BGH-pTx Reverse	$(T)_{100}$TAGAAGGCACAGTCGAGG
pcDNA5 Reverse	GAAAGGACAGTGGGAGTGGC

2.1.7.2 Primers for quantitative PCR

Table 2.5 - List of primers for quantitative PCR

Gene	Direction	Sequence
Adiponectin	Forward	ATGACCAGGAAACCACGACTC
	Reverse	GGTACTCCGGTTTCACCGAT
ADRB2	Forward	TGATCGCAGTGGATCGCTAC
	Reverse	CCACCTGGCTAAGGTTCTGG
ADRB3	Forward	TCAACCCGCTCATCTACTGC
	Reverse	AAGGATCCCTCCTTGGGTCA
CCL2	Forward	CTCGCTCAGCCAGATGCAAT
	Reverse	TTGGGTTTGCTTGTCCAGGT
FABP4	Forward	GGCTTTGCCACCAGGAAAGT
	Reverse	CTCGTGGAAGTGACGCCTTT
FFA1	Forward	GCATCAACACACCGGTCAAC
	Reverse	GACCCCTTCCCAAGTAACCG
FFA2	Forward	GGTGTGCTTCGGACCTTACA
	Reverse	CCGAACTTGGCATCCCTTCT
FFA3	Forward	AACGGAGCTCAAGGCATCTA
	Reverse	TGGTGGCCACTGCTTCT
FFA4	Forward	AATTTTACAGATCACAAAGGCATCA
	Reverse	CTTCCACTCATTCCTGCACAGT
GAPDH	Forward	ATCACCATCTTCCAGGAGCGA
	Reverse	TGGACTCCACGACGTACTCA
GLUT1	Forward	GAACTCTTCAGCCAGGGTCC
	Reverse	ACCACACAGTTGCTCCACAT

GLUT4	Forward	CGTCGGGCTTCCAACAGAT
	Reverse	TCCTTCCAAGCCACTGAGAG
HCA1	Forward	CCGTGGCTGATTTCCTCCTT
	Reverse	TCTTGCACGCAGAGATGGTT
HCA2	Forward	CACACAGACACACACCTCCTT
	Reverse	TCTCGGAACACACAGCAGTT
HCA3	Forward	TGCTGATCCAGAATGGCACT
	Reverse	GTGTGCAGGAGCCAGAAGAT
HSL	Forward	AGCCAAAAGGGAGCCATCTG
	Reverse	ACCAGCGACTGTGTCATTGT
IL-1B	Forward	CGATGCACCTGTACGATCAC
	Reverse	CATGGAGAACACCACTTGTTGC
KRT19	Forward	GTTCACCAGCCGGACTGAA
	Reverse	GCAGGTCAGTAACCTCGGAC
LPL	Forward	TTGCCCTAAGGACCCCTGAA
	Reverse	ATCCTGTCCCACCAGTTTGG
PLIN1	Forward	CAAGTTCAGTGAGGTAGCAGC
	Reverse	CACCACGTTGTCAGTAACGC
PPARG	Forward	GTGCAATCAAAGTGGAGCCT
	Reverse	CTCTGGATTCAGCTGGTCGAT
Sp1	Forward	ACAAACGTACACACACAGGTGA
	Reverse	GCCCACACTCAGAGCTACAC
SUCNR1	Forward	CTGGGGATCATGGCATGGAA
	Reverse	GGACTCCCACAACGAACTCA
UCP1	Forward	ACGGGTCTTTGGAAAGGGAC
	Reverse	ACGTTCCAGGATCCAAGTCG

2.1.8 List of plasmids

Table 2.6 - List of plasmids

	Plasmid	Insert	Vector	Source	Cloning Method
Vectors	pcDNA3	-	-	ThermoFisher	-
	pcDNA5/FRT/TO	-	-	ThermoFisher	-

SpNB Biosensors	FFA4-SpNBa-G15	hFFA4-LgBiT-ER/K-SmBiT-G15 biosensor	pcDNA5/ FRT/TO	This Thesis	AQUA Cloning
	FFA4-SpNBa-Gi3	hFFA4-LgBiT-ER/K-SmBiT-Gi3 biosensor	pcDNA5/ FRT/TO	This Thesis	AQUA Cloning
	FFA4-SpNBa-Gz	hhFFA4-LgBiT-ER/K-SmBiT-Gz biosensor	pcDNA5/ FRT/TO	This Thesis	AQUA Cloning
	FFA4-SpNBb-G15	hFFA4-SmBiT-ER/K-LgBiT-G15 biosensor	pcDNA5/ FRT/TO	This Thesis	AQUA Cloning
	FFA4-SpNBb-Gi3	hFFA4-SmBiT-ER/K-LgBiT-Gi3 biosensor	pcDNA5/ FRT/TO	This Thesis	AQUA Cloning
	FFA4-SpNBb-Gz	hFFA4-SmBiT-ER/K-LgBiT-Gz biosensor	pcDNA5/ FRT/TO	This Thesis	AQUA Cloning
Membrane-localised biosensor components	FFA4-LgBiT	hFFA4 receptor tagged with LgBiT on C terminus	pcDNA3	Unpublished from our laboratory	Restriction cloning
	FFA1-LgBiT	hFFA1 receptor tagged with LgBiT on C terminus	pcDNA3	Unpublished from our laboratory	Restriction cloning
	Lyn11-LgBiT	Lyn11 membrane anchor fused to LgBiT	pcDNA5/ FRT/TO	This Thesis	AQUA cloning
	Lyn11-FL-LgBiT	Lyn11-$(GSG)_4$ flexible linker-LgBiT	pcDNA5/ FRT/TO	This Thesis	AQUA cloning
	Lyn11-SmBiT	Lyn11 fused to SmBiT	pcDNA5/ FRT/TO	This Thesis	AQUA cloning
	Lyn11-FL-SmBiT	Lyn11-$(GSG)_4$-SmBiT	pcDNA5/ FRT/TO	This Thesis	AQUA cloning
	Lyn11-mNG-SmBiT	Lyn11-$(GSG)_4$-mNeonGreen-SmBiT	pcDNA5/ FRT/TO	This Thesis	AQUA cloning
	Lyn11-mNG-FL-SmBiT	Lyn11-$(GSG)_4$-mNeonGreen-$(GSG)_4$-SmBiT	pcDNA5/ FRT/TO	This Thesis	AQUA cloning
	SmBiT-CAAX	SmBiT-$(GSG)_4$-CAAX membrane anchor	pcDNA3	This Thesis	AQUA cloning
	SmBiT-mNG-CAAX	SmBiT-mNeonGreen-$(GSG)_4$-CAAX	pcDNA3	This Thesis	AQUA cloning
	SmBiT-FL-mNG-CAAX	SmBiT-$(GSG)_4$-mNeonGreen-$(GSG)_4$-CAAX	pcDNA3	This Thesis	AQUA cloning

Arrestin biosensors	SmBiT-Arrestin	Bovine Arrestin-3 tagged on its N terminus with SmBiT	pcDNA3	Unpublished from our laboratory	Restriction cloning
	Arrestin-SmBiT	Bovine Arrestin-3 tagged on its C terminus with SmBiT	pcDNA3	Unpublished from our laboratory	Restriction cloning
	SmBiT-Arrestin-SmBiT	Bovine Arrestin-3 tagged on both termini with SmBiT	pcDNA3	This Thesis	AQUA cloning
	LgBiT-Arrestin	Bovine Arrestin-3 tagged on its N terminus with LgBiT	pcDNA3	Unpublished from our laboratory	Restriction cloning
	Arrestin-LgBiT	Bovine Arrestin-3 tagged on its C terminus with LgBiT	pcDNA3	Unpublished from our laboratory	Restriction cloning
	NBA Plasmid	Lyn11-LgBiT and SmBiT-Arrestin constructs separated by P2A ribosomal skipping sequence	pcDNA3	This Thesis	AQUA cloning
	pIRES arrestin recruitment	Lyn11-mNeonGreen and human Arrestin-3 tagged on its N terminus with NanoLuciferase separated by internal ribosome entry site (IRES)	pIRES	(Marsango et al., 2022)	Restriction cloning
MiniG biosensors	SmBiT-miniGq	MiniGsq protein tagged on its N terminus with SmBiT	pcDNA3	Dr Bianca Plouffe, Queen's University Belfast	-
	SmBiT-miniGi	MiniGsi protein tagged on its N terminus with SmBiT	pcDNA3	This Thesis	AQUA cloning
Receptors	FFA4-HA	Human FFA4 receptor with C terminal HA tag	pcDNA5/ FRT/TO	(Butcher et al., 2014)	-
	HCA2	Human HCA2 receptor	pcDNA5/ FRT/TO	Unpublished from our laboratory	AQUA cloning
	GPR35	Human GPR35 receptor	pcDNA5/ FRT/TO	(Jenkins et al., 2012)	-

	GPR84-HA	Human GPR84 receptor with C terminal HA tag	pcDNA5/ FRT/TO	(Jenkins et al., 2021)	-
	FFA2-HA	Human FFA2 receptor with C terminal HA tag	pcDNA5/ FRT/TO	(Bolognini et al., 2019)	-
	FLAG-FFA3	Human FFA3 receptor with N terminal FLAG tag	pcDNA3	Dr Leigh Stoddart, unpublished	-
Colour-shifted Biosensors	mNG-NLuc	mNeonGreen-NanoLuciferase fusion protein	pcDNA3	Unpublished from our laboratory	Restriction cloning
	GeNL	Green NanoLantern construct (mNeonGreen fused with NanoLuciferase)	pcDNA3	(Suzuki et al., 2016)	AQUA cloning
	YeNL	Yellow NanoLantern construct (Venus fused with NanoLuciferase)	pcDNA3	(Suzuki et al., 2016)	AQUA cloning
	CeNL	Cyan NanoLantern construct (mTurquoise fused with NanoLuciferase)	pcDNA3	(Suzuki et al., 2016)	AQUA cloning
	Lyn11-GeLgBiT	Lyn11-$(GSG)_4$-mNeonGreen-LgBiT	pcDNA5/ FRT/TO	This Thesis	AQUA cloning
	Lyn11-YeLgBiT	Lyn11-$(GSG)_4$-Venus-LgBiT	pcDNA5/ FRT/TO	This Thesis	AQUA cloning
	Lyn11-CeLgBiT	Lyn11-$(GSG)_4$-mTurquoise-LgBiT	pcDNA5/ FRT/TO	This Thesis	AQUA cloning
	SmBiT-mNG-Arrestin	SmBiT-mNeonGreen-Bovine Arrestin-3	pcDNA3	This Thesis	AQUA cloning
	SmBiT-FL-mNG-Arrestin	SmBiT-$(GSG)_4$-mNeonGreen-Bovine Arrestin-3	pcDNA3	This Thesis	AQUA cloning
Other	pOG44	Flp Recombinase	pOG44	ThermoFisher	-

2.1.9 List of cell lines

Table 2.7 - List of cell lines

Cell Line	Parental Cell Line	Expressing	Source
Human Embryonic Kidney (HEK) 293-T	-	-	ATCC
Simpson Golabi Behmel Syndrome (SGBS)	-	-	Wabitsch Group, University of Ulm, Germany
Parental Flp-In™ T-REx™ 293	-	-	ThermoFisher
Primary human adipose-derived stromal cells (ADSCs)	-	-	Dr Gillian Higgins, University of Glasgow [Biobank 314]
FFA4-SpNBa-G15	Flp-In™ T-REx™ 293	FFA4-LgBiT-ER/K-SmBiT-G15 biosensor	This Thesis
FFA4-SpNBa-Gi3	Flp-In™ T-REx™ 293	FFA4-LgBiT-ER/K-SmBiT-Gi3 biosensor	This Thesis
FFA4-SpNBa-Gz	Flp-In™ T-REx™ 293	FFA4-LgBiT-ER/K-SmBiT-Gz biosensor	This Thesis
FFA4-SpNBb-G15	Flp-In™ T-REx™ 293	FFA4-SmBiT-ER/K-LgBiT-G15 biosensor	This Thesis
FFA4-SpNBb-Gi3	Flp-In™ T-REx™ 293	FFA4-SmBiT-ER/K-LgBiT-Gi3 biosensor	This Thesis
FFA4-SpNBb-Gz	Flp-In™ T-REx™ 293	FFA4-SmBiT-ER/K-LgBiT-Gz biosensor	This Thesis

2.1.10 Specialised equipment

BMG PHERAstar, CLARIOstar & POLARstar microplate readers (BMG Labtech)

Countess™ 3 Automated Cell Counter (Thermo Scientific, Invitrogen)

EVOS™ FL Auto 2 Imaging System (Thermo Scientific, Invitrogen)

LI-COR Odyssey Sa Infrared Imaging System (LI-COR Biosciences)

LSM980 Confocal Laser Scanning Microscope (Zeiss)

Neon™ Transfection System (Thermo Scientific, Invitrogen)

NuGenius XE Gel Documentation System (Syngene)

QuantStudio™ 5 Real-Time PCR System (Thermo Scientific, Invitrogen)

Vivatome Spinning Disk Confocal Microscope (Zeiss)

2.2 Cell Culture

All cell culture protocols were carried out in sterile conditions in a laminar flow biosafety hood. Reagents were warmed to 37°C in a water bath before use. Cell lines were routinely tested for mycoplasma using MycoStrip® Mycoplasma Detection Kit following manufacturer's instructions.

2.2.1 General cell culture methods

2.2.1.1 Cell line maintenance

All cell lines used were routinely cultured in their respective complete medium solutions as described in **Table 2.1**. Human Embryonic Kidney (HEK) 293-T cells, Parental Flp-In™ T-REx™ 293 cells and Flp-In™ T-REx™ 293 cells stably expressing biosensor constructs were maintained in HEK293-T complete medium.

Cells were maintained in T75 tissue culture flasks in a humidified incubator at 37°C and 5% CO_2. Once confluent, culture medium was aspirated, and cells were incubated with TrypLE Express enzyme for approximately 3-5 minutes until cells detached from the flask. Complete medium was added to neutralise the enzyme and cell suspension was centrifuged at 290 *g* for 5 minutes. The resulting cell pellet was resuspended in fresh medium. Cell counts and viability were determined by diluting cell suspension 1:1 in 0.4% trypan blue solution and reading on Countess™ 3 Automated Cell Counter. Cells were then diluted to desired concentration for plating, and an appropriate volume transferred to a new T75 flask containing fresh medium.

2.2.1.2 Cell line cryopreservation

For long-term storage, cell lines were cryopreserved and stored at -80°C or -150°C. To prepare cells for cryopreservation, confluent flasks were harvested and centrifuged as described in section 2.2.1.1. Pellets were resuspended in the relevant complete medium containing 10% (v/v) Dimethyl Sulfoxide (DMSO) as a cryoprotectant and transferred to cryovials. Cryovials were placed in a Mr. Frosty™ Freezing Container (ThermoFisher) at -80°C to slow the rate of freezing to approximately -1°C/minute. After 24 hours, cryovials were transferred to storage in the -80°C or -150°C freezers. Cryopreserved cells

were revived by thawing rapidly in a water bath and resuspending in complete medium. The cell suspension was centrifuged at 290 *g* for 5 minutes, pellet resuspended in fresh medium and transferred to a sterile culture flask. Cell lines were then maintained as described in section 2.2.1.1.

2.2.2 Transient transfection

2.2.2.1 DNA transfection using Polyethylenimine

Plasmid DNA expressing relevant constructs was introduced into mammalian cell lines using the cationic polymer, polyethylenimine (PEI). PEI complexes with DNA to form positively-charged particles which bind to the anionic cell membrane and are endocytosed to the cytoplasm (Boussif et al., 1995).

Plasmid DNA was diluted in 150 mM sodium chloride solution and mixed with an equal volume of PEI transfection solution (120 µg/mL in 150 mM sodium chloride), using 720 ng PEI per µg of DNA. Total amounts of DNA and PEI used for different vessel types are given in **Table 2.8.** The mixture was vortexed and incubated at room temperature for 10 minutes to allow DNA and PEI to complex. The DNA-PEI mixture was then added dropwise to adherent cells or mixed with the cell suspension immediately prior to plating. Cells were incubated with the transfection mixture for at least 24 hours before cells were used in assays.

Table 2.8 - Transfection conditions for different vessel sizes

Vessel Type	Total DNA/well	PEI used/well	Volume DNA-PEI mixture/well
10 cm dish	5 µg	3.6 µg	500 µL
6-well plate	1 µg	720 ng	100 µL
96-well plate	100 ng	72 ng	10 µL

2.2.2.2 Alternative DNA lipofection methods

To optimise transfection of SGBS cells, alternative lipofection reagents Lipofectamine™ 3000 (Invitrogen) and TransIT®-LT1, -2020 and -X2 (Mirus Bio) were investigated for their potential to improve transfection efficiency. Plasmid DNA was prepared at 100 ng/well for 96-well plates and transfection was carried out following manufacturer's guidelines.

Per well, working stocks of Lipofectamine™ 3000 and P3000 reagent were prepared by diluting 0.15 µL reagent in 5 µL serum free medium. P3000 stock was mixed first with DNA, then mixed with the Lipofectamine™ 3000 reagent. The solution was incubated at room temperature for 10 minutes and 10 µL DNA-lipid transfection mixture was added dropwise to adherent cells. Cells were incubated with the transfection mixture for at least 24 hours before use.

For all TransIT® reagents, DNA was initially mixed with serum-free medium and TransIT® reagent added to a final dilution of 1:30. The mixture was incubated at room temperature for 15-30 minutes and added dropwise to adherent cells. Cells were incubated with the transfection mixture for at least 24 hours before use.

2.2.2.3 mRNA transfection using Lipofectamine™ MessengerMAX™

mRNA was prepared as described in section 2.3.4 and transfected into SGBS cells using Lipofectamine™ MessengerMAX™ reagent. Per well, 100 ng mRNA was mixed with 5 µL serum free medium. Lipofectamine™ MessengerMAX™ reagent was prepared by diluting 0.15 µL reagent in 5 µL serum free medium and added to mRNA mixture. The solution was incubated at room temperature for 5 minutes and 10 µL RNA-lipid transfection mixture was added dropwise to adherent cells. Cells were incubated with the transfection mixture for at least 24 hours before use.

2.2.2.4 Electroporation

In cases when lipofection methods resulted in poor transfection efficiency, electroporation was carried out using the Neon™ Transfection System.

SGBS cells were harvested and counted, then cell suspension was centrifuged at 290 *g* for 5 minutes and pellet washed with PBS. Following a further centrifugation at 290 *g* for 5 minutes, cells were resuspended at a final density of 0.5 x 10^7 cells/mL in Resuspension Buffer R. Cell suspension was mixed with 500 ng plasmid DNA/well of a 24-well plate.

The Neon™ device and pipette station were set up following the manufacturer's guidelines with 3 mL Electrolytic Buffer E. 10 µL DNA-cell mixture was aspirated into the Neon™ pipette tip and electroporation carried out at 1275 V with 10 ms

pulse width for 3 pulses, or with voltage, pulse and time parameters as described in relevant figures.

Electroporated cell suspension was then slowly dispensed into pre-warmed 24-well plates containing SGBS complete medium without antibiotics. Electroporated cells were incubated at 37°C and 5% CO_2 in a humidified incubator for 24 hours before transfection efficiency was assayed as described in section 2.2.2.5.

For spheroid electroporation, 16-24 spheroids were pooled, washed with PBS and resuspended in 10 µL Resuspension Buffer R. 1 µg of DNA was added and 10 µL DNA-spheroid mixture aspirated into the Neon™ pipette tip. Electroporation was carried out as described above and spheroids were dispensed into eppendorf tubes containing 1 mL pre-warmed SGBS complete medium without antibiotics. Spheroids were then collected and individually dispensed into a 96-well ultra-low adhesion plate also containing pre-warmed SGBS complete medium without antibiotics. Electroporated spheroids were incubated at 37°C and 5% CO_2 in a humidified incubator for 24 hours before transfection efficiency was assayed as described in section 2.2.2.5.

2.2.2.5 Assessment and evaluation of transfection

When cells had been transfected with a construct expressing a green fluorescent protein, cells in a clear 96-well plate were visualised using the FITC filter (Ex: 480 nm, Em: 510 nm with bandpass of 20 nm) on the NIKON Ti S screening microscope to visually confirm expression.

For quantitative analysis, appropriate fluorescent or luminescent measurements were taken using the CLARIOstar depending on specific constructs expressed and is described in relevant figures. Typically, cells were washed twice with 200 µL HBSS-H and incubated in 90 µL HBSS-H for 30 minutes at 37°C. NanoGlo furimazine substrate was prepared at final 1:800 dilution and added to cells before incubation for a further 10 minutes at 37°C in the dark. Raw luminescence measurements were taken on the CLARIOstar before and after addition of NanoGlo furimazine substrate. Furthermore, luminescent emission

spectra were generated using the CLARIOstar spectral scan mode, measuring luminescent signal at 2-5 nm intervals across the range 420 nm to 580 nm.

mNeonGreen fluorescence intensity was measured on the CLARIOstar with excitation at 483 nm (bandpass 15 nm) and emission at 530 nm (bandpass 20 nm). Finally, cells were stained with Hoescht 33342 as described in section 2.5.3 and fluorescence intensity measured on the CLARIOstar with excitation at 355 nm (bandpass 20 nm) and emission at 455 nm (bandpass 30 nm). For 96-well plates, a single measurement read was taken per well. For 24-well plates, measurements were taken in a 5 x 5 matrix using well scan mode and an average taken.

2.2.3 Generation of Flp-In™ T-REx™ 293 cells stably expressing biosensor constructs

Flp-In™ T-REx™ 293 cell lines inducibly expressing the SpNB biosensor constructs were generated following manufacturer guidelines and as previously described (Ward et al., 2011). Briefly, a donor plasmid is generated in a pcDNA5/FRT/TO vector containing a FRT recombination site and the biosensor construct of interest under the control of a CMV promoter containing TetO2 operator sequences. Flp-In™ parental cells contain a FRT site at a defined genomic locus and stably express the Tet repressor protein. When the donor plasmid is co-transfected with a Flp recombinase into the parental cells, recombination occurs between the FRT sites resulting in site-specific stable integration of the biosensor construct into the genome of the Flp-In™ host cells. Expression of the biosensor can be induced by application of doxycycline which releases the Tet repressor protein from the TetO2 sites and allowing transcription

Parental Flp-In™ T-Rex™ 293 cells were grown to 80% confluence in 10 cm tissue culture dishes and transfected with 4 µg pOG44 plasmid expressing the Flp recombinase and 1 µg SpNB construct in pcDNA5/FRT/TO vector using standard PEI transfection as described in section 2.2.2.1. After 24 hours, cells were passaged into new dishes and after a further 24 hours, cells were cultured in Flp-In™ T-REx™ 293 selection medium **(Table 2.1)**. Only cells where the desired construct has integrated at the FRT site within the parental cell line will survive. After approximately 2 weeks, isogenic colonies were harvested, pooled, and

maintained as new stable inducible cell lines. Expression of the biosensor constructs could be induced 24 hours prior to use by replacing culture medium with fresh HEK293-T complete medium containing doxycycline at 0.5-100 ng/mL.

2.2.4 SGBS adipocyte culture

Simpson Golabi Behmel Syndrome (SGBS) preadipocyte cells were kindly provided by Prof. Martin Wabitsch at the University of Ulm, Germany. Cells were maintained in SGBS complete medium **(Table 2.1)** in T150 culture flasks as described in section 2.2.1, with culture medium changed every 2-3 days and passaged when near-confluence. Where possible, cells were not used beyond passage 6.

2.2.4.1 Assessing growth of SGBS cells in different culture media

To assess the growth of SGBS cells in different culture media, cells were gradually transitioned from standard SGBS complete medium containing 10% FBS to the indicated medium containing Human Serum or Human Platelet Lysate by daily partial medium changes (i.e. 1:0, 3:1, 1:1, 1:3, 0:1). Cells were then plated at 3000 cells/cm^2 in 12- or 24-well plates in growth medium and incubated at 37°C/5% CO_2 overnight. Cells were washed and indicated medium added as described. Cells were incubated for up to 7 days at 37°C/5% CO_2, with fresh medium added after 3 days. Cell counts were quantified at indicated time points as described in section 2.5.3.

2.2.4.2 Differentiation of SGBS adipocytes in 2D

Unless otherwise indicated, SGBS cells were differentiated as previously described (Lee and Fried, 2014). Multi-well tissue culture plates were coated with 20 µg/cm^2 collagen in sterile water, incubated at 4°C overnight or at 37°C for 4 hours and washed in sterile water before use. Cells were plated at an appropriate density for plate type. When near confluent, cells were washed in Phosphate Buffered Saline (PBS) and the medium was changed to SGBS 0F medium containing differentiation cocktail of 10 µg/mL apo-Transferrin, 100 nM human insulin, 2 nM triiodothyronine (T3), 100 nM dexamethasone, 500 µM 3-isobutyl-1-methylxanthine (IBMX) and 1 µM rosiglitazone (day 0). On day 4, medium was changed to serum-free growth medium containing maintenance

cocktail of 10 µg/mL apo-Transferrin, 10 nM insulin and 10 nM dexamethasone. Maintenance medium was replaced on day 8 and day 12, and adipocytes used on day 14.

2.2.4.3 Generation of SGBS adipocyte spheroids

Unless otherwise stated, SGBS preadipocytes were counted and seeded at 10,000 cells/well in 50 µL complete culture medium into 384-well Ultra Low Adhesion (ULA) plates. ULA plates have been treated with a hydrophilic coating which results in cells adhering to each other rather than to the plate. Plates were incubated at 37°C/5% CO_2 for 48 hours to allow spheroids to form then differentiated to adipocytes as described in section 2.2.4.1.

To ensure spheroids remained in the plates, multiple partial media changes were carried out; starting with a volume of 50 µL medium, 30 µL medium was removed using a manual multichannel pipette and replaced with 60 µL PBS or differentiation medium. At least two 60 µL washes were carried out before a final 60 µL was removed and replaced with 30 µL differentiation medium.

Undifferentiated spheroids were used on day 0 of differentiation for RNA extraction and fixation for imaging, or maintained for 14 days in SGBS complete culture medium for assays to run simultaneously with differentiated spheroids.

For experiments where adipocyte spheroids were treated with Tumor Necrosis Factor (TNF) for 14 days, differentiation occurred as described above with differentiation and maintenance cocktails supplemented with 10 ng/mL TNF. An additional change in maintenance medium occurred at day 13 where TNF was also included for spheroids treated with TNF for 24 hours.

2.2.5 Primary human adipose-derived stromal cell culture

Primary human adipose-derived stromal cells (ADSCs) were obtained from Dr Gillian Higgins and Dr Mathis Riehle at the University of Glasgow.

Human abdominal adipose tissue was obtained from consenting donors, with ethical approval from Biobank (314) and in line with the Human Tissue Act (2004). All of the adipose was from females who were having reconstructive

surgery as part of their breast cancer treatment. Patients who had received neo-adjuvant chemotherapy were excluded from the study. The ADSCs were extracted utilising standardised protocols (Kingham et al., 2007).

Cells were maintained in ADSC complete medium **(Table 2.1)** in T75 culture flasks as described in section 2.2.1, with regular changes of culture medium until near-confluence. Cells were harvested and seeded into 384-well ULA plates at 2000 cells/well. Spheroids were maintained and differentiated as described in sections 2.2.4.1 and 2.2.4.3 in SGBS 0F medium containing differentiation cocktail.

2.3 Molecular Biology Techniques

2.3.1 Bacterial techniques

Molecular biology techniques involving *Escherichia coli (E. coli)* cells were carried out using aseptic technique by a Bunsen burner flame. Contaminated liquid waste was collected and treated with chlorine tablets before disposal.

2.3.1.1 Preparation of chemically competent *E. coli* cells

Frozen stocks of XL1-Blue *E. coli* were thawed on ice and streaked onto Lysogeny Broth (LB) 1.5% (w/v) agar plates without selection antibiotics **(section 2.1.3)** using a sterile hoop to obtain single colonies and incubated at 37°C overnight. Single colonies were picked using sterile pipette tips and incubated in 5 mL LB at 37°C overnight in a shaking incubator at 200 rpm. Overnight cultures were sub-cultured into 100 mL LB in conical flasks and incubated in a shaking incubator at 37°C and 200 rpm for approximately 90 minutes until an optical density (OD) of 0.48 at 600 nm was reached. Cells were chilled on ice for 5 minutes to slow growth and centrifuged for 10 minutes at 1,800 *g* at 4°C. The pellet was resuspended in 20 mL pre-chilled solution 1 (30 mM potassium acetate, 10 mM RbCl, 10 mM $CaCl_2$, 50 mM $MnCl_2$, adjusted to pH 5.8 using 100 mM acetic acid, 15% (v/v) glycerol and sterilised through a 0.2 µm filter) and incubated on ice for 5 minutes. The cell suspension was further centrifuged for 10 minutes at 1,800 *g* at 4°C and supernatant discarded. The pellet was then resuspended in 2 mL pre-chilled solution 2 (10 mM 3-morpholinopropane-1-sulfonic acid (MOPS), 10 mM RbCl, 75 mM $CaCl_2$, 15% (v/v) glycerol and sterilised through a 0.2 µm filter) and incubated on ice for 15 minutes. Cell suspension was aliquoted into sterile 1.5 mL eppendorf tubes and stored at -80°C.

2.3.1.2 Transformation of competent *E. coli* cells by heat shock

Plasmid DNA, AQUA cloning reactions or ligation reactions were transformed into chemically competent XL1-Blue *E. coli* by a heat shock method. DNA to be transformed was mixed with 50 µL competent *E. coli* (section 2.3.1.1) and incubated on ice for 10 minutes. Cells were heat shocked in a water bath at 42°C for exactly 45 s to allow cells to take up DNA and recovered on ice for 2 minutes. 450 µL LB was added to cell suspension and incubated in a shaking

incubator at 37°C and 200 rpm for 60 minutes. For transformation of complete plasmids, 100 µL cell suspension was spread on LB agar plates containing 100 µg/mL ampicillin selection antibiotic. For cloning transformation, cell suspension was centrifuged at 1,500 *g* for 3 minutes, supernatant discarded and pellets resuspended in 100 µL LB. The entire cell suspension was then spread on LB agar plates containing 100 µg/mL ampicillin selection antibiotic. Agar plates were inverted to prevent condensation and incubated at 37°C overnight.

2.3.1.3 Isolation of plasmid DNA from *E. coli* cultures

Plasmid DNA was isolated from *E. coli* cultures using the QIAprep Spin Miniprep kit. Single colonies were picked from transformed plates (section 2.3.1.2) using sterile pipette tips and incubated overnight in 5 mL LB containing 100 µg/mL ampicillin in a shaking incubator at 37°C and 200 rpm. Cells were then centrifuged for 10 minutes at 1,800 *g* at 4°C and pellets lysed. Plasmid DNA was isolated using the QIAprep Spin Miniprep kit following manufacturer's guidelines and eluted in 50 µL sterile nuclease-free dH_2O.

When larger quantities of plasmid DNA were required, the QIAGEN Plasmid Maxiprep kit was used. Single colonies were picked from transformed plates as above and incubated for 8 hours in 5 mL LB containing 100 µg/mL ampicillin in a shaking incubator at 37°C and 200 rpm. 5 mL cultures were sub-cultured into 100 mL LB containing 100 µg/mL ampicillin and incubated overnight in a shaking incubator at 37°C and 200 rpm. Cells were pelleted and lysed as described above and DNA isolated using QIAGEN Plasmid Maxiprep kit following manufacturer's guidelines.

2.3.1.4 Quantification of nucleic acid concentration

Isolated DNA or RNA was quantified using an LVis plate (BMG Labtech) on the POLARstar microplate reader (BMG Labtech), using nuclease-free dH_2O as sample blank. Absorbance was measured at 260 nm, 280 nm, 230 nm and 340 nm to determine concentration and assess purity. Concentration was calculated using Beer's law: A_{340} background measurement was subtracted from blank-corrected A_{260} measurement and multiplied by 40 for RNA or 50 for DNA. The A_{260}/A_{280} ratio was used to assess nucleic acid purity from protein contaminants, with a ratio of 1.8 considered pure for DNA, and 2.0 considered pure for RNA. The A_{260}/A_{230}

ratio was used to assess purity from other organic compounds, with 2.0-2.2 considered pure.

2.3.2 Polymerase Chain Reaction

Polymerase Chain Reaction (PCR) was carried out to amplify DNA fragments with the Herculase II Fusion PCR kit following manufacturer's instructions.

For short DNA fragments (<5 kb), 50 µL PCR reactions were prepared with 1 µL Herculase II DNA Polymerase, 250 µM dNTPs, 25 ng template DNA, 0.25 µM forward and reverse oligonucleotide primers and 2% DMSO in 1X Herculase II reaction buffer. Reactions were incubated on a thermocycler using the protocol described in **Table 2.9**.

Table 2.9 - Thermocycler protocol for <5 kb PCR reactions

Segment	Cycles	Temperature	Duration
Initial Denaturing	1	95°C	2 minutes
Denaturing	30	95°C	20 s
Annealing		55°C	20 s
Extension		72°C	30 s per kb
Final Extension	1	72°C	3 minutes
Hold	-	4°C	Hold

To improve amplification of longer DNA fragments (>5 kb), reactions were prepared as above with oligonucleotide primer concentration increased to 0.5 µM. Reactions were incubated on a thermocycler using an extended protocol as described in **Table 2.10**.

Table 2.10 - Thermocycler protocol for >5 kb PCR reactions

Segment	Cycles	Temperature	Duration
Initial Denaturing	1	95°C	2 minutes
Denaturing	12	95°C	20 s
Annealing		55°C	20 s
Extension		68°C	5 minutes
Denaturing	20	95°C	20 s
Annealing		55°C	20 s
Extension		68°C	5 minutes + 20 s incremental increase for each cycle
Final Extension	1	68°C	8 minutes
Hold	-	4°C	Hold

Following completion of PCR for longer DNA fragments, template DNA was digested at methylated GATC motifs by incubating with 1 µL DpnI restriction enzyme (New England Biolabs, NEB) at 37°C for 2-4 hours. PCR reaction components were removed using the QIAquick PCR Purification kit following manufacturer's guidelines.

2.3.3 Generation of new plasmids expressing biosensor constructs

2.3.3.1 AQUA cloning

Plasmids expressing new biosensor constructs were primarily generated using Advanced Quick Assembly (AQUA) cloning (Beyer et al., 2015), an enzyme-free seamless cloning approach based on the ability of *E. coli* to process linear DNA with overlapping sequence homology.

To construct new plasmids, linear insert and vector fragments were amplified by PCR (section 2.3.2) using oligonucleotide primers designed to result in >24 bp overlapping end sequence homology. PCR products were combined with DNA gel loading dye (NEB) and separated by gel electrophoresis using a 1% (w/v) agarose gel in Tris-Acetate-EDTA (TAE) buffer (section 2.1.3) containing SYBR safe DNA gel stain at 1:10,000 dilution. Gels were visualised on a blue light transilluminator, and desired bands were cut out using a scalpel blade. DNA was then isolated using QIAquick Gel Extraction Kit (QIAGEN) following

manufacturer's instructions. Samples of gel extracted DNA were separated on a further 1% (w/v) agarose gel containing SYBR safe DNA gel stain and visualised using NuGenius XE imaging system to assess purity of fragment and determine approximate DNA concentration relative to 1 kb HyperLadder™ (Bioline).

AQUA cloning reactions were set up with 12 ng linear vector DNA per 1 kb vector length, combined with linear insert DNA at a 5:1 molar ratio with vector, and made up to 10 µL final volume in nuclease-free dH_2O. DNA fragments were incubated at room temperature for up to 1 hour, and 5 µL of the DNA mixture transformed into competent *E. coli* as described in section 2.3.1.2 for *in vivo* plasmid assembly to occur. Plasmid DNA was isolated and purified as described in section 2.3.1.3.

2.3.3.2 Restriction cloning

Where appropriate restriction sites were present in parental plasmids, restriction enzyme cloning was used to generate new plasmids. Vector and insert DNA were digested with complementary restriction enzymes.

1 µg template DNA was combined with 20 Units restriction enzymes in supplied 1X CutSmart buffer (NEB) at 50 µL final volume in nuclease-free water. Reactions were incubated at 37°C for 4 hours, and 1 µL QuickCIP (NEB) added to vector samples for a further 30 mins to dephosphorylate DNA sticky ends and prevent re-ligation. Restriction digest products were purified by gel extraction and quantified as described in section 2.3.3.1.

T4 ligase reactions were set up with 30 ng linearised vector DNA, linear insert DNA at a 3:1 molar ratio and 1 Unit of T4 DNA ligase (Invitrogen) in 1X supplied ligase buffer. Reactions were incubated overnight at 15°C and 5 µL product transformed into 45 µL competent *E. coli* as described in section 2.3.1.2. Plasmid DNA was isolated and purified as described in section 2.3.1.3.

2.3.3.3 Confirmation of new plasmid sequence

To confirm new plasmid DNA contained the expected construct, diagnostic restriction digests were performed followed by gel electrophoresis to visualise band sizes. Two restriction enzymes were selected to give DNA fragment bands

which would differ in size or pattern between the new plasmid and the original vector plasmid, as conceptually the most likely issue is accidental isolation of the parental plasmid.

Restriction digests were set up by combining 500 ng plasmid DNA with 10 Units restriction enzymes in supplied 1X CutSmart buffer (NEB) at 10 µL final volume in nuclease-free water. Digests were incubated for 30 minutes at 37°C and products separated on a 1% (w/v) agarose gel containing SYBR safe DNA gel stain in TAE buffer. Bands were visualised using NuGenius XE imaging system and size determined relative to 1 kb HyperLadder™ (Bioline).

The identity of plasmids with expected bands in the diagnostic restriction digests was then confirmed by DNA sequencing. Samples were diluted to 50-100 ng/µL and in 5 µL nuclease-free dH_2O and combined with 5 µL of 5 µM appropriate sequencing primer (**Table 2.4**). Typically, primers targeting the CMV promoter sequence (forward) and BGH-poly(A) signal (reverse) were used to give complete coverage of the expressed construct. Samples were shipped to EuroFins Genomics (Germany) for processing. The resulting sequence was aligned to desired construct using SnapGene (version 8.0).

2.3.4 *In vitro* transcription of mRNA

For transfection into SGBS adipocytes, mRNA was produced from pcDNA3 plasmid DNA by *in vitro* transcription using the mMESSAGE mMACHINE® T7 kit (ThermoFisher). First, the desired construct was amplified by PCR (Section 2.3.2) using the CMV Forward and BGH-pTx Reverse primers (**Table 2.4**). These primers allowed amplification of the complete coding region as well as the upstream T7 promoter region and incorporate addition of a poly adenosine tail. PCR products were gel purified on a 1% (w/v) agarose gel as described in section 2.3.3.1, with at least two PCR reactions pooled to increase concentration of DNA. 5 µL gel extraction product was assessed for purity on a 1% (w/v) agarose gel as described in section 2.3.3.1 and DNA concentration quantified as described in section 2.3.1.4.

In vitro transcription reactions were assembled on ice using components of the mMESSAGE mMACHINE® T7 kit, comprising up to 1 µg linear template DNA, 1X

NTP/CAP, 1X reaction buffer and 2 µL enzyme mix per 20 µL reaction. Reactions were incubated at 37°C for 90 minutes and RNA recovered using the MEGAclear™ kit following manufacturer's instructions. Samples were brought to a volume of 100 µL using Elution Solution and mixed with 350 µL Binding Solution Concentrate and 250 µL ethanol. Samples were applied to filter column and washed twice with 500 µL Wash Solution, with centrifugation for 1 minute at 13,400 *g* between steps. To elute RNA, 50 µL nuclease-free water was applied to the filter, incubated at 70°C for 10 minutes and centrifuged for 1 minute at 13,400 *g*. The elution step was repeated to give a final volume of 100 µL, before purified RNA was quantified as described in section 2.3.1.4 and stored at -80°C until required.

2.4 NanoBiT Protocols

2.4.1 SPASM NanoBiT assay

Flp-In™ T-Rex™ 293 cells stably expressing SPASM NanoBiT (SpNB) biosensors were plated at 40,000 cells/well in a white tissue culture-treated 96-well plate coated with 40 µL of 5 µg/mL poly-D-lysine (PDL) and incubated at 37ºC and 5% CO_2 overnight. Unless otherwise stated, expression of SpNB constructs was induced with 0.5 ng/mL doxycycline in HEK293-T complete medium and incubated overnight. On the day of the assay, cells were washed twice with HBSS-H and incubated in 80 µL HBSS-H for 30 minutes at 37˚C. NanoGlo® substrate was added by injection using the POLARstar at a final dilution of 1:800 and incubated for 10 minutes at 37˚C. Luminescence signal was measured on the CLARIOstar by kinetic read (well mode) at 37ºC. Measurements were taken with 0.5 s read time and 0.5 s interval for 100 s in triplicate. After 10 s, test compound or vehicle control was added by injection and measurements continued. Luminescence fold change was calculated by dividing measurement reads by baseline signal (average of last 5 data points prior to compound addition) and subtracting vehicle measurements from agonist treatment.

2.4.2 Receptor NanoBiT protein recruitment assays

HEK293-T cells were plated at 40,000 cells/well in a white tissue culture-treated 96-well plate coated with 40 µL of 5 µg/mL PDL and incubated at 37ºC and 5% CO_2 overnight.

Unless otherwise stated, cells were transfected using PEI as described in section 2.2.2.1 with 5 ng/well plasmid DNA of each biosensor component (SmBiT and LgBiT) as indicated in **Table 2.11** and adjusted to 100 ng/well total DNA with pcDNA3 empty vector. Cells were incubated at 37ºC and 5% CO_2 overnight.

On the day of assay, cells were washed twice in HBSS-H and incubated in 80 µL HBSS-H for 30 minutes at 37˚C. NanoGlo® substrate was added at a final dilution of 1:800 and incubated for 10 mins at 37ºC. Luminescence signal was measured on the CLARIOstar by kinetic read (plate mode) at 37ºC. Measurements were taken with 0.5 s read time and 30-40 s interval for 20 minutes in quadruplicate. After 5 cycles, test compound or vehicle control was added by injection and

measurements continued. Luminescence fold change was calculated by dividing measurement reads by baseline signal (average of first 5 data points prior to compound addition) and subtracting vehicle measurements from agonist treatment.

For concentration response curve experiments, measurements were taken at 2 minute intervals and serial dilutions of compounds were added manually in triplicate after 6 minutes. Data analysis was completed as previously and area under curve calculated. Where appropriate, data were normalised to the maximum concentration of reference compound and curves plotted using a three parameter log agonist vs. response model.

Table 2.11 - Plasmid combinations used in receptor NanoBiT protein recruitment assays

Assay	Receptor Expressed	Recruited Protein
FFA4 Arrestin Recruitment	FFA4-LgBiT	SmBiT-ß-arrestin-2
FFA4 Mini Gi	FFA4-LgBiT	SmBiT-miniGi
FFA4 Mini Gq	FFA4-LgBiT	SmBiT-miniGq
FFA1 Arrestin Recruitment	FFA1-LgBiT	SmBiT-ß-arrestin-2
FFA1 Mini Gi	FFA1-LgBiT	SmBiT-miniGi
FFA1 Mini Gq	FFA1-LgBiT	SmBiT-miniGq

2.4.3 Bystander NanoBiT protein recruitment assays

Bystander NanoBiT recruitment assays were completed exactly as described for the receptor NanoBiT recruitment assays (section 2.4.2) but with changes in transfection protocol.

Unless otherwise indicated, cells were transfected using PEI as described in section 2.2.2.1 with 5 ng/well Lyn11-LgBiT, 5 ng/well SmBiT construct, 30 ng/well receptor DNA and adjusted to 100 ng/well total DNA with pcDNA3 empty vector. Cells were incubated at 37ºC and 5% CO_2 overnight and assay continued as described in section 2.4.2.

2.4.4 Colour-shifted NanoBiT arrestin assays

Colour-shifted NanoBiT arrestin recruitment assays were completed as described in section 2.4.3, transfecting 10 ng of the indicated biosensor components and

30 ng of FFA4 receptor per well. During the assay, luminescence measurements were made using the CLARIOstar with the monochromator set for 475 nm (blue) or 550 nm (yellow) light with 30 nm bandwidth, in addition to measuring total luminescence signal. To compare the amount of light emitted at each wavelength, measurements at 475 nm and 550 nm were expressed as a fold change of the total luminescence baseline signal (average of first 3 data points prior to compound addition) and subtracting vehicle measurements from agonist treatment.

After the completion of assays, emission spectra were generated by measuring luminescent signal at 2 or 5 nm intervals using the CLARIOstar in spectral scan mode. Where indicated, the degree of colour shifting was measured by calculating the area under the curve for the blue (420-480 nm) and green (500-560 nm) regions and expressing the ratio of green to blue.

2.5 Staining & Imaging Protocols

2.5.1 Visualisation of membrane-anchored SmBiT constructs by confocal microscopy

Confocal microscopy was used to assess the localisation of the Lyn11- or CAAX-anchored SmBiT biosensors expressing mNeonGreen.

HEK293-T cells were plated at 40,000 cells/well in an 8-well glass chamber slide coated with 100 µg/mL PDL and incubated at 37ºC and 5% CO_2 overnight. Cells were then transfected with 200 ng/well plasmid DNA using PEI as described in section 2.2.2.1 and incubated at 37ºC and 5% CO_2 overnight. Cells were washed in HBSS-H and incubated with 10 µg/mL Hoeschst 33342 prepared in HBSS-H at room temperature in the dark for 15 minutes to stain nuclei. Cells were again washed in HBSS-H with fresh HBSS-H added for imaging.

Cells were imaged as Z-stacks on a Zeiss Vivatome spinning disk confocal microscope using 40X oil-immersion objective lens. Images were viewed and processed using FIJI (version 2.16.0).

2.5.2 In Cell Western of transfected HEK293-T cells

In Cell Western was used to measure protein expression of transiently transfected FFA4-HA in HEK293-T cells.

HEK293-T cells were plated in a black 96-well plate with clear bottom and transfected for a bystander NanoBiT arrestin recruitment assay (section 2.4.3) using different amounts of plasmid expressing haemagglutinin tagged FFA4 receptor (FFA4-HA) and incubated at 37°C/5% CO_2 overnight. Culture medium was aspirated, and cells were fixed in 10% formalin for 15 minutes at room temperature. Formalin was removed and cells washed twice in PBS. Cells were permeabilised in 0.1% Triton X-100 in PBS and incubated at room temperature for 20 minutes with gentle shaking. Triton X-100 was removed, and plate was washed in PBS for 5 minutes three times. Blocking buffer (5% Bovine Serum Albumin (BSA) in PBS) was added to reduce non-specific antibody binding, and plates were incubated at room temperature for 1-2 hours. Blocking buffer was removed and replaced with rat haemagglutinin primary antibody (Table 2.2) at

1:1000 dilution in blocking buffer and incubated overnight at 4°C with gentle shaking.

The following day, primary antibody was collected and cells washed in PBS for 5 minutes three times. Goat anti-rat secondary antibody (Table 2.3) was added at 1:1000 dilution in blocking buffer and incubated at room temperature for 1 hour in the dark with gentle shaking. Cells were again washed three times in PBS, before PBS was removed and CellTag™ 700 stain added at 1:500 dilution in blocking buffer and incubated at room temperature for 1 hour in the dark with gentle shaking. Cells were washed three times in PBS, PBS removed and plates imaged on the LI-COR Odyssey using 700 and 800 nm channels. LI-COR Image Studio™ software was used to select individual wells and quantify fluorescence intensity in both the 700 nm (Ex: 675 nm, Em: 697 nm) and 800 nm (Ex: 778 nm, Em: 795 nm) channels. Background signal was subtracted from each of the respective channels: wells with no cells for the CellTag™ 700 nm measurement and wells where no primary antibody was used for the 800 nm channel, and the ratio of 800/700 channel taken to express primary signal normalised to cell count.

2.5.3 Assessment of cell growth by measurement of cell number

To assess the growth rate of SGBS cells in different culture medium, cells were plated and allowed to grow as described in section 2.2.4.1. On indicated days, medium was aspirated and cells washed in filtered PBS. Cells were fixed by incubation with 10% formalin at room temperature for 15 minutes. Formalin was removed and cells washed twice in PBS.

Hoeschst 33342 was prepared at a final concentration of 10 µg/mL in PBS, added to plates and incubated at room temperature in the dark for 15 minutes to stain nuclei. Cells were washed twice in PBS and fresh PBS added for imaging.

Cells were imaged on the EVOS FL Auto 2 system using the DAPI channel with 4X magnification and an appropriate number of Fields of View (FOV) to cover >50% well area. For 12-well plates, 16 FOV were captured and for 24-well plates, 6 FOV were captured. Tiled images were saved and imported to (Fiji is Just) ImageJ (FIJI; version 2.14.0) for analysis.

In FIJI, a colour threshold was initially set to isolate individual nuclei brightspots. The *Analyze Particles* command was then used to count particles with area up to 1000 pixel units to exclude large pieces of debris. The number of nuclei was then expressed as a fold increase relative to the day 1 count.

2.5.4 Staining and quantification of lipid droplets using Oil Red O

Accumulation of lipid droplets in adipocytes, differentiated SGBS cells were washed in PBS and fixed in 10% formalin for 15 minutes at room temperature. Formalin was removed, cells washed twice in PBS and stored at 4°C in PBS until required.

Fixed cells were washed twice in dH_2O and incubated in 60% isopropanol for 5 minutes. Cells were then stained with 1.8 mg/mL Oil Red O (ORO) solution in 60% isopropanol for 20 minutes with gentle shaking. Cells were washed five times with dH_2O to remove residual dye and imaged using colour camera on the EVOS FL Auto 2 Imaging System.

To quantify ORO staining, cells were washed a further three times with 60% isopropanol. ORO was extracted by incubating cells in 100% isopropanol and incubating at room temperature for 5 minutes with gentle shaking. 50 µL samples of isopropanol containing extracted ORO were transferred in duplicate to a 96-well plate and absorbance at 492 nm measured with appropriate path length correction on the POLARstar. A_{492} measurement of 100% isopropanol was subtracted as a baseline control.

For adipocyte spheroids, an equivalent process was followed. 12-24 spheroids were pooled in an eppendorf tube, washed once in PBS and fixed in 50 µL of 10% formalin for 1 hour at room temperature. Fixed spheroids were washed twice in 1 mL dH_2O and incubated in 60% isopropanol for 15 minutes at room temperature with gentle shaking. ORO was added and incubated for 1 hour at room temperature with gentle shaking, before washing off excess with three 10-minute washes in 60% isopropanol. 8-10 stained spheroids were transferred to clean eppendorf tubes and buffer removed. ORO was extracted in 120 µL 100% isopropanol, 50 µL samples transferred in duplicate to a clear 96-well plate and quantified as above.

2.5.5 Confocal imaging of adipocyte spheroids

To visualise adipocyte spheroids using confocal microscopy, 12-50 spheroids were pooled in eppendorf tubes and culture medium removed. Spheroids were washed in 1 mL PBS and fixed in 50 µL 10% formalin for 1 hour at room temperature. Formalin was removed and collected for appropriate disposal, and spheroids washed twice in 1 mL PBS. Fixed spheroids could then be stored at 4°C until required.

To stain cell nuclei and lipid droplets, spheroids were stained with Hoescht 33342 and LipidSpot™ 488 dyes respectively. Both dyes were diluted 1:1000 in PBS, added to spheroid tubes and incubated for 30 minutes at room temperature in the dark. Spheroids were transferred to an 8-well chamber slide and covered with one drop of mounting solution containing DAPI.

Spheroids were imaged as Z-stacks on a Zeiss LSM980 laser scanning confocal microscope using 10X objective lens. Images were viewed using FIJI (version 2.16.0) and processed with 'subtract background' plugin and maximum intensity Z-stack projection obtained.

2.5.6 Immunocytochemistry of adipocyte spheroids

Immunocytochemistry (ICC) was performed on adipocyte spheroids to identify protein expression of adipocyte markers.

20-25 spheroids were pooled in eppendorf tubes and fixed in 10% formalin as described in section 2.5.5. Formalin was removed and spheroids washed twice in 1 mL PBS. Spheroids were permeabilised in 0.1% Triton X-100 in PBS for 10 minutes at room temperature with gentle shaking. A short incubation time was chosen to reduce potential effects to lipid droplet morphology. Triton X-100 was removed and washed off with three 5-minute PBS washes with gentle shaking. Spheroids were incubated with blocking buffer (5% BSA in PBS) for 1-2 hours at room temperature with gentle shaking. Primary mouse Perilipin 1 antibody **(Table 2.2)** was added at 1:500 dilution in blocking buffer overnight at 4°C on a rotator. Primary antibody was collected, and spheroids were washed three times in PBS for 10 minutes at room temperature with gentle shaking. Secondary goat anti-mouse antibody **(Table 2.3)** was added at 1:400 dilution in blocking buffer

and incubated for 1 hour in the dark with gentle shaking. Secondary antibody was removed, and spheroids washed three times in PBS for 10 minutes at room temperature with gentle shaking.

Wash buffer was removed and spheroids were collected using a cut P200 pipette tip which had been pre-coated in blocking buffer to prevent spheroids sticking to the inside of the tip. Spheroids were transferred to a glass microscope slide and any remaining buffer removed with a pipette tip. Spheroids were covered with one drop of mounting solution containing DAPI nucleic acid stain and a coverslip added. Slides were incubated in the dark for 2 hours at room temperature or overnight at 4°C to allow slide to dry and then sealed with nail varnish.

Spheroids were imaged on a Zeiss LSM980 laser scanning confocal microscope using 40X oil-immersion objective lens. Images were viewed using FIJI (version 2.16.0) and processed with 'subtract background' plugin.

2.5.7 Preparation of spheroids for paraffin sectioning

Paraffin sectioning was carried out with the support of Frazer Bell and the team at the University of Glasgow Veterinary School.

50 spheroids at indicated time points of differentiation were pooled and fixed in 10% formalin as described in section 2.5.5. PBS wash was aspirated and spheroids were stained in 50 µL haematoxylin for 2 minutes at room temperature to improve visibility of the spheroids within paraffin blocks. Haematoxylin was removed and spheroids washed several times in PBS until wash buffer remained clear.

To better contain spheroids for manipulation through processing, spheroids were embedded in 2% agarose in water. Molten 2% agarose was prepared and 200 µL added to a pre-warmed eppendorf tube on a heat block at 60°C. Wash buffer was removed from stained spheroids, leaving <50 µL remaining, and spheroids transferred into the molten agarose using a cut P200 pipette tip. Agarose was gently stirred with a pipette tip to disperse spheroids and tubes immediately placed on ice to set. Embedded spheroids were then transferred to the University of Glasgow Veterinary School for processing, sectioning and staining.

Agarose plugs were removed from eppendorf tubes and processed as individual blocks using a standard histology protocol. Samples were dehydrated through alcohols, cleared through xylenes and impregnated with plasticised paraffin wax. Wax blocks were sectioned using a microtome and sections collected on PDL-coated glass slides.

Sections on glass microscope slides and stained for haematoxylin and eosin (H&E) were returned and imaged using the colour camera on the EVOS FL Auto 2 Imaging System.

2.5.8 Preparation of spheroids for cryosectioning

Cryosectioning was carried out with the support of Tyler Shaw at the Glasgow Imaging Facility, University of Glasgow to obtain sequential sections through SGBS spheroids.

25 spheroids at day 0 or day 14 were pooled and fixed in 50 µL 4% paraformaldehyde (PFA) overnight at 4°C. PFA was removed and spheroids washed twice in 1 mL PBS. Spheroids were again stained in haematoxylin for 2 minutes to improve visibility within the sample and washed thoroughly to remove excess stain. Wash buffer was removed, and samples were incubated overnight in 30% (w/v) sucrose in PBS at 4°C to protect against freezing artifacts.

Spheroids samples were then embedded in 7.5% (w/v) gelatin solution in 10% (w/v) sucrose solution for 1 hour at 37°C. Samples were then snap frozen and sectioned at 7 µm on the cryostat. Cryosections were mounted on glass microscope slides and stored at -80°C until required.

2.5.9 Haematoxylin & Eosin staining of adipocyte spheroid sections

Cryosections of adipocyte spheroids were stained with haematoxylin & eosin (H&E) to assess morphology and structure. Sections were thawed under foil for 1 hour and placed in a staining rack. Slides were initially rinsed in warm tap water to remove any residual gelatin then submerged in filtered haematoxylin for 5 minutes with regular agitation to stain nuclei. Haematoxylin was rinsed well in

tap water to remove excess stain and set nuclei staining through bluing. Slides were counterstained by submerging in Eosin Y for 10 seconds. H&E staining was then differentiated by submerging in two changes of 95% ethanol, and samples dehydrated by submerging in two changes of 100% ethanol for 5 minutes each. Samples were cleared by incubating for 10 minutes in two changes of Histo-Clear II xylene alternative and coverslips mounted using Dibutylphthalate Polystyrene Xylene (DPX) mounting medium. Once dried, slides were imaged on the EVOS FL Auto 2 Imaging System.

2.5.10 Immunohistochemistry of adipocyte spheroid sections

Immunohistochemistry (IHC) was completed on cryosections of adipocyte spheroids to assess expression of protein markers. IHC was completed using the horseradish peroxidase (HRP) method, where a secondary antibody is conjugated to the HRP enzyme which converts the 3,3'-diaminobenzidine (DAB) with Nickel substrate into a dark brown precipitate which can be visualised using brightfield microscopy.

Sections were thawed under foil for 20 mins and placed in a staining rack. Slides were rinsed four times for 10 minutes in Tris Buffered Saline (TBS; section 2.1.3) warmed to 37°C to remove residual gelatin. Slides were incubated in 3% (v/v) H_2O_2 in methanol for 20 minutes to block endogenous peroxidase activity which may interfere with antigen detection. Slides were washed for 10 minutes in tap water and transferred to fresh TBS. Sections were circled with a hydrophobic pen and blocked with 2.5% horse serum for 2 hours at room temperature. Primary antibodies were diluted to an appropriate working concentration **(Table 2.2)** in PBS containing 1% (w/v) BSA, added to slides and incubated overnight at 4°C. Controls were included where primary antibody was replaced with an equal concentration of rabbit IgG control antibody, or buffer alone. Primary antibody was collected and slides were washed twice for 10 minutes in TBS. Secondary ImmPRESS HRP Horse Anti-Rabbit IgG antibody **(Table 2.3)** was added for 1 hour at room temperature and washed in TBS containing 0.1% (v/v) Tween-20 for 10 minutes followed by a final 10 minute wash in TBS.

DAB with Nickel substrate solution (Vector Laboratories) was prepared following manufacturer's instructions and added to slides. The development of staining

was observed under a microscope and quenched in water after 3-5 minutes. Slides were then counterstained with haematoxylin, dehydrated and imaged as described in section 2.5.9.

2.5.11 Electron microscopy of adipocyte spheroids

Electron microscopy was carried out with the support of Margaret Mullen at the Glasgow Imaging Facility, University of Glasgow.

Spheroids at day 0 or day 14 of differentiation were pooled and fixed in 1.5% glutaraldehyde in 0.1 M sodium cacodylate for 1 hour at room temperature. Residual fixative was removed and samples were stored in 0.1 M sodium cacodylate at 4°C until required.

Samples were rinsed three times for 5 minutes in 0.1 M sodium cacodylate before negative staining in 1% (w/v) osmium tetroxide in 0.1 M sodium cacodylate for 1 hour at room temperature. Osmium tetroxide was removed and samples were washed three times for 10 minutes in dH_2O. Samples were then treated with 0.5% (w/v) uranyl acetate in dH_2O for 1 hour at room temperature.

Samples were rinsed in dH_2O and then dehydrated in increasing concentrations of ethanol (30%, 50%, 70%, 90%) for 10 minutes each. Samples were washed four times for 5 minutes in two changes of 100% ethanol.

2.5.11.1 Scanning Electron Microscopy

For Scanning Electron Microscopy (SEM), dehydrated samples were washed three times in hexamethyldisilazane (HMDS) for 5 minutes and allowed to dry overnight. Individual spheroids were mounted onto SEM stubs coated with conductive tape and coated with 20 nm Au/Pd before imaging on the JEOL IT 100 Scanning Electron Microscope.

2.5.11.2 Transmission Electron Microscopy

For Transmission Electron Microscopy (TEM), dehydrated spheroids were washed with propylene oxide (PO) three times for 5 minutes, and incubated in a 1:1 solution of PO:EPON™ epoxy resin overnight. Solution was removed, spheroids

incubated in pure EPON™ resin overnight and changed to fresh EPON resin for embedding. Samples were transferred to block moulds and incubated at 60°C for 48 hours. Ultrathin sections were cut from the blocks and either stained with toluidine blue to assess section morphology at a lower magnification, or imaged on the JEOL 1400 Flash Transmission Electron Microscope.

2.6 Adipocyte Assay Protocols

2.6.1 Analysis of spheroid viability using CellTitre-Glo®

Spheroid viability was assessed using CellTitre-Glo® 3D reagent (Promega), which measures ATP as an indicator of viability, and generates a luminescent signal.

Individual or pools of 4 spheroids were collected from a ULA spheroid culture plate and transferred to a white 96-well plate using a P100 micropipette with cut tip. The volume of culture medium was estimated using a micropipette, reduced to 40 µL and plate was allowed to sit at room temperature for 30 minutes. 40 µL CellTitre-Glo 3D reagent was added to each well, the plate was shaken on a plate shaker for 5 minutes at 200 rpm then incubated at room temperature in the dark for 30 minutes. Total luminescence emission was then measured on the CLARIOstar.

2.6.2 Analysis of gene expression using qPCR

RNA from SGBS cells was isolated using an RNeasy Mini Kit (QIAGEN) following manufacturer's instructions. In 2D, cells from 1 well of a 6-well plate or 4 wells of a 24 well plate were rinsed with sterile PBS and lysed with 500 µL RLT buffer with vigorous pipetting to ensure lysis. In 3D, >20 spheroids were pooled in a sterile eppendorf tube, washed in PBS and lysed in 250 µL RLT buffer. Samples were vortexed for 3-5 minutes to ensure complete lysis. RNA isolation was then completed following the RNeasy Mini Kit protocol, including 15 minute on-column DNAse digestion using the RNAse-free DNAse set (QIAGEN) to digest genomic DNA. RNA was eluted in 30 µL nuclease-free dH_2O, quantified as described in section 2.3.1.4 and stored at -80°C until required.

cDNA was synthesised using a Moloney Murine Leukemia Virus (M-MLV) reverse transcriptase kit (Invitrogen). Up to 1 µg RNA was mixed with 0.5 mM each dNTPs and 2.5 µM random hexamer primers and incubated at 65°C for 5 minutes. Master mix, containing 1X included first strand buffer, 10 mM dithiothreitol (DTT) and 40 Units RNAseOUT™ recombinant ribonuclease inhibitor (Invitrogen) to reduce RNA degradation, was added and incubated at 37°C for 2 minutes before 200 Units M-MLV reverse transcriptase enzyme was added. Samples were

incubated on a thermocycler at 25°C for 10 minutes, 37°C for 50 minutes to allow reaction to occur, and 70°C for 15 minutes to deactivate the enzyme. Samples were diluted in nuclease-free water to a concentration between 2.5 and 10 ng/µL RNA equivalent of cDNA and stored at -20°C until required.

Real Time Quantitative PCR (RT-qPCR) was carried out using the Fast SYBR™ Green reagent (Invitrogen). 10 ng RNA equivalent of cDNA was added to a 384-well qPCR plate (Invitrogen) and combined with 1X Fast SYBR™ Green master mix and 400 nM forward and reverse primers specific to each gene of interest as described in Table 2.5. qPCR primers were designed using NCBI Primer-BLAST tool (Ye et al., 2012). Where possible, primers were designed to span exon-exon junctions and amplify 100-500 bp regions of the gene coding sequence.

PCR reactions were carried out in duplicate using the QuantStudio 5 Real-Time PCR System (Invitrogen) using the fluorescence channel for SYBR Green and protocol as described in Table 2.12.

Table 2.12 - qPCR thermocycler protocol

Segment	Cycles	Temperature	Duration
Initial Denaturing	1	95°C	20 s
Denaturing	44	95°C	1 s
Annealing, Extension & Imaging		60°C	20 s

C_T values were generated using Design and Analysis 2 instrument software (ThermoFisher) and analysed using the $2^{-\Delta\Delta CT}$ method to express fold change relative to reference samples.

2.6.3 Lipolysis assay using Free Glycerol reagent

SGBS adipocyte spheroids were generated and differentiated as described in section 2.2.4.3. On day 14 of differentiation, 20 spheroids were pooled into eppendorf tubes. Culture medium was removed and spheroids were washed three times with HBSS-H. Between washes, tubes were centrifuged at 1,500 *g* for 2 minutes to gather spheroids at the bottom of the tubes. Wash buffer was removed and spheroids were incubated in 600 µL HBSS-H containing 1% fatty-acid free bovine serum albumin (BSA) for 10 minutes. 120 µL samples were taken (time 0) and replaced with 120 µL test compounds prepared in HBSS-H/1% BSA at

five times final concentration. Samples were incubated at 37°C for 6 hours, with 120 µL samples taken after 2, 4, and 6 hours. Glycerol standards were prepared with 200 mg/L equivalent triolein top concentration with serial dilution. 50 µL sample or standard was transferred in duplicate into a 96-well flat-bottomed clear plate and mixed with 50 µL free glycerol reagent. Plates were incubated at 37ºC for 10 mins and absorbance at 540 nm measured on the POLARstar microplate reader. The glycerol standard was used to interpolate glycerol concentrations in samples and corrected for the volume of buffer in assay tubes at each time point.

2.6.4 Lipolysis assay using Glycerol-Glo™ reagent

SGBS adipocyte spheroids were generated and differentiated as described in section 2.2.4.3. On day 14 of differentiation, 8-10 spheroids were pooled into eppendorf tubes using a VOYAGER Adjustable Tip Spacing Pipette (Integra Biosciences). Culture medium was removed and spheroids were washed as described in section 2.6.3. Wash buffer was removed and spheroids were incubated in 200 µL HBSS-H containing 0.5% fatty-acid free bovine serum albumin (BSA) for 10 minutes. 50 µL samples were taken (time 0) and replaced with 50 µL test compounds prepared in HBSS-H/0.5% BSA at four times final concentration. Samples were incubated at 37°C for 3 hours and 50 µL samples taken. Glycerol-Glo™ detection reagent was prepared following manufacturer's guidance, by diluting Reductase Substrate at 1:100 in Glycerol Detection Solution one hour before use. Kinetic Enhancer was added at 1:100 immediately before use. Glycerol standards were prepared with 80 µM top concentration with 1:2 serial dilution. 5 µL sample or standard was transferred into a white low volume 384-well plate in quadruplicate and mixed with 5 µL detection reagent. Assay plate was incubated for 1 hour at room temperature in the dark and raw luminescence signal measured on the CLARIOstar. Signal was expressed as a fold change relative to the baseline before compound addition.

In assays comparing the performance of Free Glycerol and Glycerol-Glo™ reagents, the assay was performed following the protocol for the Free Glycerol reagent (section 2.6.3) in an initial volume of 600 µL HBSS-H containing 1% BSA. 150 µL samples were taken and replaced with 150 µL compounds prepared at four times final concentration, and 150 µL samples taken at each time point.

After incubation period, 50 µL samples were taken in duplicate to a clear 96-well plate for Free Glycerol assay, and 5 µL samples were taken in quadruplicate to a white 384-well plate for Glycerol-Glo™ assay. The assays were then continued following their respective protocols.

2.6.5 Glucose uptake assay

SGBS adipocyte spheroids were generated and differentiated as described in section 2.2.4.2, with insulin removed from differentiation medium on day 13. On day 14 of differentiation, medium was changed to SGBS 0F medium (Table 2.1) and incubated at 37°C/5% CO_2 for 4 hours to serum starve the spheroids in advance of the assay.

8 spheroids were pooled into eppendorf tubes using a VOYAGER Adjustable Tip Spacing Pipette (Integra Biosciences). Culture medium was removed, and spheroids were washed twice with KRP-H. Between washes, tubes were centrifuged at 1,500 *g* for 2 minutes to gather spheroids at the bottom of the tubes. Spheroids were incubated at 37°C in 100 µL KRP-H buffer for 15 minutes. 1 µM insulin or vehicle was added to stimulate glucose uptake and tubes incubated at 37°C for a further hour. In some experiments, 40 µM cytochalasin B (or vehicle) was added to block actin polymerisation and act as a baseline control. Glucose Uptake-Glo™ detection reagent was prepared following manufacturer's guidance, by combining 100 µL luciferase reagent, 1 µL $NADP^+$, 2.5 µL Glucose-6-Phosphate Dehydrogenase, 0.5 µL reductase and 0.0625 µL reductase substrate per reaction, and resting for one hour at room temperature before use. After incubation time, KRP-H assay buffer containing compounds was removed and replaced with 50 µL KRP-H containing 1 mM 2-deoxyglucose (2DG) for 20 minutes at room temperature unless otherwise stated. 25 µL stop buffer was added and samples vortexed to lyse spheroids. 25 µL neutralisation buffer was added simultaneously with 100 µL detection reagent and samples vortexed. 90 µL samples were transferred in duplicate to a white 96-well plate and incubated at room temperature for 1 hour. Luminescence signal was measured on the CLARIOstar, technical replicates averaged, and data expressed relative to vehicle result.

2.6.6 Bystander BRET arrestin recruitment assay

Arrestin recruitment was measured in electroporated samples using a single plasmid which expresses both components of a BRET bystander arrestin recruitment biosensor - Lyn11-mNG and NLuc-Arrestin-3 - separated by an Internal Ribosome Entry Site (IRES). Differentiated or undifferentiated SGBS cells and spheroids were electroporated as described in section 2.2.2.4 with equal amounts of pIRES plasmid and plasmid expressing FFA4-HA.

For SGBS cells in 2D, 250,000 undifferentiated cells were electroporated with 1 µg pIRES plasmid and 1 µg FFA4-HA plasmid or pcDNA control and dispensed into a 24-well plate for incubation at 37ºC and 5% CO_2 overnight. The following day the cells were harvested from the 24-well plate, each well was resuspended in 800 µL SGBS complete medium and 100 µL cell suspension plated per well of a collagen-coated white 96-well plate. Cells were again incubated at 37ºC and 5% CO_2 overnight. On the day of assay, cells were washed twice in HBSS-H and incubated in 80 µL HBSS-H for 30 minutes at 37°C. NanoGlo® substrate was added at a final dilution of 1:800 and incubated for 10 mins at 37ºC. BRET signal was measured on the PHERAstar using the BRET 1 plus optic module with luminescent readings made at 475 nm (donor) and 535 nm (acceptor) and expressed as the acceptor/donor ratio. Kinetic measurements were taken at 37ºC with 1 s read time and 1 minute interval for 20 minutes in triplicate. After 3 cycles, 10 µM TUG-891 or vehicle control was added by injection and measurements continued. Net BRET was calculated by dividing BRET ratio by baseline signal (average of first 3 data points prior to compound addition) and subtracting vehicle measurements from agonist treatment.

For spheroids assays, 36-48 spheroids were electroporated with 1 µg pIRES plasmid and 1 µg FFA4-HA plasmid or pcDNA control and dispensed into individual wells of a 96-well ULA plate for incubation at 37ºC and 5% CO_2 overnight. On the day of assay, 4 spheroids were pooled into eppendorf tubes and washed twice in HBSS-H. 80 µL HBSS-H containing the spheroids was transferred to a white 96-well plate and incubated for 30 minutes at 37°C. Raw luminescence measurements were made using the CLARIOstar before and after addition of NanoGlo® substrate and plate was incubated for 10 mins at 37ºC. The BRET ratio was measured on the PHERAstar (endpoint mode) with 15 s

measurement read time. 10 μM TUG-891 or vehicle control was added to each well at 15 s intervals to ensure a consistent 5 minute incubation time across the plate and BRET ratio was again measured. BRET ratio fold change was calculated by dividing the BRET ratio after compound addition by the baseline signal.

2.7 Nanoindentation

Nanoindentation experiments were carried out with the support of Dr. Giuseppe Ciccone at the University of Glasgow. Differentiated or undifferentiated SGBS spheroids at day 14 were transferred to 35 mm petri dishes coated with 3.5 µg/cm^2 Cell-Tak coating solution and covered with PBS. Nanoindentation was carried out using the Chiaro nanoindenter (Optics11 Life) as previously described (Ciccone et al., 2022) using a cantilever with 0.03 N/m stiffness and spherical tip of radius 8 µm. A 5 x 5 matrix scan was completed twice per spheroid, with 4 spheroids scanned per condition across two experimental days. Data was analysed using an open-source Python software (Ciccone et al., 2022) to determine Young's modulus.

2.8 Data Analysis

Data analysis was completed in GraphPad Prism 10 (version 10.4.1) as indicated in the relevant assay protocols. Data are presented as mean ± standard error of the mean (SEM) of replicates indicated in figure legends.

Statistical comparisons were made using unpaired t-tests to compare two samples, 1-way Analysis of Variance (ANOVA) to compare 3 or more samples or 2-way ANOVA to compare grouped data. Appropriate post hoc analyses were used with ANOVAs to compare individual conditions and are indicated in figure legends. Throughout, a P value less than 0.05 was considered statistically significant and is represented as follows: *$p < 0.05$, **$p < 0.01$, ***$p < 0.001$, ****$p < 0.0001$.

Where concentration response curves were generated, response was typically calculated as the area under curve (AUC) of kinetic traces and plotted against the log concentration of the ligand. Vehicle controls are plotted one log unit lower than the lowest concentration used. Curves were fitted using a three-parameter log(agonist) vs. response model, EC_{50} values calculated as the concentration where a half-maximal response is obtained, and the negative logarithm taken to obtain pEC_{50} values for each ligand.

Biosensor illustrations were created using biorender.com.

3 The design and optimisation of NanoBiT biosensors to investigate FFA4 signalling

3.1 Introduction

G Protein-Coupled Receptors (GPCRs) are the largest family of transmembrane receptors in the mammalian genome, and act to transduce extracellular signals into diverse biological effects through a variety of intracellular signalling pathways (Odoemelam et al., 2020; Yang et al., 2021). Recently, a sub-family of GPCRs has emerged which respond to intermediates of energy metabolism, typically produced by the gut microbiota or released by metabolic tissues (Husted et al., 2017). These metabolites can therefore act as signalling molecules, and metabolite-sensing GPCRs (m-GPCRs) have been reported to play an important role in the communication between adipose tissue and invading immune cells in metabolic disorders (Duncan et al., 2023). FFA4, formerly GPR120, is a m-GPCR activated by long chain unsaturated fatty acids. It is expressed on both macrophages and adipocytes with reported anti-inflammatory and insulin-sensitising effects (Oh et al., 2010, 2014; Husted et al., 2020), and several autocrine and paracrine signalling loops have been proposed (Duncan et al., 2023). As GPCRs are historically successful drug targets (Hauser et al., 2017; Lorente et al., 2025), there has been significant interest in developing agonists for FFA4 as treatments for T2D and MASH, however no candidates have yet reached clinical trials (Carullo et al., 2021).

Measuring the real-time activity of GPCRs in living cells is essential to characterise their signalling, function, and pharmacology. In the past two decades, genetically encoded biosensors have become widely used to measure different aspects of the GPCR signalling cascade such as ligand binding, G protein coupling or arrestin recruitment (Hudson, 2017; Olsen and English, 2023). Many of these technologies were developed using Bioluminescence Resonance Energy Transfer (BRET) approaches to measure protein-protein interactions (Xu et al., 1999; Boute et al., 2002; Pfleger and Eidne, 2006). Briefly, BRET occurs when a bioluminescent protein ‘donor’ comes into close proximity (10-100 Å) with a fluorescent protein ‘acceptor’, resulting in a transfer of energy allowing the fluorescent protein to emit light. Practically, this involves fusing the proteins of interest to a bioluminescent donor and fluorescent acceptor and measuring the ratio of their emissions following ligand treatment to determine protein interactions (Masuho et al., 2015a). BRET techniques have been used for several years to study many aspects of GPCR signalling including G

protein and arrestin recruitment as well as downstream signals (Salahpour et al., 2012), and are well suited to high throughput plate-based assays (Boute et al., 2002).

One alternative method to BRET for measuring GPCR signalling in living cells is through fragment complementation assays. In these assays, a bioluminescent protein is split into two non-functional parts which recombine to form a full-length functional reporter when brought together (Wehr and Rossner, 2016). These were not widely used in the GPCR field until the development of the NanoBiT system by Promega Inc., which comprises two non-functional small (SmBiT) and large (LgBiT) fragments of the NanoLuciferase (NLuc) luminescent protein (Dixon et al., 2015). This system has proven to be more popular than previous alternatives due to the small size and bright emission of the parent protein, but also due to significant protein engineering efforts to optimise the affinity, stability and steric hinderance of the final fragments (Dixon et al., 2015).

Within the wider context of my PhD, I aimed to express genetically encoded biosensors within a 3D adipocyte spheroid model to measure the signalling of m-GPCRs. I hypothesised that a NanoBiT biosensor design would be ideal for this purpose as this would allow real-time measurement of receptor activity with only a single wavelength of light, compared to the ratiometric BRET measurement. This typically results in a greater dynamic range which I believed would allow easier measurement in a 3D system, and would minimise potential complications arising by light penetration differing between two wavelengths within the spheroid (Dragulescu-Andrasi et al., 2011). Furthermore, there is potential to colour-shift the emission wavelength of the NanoBiT fragments which may improve the light penetration of the biosensor and allow multiplexing of additional assays (Liu et al., 2021).

In this chapter, I aimed to design, generate, and optimise genetically encoded NanoBiT biosensors to measure signalling of the FFA4 receptor. These constructs were based on previously reported biosensor designs and reengineered to a single-wavelength format. Furthermore, I explored the potential to colour-shift the NanoBiT biosensors to a yellow or green emission wavelength to allow multiplexing of assays. Together, these biosensors allow measurement of

different aspects of FFA4 signalling, and offer an extensive toolkit to investigate FFA4 activity and its therapeutic potential in a more physiologically relevant cell model system.

3.2 Single molecule SPASM-style NanoBiT (SpNB) biosensors measure interactions between FFA4 and Gα peptides

The first biosensor considered was based on the Systematic Protein Affinity Strength Modulation (SPASM) design, where a GPCR is modified with a C-terminal extension comprising both parts of a biosensor separated by a flexible linker, with either a full length or 27 amino acid fragment of the C terminal of a Gα protein at the C terminus (Sivaramakrishnan and Spudich, 2011; Malik et al., 2013, 2017). When the receptor is activated, the Gα peptide binds the active conformation of the receptor allowing a signal to be measured. These biosensors were originally developed using Förster resonance energy transfer (FRET) tags but have since been developed in the BRET format (Mackenzie et al., 2019; Maziarz et al., 2020). In order to adapt this sensor design for a NanoBiT (SpNB) assay **(Figure 3.1)**, the SmBiT and LgBiT components of the NanoBiT system have been separated by an ER/K flexible linker and tethered to the FFA4 receptor, with the final 27 amino acids of selected Gα proteins at the C-terminus. Initially the Gα15, Gαi3 and Gαz peptides were selected for testing in SpNB biosensors, as these resulted in the greatest signal window in previous data from our laboratory when tested at FFA4 in a BRET-based format (Hudson, unpublished). Both ‘a’ and ‘b’ orientations were made and tested, where the orientation of the SmBiT and LgBiT is inverted. Flp-In 293 T-REx cell lines were generated which express each biosensor under an inducible promoter.

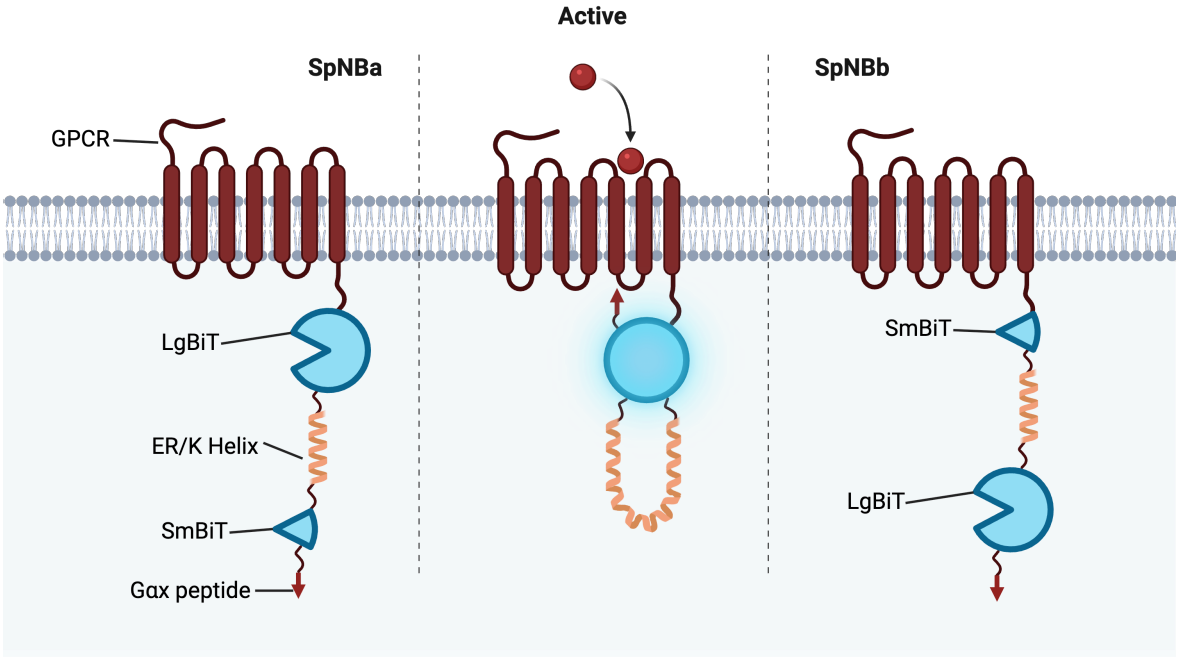

Figure 3.1 - SpNB biosensors design. Schematic of unimolecular NanoBiT FFA4 biosensors (SpNB). Gα peptides are comprised of the final 27 amino acids of the indicated G protein. When the receptor is activated, the Gαx peptide docks into the active conformation of the GPCR, allowing complementation of the split luciferase and increased luminescent signal. Both 'a' (left) and 'b' (right) orientations were designed, where the orientation of the LgBiT and SmBiT are inverted.

Initially, a titration experiment was carried out using the SpNBa-G15 biosensor to identify the optimal concentration of doxycycline to induce expression of the biosensor **(Figure 3.2)**. During the assay, the receptor was activated by 10 μM FFA4 agonist, TUG-891, and luminescent signal measured at 0.5 s intervals. Increasing the concentration of doxycycline resulted in a significant increase in the baseline luminescence signal of the biosensor **(Figure 3.2A)**, confirming that the expression levels of the biosensor increases with increasing concentrations of doxycycline. Similarly, increasing doxycycline concentration also increased the net raw luminescent response following TUG-891 treatment **(Figure 3.2B)**. However, when this response is expressed as a 'net fold' change above the baseline signal, there is little difference in the kinetic traces between the doxycycline concentrations **(Figure 3.2C),** and no significant differences in either peak fold response or area under curve (AUC) quantification **(Figure 3.2D)**. If anything, the TUG-891 response with 0 ng/mL doxycycline, where expression is not induced and therefore driven by 'leaky' promoter activity (Pham et al., 2008; Senkel et al., 2009), is more sustained than the higher concentrations. Perhaps suggesting that very low biosensor expression level may be preferred for this assay. As the 0 ng/mL condition results in very low raw

luminescence values, a doxycycline concentration of 0.5 ng/mL was selected for further experimentation.

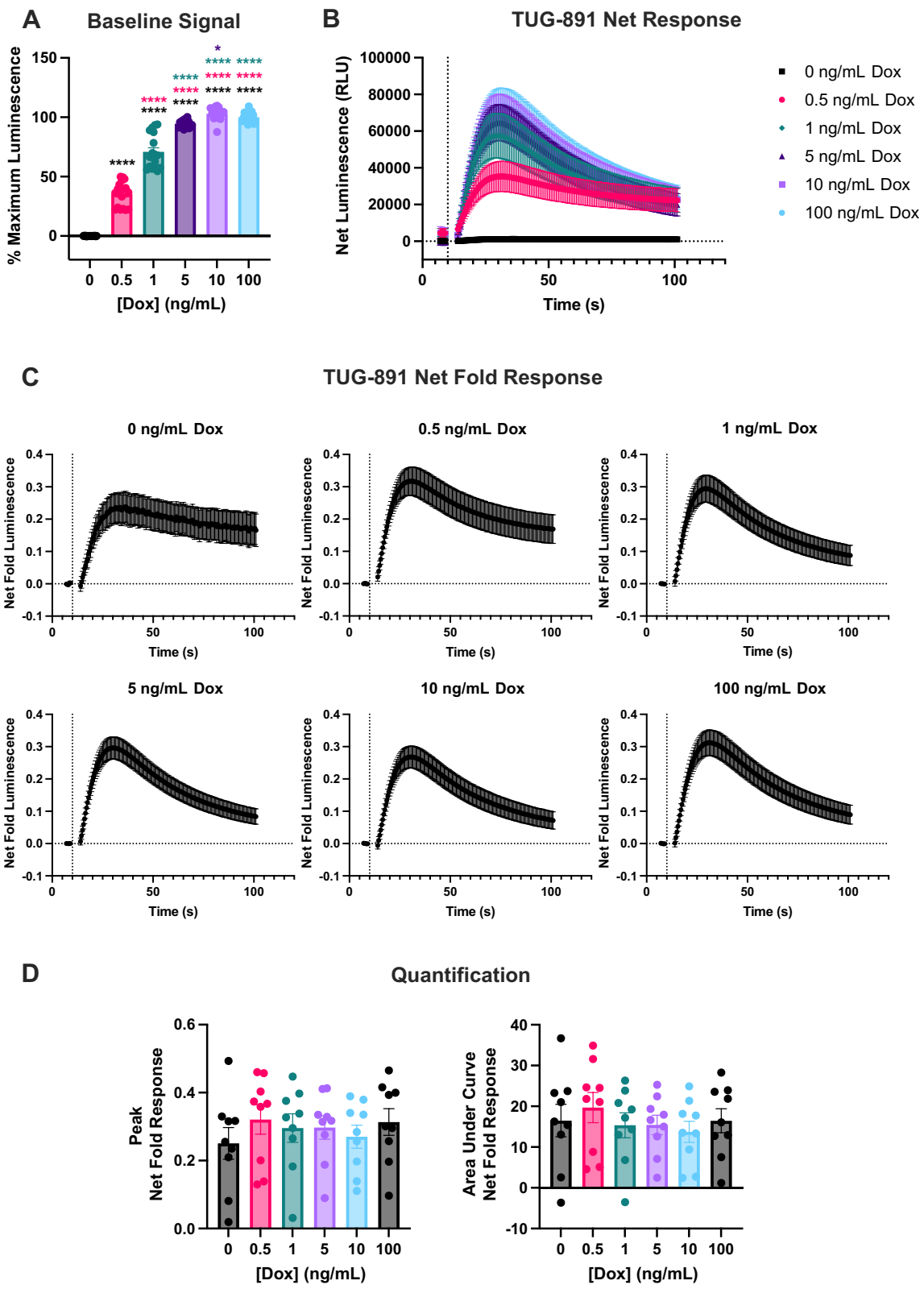

Figure 3.2 – FFA4-SpNB biosensors are effective across a wide expression level range. A) Baseline luminescence measurements at increasing doxycycline concentrations. Data were normalised to maximum doxycycline concentration and presented as mean ± SEM from N=3 independent experiments with n=6 technical replicates. **B)** Kinetic measurements from doxycycline titration experiment. Flp-In cells expressing FFA4-SpNBa-G15 biosensor were induced with the indicated concentration of doxycycline and luminescence measured before and after receptor

activation with 10 μM TUG-891 after 10 seconds (indicated by the dotted line), and vehicle response subtracted. Data presented as mean ± SEM from N=3 independent experiments with n=3 technical replicates. **C)** Data in B expressed as 'net fold luminescence'; raw luminescence values were divided by baseline signal (average of 5 measurements before TUG-891 addition) and vehicle response subtracted. **D)** Quantification of SpNB kinetic curves (shown in C). Peak response and area under curve (AUC) were calculated from net fold luminescence traces for each doxycycline concentration. Individual measurements plotted with mean ± SEM indicated from N=3 independent experiments with n=3 technical replicates. Statistical comparisons in A and C were made using one-way ANOVA with Tukey's multiple comparisons test. *p < 0.05, **p < 0.01, ****p < 0.0001 where colour indicates the relevant comparison. All other comparisons were not significant.

Next, the Gα15, Gαi3 and Gαz SpNB biosensors were tested in both the 'a' and 'b' orientations for their response to 10 μM TUG-891 **(Figure 3.3A-B)**. The kinetic responses were then quantified by calculating peak signal, luminescence signal at 100 s and AUC for each biosensor **(Figure 3.3C)**.

For the SpNBa orientation, TUG-891 activation resulted in a significant increase in peak response and AUC over vehicle for all three Gα peptides tested ($p < 0.0001$), with an increase in signal of 30.0%, 29.7% and 34.3% for the G15, Gi3 and Gz sensors respectively. No significant difference was observed among the different Gα peptides. However, differences in the kinetics among the three sensors were observed, as shown from the comparisons made using net fold change at the 100 s time point. Notably, the Gi3 biosensor response to TUG-891 appears to decrease following an initial peak, compared to the relative stability of the G15 and Gz responses. This is supported by the observation that the Gi3 measurement at 100 s is significantly lower than the G15 ($p < 0.05$) and Gz ($p < 0.001$) measurements.

Conversely, with the SpNBb biosensors, significant differences between the three Gα peptides were measured in the peak and AUC responses to TUG-891. Both the G15 and Gz biosensors produced a significant response over vehicle with an increase in signal of 22.3% and 33.0% respectively, whereas no significant peak or AUC TUG-891 response was measured for the Gi3 biosensor. Critically, the kinetic responses were more transient for the SpNBb biosensors than the SpNBa biosensors, with a significant decrease in net fold change observed at 100 s using the G15 and Gi3 biosensors. The SpNBa biosensor orientation was therefore prioritised for further work.

To demonstrate the potential of the SpNBa biosensors to measure compound potency, a concentration response curve experiment was completed using the

SpNBa-Gz construct. AUC was calculated from kinetic experiments and plotted against the log concentration of TUG-891. A curve was fit using a three-parameter model and a pEC_{50} of 5.63 ± 0.15 was determined **(Figure 3.3D)**.

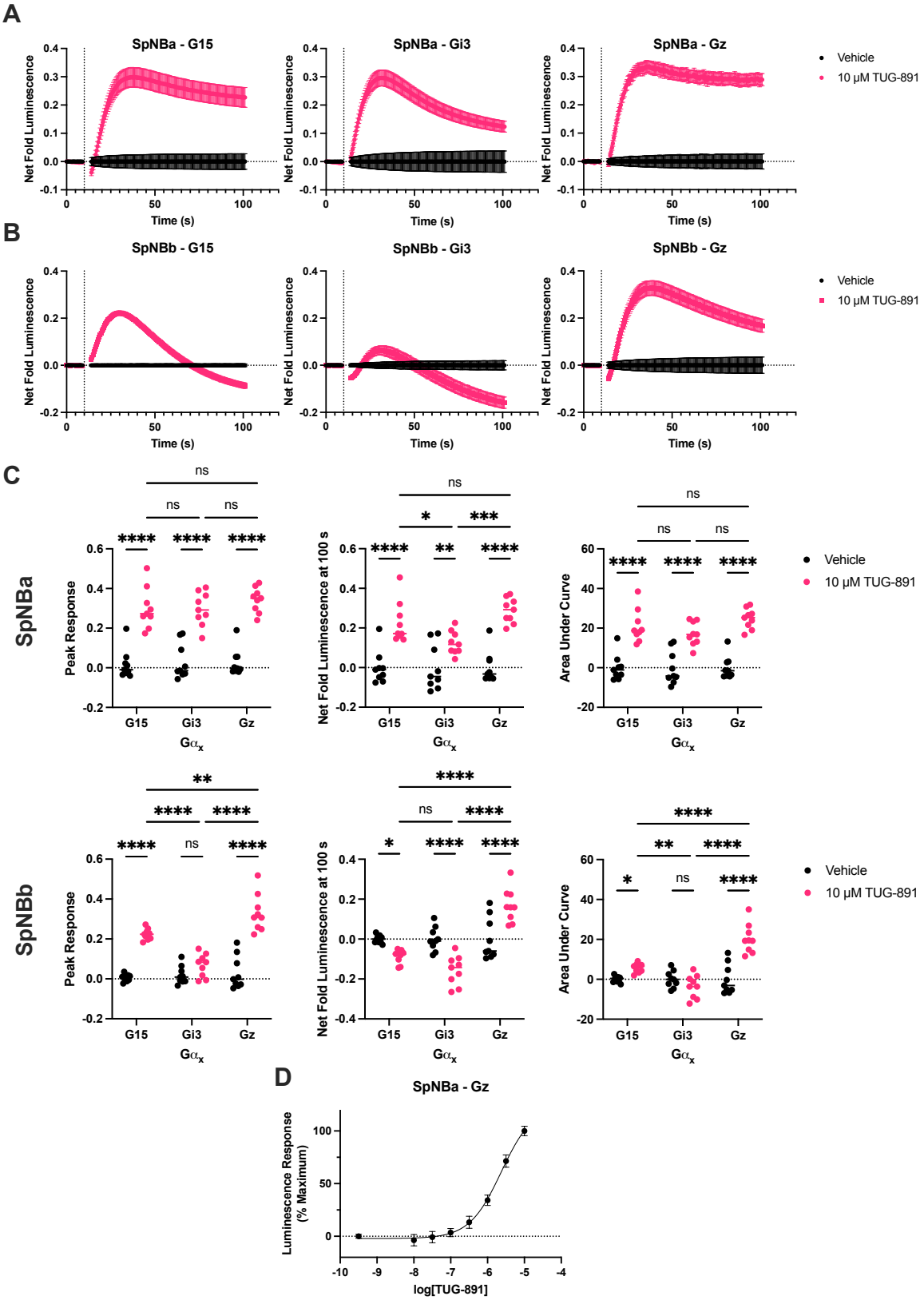

Figure 3.3 - SpNBa biosensors produce a larger and more stable response than SpNBb biosensors. A-B) Kinetic measurements of luminescent signal recorded when SpNB biosensors are activated by 10 μM TUG-891 after 10 seconds (indicated by the dotted line). SpNB biosensors

were created and tested in the **(A)** a or **(B)** b orientation with Gα peptides G15, Gi3 or Gz. Raw luminescence values were divided by baseline signal (average of 5 measurements before compound addition) and vehicle response subtracted. Data presented as mean ± SEM from N=3 independent experiments with n=3 technical replicates. **C)** Quantification of SpNB kinetic curves (shown in A-B). Maximum luminescence signal, net luminescence signal at 100 s time point and AUC were calculated for each Gα peptide. Statistical comparisons made using two-way ANOVA with Tukey's multiple comparisons test. *p < 0.05, **p < 0.01, ***p < 0.001, ****p < 0.0001. Individual measurements plotted with median indicated from N=3 independent experiments with n=3 technical replicates. **D)** Concentration response curve of TUG-891 using SpNBa-Gz biosensor. Data plotted as mean ± SEM from N=3 independent experiments with n=3 technical replicates.

To summarise, SpNB biosensors have been designed, optimised, and used to measure real time activation of the FFA4 receptor. In particular, the SpNBa biosensor demonstrated that FFA4 activation results in coupling to G15, Gi3 and Gz peptides and can measure the concentration-dependent response to TUG-891. However, the transient nature of the kinetic response coupled with the low signal window observed of only ~30% increase in light emission, limits the usefulness of the SpNB biosensors for higher throughput assays. Therefore, additional biosensor designs must be considered.

3.3 Mini G and arrestin recruitment assays to the FFA4 receptor demonstrate high signal windows

It was hypothesised that the low signal window observed for the SpNB biosensors was due to their unimolecular design; as the two NanoBiT components were tethered by a linker, random interactions would result in a higher background signal and therefore a lower fold increase in luminescence on agonist binding. Additionally, the 1:1 effective concentration of GPCR and Gα peptide would prohibit any amplification of the signal. Although NanoBiT itself does not allow 'amplification' (as a signal is only obtained when the LgBiT and SmBiT complement at a 1:1 ratio), intermolecular assays could perhaps improve the potency recorded for agonists through the contribution of receptor reserve (Sum et al., 2019). Therefore, intermolecular recruitment assays to the FFA4 receptor were investigated.

G protein recruitment assays have historically been challenging to develop due to the transient nature of their interactions (Olsen and English, 2023). However, the recently developed 'Mini G' (mG) proteins have overcome this kinetic limitation through a series of deletions which remove membrane anchors, the Gßγ-binding surface and α-helical domain, as well as mutations to improve *in vitro* protein stability and uncouple GPCR binding from nucleotide release, leading to a stable interaction (Carpenter and Tate, 2016). These constructs have been of particular benefit for expression in *E. coli* and use in biophysical and structural studies, but due to challenges with expressing the mG proteins in mammalian cells, a full suite of mG sensors for all G protein types is not available. However, chimeras of the mGs sequence, where residues of the α5 helix and other regions of the $G\alpha_s$ protein which make direct contact with the GPCR have been mutated to those from other Gα subtypes, have allowed the development of Gi/o, Gq/11 and G12/13 variants (Nehmea et al., 2017; Wan et al., 2018). I have developed NanoBiT mG receptor recruitment biosensors where the FFA4 receptor is tagged with the LgBiT on its C terminus (FFA4-LgBiT), and the mGq and mGi proteins are tagged with SmBiT on their N termini (SmBiT-mG) **(Figure 3.4A)**. When the receptor is activated, the mG protein is recruited, NanoBiT complementation occurs and an increase in luminescent emission is measured.

Arrestin recruitment assays were one of the first to be developed using BRET-based biosensors (Angers et al., 2000; Bertrand et al., 2002), and are commonly used as the basis of high-throughput GPCR drug screening assays (Zhang and Xie, 2012). Unlike G proteins, where each GPCRs typically couples to one or more of the 16 Gα proteins available, there are only two ubiquitously expressed arrestin isoforms (ß-arrestin-1 and -2) which were traditionally seen as a universal 'off switch' for GPCR signalling, although have now been shown to act as signal transducers in their own right (Jean-Charles et al., 2017). FFA4 is a GPCR which robustly recruits ß-arrestins (Milligan et al., 2017a), and it is thought that this ß-arrestin-mediated signalling results in the reported anti-inflammatory effects of FFA4 in macrophages (Oh et al., 2010). Therefore, I have developed NanoBiT arrestin recruitment (NBA) biosensors where the FFA4 receptor is tagged with the LgBiT on its C terminus (FFA4-LgBiT), and ß-arrestin-2 is tagged with SmBiT on its N terminus (SmBiT-Arr) **(Figure 3.4B)**. When the receptor is activated and phosphorylated, the SmBiT-Arr translocates to the receptor and increased luminescent signal is observed.

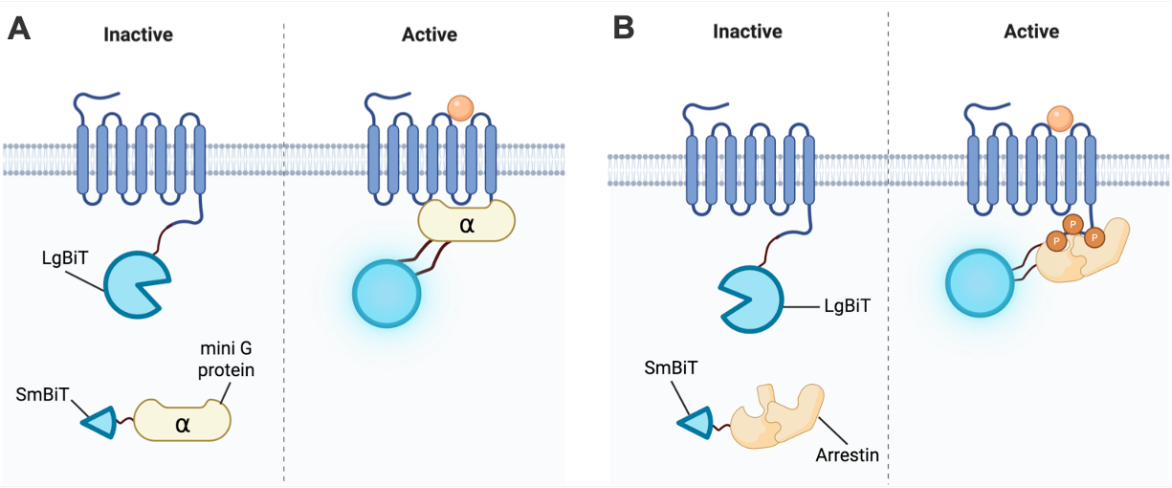

Figure 3.4 - Receptor recruitment biosensor design. Schematics of NanoBiT **(A)** miniG or **(B)** arrestin recruitment biosensors. In both cases, the receptor is tagged with LgBiT on its C-terminus and the recruited proteins tagged with SmBiT on their N-termini. When the receptor is activated, the effector protein is recruited, NanoBiT complementation occurs and a luminescent signal is measured.

First, FFA4-LgBiT and SmBiT-mG constructs were transfected into HEK293-T cells and response to 10 μM TUG-891 was observed **(Figure 3.5A-B).** No response was observed following TUG-891 treatment when using the mGq biosensor **(Figure 3.5A)**, whereas a clear increase in signal is measured when the mGi biosensor is used **(Figure 3.5B),** reaching a peak response of 288% increase in luminescent signal 5 minutes after compound addition which was sustained for the rest of the

assay. As a control for the mG biosensors, receptor recruitment biosensors were also tested for the FFA1 receptor **(Figure 3.5C-D)**, which is known to couple strongly to Gq (Briscoe et al., 2003; Shapiro et al., 2005). On stimulation with an FFA1 full agonist, T-3601386 (T360) (Ueno et al., 2019), a clear Gq response was observed with a maximum increase in luminescence of 118% **(Figure 3.5C)**, thus demonstrating the mGq biosensor is functional. This compound also resulted in a large response to the mGi biosensor **(Figure 3.5D)**, which notably was substantially larger than its mGq response at a maximum 366% increase. Interestingly, the kinetics of the FFA1 response were much slower than FFA4, with the signal not appearing to reach a peak over the 30-minute measurement time.

Next, SmBiT-Arr constructs were co-transfected into HEK293-T cells with FFA4-LgBiT or FFA1-LgBiT and response to agonists observed **(Figure 3.5E-F).** After addition of 10 μM TUG-891, rapid arrestin recruitment is observed to the FFA4 receptor, with 738% increase in signal observed 2 minutes after compound addition which decreases to ~50% maximal response over the following 25 minutes **(Figure 3.5E).** Conversely, a limited arrestin recruitment response is observed to the FFA1 receptor, with a maximum signal increase of 64% sustained throughout the experiment **(Figure 3.5F)**. The FFA4 NBA biosensor therefore represents the highest peak signal observed thus far ($p < 0.0001$, one-way ANOVA with Tukey's multiple comparisons).

Both the receptor mGi and NBA recruitment assays can be used to generate concentration response curves of key FFA4 reference agonists **(Figure 3.5G-H)**. α-linolenic acid (aLA) is a long-chain polyunsaturated omega-3 fatty acid with an 18-carbon chain and represents one of the endogenous ligands of FFA4 (Hirasawa et al., 2005). TUG-891 was the first potent synthetic agonist reported for FFA4 with high selectivity over FFA1 and has been used extensively to characterise the pharmacology of the receptor (Shimpukade et al., 2012; Hudson et al., 2013). GSK137647A was developed by GlaxoSmithKline from a series of diarylsulfonamides but did not have appropriate physiochemical properties for use *in vivo* (Sparks et al., 2014). TUG-1197 was a derivative from patent literature with greater selectivity over FFA1 and suitability for *in vivo* studies (Azevedo et al., 2016). Kinetic experiments were carried out as before by co-transfecting HEK293-T cells with FFA4-LgBiT and SmBiT-mGi **(Figure 3.5G)** or

SmBiT-Arr **(Figure 3.5H)** and measuring luminescent response following treatment with increasing concentrations of each agonist. AUC was calculated, data were expressed as a percentage of maximal TUG-891 response and three-parameter curves fit. The potency of compounds tends to be slightly higher in the NBA assay than the mGi assay, however this is only significant for α-LA ($p < 0.01$, two-way ANOVA with Tukey's multiple comparisons). The compounds tested share the same potency rank order, with TUG-891 and TUG-1197 having the highest potency followed by GSK137647A and α-LA, and this rank order is consistent with previously reported pEC_{50} values **(Table 3.1).**

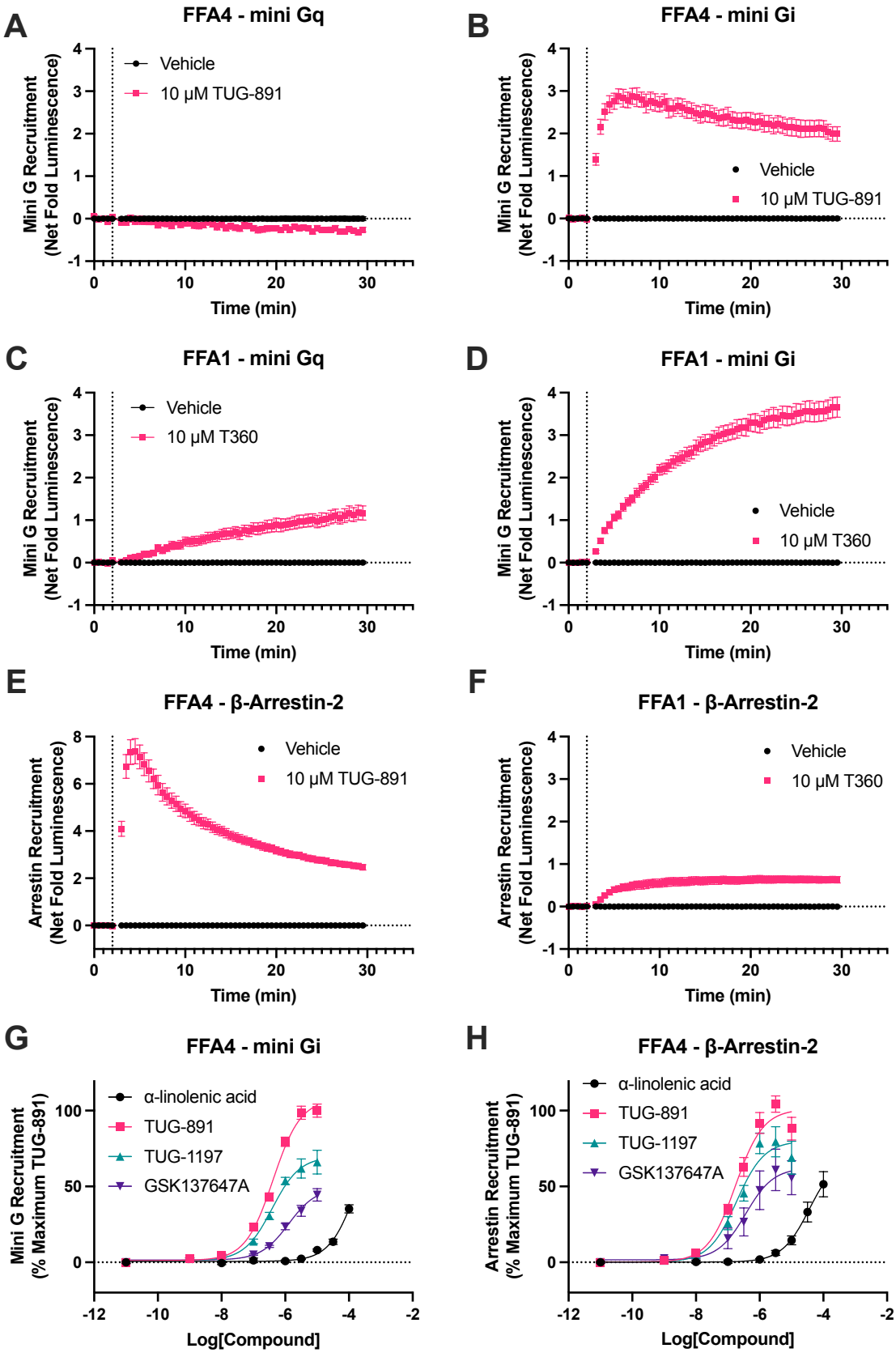

Figure 3.5 – NanoBiT biosensors measure miniG and β-arrestin-2 recruitment to FFA4 and FFA1 receptors. A-D) Kinetic measurements of luminescent signal recorded when **(A,C)** SmBiT-mGq or **(B,D)** SmBiT-mGi are co-transfected with **(A-B)** FFA4-LgBiT or **(C-D)** FFA1-LgBiT and agonist added after 2 minutes (indicated by the dotted line). FFA4 was activated by 10 μM TUG-891 and FFA1 was activated by 10 μM T360. **E-F)** Kinetic measurements of luminescent signal recorded when SmBiT-β-arrestin-2 biosensors are co-transfected with **(E)** FFA4-LgBiT or **(F)** FFA1-LgBiT and agonist added as in **(A-D)**. Raw luminescence values were divided by baseline signal (average of 5 measurements before compound addition) and vehicle response subtracted.

Data presented as mean ± SEM from N=3 independent experiments with n=4 technical replicates. **G-H)** AUC of kinetic traces were calculated and plotted to generate concentration response curves of selected compounds using FFA4-LgBiT and **(G)** SmBiT-mGi or **(H)** SmBiT-β-arrestin-2 biosensor combinations. Data plotted as mean ± SEM from N=3 independent experiments with n=3 technical replicates.

Table 3.1 - pEC50 values determined from receptor NanoBiT assays with previously reported values. pEC50 values presented as mean ± SEM from 3 independent experiments.

Compound	mGi Receptor	Arrestin Receptor	Literature [Assay Type]	Reference
α-linolenic acid	3.56 ± 0.27	4.36 ± 0.11	4.29 [BRET arrestin recruitment]	(Hudson et al., 2013)
TUG-891	6.38 ± 0.04	6.75 ± 0.18	7.19 [BRET arrestin recruitment]	(Hudson et al., 2013)
TUG-1197	6.41 ± 0.19	6.73 ± 0.04	6.91 [BRET arrestin recruitment]	(Azevedo et al., 2016)
GSK137647A	5.84 ± 0.18	6.03 ± 0.06	6.3 [Ca^{2+} mobilisation]	(Sparks et al., 2014)

The mG and NBA receptor recruitment assays show clear advantages in signal window and kinetic profile compared to the SpNB assay, with peak responses occurring 2-5 minutes after compound addition and luminescent signal sustained for up to 30 minutes, compared to the SpNB sensors which have a transient response which peaks 25 seconds after compound addition. The mG and NBA assays are therefore suitable for higher throughput compound screening as an entire plate can be read within each kinetic cycle rather than being limited to individual wells. However, as with the SpNB sensors, a major disadvantage is the need to express modified forms of the receptor of interest, thus prohibiting measurement of signalling from endogenously expressed receptors. Therefore, a different biosensor design may be more appropriate for exploring FFA4 signalling in physiologically relevant cell types.

3.4 Bystander recruitment assays allow measurement of mG and arrestin recruitment to unmodified receptors

The bystander assay format has been proposed as an alternative to direct receptor recruitment assays to allow measurement of signalling to unmodified GPCRs (Donthamsetti et al., 2015). In this assay format, one component of the biosensor is tethered to the plasma membrane using a lipid anchor, rather than being attached directly to the GPCR. As a result, the assay specifically measures recruitment to the plasma membrane, instead of to a specific receptor. Versions of BRET arrestin and mG recruitment bystander assays have been widely used in the literature (Donthamsetti et al., 2015; Wright et al., 2021; Daly et al., 2023), including use of different subcellular localisation tags to measure receptor trafficking and activation within different internal compartments (Lan et al., 2012; O'Brien et al., 2025). NanoBiT bystander recruitment assays have also been developed previously, although the specific lipid anchor and NLuc split site can vary (Spillmann et al., 2020; Pedersen et al., 2021; Zheng et al., 2023).

Bystander versions of both the mG and NBA recruitment assays have been designed here, where the LgBiT biosensor component is attached to an 11-amino acid N-terminal fragment of the kinase Lyn (Lyn11), which undergoes myristylation and palmitoylation to anchor the LgBiT to the cytosolic leaflet of the cell membrane (Inoue et al., 2005) **(Figure 3.6)**. Following activation, the mG or arrestin protein is recruited to the receptor, and complementation occurs between the SmBiT on the recruited protein and the LgBiT anchored to the membrane.

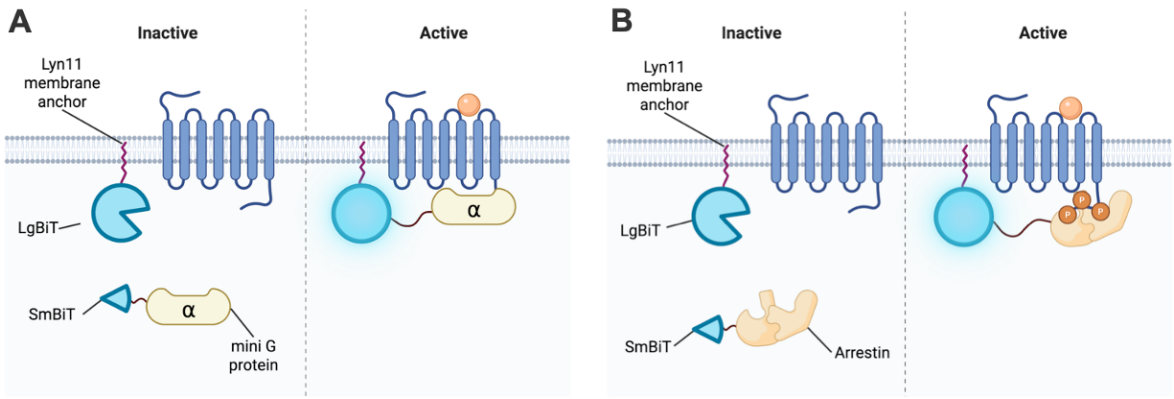

Figure 3.6 - Bystander recruitment assay design. Schematics of bystander NanoBiT **(A)** miniG or **(B)** arrestin recruitment biosensors. In these biosensors, the LgBiT is anchored to the plasma membrane using a Lyn11 motif, which undergoes lipid modification to associate with the cell membrane. When the receptor is activated, the effector protein is recruited to the receptor, bringing the SmBiT and LgBiT in close enough proximity to allow NanoBiT complementation to occur.

When transfected into HEK293-T cells with FFA4 receptor and activated with 10 μM TUG-891, a measurable signal is observed for both mGi and arrestin biosensor combinations **(Figure 3.7A-B)**. The mGi and NBA luminescent signals increased by 362% and 445% respectively, with a peak approximately 4 minutes after compound addition and decreasing to ~60% of the maximum after 25 minutes. Crucially, when the FFA4 receptor is not transfected and instead replaced with an equal amount of pcDNA empty vector (- FFA4), no response is observed. As with the receptor versions, concentration response curves can be generated for key FFA4 reference ligands by calculating the AUC of kinetic traces, plotting against the log concentration of compound and fitting a three-parameter curve to derive pEC_{50} values **(Figure 3.7C-D, Table 3.2)**.

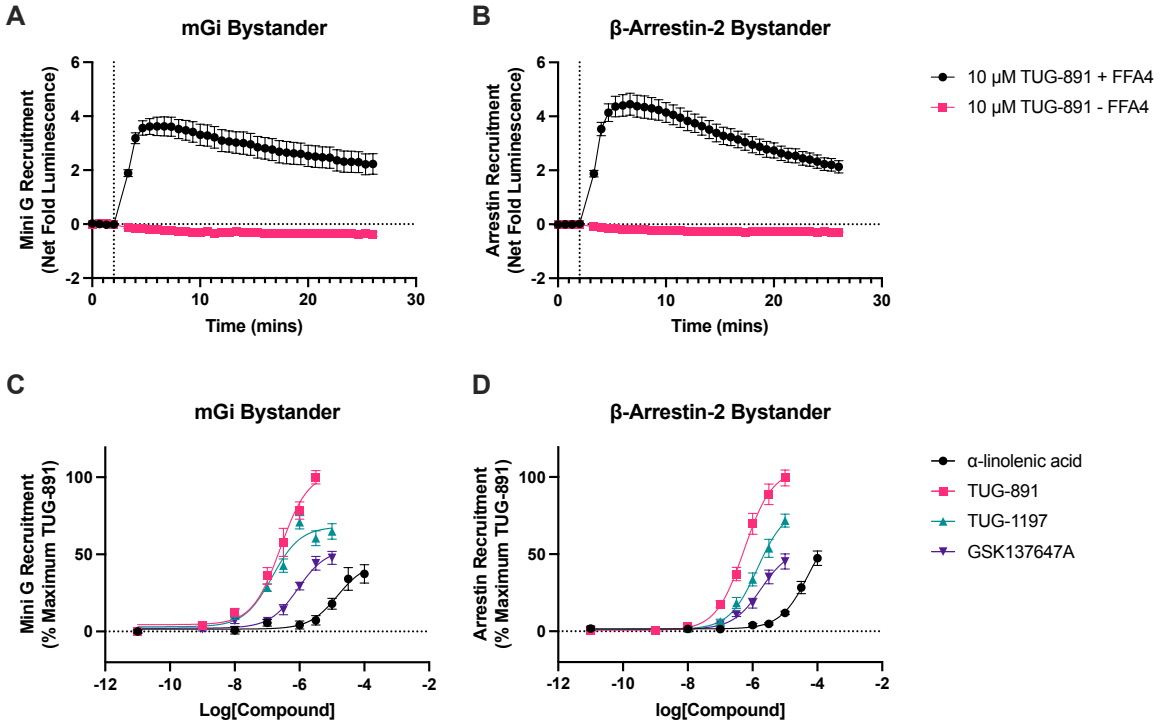

Figure 3.7 - Bystander NanoBiT biosensors measure miniG and β-arrestin-2 recruitment to unmodified FFA4 receptor. A-B) Kinetic measurements of luminescent signal recorded when **(A)** SmBiT-mGi or **(B)** SmBiT-β-arrestin-2 biosensors are co-transfected with Lyn11-LgBiT and FFA4 receptor (+ FFA4) or an equal amount of pcDNA empty vector (- FFA4) and activated by 10 μM TUG-891 after 2 minutes (indicated by the dotted line). Raw luminescence values were divided by baseline signal (average of 5 measurements before compound addition) and vehicle response subtracted. Data presented as mean ± SEM from N=3 independent experiments with n=4 technical replicates. **D-E)** AUC of kinetic traces were calculated and plotted to generate concentration response curves of selected compounds when cells are transfected with FFA4 receptor, Lyn11-LgBiT & **(C)** SmBiT-mGi or **(D)** SmBiT-β-arrestin-2 biosensor combinations. Data plotted as mean ± SEM from N=3 independent experiments with n=3 technical replicates.

Table 3.2 - pEC_{50} values determined from bystander NanoBiT assays. pEC50 values presented as mean ± SEM from 3 independent experiments.

Compound	mGi Bystander	Arrestin Bystander
α-linolenic acid	4.71 ± 0.10	4.22 ± 0.10
TUG-891	6.61 ± 0.20	6.16 ± 0.24
TUG-1197	6.84 ± 0.03	5.73 ± 0.28
GSK137647A	6.04 ± 0.14	5.67 ± 0.13

It has therefore been shown that bystander NanoBiT biosensors can measure real-time activation of unmodified FFA4 receptor through mGi and arrestin recruitment and can be used to measure the potency of test compounds. The NBA bystander biosensor had a slightly higher (although non-significant) peak response than the mGi biosensor ($p = 0.15$, unpaired t test), so this was selected for further investigation.

3.4.1 Optimisation of the NanoBiT bystander arrestin recruitment assay

Following the initial success of the NBA bystander assay, a series of optimisation experiments were carried out to maximise the signal window of the assay **(Figure 3.8).** Firstly, the transfection reagents polyethyleneimine (PEI) or Lipofectamine 3000 (L3000) were compared **(Figure 3.8A-B)**. Equal amounts of FFA4 receptor, Lyn11-LgBiT and SmBiT-Arr were co-transfected at 33 ng each plasmid per well of a 96-well plate. Although the basal luminescence was significantly higher for L3000 than PEI, indicating higher expression of the constructs was achieved ($p < 0.01$, Welch's t test) **(Figure 3.8A)**, no difference was observed in the net fold luminescence increase on addition of 10 μM TUG-891 **(Figure 3.8B).** Due to the cheaper cost of PEI compared to L3000, transfection of HEK293-T cells using PEI was selected for future experiments.

Next, the amount of biosensor DNA transfected was optimised **(Figure 3.8C-D).** Equal amounts of Lyn11-LgBiT and SmBiT-Arr were co-transfected from 1-30 ng DNA of each plasmid/well, with 30 ng/well FFA4 receptor and total DNA made up to 100 ng/well with empty vector. As observed with the SpNB biosensors, I hypothesised that lower biosensor expression may result in an increased signal window due to the lower background signal. The basal luminescence measured decreased as the amount of biosensor decreased, confirming that expression

levels of the biosensor were successfully altered **(Figure 3.8C).** The increase in signal between the 7.5 ng conditions is due to using different gain settings used on the plate reader between the two plates used, indicated by the split in the graph, where gain was set at 5% to the highest expressing condition. It was found that net fold luminescence increase was broadly unaffected by biosensor expression level, although very high (30 ng/well) or low (1 ng/well) DNA concentrations did reduce the window **(Figure 3.8D)**. 5 ng/well biosensor DNA was selected for further work.

Finally, the ratio of the two biosensor components was adjusted **(Figure 3.8E-F).** In BRET-based biosensors, typically assays require higher expression of the 'acceptor' fluorophore than the 'donor' luciferase. As the 'donor' is the source of background signal, expression should be minimised to increase the signal:background window. In the NanoBiT assay, the LgBiT is the source of much of the background luminescence, compared to the 11 amino acid SmBiT fragment, therefore I hypothesised that increasing the ratio of SmBiT:LgBiT may increase the signal window. In this experiment, 5 ng/well Lyn11-LgBiT was co-transfected with 5-45 ng/well SmBiT-Arr, thus increasing the SmBiT:LgBiT ratio. As before, 30 ng/well FFA4 receptor was transfected for each condition and total DNA made up to 100 ng/well with empty vector. Increasing the amount of SmBiT-Arr had no significant effect on baseline luminescence ($p = 0.39$, one-way ANOVA). Generally, the assay trend suggested that as SmBiT-Arr increased, the signal window decreased, with the 1:1 ratio performing best. Therefore, the final assay protocol involved transfection of 5 ng/well of each biosensor component, 30 ng/well FFA4 receptor and 60 ng/well empty vector into HEK293-T cells using PEI.

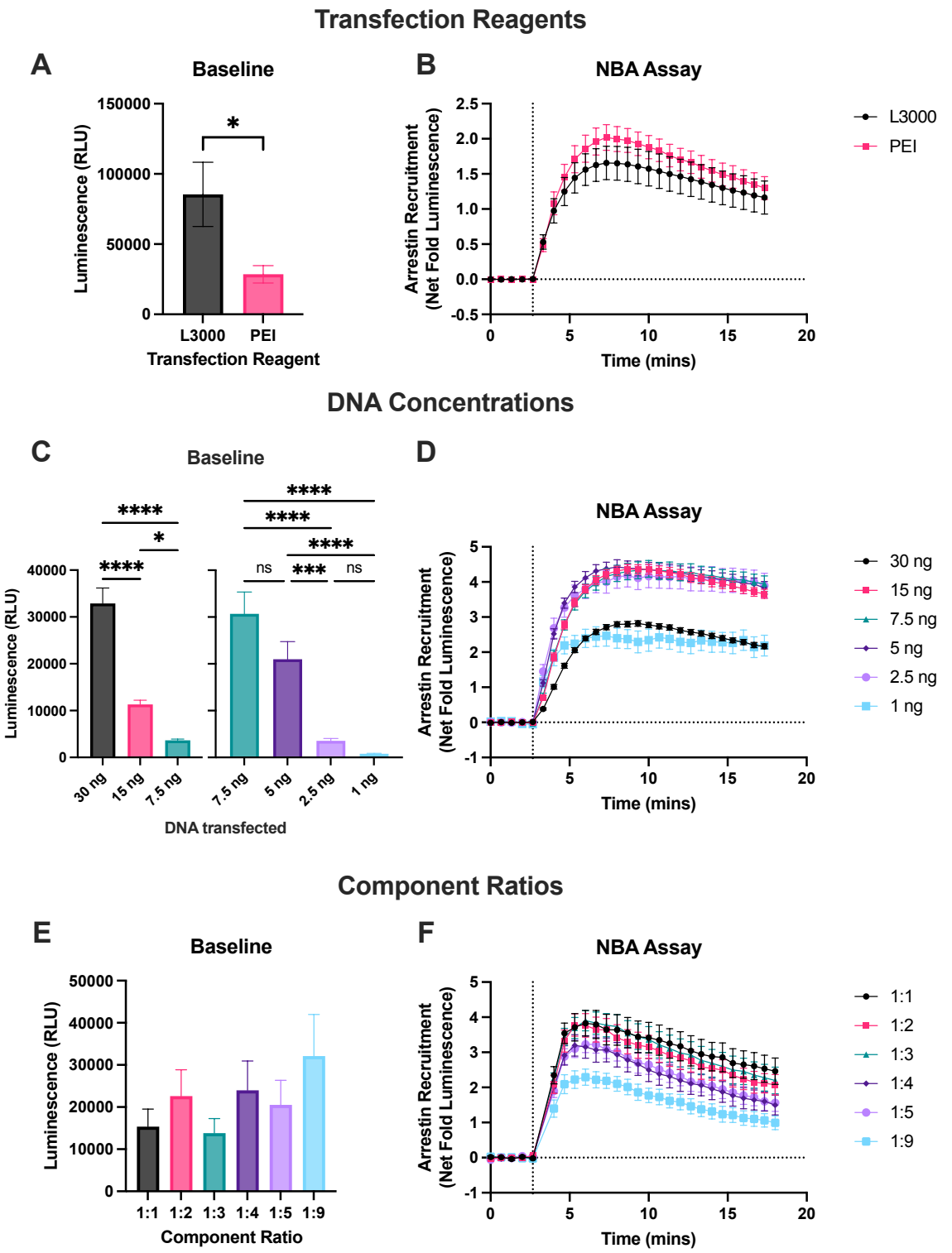

Figure 3.8 – Adjusting transfection conditions alters baseline signal and NBA assay response. A-B) Equal amounts of FFA4 receptor, Lyn11-LgBiT and SmBiT-Arr were co-transfected into HEK293-T cells. **C-D)** Lyn11-LgBiT and SmBiT-Arr were transfected in equal ratio to HEK293-T cells at the indicated DNA concentrations per well. 30 ng FFA4 DNA was transfected for all conditions, and DNA prepared to 100 ng total per well with empty vector. **E-F)** Increasing ratios of Lyn11-LgBiT:SmBiT-Arr were transfected into HEK293-T cells. Per well, 30 ng FFA4 DNA and 5 ng Lyn11-LgBiT were transfected, with increasing concentration of SmBiT-Arr (from 5 to 45 ng/well) at the indicated ratios, and DNA prepared to 100 ng total with empty vector. For each optimisation experiment, baseline luminescence measurements **(A,C,E)** and kinetic assay measurements **(B,D,F)** when NBA biosensors are activated by 10 μM TUG-891 (indicated by the dotted line) are given. **A,C,E)** Baseline luminescence measurements are given as raw luminescence values from the final measurement before compound addition and are presented as mean ± SEM from N=3 independent experiments with n=8 technical replicates. Statistical comparisons made using unpaired t test (A) or one-way ANOVA with Tukey's multiple comparisons

(C). **B,D,F)** For kinetic measurements, raw luminescence values were divided by baseline signal (average of 5 measurements before compound addition) and vehicle response subtracted. Data presented as mean ± SEM from N=3 independent experiments with n=4 technical replicates.

Considering the design of other arrestin recruitment bystander assays (Namkung et al., 2016; Pedersen et al., 2021), and to further optimise the assay, variants of the biosensor components were generated with reversed orientations (i.e. SmBiT on membrane and LgBiT on arrestin) or where the arrestin was labelled on its N- and/or C-terminus **(Figure 3.9A)**. Appropriate construct pairs were transfected into HEK293-T cells and luminescence response to 10 μM TUG-891 measured.

Where the LgBiT was localised to the cell membrane with Lyn11, the highest baseline luminescence was observed for SmBiT-Arr-SmBiT, followed by SmBiT-Arr then Arr-SmBiT, although these values were only significantly different for the SmBiT-Arr-SmBiT vs. Arr-SmBiT comparison **(Figure 3.9B).** A response to TUG-891 was measured for all ß-arrestin-2 constructs, with signal window for SmBiT-Arr > SmBiT-Arr-SmBiT > Arr-SmBiT **(Figure 3.9C)**. All biosensor pairs resulted in a significant peak response over baseline with the SmBiT-Arr sensor showing statistically significant improvement over the Arr-SmBiT ($p < 0.0001$) and SmBiT-Arr-SmBiT ($p < 0.01$) constructs **(Figure 3.9D)**. When the SmBiT is linked to both termini of the arrestin protein, the peak response is decreased compared to the N-terminal tag alone, potentially due to the increase in baseline signal caused by an expected increase in nonspecific interactions between LgBiT and SmBiT. Conversely, the C-terminal tagged arrestin has a lower baseline signal but also a reduced peak response, suggesting this orientation does not recruit as well to activated GPCRs.

In the reverse orientation, where SmBiT was localised to the cell membrane and arrestin tagged with LgBiT, the basal signal for Arr-LgBiT constructs was very low, suggesting expression of this construct was poor **(Figure 3.9E)**. The basal signal of LgBiT-Arr was similar to that observed for SmBiT-Arr, however no agonist response was observed **(Figure 3.9F)**. As the Lyn11-SmBiT construct is very small (25 amino acids), it was hypothesised that the SmBiT fragment may not be properly expressed in the cell membrane or protrude sufficiently into the cytoplasm to allow complementation. However, even separating the Lyn11 and SmBiT sequences with a 12 amino acid Glycine-Serine-Glycine $(GSG)_4$ flexible

linker (FL) (Sivaramakrishnan and Spudich, 2011) was not sufficient to result in a response to TUG-891 **(Figure 3.9F)**.

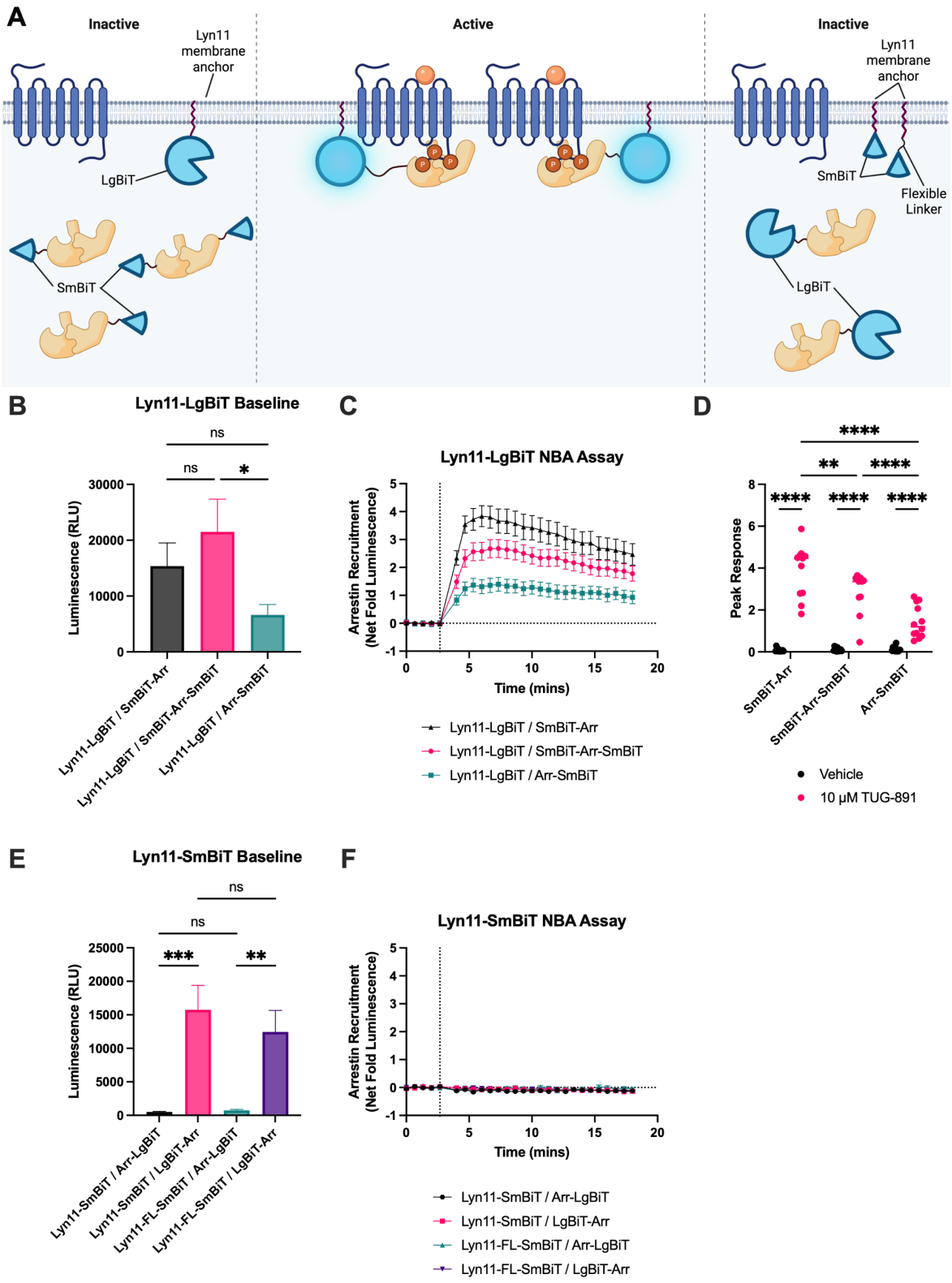

Figure 3.9 – Positioning of NanoBiT components in NBA biosensors affects the baseline signal and assay response. A) Schematic of NBA recruitment biosensor combinations. **B)** Baseline luminescence measurements from Lyn11-LgBiT biosensor combinations are given as raw luminescence values from the final measurement before compound addition and are presented as mean ± SEM from N=3 independent experiments with n=8 technical replicates. Statistical comparisons were made using one-way ANOVA with Tukey's multiple comparisons test. **C)** Kinetic measurements of luminescent signal recorded when Lyn11-LgBiT biosensors are activated by

10 μM TUG-891 at 2.67 minutes (indicated by the dotted line). Raw luminescence values were divided by baseline signal (average of 5 measurements before compound addition) and vehicle response subtracted. Data presented as mean ± SEM from N=3 independent experiments with n=4 technical replicates. **D)** Peak responses after vehicle or TUG-891 treatment were calculated using each SmBiT arrestin construct with Lyn11-LgBiT. Individual measurements plotted with median indicated from N=3 independent experiments with n=4 technical replicates. Statistical comparisons were made using two-way ANOVA with Tukey's multiple comparisons test. **E)** Baseline measurements and **F)** kinetic measurements of luminescent signal recorded when Lyn11-SmBiT biosensors are activated by 10 μM TUG-891. Data presented as in B-C. Throughout, *p < 0.05, **p < 0.01, ***p < 0.001, ****p < 0.0001.

In BRET bystander assays, typically the acceptor is used as the membrane-localised component, with high expression of the fluorophore 'coating' the whole cell membrane, with a lower expression of the luciferase-tagged arrestin (Namkung et al., 2016). This allows the measurement of arrestin recruitment to anywhere on the membrane while maintaining a low background signal, therefore resulting in a high signal:background assay window. In the NanoBiT assay, where we can loosely consider LgBiT as the donor and SmBiT as acceptor, it seemed surprising that the equivalent conformations – i.e. with SmBiT on the membrane and LgBiT on arrestin – were not functional. We therefore wanted to interrogate this further by generating a series of new membrane-localised SmBiT constructs **(Figure 3.10).**

In the split luciferase design, the SmBiT fragment forms the C-terminus of the complete NLuc sequence. I therefore hypothesised that adding a Lyn11 N-terminal tag may somewhat prohibit the NanoBiT complementation with a small peptide construct, and therefore greater functionality may be observed by using a C-terminal membrane tag. Therefore, constructs were generated using the polybasic domain and CAAX motif of KRas (Zacharias et al., 2002) to attempt to anchor SmBiT to the plasma membrane in the reverse orientation. It is also possible that these constructs are simply not being expressed or correctly localised to the plasma membrane, but this is not easy to determine with the very small Anchor-SmBiT peptides. Therefore, the fluorescent protein mNeonGreen (mNG) was included in the construct to both increase the size of the protein, thus allowing SmBiT to protrude further into the cytoplasm, but also allow visualisation of these constructs **(Figure 3.10A).**

mNG-tagged constructs were transfected into HEK293-T cells and confocal microscopy confirmed successful expression of the Lyn11-mNG-SmBiT and SmBiT-mNG-CAAX constructs localised to the plasma membrane of cells **(Figure 3.10B).**

As before, constructs were co-transfected with LgBiT-Arr in HEK293-T cells and luminescence response to 10 μM TUG-891 measured. For Lyn11, some activity was observed with the biosensor where SmBiT was separated from mNG with a flexible linker, whereas no response was observed when SmBiT was directly attached at its N-terminus to mNG, suggesting that the SmBiT needs to both protrude further into the cytoplasm and maintain some degree of flexibility **(Figure 3.10C).**

Similarly for CAAX, only the mNG constructs were functional, suggesting that the larger protein is required for efficient synthesis and trafficking or to allow protrusion of SmBiT to the cytoplasm. Unlike the Lyn11 construct, a response was still observed when SmBiT was directly attached by its C-terminus to mNG. However, a greater window was observed when SmBiT and mNG were separated by a linker, reinforcing that the flexibility of SmBiT is critical to a successful NanoBiT assay response **(Figure 3.10D)**.

Even though these designs clearly offered some improvement, the assay window for the SmBiT-mNG-CAAX sensor was still ~10-fold smaller than the Lyn11-LgBiT/SmBiT-Arr pair. Further optimisation may still be possible, but I decided to progress with the established Lyn11-LgBiT/SmBiT-Arr assay.

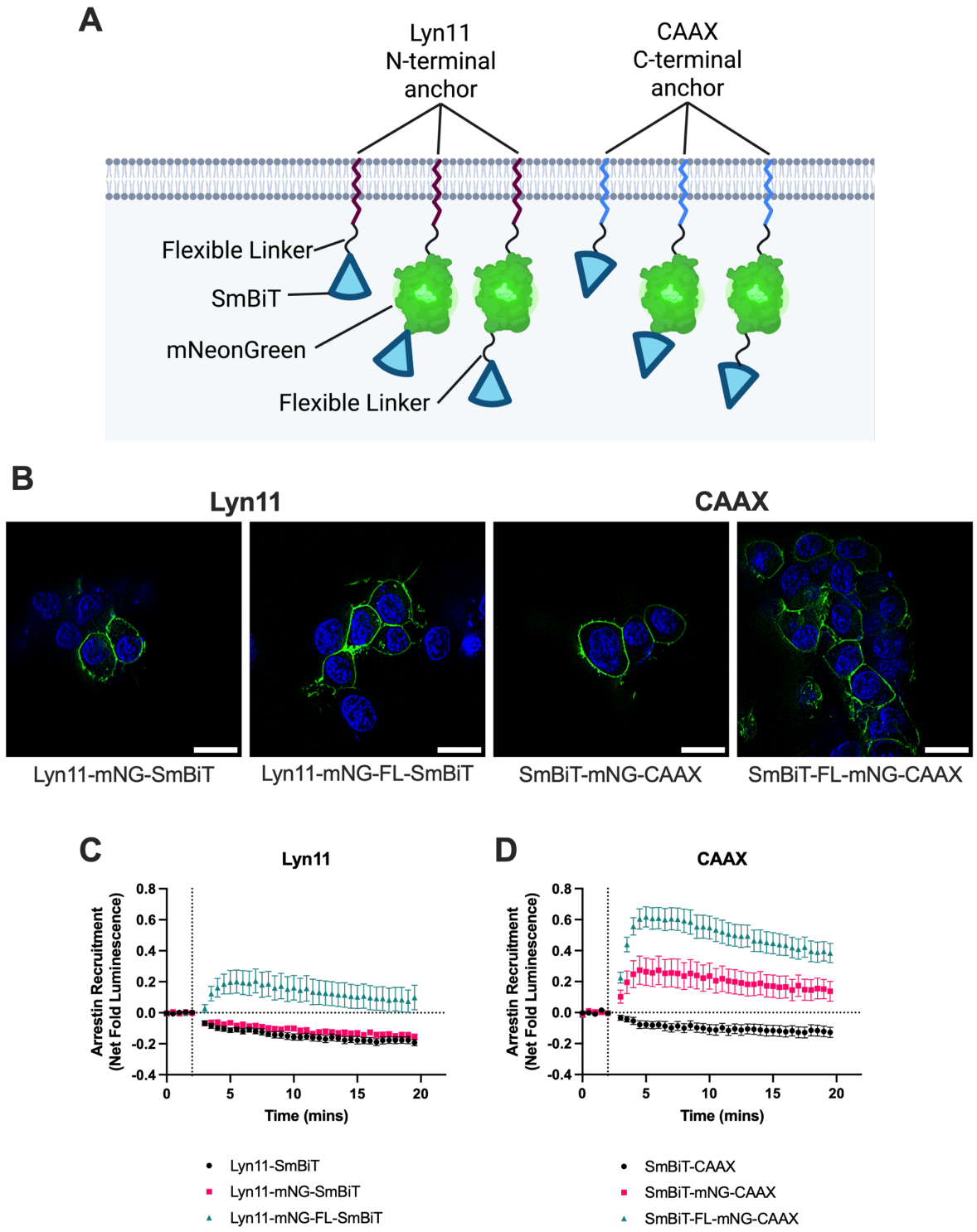

Figure 3.10 – Adding mNG to membrane-localised SmBiT constructs improves the performance of the arrestin recruitment assay. A) Schematic of membrane-localised SmBiT constructs with N-terminal Lyn11 or C-terminal CAAX tag, with or without mNeonGreen (mNG). **B)** Representative images of HEK293-T cells transfected with the indicated SmBiT construct and imaged using a Zeiss Vivatome confocal microscope with 40X objective. mNG fluorescence is shown in green and nuclei were stained with Hoescht (blue). Scale bar = 20 µm. **C-D)** Kinetic measurements of luminescent signal recorded when **(C)** Lyn11-SmBiT or **(D)** SmBiT-CAAX biosensors are co-transfected with LgBiT-Arr and FFA4 receptor and activated by 10 µM TUG-891 at 2 minutes (indicated by the dotted line). Raw luminescence values were divided by baseline signal (average of 5 measurements before compound addition) and vehicle response subtracted. Data presented as mean ± SEM from N=3 independent experiments with n=3 technical replicates.

3.4.2 Bystander NBA assay can measure arrestin recruitment to unmodified GPCRs at a range of expression levels

One advantage of the bystander assay format is the ability to measure signalling from unmodified, and potentially, endogenous receptor. As a proof of concept, the biosensor was used to measure FFA4 activation at different expression levels by transfecting different amounts of receptor DNA **(Figure 3.11)**. Different amounts of plasmid expressing haemagglutinin-tagged FFA4 receptor (FFA4-HA) were co-transfected with NBA biosensor components in HEK293-T cells, and an In Cell Western (ICW) was used to quantify expression of the FFA4 protein using the HA tag. Increasing the quantity of FFA4-HA DNA transfected increased the observed ICW signal, however the relationship is not linear and differences are only significant at the lowest concentrations of DNA (0-20 ng/well) **(Figure 3.11A)**. This is consistent with NBA assay data; as receptor expression increases, the signal window also increases **(Figure 3.11B)**, with the biggest differences again seen between the lower concentrations of DNA **(Figure 3.11C).** Notably, FFA4 activation is still measurable in this assay at lower expression levels (1 ng), suggesting the assay may still be functional in more physiologically relevant cell lines with low endogenous FFA4 expression.

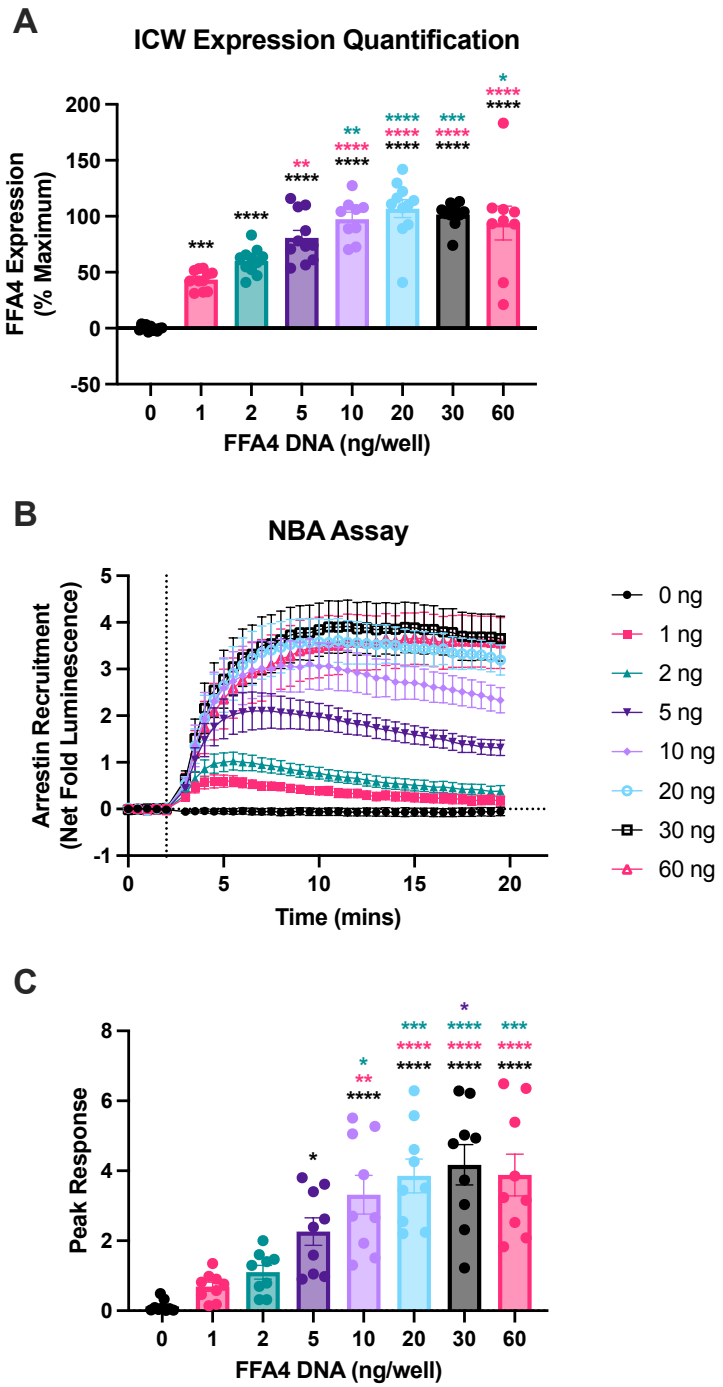

Figure 3.11 – NBA assay can measure arrestin recruitment at a range of FFA4 expression levels. HEK293-T cells were co-transfected with the Lyn11-LgBiT/SmBiT-Arr biosensor pair and indicated amounts of FFA4-HA plasmid DNA. **A)** Quantification of In Cell Western (ICW) analysis of FFA4-HA expression using primary antibody against C-terminal HA tag. Data was corrected for non-specific background signal by subtracting signal from no primary control and expressed as a ratio over the signal obtained from a CellTag™ counterstain. Data were then normalised to express percent signal relative to maximum FFA4 signal (30 ng DNA/well) and are presented as individual measurements with mean ± SEM indicated from N=3 independent experiments with n=3 technical replicates. **B)** Kinetic measurements of luminescent signal recorded when NBA assay is performed with different transfected amounts of FFA4 receptor and activated with 10 μM TUG-891 at 2 minutes (indicated by the dotted line). Raw luminescence values were divided by baseline signal (average of 5 measurements before compound addition) and vehicle response subtracted. Data presented as mean ± SEM from N=3 independent experiments with n=3 technical replicates. **C)** Quantification of peak responses after TUG-891 treatment from **(B)**. Individual measurements presented with mean ± SEM indicated from N=3 independent experiments with n=3 technical replicates. Statistical comparisons in A and C were made using one-way ANOVA with Tukey's multiple comparisons test. *p < 0.05, **p < 0.01, ***p < 0.001, ****p < 0.0001 where colour indicates the relevant comparison. All other comparisons were not significant.

Finally, to demonstrate the flexibility and universality of the bystander NBA recruitment biosensors, FFA4 was replaced with a range of different GPCRs and their respective reference agonists in concentration response curve experiments. Kinetic experiments were carried out as before, AUC calculated and plotted against log agonist concentration **(Figure 3.12)**. FFA2 (GPR43) and FFA3 (GPR41) are short chain free fatty acid receptors, responding to ligands released by the gut microbiota such as propionate (C3) (Brown et al., 2003). HCA_2 is a receptor for the metabolite beta-hydroxybutyrate and, like FFA4, has been suggested to be a key player in the communication between adipocytes and macrophages in metabolic disorders (Duncan et al., 2023). HCA_2 is also a high affinity receptor for niacin, a nutrient with well-known antilipolytic effects mediated through this GPCR (Tunaru et al., 2003). GPR84 and GPR35 are both classed as 'orphan' GPCRs, meaning no endogenous ligand is known, however several potent synthetic agonists for both are available. In this assay, 2-(hexylthiol)pyrimidine-4,6 diol (2-HTP), was used as an agonist for GPR84 and lodoxamide for GPR35 as both have previously been used in ß-arrestin-2 recruitment assays (MacKenzie et al., 2014; Mancini et al., 2019).

By comparing the maximum AUC obtained in the NBA assay for each receptor, the relative abilities of each receptor to recruit arrestin can be determined. In this assay, FFA4 and GPR35 showed the highest responses **(Figure 3.12A-B),** GPR84, HCA_2 and FFA2 showed moderate responses **(Figure 3.12C-E)**, and FFA3 **(Figure 3.12F)** showed a limited response to arrestin recruitment with their respective reference agonists. The NBA bystander assay can therefore be used not only as a universal approach to measure activation across many different GPCRs, but also in comparative studies determining the relative arrestin-coupling properties of these receptors.

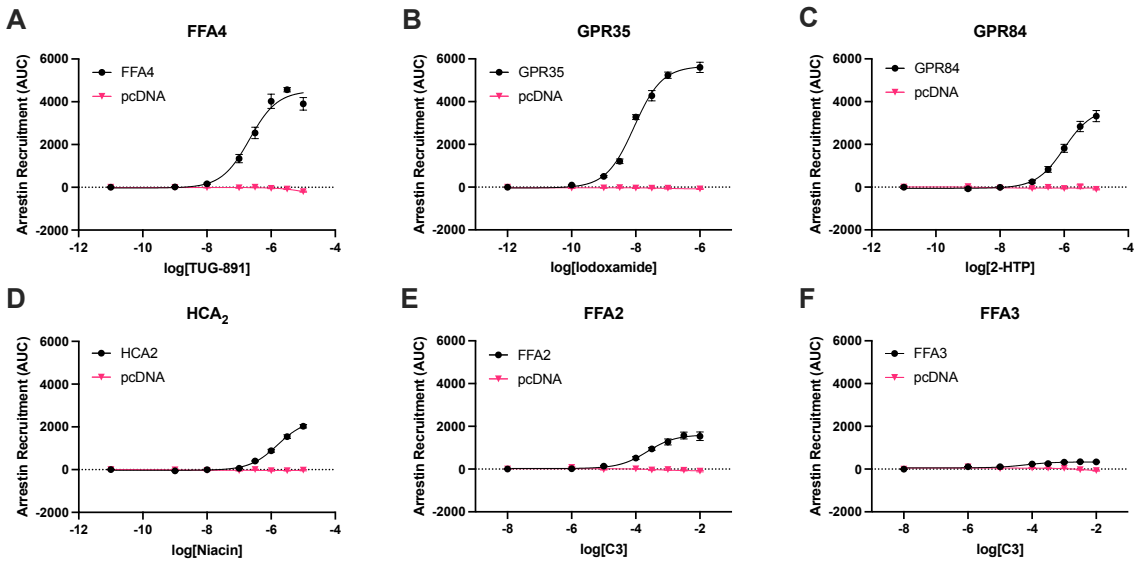

Figure 3.12 – Bystander NBA assay can measure arrestin recruitment to different GPCRs. HEK293-T cells were co-transfected with the Lyn11-LgBiT/SmBiT-Arr biosensor pair and indicated GPCR or empty vector control. Concentration response curves were generated for reference ligands by plotting the area under curve of kinetic traces. Data presented as mean ± SEM from N=3 independent experiments with n=3 technical replicates.

In summary, the NBA bystander biosensors generated and optimised here provide a robust and reliable method of measuring GPCR activity across a range of receptors and expression levels, and provide a strong foundation for future biosensor development or mechanistic studies.

3.5 Colour-shifted NanoBiT biosensors allow measurement of arrestin recruitment at different emission wavelengths

In recent years, substantial effort has explored the potential to engineer bioluminescent proteins with red-shifted emission spectra for use in *in vivo* imaging (Liu et al., 2021). Many commonly used luciferase enzymes emit blue light, however wavelengths < 600 nm are rapidly absorbed by biological tissues (Zhao et al., 2005). Several colour-shifted NLuc proteins and substrates have now been reported, with a particular focus on using these in calcium-sensing biosensors (Suzuki et al., 2016; Shakhmin et al., 2017; Yang and Johnson, 2021).

I hypothesised that blue light absorption may also be a challenge with spheroids, and therefore developing a red-shifted version of the NBA biosensor may improve signal penetration from the centre of the 3D cell model. Additionally, different coloured variants of the NBA biosensor may allow multiplexing of different cell types, or different responses in the same cell type. For example, in a co-culture model, if a blue NBA sensor was expressed in adipocytes and a yellow NBA sensor was expressed in macrophages, their individual responses to agonist application could be measured. Critically, this approach would allow measurement of physiological responses, for example by stimulating lipolysis in adipocytes to observe activation of autocrine and/or paracrine signalling due to released fatty acids. Similarly, if colour variants of bystander biosensors are localised to different subcellular compartments, this approach may allow direct measurement of intracrine signalling (O'Brien et al., 2025).

Initially, the Green-, Yellow- and Cyan-enhanced NanoLantern constructs reported by Suzuki et al. were generated and luminescence emission spectra validated **(Figure 3.13).** The enhanced NanoLantern (eNL) constructs shift the luminescence emission wavelength by fusing the NLuc protein to a fluorescent protein, resulting in constant BRET between the pair (Hoshino et al., 2007). Although the peak emission wavelength is shifted from ~450 nm in NLuc to ~525 nm in the green eNL (GeNL) and ~535 nm in the yellow eNL (YeNL) construct, there is still a small peak seen in the 450 nm range, and there is substantial overlap between the two. The spectrum of the cyan eNL (CeNL) is

similar to NLuc but with a somewhat broader emission and a peak shifted to ~475 nm.

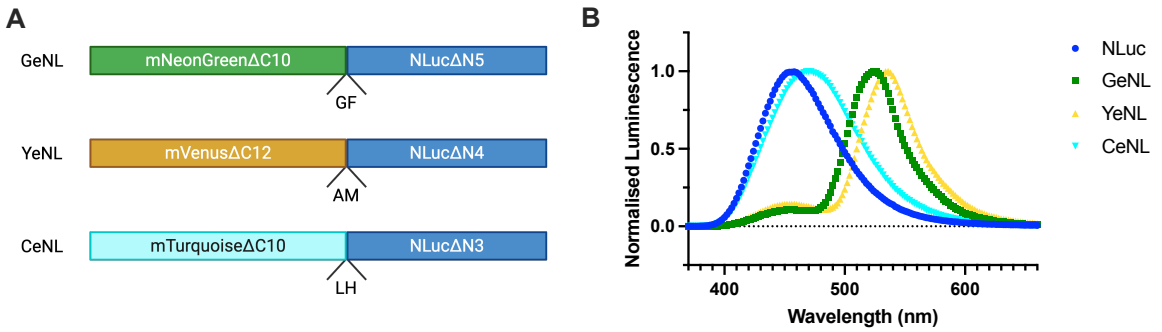

Figure 3.13 – NanoLantern constructs shift the emission spectrum of NLuc. A) Schematic diagram of Green, Yellow and Cyan NanoLantern (NL) fusion protein constructs (adapted from Suzuki et al., 2016). **B)** Luminescent spectral scans of NLuc, GeNL, YeNL and CeNL measured in triplicate and normalised to minimum and maximum peak.

Using the principles of the eNL constructs, fluorescent proteins were fused to the LgBiT component of the NBA system to generate Lyn11-YeLgBiT and Lyn11-CeLgBiT constructs **(Figure 3.14)**. These were tested in the standard NBA kinetic assay format following addition of 10 μM TUG-891, however as well as raw luminescence, luminescence measurements were made at 475 nm (blue) and 550 nm (yellow) to investigate the potential for these biosensors to be used in multiplexed assays**.** To compare the amount of light emitted at each wavelength, the raw measurements at 475 nm and 550 nm were expressed as a fold change of the total luminescence baseline signal and vehicle response subtracted.

For the unmodified Lyn11-LgBiT biosensor **(Figure 3.14A-B)**, a larger response was observed in the 475 nm measurement than the 550 nm measurement, consistent with the blue emission of full length NLuc. Conversely, with the Lyn11-YeLgBiT biosensor **(Figure 3.14C-D)**, the observed signal was higher in the yellow than blue range, confirming successful shift of the peak emission wavelength. As expected, the Lyn11-CeLgBiT biosensor **(Figure 3.14E-F)** resulted in a similar profile to unmodified Lyn11-LgBiT.

The kinetic responses were then quantified by calculating peak response and AUC for each biosensor at both wavelengths **(Figure 3.14G)**. For each biosensor combination, a significant difference in peak response and AUC was observed between the 475 nm and 550 nm measurements.

At the 475 nm wavelength, the Lyn11-YeLgBiT response was significantly reduced, with a decrease in peak response of 41% and 47% to Lyn11-LgBiT and Lyn11-CeLgBiT respectively. The differences at the 550 nm wavelength were more pronounced, with Lyn11-YeLgBiT resulting in an increase in peak response of 1087% and 481% to Lyn11-LgBiT and Lyn11-CeLgBiT respectively. There was no significant difference between the Lyn11-LgBiT and Lyn11-CeLgBiT responses at either wavelength.

Thus, these colour-shifted NBA biosensors demonstrate the potential to measure NanoBiT response at different emission wavelengths. However, the ‘bleed through’ response observed in the blue channel of the Lyn11-YeLgBiT biosensor suggests that further optimisation of this assay format may be required before multiplexing is possible.

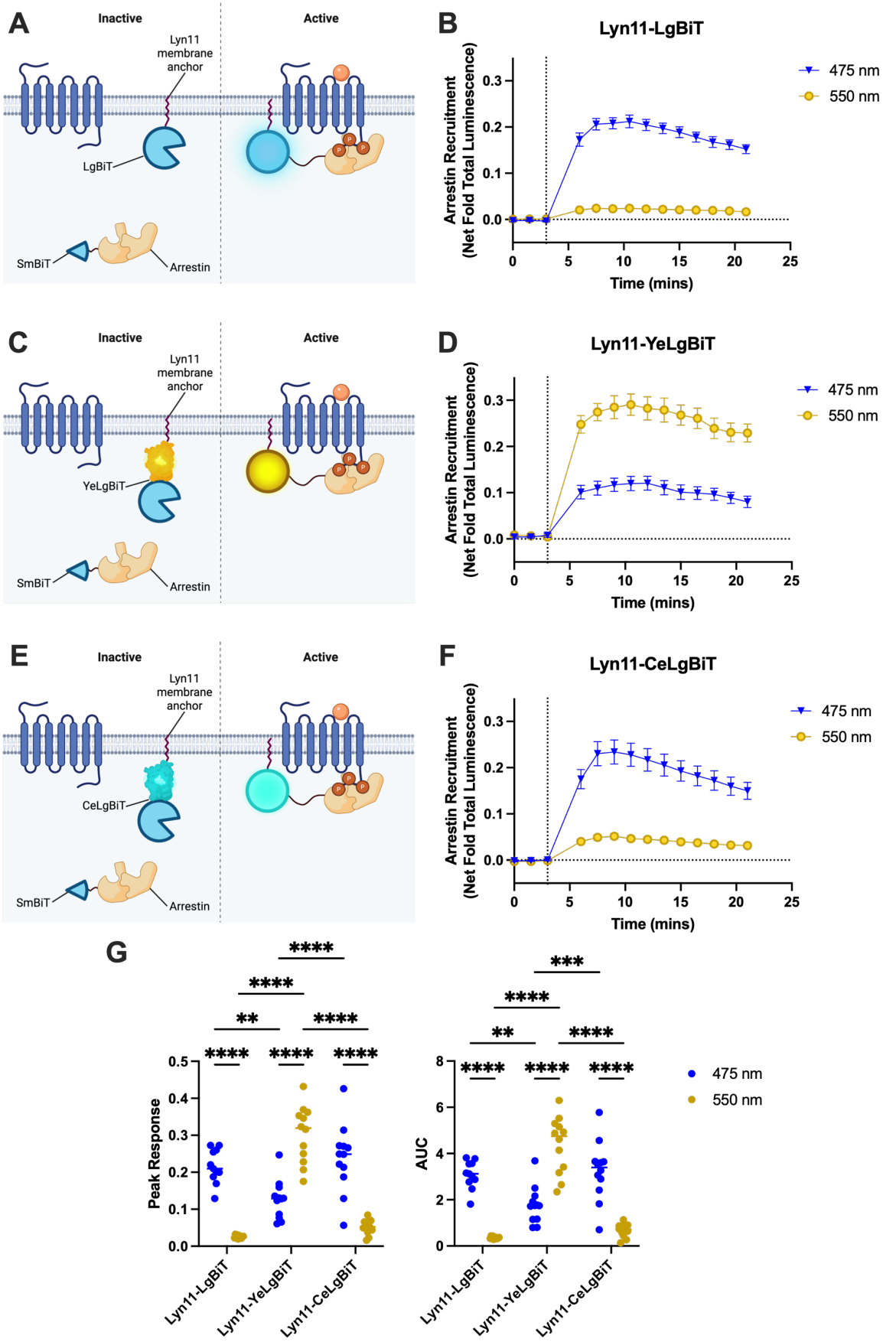

Figure 3.14 – Incorporating a fluorescent protein into Lyn11-LgBiT shifts the emission wavelength of the NBA assay. Schematic diagrams **(A, C, E)** and kinetic measurements of luminescence signal recorded at 475 nm or 550 nm on activation with 10 μM TUG-891 after 3 minutes (indicated by the dotted line) **(B, D, F)** for SmBiT-Arr paired with Lyn11-LgBiT **(A-B)**, Lyn11-YeLgBiT **(C-D)** or Lyn11-CeLgBiT **(E-F)**. Raw luminescence values at each wavelength were divided by total luminescence baseline signal (average of 3 measurements before compound

addition) and vehicle response subtracted. Data presented as mean ± SEM from N=3 independent experiments with n=4 technical replicates. **G)** Quantification of kinetic responses. Peak response and AUC were calculated for each wavelength. Statistical comparisons were made using two-way ANOVA with Tukey's multiple comparisons test. **p < 0.01, ***p < 0.001, ****p < 0.0001. Individual measurements plotted with median indicated from N=3 independent experiments with n=4 technical replicates.

It was hypothesised that the wavelength shift may be improved by adding a fluorescent protein to both the LgBiT and SmBiT components, and thus to both termini of the full length NLuc protein. To assess this, variations of the SmBiT-Arr construct were designed and generated which incorporated an mNG adjacent to the SmBiT, either directly attached or separated by a flexible linker **(Figure 3.15A).** 5 ng/well of these constructs were co-transfected into HEK293-T cells with 30 ng/well FFA4 receptor and 5 ng/well of either the Lyn11-LgBiT or Lyn11-GeLgBiT construct and total DNA prepared to 100 ng/well with empty vector. Biosensors were tested in the standard NBA kinetic assay format following addition of 10 μM TUG-891 **(Figure 3.15)**.

All plasmid combinations where mNG had been incorporated resulted in a significant drop in baseline luminescence signal compared to the standard format **(Figure 3.15B).** I hypothesised this may be due to a reduction in expression level, perhaps due to the larger size of these constructs compared to the non-mNG containing versions and suggest that re-optimisation of the amounts of DNA to transfect for these constructs may be required to ensure this is a robust assay.

In the arrestin recruitment assay, when the signal has been baseline corrected, the constructs incorporating mNG typically result in a higher peak response than the original assay **(Figure 3.15C-D).** This may be a result of the lower background signal but may also be due to the complemented GeNL protein being brighter than NLuc alone (Suzuki et al., 2016). The exceptions to this trend are the two combinations that use the SmBiT-mNG-Arr construct lacking a flexible linker, which have a lower background signal than the constructs including the linker and result in a lower peak luminescence response. This may suggest that attaching SmBiT directly to the fluorescent protein may be affecting the function of this construct.

To assess the wavelength shift of the green NBA constructs, luminescent spectral scans were measured following the kinetic assay **(Figure 3.15E-F).** As anticipated, the constructs incorporating mNG showed a peak at ~525 nm in addition to the traditional NLuc peak at ~450 nm, with the amplitude of these peaks increasing on activation with 10 μM TUG-891. To quantify the shift in wavelength, AUC was calculated for the activated condition in the blue region (420-480 nm) and the green region (500-560 nm), and the ratio of green/blue calculated **(Figure 3.15G).** Incorporation of mNG anywhere within the biosensor resulted in a shift towards the green wavelength, with the 530 nm/450 nm ratio increasing for all constructs relative to the Lyn11-LgBiT / SmBiT-Arr baseline. For unmodified SmBiT-Arr, incorporating mNG in the LgBiT resulted in a significant increase in wavelength shift from 0.2 to 4.5. Including mNG into SmBiT-Arr constructs with a flexible linker resulted in a smaller increase from 0.2 to 1.1 for Lyn11-LgBiT and 4.5 to 5.2 for Lyn11-GeLgBiT. These shifts were not significant in the one-way ANOVA presented but did become significant when using unpaired t tests to make direct comparisons between pairs of conditions.

Therefore, it can be concluded that incorporation of mNG to the N-terminal of the NanoBiT construct has a greater contribution to wavelength shift than incorporation at the C-terminal. However, addition at the C-terminal does further contribute to the wavelength shift. The greatest wavelength shift is observed in the Lyn11-GeLgBiT / SmBiT-FL-mNG-Arr combination, and this would be progressed for further optimisation work.

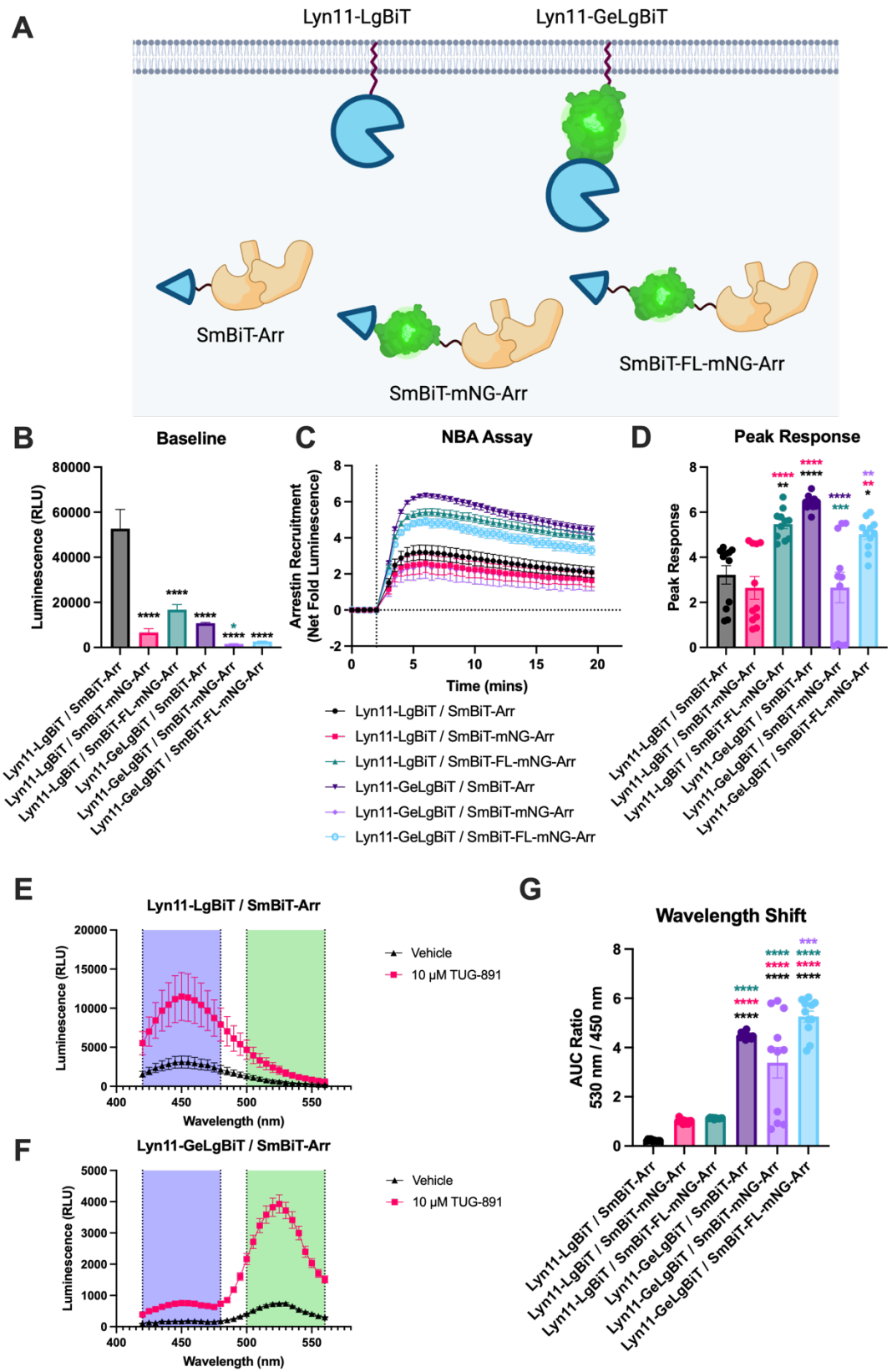

Figure 3.15 – Adding mNG to both SmBiT and LgBiT improves the wavelength shift of the green NBA biosensor. A) Schematic of green NBA biosensor components. Each possible LgBiT/SmBiT combination was transfected into HEK293-T cells for testing. **B)** Baseline raw luminescence measurements of biosensor combinations. **C)** Kinetic measurements of luminescent signal recorded when green NanoBiT plasmid combinations are transfected into HEK293-T cells and activated with 10 µM TUG-891 at 2 minutes (indicated by the dotted line). Raw luminescence values were divided by baseline signal (average of 5 measurements before compound addition) and vehicle response subtracted. **D)** Quantification of peak responses after TUG-891 treatment from **(C)**. **E-F)** Luminescent spectral scans of **(E)** Lyn11-LgBiT / SmBiT-Arr or **(F)** Lyn11-GeLgBiT /

SmBiT-Arr combinations following 20-minute incubation with 10 μM TUG-891 or vehicle control. **G)** Quantification of green wavelength shift. The area under curve was calculated from the blue (420-480 nm) and green (500-560 nm) regions of the 10 μM TUG-891 spectral scans (highlighted in **(D-E)**). For each technical replicate, the ratio of green/blue AUC was calculated. Throughout, data presented as mean ± SEM from N=3 independent experiments with n=3-4 technical replicates. Individual measurements are indicated in **(D)** and **(G)**. Statistical comparisons in **B**, **D** and **G** were made using one-way ANOVA with Tukey's multiple comparisons test. *p < 0.05, **p < 0.01, ***p < 0.001, ****p < 0.0001 where colour indicates the relevant comparison. All other comparisons were not significant.

Overall, the colour-shifted NBA biosensors can measure arrestin recruitment at different emission wavelengths and represent a promising future direction for complex genetically encoded biosensors in GPCR research.

3.6 Discussion

In this chapter, I have designed, generated, and optimised a series of genetically encoded NanoBiT biosensors to measure signalling of the FFA4 receptor. Each biosensor design has been reengineered from a previously reported BRET-based design and allows measurement of different aspects of FFA4 signalling, with each design highlighting individual advantages and challenges.

Firstly, the SpNB assay was successful in allowing measurement of FFA4 activation in response to its agonist, TUG-891. The signal window observed is comparable to the equivalent BRET SPASM sensors (Malik et al., 2017), however this is approximately 100-fold lower (0.3-fold increase) than the possible signal increase observed in intermolecular NanoBiT constructs (30-fold increase) (Littmann et al., 2019). The key advantage of this SpNB system is that it a single molecule, meaning only one component must be transfected into the relevant cell type. This is important as evidence suggests co-transfection of multiple plasmids is more challenging than a single plasmid transfection, with use of multiple plasmids reducing the overall transfection efficiency and the reduced likelihood of all cells receiving all transfected components in the correct stoichiometry (Di Blasi et al., 2021; Christoffers et al., 2024; Baliga et al., 2025).

In these experiments, no significant difference was observed between the G15, Gi3 and Gz sensors. This may be expected as these Gα peptides were selected as all gave a maximal response in the BRET assay (Hudson, unpublished), and thus the full suite of Gα peptides should be tested to assess the complete G protein coupling of FFA4 and identify significant changes in response. A further advantage of the SpNB biosensors is that it is possible to measure the full suite of Gα peptides, which is not the case with other biosensor designs including the miniG (Wan et al., 2018) or BERKY (Maziarz et al., 2020) systems. However, as the receptor is part of the biosensor, it is not possible to measure the activity of endogenous FFA4 using physiologically relevant cell types or expression levels, suggesting that another biosensor design may be better suited for this purpose. Additionally, the pEC_{50} value for TUG-891 generated from the SpNB assay (5.63 ± 0.15) was much lower than the reported pEC_{50} of 7.19 for TUG-891 (Hudson et al., 2013). However, due to the single-molecule nature of the biosensor, this may be more reflective of the affinity of the compound for FFA4 than the

potency recorded for an arrestin recruitment assay (Hudson et al., 2011; Herenbrink et al., 2016). Taken together, although the SpNB biosensors have a role in elucidating the signalling of GPCRs, these biosensors are likely not best suited for expression in an adipocyte spheroid model to understand endogenous signalling of the FFA4 receptor.

In the initial assays, the mG and arrestin receptor recruitment assays showed a higher signal window than the SpNB formats, which is preferable for compound screening purposes (Zhang and Xie, 2012). Furthermore, the sustained kinetic profile of the responses leads to less intensive assay protocols and improves the throughput of the assay.

Additionally, in the concentration response curve experiments, the compounds tested share the same potency rank order and are within range of previously reported pEC_{50} values for FFA4 **(Table 3.1).** The reported pEC_{50} of TUG-891 in a BRET receptor arrestin recruitment assay is 7.19 (Hudson et al., 2013), whereas in these data the pEC_{50} was determined to be 6.75 in the receptor arrestin assay. Similarly, the potencies of TUG-1197 and GSK137647A have been reported as 6.91 and 6.3 respectively, and in this receptor arrestin assay these were determined as 6.73 and 6.03. This slight reduction in potency may be due to the reduced amplification possible with a fragment complementation assay compared to a BRET assay; although both are expected to be a 1:1 interaction, hypothetically it may be possible for BRET to occur between one GPCR and two arrestin molecules, whereas this is not possible for NanoBiT when complementation will only occur in a 1:1 stoichiometric ratio. Interestingly, in these data TUG-1197 appears to be a partial agonist with respect to TUG-891, despite previous reports that it is a full agonist in BRET arrestin recruitment assays (Azevedo et al., 2016). Although evidence has shown that FFA4 can couple to Gi pathways, no data is available to compare the potency of the synthetic compounds in mGi or equivalent assays (Inoue et al., 2019; Husted et al., 2020; Avet et al., 2022).

When comparing the mGq, mGi and arrestin responses to FFA4, the results were somewhat surprising. Although FFA4 has been classically considered a Gq-coupled receptor (Hirasawa et al., 2005; Milligan et al., 2017a), no activation was seen using the mGq biosensor, whereas a large increase in signal is

measured when the Gi biosensor is used. This Gi response is somewhat supported by the literature; some functions of FFA4 are known to be dependent on Gi signalling (Milligan et al., 2017a), and current literature suggests Gi may in fact be the dominant G protein coupling for FFA4 in HEK293-T cells when measured using mG proteins (Husted et al., 2020). The increase in luminescence signal observed using the NBA biosensor was higher than all other biosensors tested, highlighting the robustness of the FFA4-arrestin coupling (Oh et al., 2010).

The physiological role of FFA1 is largely believed to be a result of Gq signalling (Briscoe et al., 2003; Hauge et al., 2015), so it was also surprising to note that although a measurable Gq response was observed, this response was small compared to the FFA1 mGi response. Gi signalling has been previously observed for FFA1 through pertussis-toxin sensitive responses in dynamic mass redistribution and phospho-ERK experiments (Schröder et al., 2010; Qian et al., 2017), but there is no literature to suggest whether T360 specifically may elicit a Gi-mediated response in cell-based assays (Ueno et al., 2019). There is therefore a possibility that the relative magnitudes of the Gi and Gq response observed in the NanoBiT mG assay may be an artefact of this artificial system, and caution must be exercised when interpreting the data. The FFA1 arrestin recruitment response to T360 is limited, in line with literature reports that this compound is a partial agonist with regards to arrestin recruitment (Valentini et al., 2025).

Furthermore, the kinetics of the FFA1 mGi and arrestin response were slower than the TUG-891 FFA4 response, highlighting the power of these techniques to uncover complex pharmacology. These kinetics may represent differences in the binding association of the respective ligand-receptor complexes, suggesting the binding kinetics of T360 for FFA1 may be slower than those of TUG-891 for FFA4, or alternatively suggest that FFA4 activation is more transient than FFA1 due to stronger coupling to arrestin, leading to faster receptor internalisation and desensitisation. However, as with the SpNB sensors, a major disadvantage is the need to express modified forms of the receptor of interest, thus prohibiting measurement of endogenous receptor. The bystander biosensor design therefore may be more appropriate for expressing in physiologically relevant cell types.

In the bystander assay, a large signal window was again observed when cells were co-transfected with FFA4 and activated with TUG-891. Critically, no

response was observed when no receptor was transfected. This control is essential in the bystander format to validate the specificity of the response to the intended target and show that the response is not caused by the effector protein recruiting to a different receptor that is endogenously expressed in the cell system being used (Atwood et al., 2011; Zheng et al., 2023). The pEC_{50} values generated in the bystander concentration response curves were up to 10-fold lower for some compounds than the previously reported values and in the receptor recruitment assay, perhaps suggesting that the bystander assay is not as effective as the receptor assay in measuring every arrestin molecule recruited to the membrane **(Table 3.1, Table 3.2)**. However, the potency rank order of the compounds is consistent and still generally within the range expected for a novel screening assay.

The optimisation of the bystander NBA biosensor highlighted several key considerations which are applicable across biosensor formats. Throughout, the NBA biosensor was optimised for the largest fold increase observed following compound addition. For NanoBiT biosensors, the fold increase is likely predominantly driven by the amount of background signal measured, which is probably due to a combination of the small amount of light emitted by LgBiT alone and random, nonspecific interactions occurring between the LgBiT and SmBiT (Dixon et al., 2015). Thus, the expression level of the biosensor is critical to ensure the largest possible signal window. All constructs used here were expressed under the strong cytomegalovirus (CMV) promoter (Boshart et al., 1985; Qin et al., 2010), meaning that very low amounts of DNA or doxycycline were required to minimise the background signal, potentially introducing additional day-to-day variation. The commercial NanoBiT constructs supplied by Promega are offered with the herpes simplex virus thymidine kinase (HSV-TK) promoter, which is a much weaker promoter than CMV in comparative studies (Ali et al., 2018; Toktay et al., 2022). Selecting a weaker promoter to reduce biosensor expression levels may therefore be beneficial to both reduce the nonspecific interactions occurring between the LgBiT and SmBiT fusion proteins and improve the assay variation caused by transfecting very small amounts of plasmid DNA per well.

Additionally, the orientation of the different biosensor components can dramatically impact the performance of the assay. In the receptor arrestin

recruitment assays, the largest signal window may be expected when LgBiT is on the receptor and SmBiT on the arrestin, consistent with established GPCR BRET assays (Angers et al., 2000; Namkung et al., 2016). However, it may also be that the background signal for NanoBiT assays is driven more by random interactions between the SmBiT and LgBiT rather than the background light emitted by the LgBiT alone, perhaps highlighting that direct comparison between BRET and NanoBiT biosensor designs is challenging. For NanoBiT mG assays, it has been reported that the reverse orientation (i.e. with SmBiT on the receptor and LgBiT on the mG protein) results in a larger signal window and is more commonly used in the literature (Wan et al., 2018).

For bystander assays, typically the membrane-localised component is the BRET acceptor, allowing measurement of a small number of donor arrestin molecules recruiting to the membrane. It was therefore surprising that the SmBiT membrane constructs were not successful. However, this finding replicates a similar result in the literature, which also reported that the NanoBiT system did not function when SmBiT was fused to a membrane-targeting sequence (Pedersen et al., 2021). It is perhaps likely that the lack of response is due to the SmBiT constructs not being expressed or correctly trafficked to the plasma membrane, preventing successful complementation with LgBiT. However, due to the short peptide sequence of the Lyn11-SmBiT and SmBiT-CAAX constructs and the lack of suitable antibodies to assess their expression, it has not been possible to test this hypothesis.

It is also important to consider the relative expression levels of each biosensor component, and this also appears to differ between traditional BRET assays and the bystander NanoBiT assay. In a bystander BRET assay, typically a higher expression level of membrane-associated fluorescent protein compared to donor arrestin would be desired to allow measurement of few arrestin molecules to anywhere on the ‘coated’ membrane. However, with the Lyn11-LgBiT / SmBiT-Arr orientation of biosensor, increasing Lyn11-LgBiT also increases background signal, thus reducing the baseline-corrected assay window. No improvement was possible from an equal SmBiT:LgBiT ratio in this work. Expression ratio optimisation for NanoBiT assays is not typically reported in the literature, with the technical guidance from Promega stating that optimisation of the relative expression levels is not usually required (Promega Corporation, n.d.). However,

in the small number of studies which do explore this, results have been mixed, with contradicting reports suggesting more LgBiT (Heath et al., 2022), more SmBiT (Akinjiyan et al., 2020) or equal amounts of components (Nadel et al., 2020) improves the assay performance. That said, all studies agree that increased luminescence signal does correspond to an increased background signal, highlighting that reducing the background signal is critical when optimising for the greatest response window.

The final bystander NanoBiT arrestin recruitment assay proved to be a robust and useful system, capable of measuring arrestin recruitment even at very low receptor expression levels and measuring arrestin recruitment to several different GPCRs. The ability for a single biosensor to measure the activity of a diverse group of receptors is particularly useful when working in physiologically relevant cell types with endogenous receptor expression. Furthermore, an assay system which allows direct comparison of arrestin coupling between GPCRs is useful for studies assessing the signalling pathways of different receptors, particularly between related members of sub-families such as the free fatty acid or muscarinic acetylcholine receptors.

It is widely understood that different GPCRs interact with arrestin to different extents, driven by distinct binding interfaces of the receptor and arrestin molecules and influenced by factors including GPCR activation state, phosphorylation patterns, and interactions with lipids and non-GPCR membrane proteins (Haider et al., 2023; Underwood et al., 2025). These data support the previous understanding that some receptors interact more strongly with arrestin than others, and therefore use of an arrestin recruitment biosensor is better suited for some receptors than others. To confirm that this observation is not an artefact of the biosensor itself, these experiments could be repeated using a bystander BRET or direct receptor NanoBiT system to test whether the rank order of efficacy is consistent between assay formats. It is however likely that these results are a genuine measure of how well each receptor interacts with arrestin. TUG-891 and lodoxamide are known to robustly recruit arrestin to FFA4 and GPR35 respectively (Hudson et al., 2013; MacKenzie et al., 2014). Biased agonism, where a compound can show signalling preference for either G protein or arrestin pathways, has recently been investigated with GPR84, where 2-HTP is able to signal through arrestin, but alternative agonists cannot (Marsango et al.,

2022). ß-arrestin recruitment has also been measured for the HCA_2 receptor, with pharmacological assays, arrestin knock down experiments and structural studies determining that the unwanted ‘flushing’ side-effect of niacin is a result of signalling through this pathway, and G protein biased agonists can reduce the vasodilatory response (Benyó et al., 2005; Semple et al., 2008; Walters et al., 2009; Yadav et al., 2024). Finally, despite their similarities, FFA2 is known to recruit arrestin, however this has not been reported for FFA3 (Milligan et al., 2017b).

It is pertinent to mention that the SPASM, Mini G and arrestin recruitment biosensors generated here represent a fraction of the biosensor designs available to measure GPCR activity, several of which are available in both BRET and NanoBiT formats (Demby and Zaccolo, 2024; Pearce et al., 2025). As discussed throughout this chapter, each biosensor has its own advantages and challenges and will be best suited for different purposes. In this case, I was interested in measuring the activation of endogenous FFA4 receptor in complex cell models, and therefore the NanoBiT arrestin bystander sensor is ideal considering the large signal response generated. However, if the desired outcome is to explore differences in FFA4 G protein coupling with different agonists or in different cell types, a different system such as the TRUPATH G protein dissociation BRET assay (Olsen et al., 2020) or NanoBiT equivalent (Inoue et al., 2019) may be preferred. It is critical to choose the correct biosensor for the desired experiment, and therefore essential to develop a toolkit of biosensors to explore the complex signalling networks of GPCRs.

A limitation with the bystander NanoBiT assays reported here is the assumption that GPCRs are located at the plasma membrane of cells. The historical understanding that GPCRs are exclusively expressed on the plasma membrane of cells (Pierce et al., 2002) has been challenged, with growing evidence that GPCRs not only are located at intracellular compartments, but can signal from these compartments with distinct regulatory signatures (Calebiro et al., 2009, 2024; Ferrandon et al., 2009). In particular, the FFA4 receptor is reported to be located at the plasma membrane of HEK293-T cells, but predominantly intracellular in more physiologically relevant adipocyte models (O’Brien et al., 2025). It remains to be seen whether these plasma membrane localised NBA biosensors remain functional in adipocytes. However, if not, one benefit of

bystander biosensors is the potential to easily adapt the sensor by replacing the Lyn11 tag with alternative sequences to measure signalling at different cellular compartments (Lan et al., 2012). One common approach is using the Rab GTPase regulators of membrane trafficking to localise fluorescent proteins to distinct subcellular compartments, thus allowing visualisation using microscopy and BRET-based assays of basal and ligand-stimulated receptor distribution (McCaffrey and Lindsay, 2013; Tiulpakov et al., 2016), although alternative markers for each compartment are also available (Namkung et al., 2016; Wright et al., 2021). Together, these approaches have been used to follow trafficking and intracellular signalling of many GPCRs including FFA4 through early endosomes (Rab5 or FYVE), late endosomes (Rab7 & Rab9), the trans-Golgi network (Rab9 & Rab6 or Giantin), recycling endosomes (Rab4) and the endoplasmic reticulum (Rab1 or PTP1B) (Tiulpakov et al., 2016; Wright et al., 2021; O'Brien et al., 2025).

The exploratory work to develop colour-shifted NanoBiT biosensors highlighted the potential to multiplex NBA assays across different cell types or subcellular compartments. NBA biosensors were developed which emit in either blue or yellow/green wavelength ranges, and activation of these sensors resulted in an increase in signal predominantly in the 'correct' channel. However, further optimisation is required to validate these biosensors in a multiplex format.

Firstly, it was noted that the coloured biosensor variants resulted in a lower and more variable baseline luminescence signal than the standard NanoBiT components, suggesting the robust expression of these constructs requires further optimisation. This is particularly critical in multiplexed assays to ensure the baseline luminescence is approximately comparable between channels, thus allowing an increase in signal from the dimmer biosensor to be visible above the background from the brighter biosensor.

Additionally, the bleed through in luminescence signal observed, particularly from the yellow sensor in the blue wavelength, may introduce challenges when trying to separate the information obtained from the different biosensors within the same measurement reading. One potential solution to reduce bleed through may be to adjust the wavelengths used to measure each colour towards the extremes of their respective spectra (i.e. 420 nm for blue and 620 nm for

green/yellow). This is likely to be somewhat less effective for the blue wavelength due to the secondary peak observed with the green biosensors which follows the emission profile of NLuc, but an increased wavelength for the green/yellow emission may reduce the bleed through from a blue biosensor.

Conversely, the bleed through may become less of a challenge when both biosensors are simultaneously expressed in a mixed population of cells. Using the green biosensor as an example, when expressed alone, the fold change in light emitted on activation is similar between the blue and green wavelengths as the blue signal is only due to background of the green sensor. However, when a blue biosensor is also expressed, the baseline signal in the blue channel will predominantly be due to the background of the blue sensor which should not increase when only the green biosensor is activated (and vice versa). To test this hypothesis, two populations of HEK293-T cells could be transfected independently with a coloured NBA sensor and a GPCR with comparable ability to activate arrestin (e.g. FFA4 with green NBA and GPR35 with blue NBA). These cells are then mixed and total and channel-specific luminescence measured following addition of TUG-891 or lodoxamide. In this case, I would expect addition of TUG-891 to result in an increase in the fold change of green emission with limited increase in the blue channel, and vice versa for lodoxamide. This also assumes that expression level of the two constructs (and hence the background signal in each channel) is similar, but would provide essential validation to the multiplex assay format.

It is relevant to note that, to date, no colour-shifted NanoBiT multiplexed plate-based assays have been reported in the literature. Several examples of colour-shifted NLucs have been reported, including some with plate-based Ca^{2+} assays (Suzuki et al., 2016; Oh et al., 2019; Yang and Johnson, 2021), although these have typically been optimised for *in vivo* imaging approaches. In a recent study, an expanded series of NanoLantern constructs was presented with NanoBiT variations used to measure arrestin recruitment to three GPCRs simultaneously (Hattori et al., 2025). However, the observation of arrestin recruitment was only possible using a microscope equipped with a colour camera and required long exposure times of 2 minutes per image in HEK293-T cells with transfection of both receptor and arrestin constructs. Furthermore, the design of these biosensors fundamentally would not allow measurement of multiple pathways

within the same cell, e.g. at different subcellular locations. Thus, a colour-shifted NanoBiT bystander arrestin recruitment assay suitable for plate-based assays, using endogenous receptor expression in physiologically relevant cell models would be a fantastic addition to the field.

The aim of this work was to develop and optimise genetically encoded biosensors suitable for measuring real-time GPCR activity in an adipocyte spheroid model. I hypothesised that NanoBiT would be better than BRET for this purpose, however due to the inherent differences in the technologies, it is ultimately very challenging to compare them experimentally. Both techniques have advantages and disadvantages; the ratiometric BRET measurement results in a highly specific signal with intrinsic correction for cell number and expression levels, however the requirement for dual-wavelength readings limits the multiplexing potential of these biosensors within the typical measurement range of most commercial plate readers. Conversely, the single wavelength NanoBiT reading is more sensitive to variations in expression levels and cell number, but is measured with greater dynamic range and more scope for multiplexing assays. The next steps to express these biosensors in a physiologically relevant adipocyte 2D cell and 3D spheroid model will be discussed in Chapter 5.

4 Development and characterisation of a 3D *in vitro* adipocyte spheroid model

4.1 Introduction

Metabolic diseases such as obesity, MASLD and T2D are a global healthcare and economic challenge, with over 1 billion individuals living with obesity worldwide (World Obesity Federation, 2025). Obesity is a life limiting condition characterised by excessive accumulation of adipose tissue, dramatically increasing a person's risk of developing serious health conditions including T2D, CVD and some cancers (Institute for Health Metrics and Evaluation, 2024; World Health Organisation, 2025).

Adipose is a dynamic organ comprising several different cell types, including adipocytes, immune cells, endothelial cells, and fibroblasts, as well as extensive extracellular matrix (Lee et al., 2013b; Ramakrishnan and Boyd, 2018). Adipose tissue has many important roles in the physiology of energy homeostasis; however, it is only relatively recently that adipose has been fully recognised as an endocrine organ and not simply as an energy store (Rosen and Spiegelman, 2014). Crucially, our understanding of adipose tissue dysfunction and its role in the development of metabolic disease remains limited, and it is therefore essential to improve our understanding of adipose in pathophysiological contexts given the increasing prevalence of these conditions.

Common features of dysfunctional adipose tissue include adipocyte hypertrophy, hypoxia and fibrosis, leading to impaired adipokine signalling, increased circulating lipids and the development of insulin resistance (IR) (Blüher, 2024). This in turn can drive development of IR in systemic tissues such as muscle and liver, leading to elevated blood glucose levels and downstream complications including neuropathy and blindness (World Health Organisation, 2021). Despite significant effort, the exact pathophysiology of IR remains unclear, however its development is strongly associated with low-level chronic inflammation of metabolic tissues (Olefsky and Glass, 2010). Macrophage infiltration of adipose tissue is shown to be elevated in obesity in both mouse (Weisberg et al., 2003) and human (Harman-Boehm et al., 2007), with the subsequent release of pro-inflammatory cytokines contributing to IR in adipocytes (de Luca and Olefsky, 2008; Olefsky and Glass, 2010; Gasmi et al., 2020). In clinical studies, it is well known that pro-inflammatory biomarkers in adipose tissue and the wider circulation are associated with the incidence of IR and T2D (Pradhan et al.,

2001; Tsalamandris et al., 2019; Wu and Ballantyne, 2020). Metabolite-sensing GPCRs have been proposed to facilitate communication between adipocytes and infiltrating macrophages (Husted et al., 2017; Duncan et al., 2023), however it has been challenging to deconvolute these complex signalling networks and understand the mechanistic basis of these interactions using our existing models of adipose tissue.

Much of our knowledge about adipose tissue and metabolic disease has been obtained from *in vivo* studies, where a variety of genetic or diet-induced models of obesity are available to study different aspects of adipose tissue dysfunction, including development of IR, diabetes and related cardiovascular complications (Nandi et al., 2004; Wang and Liao, 2012). Although information gained from rodent studies is critical, the high cost and ethical concerns associated with these models mean that they are not suitable for higher-throughput drug screening or mechanistic studies.

In vitro, mature white adipocytes are challenging to study due to their non-proliferative phenotype and inability to be cryopreserved (Baganha et al., 2022). Thus, researchers must either rely on a constant supply of fresh adipose tissue from animal or clinical samples or use preadipocyte cultures which may be differentiated *in vitro* to an adipocyte-like phenotype (Dufau et al., 2021; Baganha et al., 2022). The most common preadipocyte cell line is the murine-derived 3T3-L1, which has been extensively used to study adipocyte biology since the 1970s (Green and Meuth, 1974; Dufau et al., 2021). 3T3-L1 cells have been widely used to study adipogenesis (Ruiz-Ojeda et al., 2016), metabolic phenotyping (Roberts et al., 2009) and IR, induced through exposure to conditions such as high insulin concentrations, TNF or hypoxia (Lo et al., 2013). However, as a murine-derived cell line, 3T3-L1 cells often lack translational relevance to human systems (Wang et al., 2014), and are reported to have significant differences in gene expression profiles compared to *in vivo* adipocytes (Soukas et al., 2001) as well as sharing phenotypic features of white, beige and brown adipocyte lineages (Morrison and McGee, 2015).

The Simpson-Golabi-Behmel syndrome (SGBS) cell strain is a human-derived alternative *in vitro* adipocyte model (Wabitsch et al., 2001; Fischer-Posovszky et al., 2008). These preadipocyte cells were isolated from a male infant patient

with Simpson-Golabi-Behmel syndrome and shown to differentiate *in vitro* to adipocytes in a similar manner to primary cells but crucially retain their differentiation capacity over many generations (Wabitsch et al., 2001). Since their isolation, SGBS cells have been used to investigate adipogenesis, insulin sensitivity and adipose tissue inflammation in a human-relevant system (Tews et al., 2022), with some studies again highlighting discrepancies between human and murine cell models (Schmidt et al., 2011; Rossi et al., 2020).

Most studies using *in vitro* differentiated adipocytes have been completed in 2D, with cells grown in monolayer cultures adhering to glass or plastic tissue culture vessels. Although these simple 2D cell models of adipocytes are cheap and high-throughput, they cannot recapitulate the complex cellular microenvironment needed to fully investigate metabolic disorders. *In vivo*, cells respond to all aspects of their surrounding microenvironment through interactions with the ECM and neighbouring cells in addition to physical factors such as stiffness and topography of the matrix (Lane et al., 2014; Langhans, 2018). Thus, 3D cell culture may improve the physiological relevance of *in vitro* systems, while avoiding the challenges of working *in vivo*.

Several adipocyte spheroid models have been reported in the literature (Luca et al., 2024), with increasingly complex phenotypes designed to mimic specific features such as inflammation (Turner et al., 2015), fibrosis (Rajangam et al., 2016), obesity-associated breast cancer (Blyth et al., 2025), and even cultured meat (Luo et al., 2024). Notably, it has been reported that adipocyte culture in 3D more accurately represents the *in vivo* morphology and gene expression signatures than 2D culture (Shen et al., 2021). Several groups have also reported significant differences in the inflammatory and metabolic responses of equivalent 2D and 3D culture conditions, suggesting 3D models may be more physiologically relevant for translational research (Turner et al., 2018; Wolff et al., 2022; Umetsu et al., 2024). However, there continue to be limitations in the applicability and accessibility of 3D cell cultures for drug discovery and pharmacology approaches. Processes such as liquid handling and imaging of 3D structures typically require specialised equipment, and traditional plate-based assays measuring the core physiological function of adipocytes, including lipolysis and glucose uptake, have not yet been translated from 2D to 3D.

In this chapter, I aimed to develop and characterise a 3D *in vitro* model of adipose tissue using SGBS cells. Initially, I explored the properties of the SGBS cells in 2D, including assessing animal-free growth medium and optimising differentiation conditions, before using the cells to generate adipocyte spheroids. The spheroid model was validated using a range of techniques including microscopy to assess spheroid morphology, qPCR and immunostaining to confirm the presence of adipogenic gene and protein markers, and functional assays to measure the biological activity of the spheroids.

4.2 Optimising SGBS cell growth in animal-free culture medium

Animals and animal-derived biomaterials have consistently been used in biomedical research, with Fetal Bovine Serum (FBS) a standard supplement for *in vitro* cell culture medium. However, the limitations of FBS are well documented, with significant issues including batch-to-batch variation, contamination risk, and animal suffering (Valk and Gstraunthaler, 2017). The recent demand for xenogenic-free cell culture medium for cell therapy approaches has resulted in increased investigation of synthetic and human-derived medium for cell culture (Karnieli et al., 2017). A further advantage of the SGBS cell strain is that the published differentiation protocol is carried out in the absence of FBS. However, there is no published literature on SGBS cells that does not use 10% FBS as the standard cell culture growth supplement.

In order to improve the ethical impact of this project and align with the Animal Free Research UK guidelines (Animal Free Research UK, 2021), a series of initial experiments were carried out to explore whether SGBS cells could be grown in an alternative FBS-free culture medium **(Figure 4.1)**. Cells were gradually transitioned into the alternative sera in tissue culture flasks then seeded at low density into tissue culture plates (day 0). After 24h, one plate of cells was fixed, nuclei stained and cells counted, while another was media changed to the indicated condition and maintained in culture. After 6 days, cells were fixed, nuclei stained and cells counted, and cell replication determined as a fold change of the nuclei count (day 6/day 1).

Firstly, direct replacement of FBS with Human Serum (HS) was unsuccessful, as only a 1.7-fold increase in cell number was observed over the 6-day period in 2.5% HS, with no increase for cells cultured in increasing serum concentrations **(Figure 4.1A)**. Batch-to-batch variation is a known issue with HS; however two batches were tested with similar performance. As a control, cells cultured in FBS showed a concentration dependent increase in cell growth, culminating in an 8-fold increase in cell number following 6 days in 10% FBS.

Heat inactivation of serum is a well-established cell culture protocol used to inactivate complement proteins, thus theoretically reducing complement-

mediated cell lysis and improving growth (Soltis et al., 1979; Triglia and Linscott, 1980). However, no improvement in cell number was observed when culturing SGBS cells in increasing concentration of heat-inactivated HS **(Figure 4.1B)**. In fact, heat-inactivation of FBS appeared to suppress its proliferative effect on SGBS cells, significantly reducing the fold increase in nuclei from 4.5 to 3.1 after 3 days of growth in 10% FBS (*p = 0.028).

Following a literature search, it was found that growth rate of Adipose Derived Stromal Cells (ADSCs) was improved by addition of epidermal growth factor (EGF) and basic fibroblast growth factor (bFGF) (Hebert et al., 2009). In SGBS cells this finding appeared to be somewhat consistent, as growth even greater than the 10% FBS control was observed with >1 ng/mL EGF supplementation of 5% HS **(Figure 4.1C)**. Addition of bFGF appeared to increase cell number with a concentration-dependent trend observed in the absence of EGF, although this was non-significant and was not sustained when EGF was also added. However, in these experiments it was visually observed that cells detached more easily in the presence of the growth factors. It is possible that culture on a coating such as human-derived collagen or fibronectin may improve cell adhesion and reduce the variability in these results.

Finally, Human Platelet Lysate (hPL) was investigated as an alternative to HS due to its high growth factor content and reports that ADSCs grow well in hPL with no need for plate coatings (Palombella et al., 2020). In this experiment, the SGBS cells grew in 10% hPL at an equivalent rate to 10% FBS, although FBS still resulted in improved growth at lower serum concentrations **(Figure 4.1D)**. However, it was noted that the viability of cells when harvesting from the flasks was much lower for cells grown in 5% hPL (51% average viability) than 10% FBS (84% average viability), suggesting further optimisation may be required.

Together, these data suggest that it may be possible to find an animal-free culture medium for SGBS cells. However, this will require significant additional optimisation, which was not possible within the scope of this project. Thus, SGBS cells were cultured in the standard medium of DMEM/F-12 supplemented with 10% non-heat-inactivated FBS for all subsequent experiments.

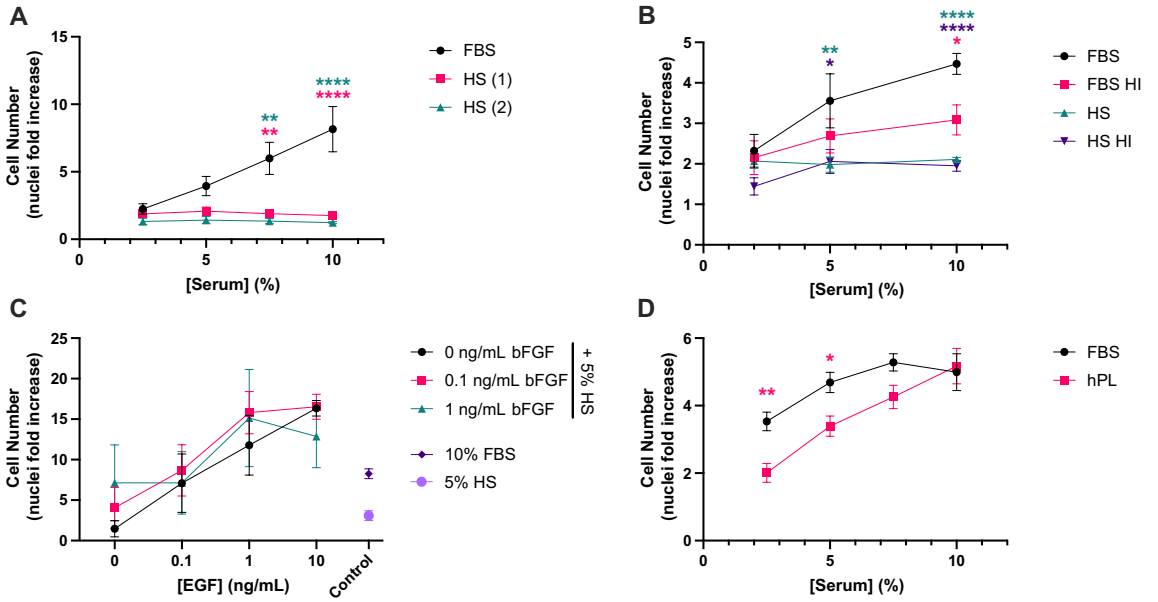

Figure 4.1 - SGBS cells grow in animal-free culture medium without FBS. Throughout, cell growth is presented as fold increase in nuclei count after 6 days in culture (3 days for panel B) and is shown as mean ± SEM of the indicated number of experiments. **A)** SGBS cell growth in medium containing titrations of fetal bovine serum (FBS) or human serum (HS) from two different batches. Data from N=4 (FBS, HS (1)) or N=2 (HS (2)) independent experiments with a single well of a 12-well plate per condition. **B)** SGBS cell growth in medium containing titrations of heat-inactivated (HI) or control FBS or HS. Data from N=3 independent experiments with 2 wells of a 24-well plate per condition. **C)** SGBS cell growth in 5% human serum with titrations of epidermal (EGF) or basic fibroblast (bFGF) growth factors. Growth in 10% FBS or non-supplemented 5% HS is included as a control. Data from N=2-4 independent experiments with a single well of a 24-well plate per condition. **D)** SGBS cell growth in titrations of FBS and human platelet lysate (hPL). Data from N=3 independent experiments with 2-3 wells of a 24-well plate per condition. Throughout, statistical comparisons were made using two-way ANOVA with Tukey's multiple comparisons test. *p < 0.05, **p < 0.01, ****p < 0.0001 with colours indicating comparison to FBS control.

4.3 Optimising and validating SGBS adipocyte differentiation in 2D & 3D cultures

4.3.1 Selecting an SGBS differentiation cocktail

SGBS differentiation protocols were initially developed and optimised by the Wabitsch group (Wabitsch et al., 2001; Fischer-Posovszky et al., 2008). In the literature, a further two protocols were identified for SGBS adipocyte differentiation which use different concentrations of components in the differentiation and maintenance cocktails (Lee and Fried, 2014; Markussen et al., 2017). To select the optimal differentiation protocol, cells were plated in 2D and differentiated according to the conditions described in **Table 4.1**. Degree of differentiation was assessed using Oil Red O staining to visualise lipid droplets and qPCR to assess transcript expression of key adipogenic markers **(Figure 4.2)**. Cells appeared to differentiate well using both the SOP and L&F protocols, with the L&F protocol showing a higher number of differentiated cells **(Figure 4.2A)**. Furthermore, the L&F protocol resulted in a greater increase in expression of adipogenic markers relative to day 0 when compared to SOP for genes including the transcription factor peroxisome proliferator-activated receptor gamma (PPARG; fold change increase of 22.3 and 37.0 for SOP and L&F respectively), the adipokine adiponectin (fold change increase from 23,266 to 99,146) and the insulin-regulated glucose transporter GLUT4 (fold change increase from 178.7 to 392.2). Critically, the FFA4 receptor had a much larger increase in expression of 50-fold in the L&F protocol compared to 3-fold for the SOP protocol. Thus, the L&F protocol was selected for further use.

Table 4.1 – Differentiation and maintenance medium components for SGBS cells

Medium Components	**SOP** (Fischer-Posovszky et al., 2008)	**TERT-hWA** (Markussen et al., 2017)	**L&F** (Lee and Fried, 2014)
Differentiation Cocktail (Day 0-4)			
Transferrin	10 µg/mL	0	10 µg/mL
Insulin	20 nM	860 nM	100 nM
Cortisol	100 nM	1 µM	0
T3	0.2 nM	1 nM	2 nM
Dexamethasone	25 nM	1 µM	100 nM

IBMX	250 µM	500 µM	500 µM
Rosiglitazone	2 µM	1 µM	1 µM
FBS	0%	2%	0%
Maintenance Cocktail (Day 4-14)			
Transferrin	10 µg/mL	0	10 µg/mL
Insulin	20 nM	0	10 nM
Cortisol	100 nM	0	0
T3	0.2 nM	1 nM	0
Dexamethasone	0	0	10 nM
FBS	0%	2%	0%

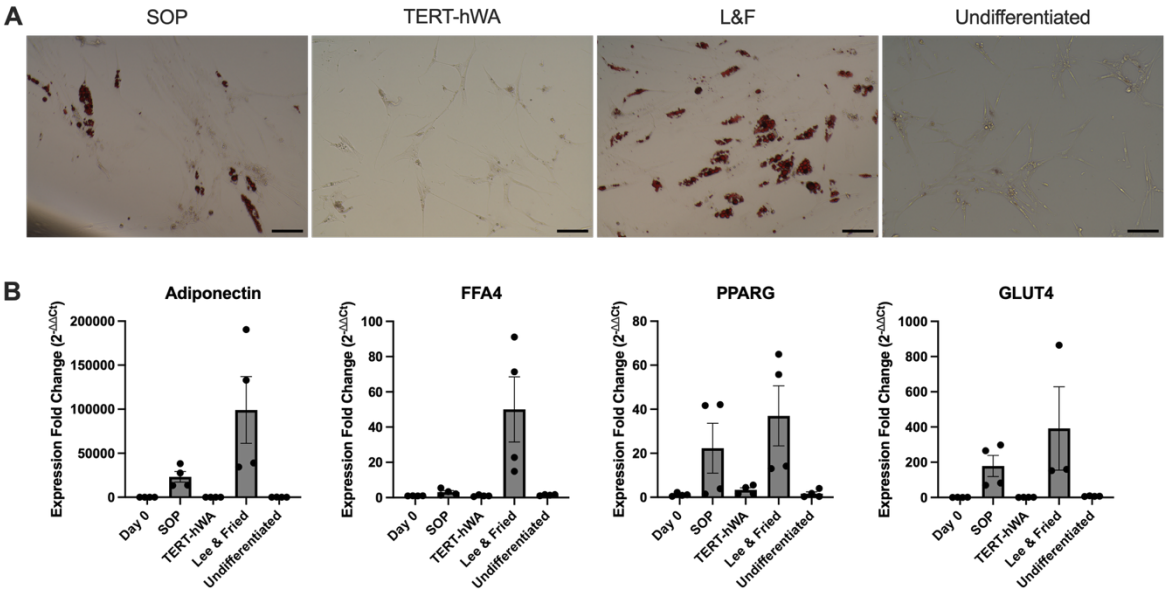

Figure 4.2 – L&F differentiation protocol improves adipogenic differentiation of SGBS cells compared to SOP. A) Representative images of Oil Red O-stained SGBS cells after differentiation with the indicated cocktail. Scale bar = 100 µm. **B)** Gene expression analysis of adipogenic markers in SGBS cells after differentiation with the indicated cocktail, determined by RT-qPCR. C_T values were analysed using the $2^{-\Delta\Delta CT}$ method to show expression fold change relative to RNA isolated from day 0 cells, using primers for GAPDH as housekeeping control. Data are presented as mean ± SEM from N=2 independent experiments with n=2 technical replicates.

4.3.2 Determining optimal SGBS spheroid size

SGBS spheroids are generated by harvesting cells from tissue culture flasks and plating in a 384-well ultra-low adhesion (ULA) plate. These plates are coated with a hydrophilic surface to encourage the cells to stick to each other rather than the plate, generating a single spheroid per well. Initially, cells were seeded into the ULA plates at different densities to generate spheroids of different sizes **(Figure 4.3A)**. It was anticipated that the number of viable cells would initially

increase with spheroid size but eventually decrease due to limited nutrient and oxygen diffusion to the centre of the spheroid leading to a hypoxic core (Curcio et al., 2007; Schmitz et al., 2021). Therefore, a CellTitre-Glo 3D assay (Promega) was used to quantify the viability of the spheroids **(Figure 4.3B)**. Initially, the relationship between cell number and viability is broadly linear, with viability plateauing at spheroids greater than 20,000 cells. A spheroid size of 10,000 cells/sphere was selected as this was the largest size before a loss in viability was observed, thus providing the best balance to obtain the most material for future studies.

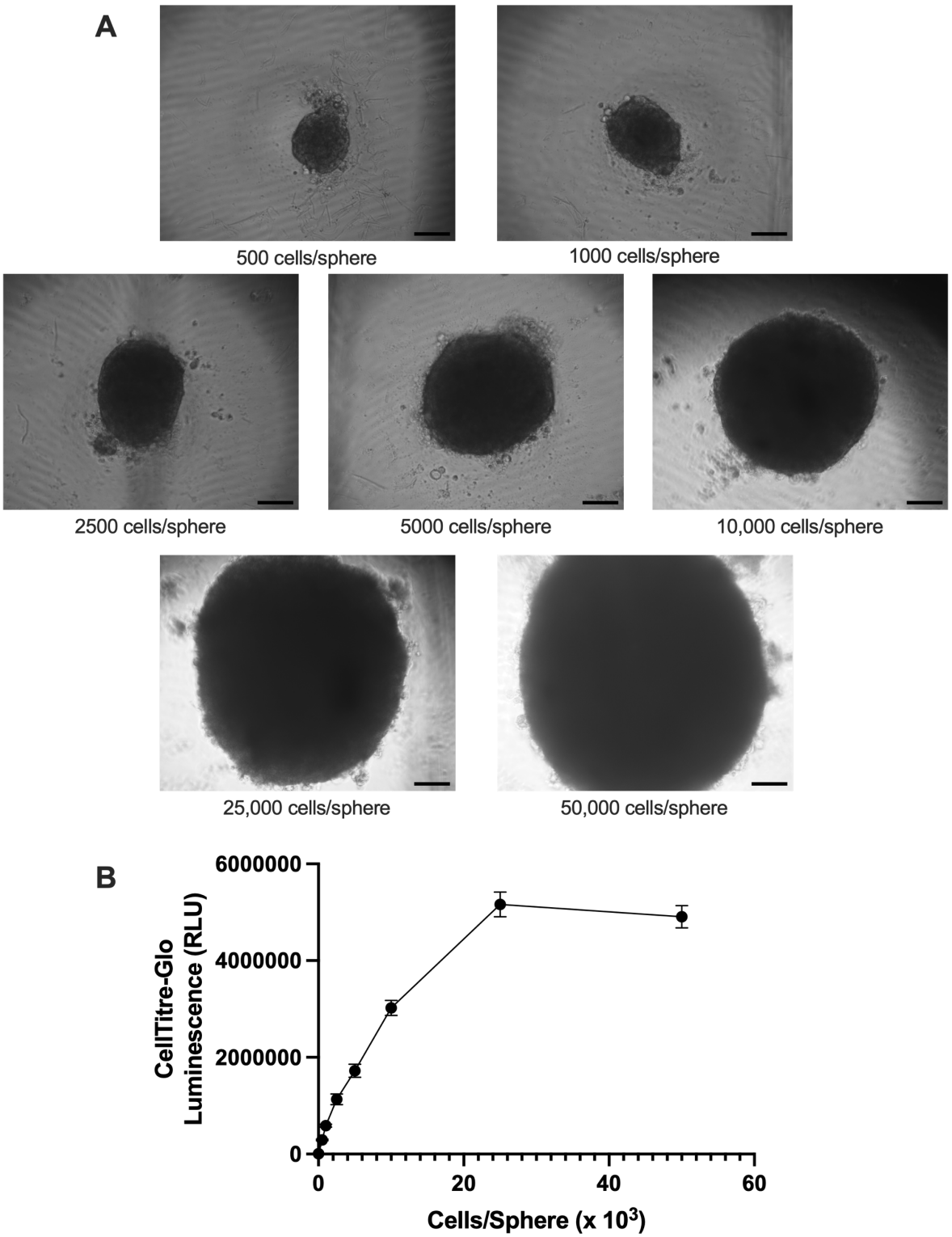

Figure 4.3 - SGBS spheroid size affects viability. A) Representative phase contrast images of SGBS spheroids generated when the indicated number of cells were seeded per well in an Ultra Low Adhesion (ULA) plate and incubated for 24 hours. Scale bar = 100 µm. **B)** CellTitre-Glo viability measurements of spheroids of indicated size. Data are presented as mean ± SEM from N=3-4 independent experiments, with n=6-8 individual spheroids per experiment.

4.3.3 SGBS cells can differentiate to adipocytes in spheroids

Differentiation of SGBS cells in 2D and 3D using the L&F protocol occurs over a 14-day period, and can be followed using phase contrast microscopy **(Figure**

4.4A-B). In 2D, adipocyte differentiation is very obvious by the morphological 'rounding up' of cells followed by the accumulation of lipid droplets **(Figure 4.4A)**. In 3D however, adipogenesis is more challenging to visualise. Although the spheroid enlarges, this is not easily assessed without a direct comparison to day 0 **(Figure 4.4B)**. Differentiated adipocytes can occasionally be seen 'migrating' out of the spheroid, but it is otherwise challenging to observe differentiation within the spheroid itself.

It was noted while completing adipocyte experiments that cells of later passage number did not differentiate as effectively as those of earlier passage. This was assessed by extracting and quantifying Oil Red O staining of 2D and 3D differentiated SGBS cells across different passage numbers, where each passage represents a 1:5 split in tissue culture flasks. In 2D cells, differentiation was not observed in cells above passage 5 **(Figure 4.4C)**. Throughout this project, it was observed that cells appeared to differentiate better and more consistently in 3D than in 2D and maintained differentiation potential to later passages. However, when trying to quantify this phenomenon using Oil Red O staining with 3D samples, it was not possible to measure a difference between day 0 and day 14 spheroids, with low absorbance values and high variability **(Figure 4.4D)**. Therefore, no trend could be observed when comparing spheroid differentiation across passage numbers. Further development is required to establish a better method to quantify the degree of differentiation in adipocyte spheroids.

Throughout the rest of this thesis, SGBS spheroids were not used for differentiation later than passage 6.

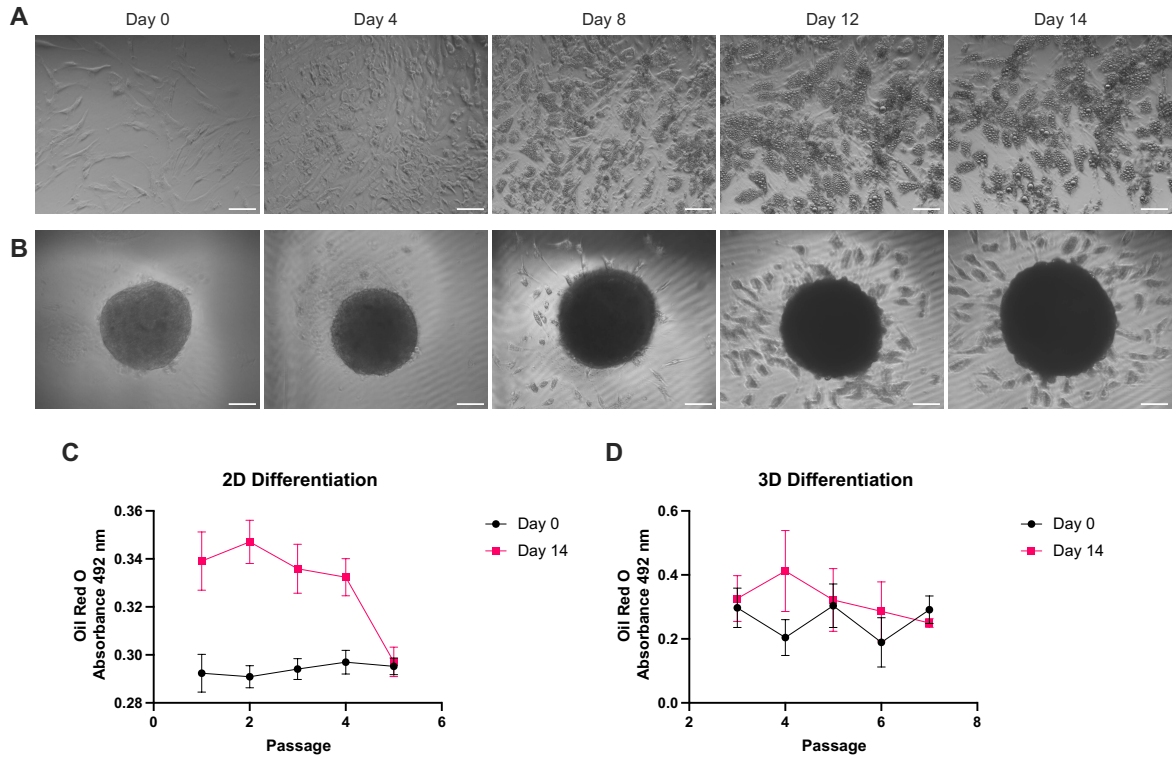

Figure 4.4 - SGBS cells and spheroids differentiate into adipocytes at low passages. A-B) Phase contrast images of SGBS cells grown and differentiated in 2D **(A)** or 3D **(B)** at the indicated day of differentiation. Scale bar = 100 µm. **C-D)** Quantification of Oil Red O staining of SGBS cells grown and differentiated in 2D **(C)** or 3D **(D)** at increasing passage numbers. Each passage represents a 1:5 split in T150 cell culture flasks. Data presented as mean ± SEM from N=4 wells per passage number with n=2 technical replicates (C), or N=2-6 pools of 10-12 spheroids from 1-4 differentiation batches with n=2 technical replicates (D).

4.4 Adipogenesis can be visualised by lipid droplet accumulation in SGBS spheroids

4.4.1 Confocal imaging of intact spheroids highlights lipid droplet accumulation during differentiation

To visualise differentiation of SGBS spheroids, a series of imaging techniques were assessed. First, intact spheroids were fixed at day 0 or day 14, stained with LipidSpot™ 488 green fluorescent neutral lipid stain and imaged using a Zeiss LSM980 confocal microscope **(Figure 4.5)**. These images clearly show accumulation of green fluorescence labelled lipid droplets across the whole differentiated spheroid **(Figure 4.5B)** which are absent in the undifferentiated spheroid **(Figure 4.5A).** However, due to the size and shape of the spheroids, it was challenging to obtain clear confocal images at higher magnification. Furthermore, the light penetration into the spheroid was poor using this laser scanning confocal microscope, resulting in images of the spheroid surface exclusively rather than internal structures. Thus, alternative microscopy approaches were investigated.

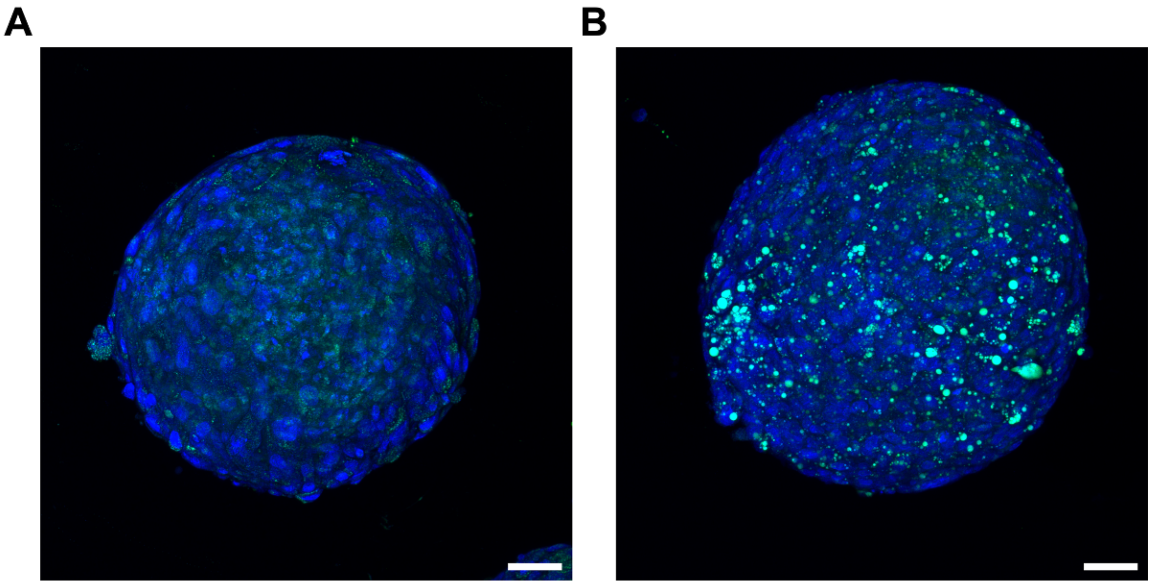

Figure 4.5 - Confocal imaging of intact SGBS spheroids shows presence of lipid droplets following differentiation. Representative images of undifferentiated **(A)** or differentiated **(B)** spheroids which were fixed, stained with Hoescht (blue, nuclei) and LipidSpot™ (green, lipid) fluorescent dyes and imaged using a Zeiss LSM980 confocal microscope with 10X objective. Scale bar = 50 µm.

4.4.2 Scanning Electron Microscopy of intact spheroids shows morphology changes during differentiation

Intact spheroids were also processed for Scanning Electron Microscopy (SEM) by fixing with 1.5% glutaraldehyde and negative staining in osmium tetroxide before dehydrating, coating with Au/Pd and imaging. Undifferentiated spheroids had a relatively smooth surface texture **(Figure 4.6A-B)** whereas the differentiated samples showed an uneven surface morphology containing structures which appear to be accumulated lipid droplets **(Figure 4.6C-D)**. At higher magnifications, the differentiated cells appeared to contain a mixture of larger individual spherical lipid droplets as well as clusters of smaller lipid droplets **(Figure 4.6E).** Interestingly, some differentiated spheroids appeared to show an asymmetric phenotype where the adipocytes on one side appeared more differentiated than the other **(Figure 4.6D)**. However, as with the confocal images, the information obtained from the SEM images is purely from the spheroid surface and thus a different approach is needed to investigate the spheroid core.

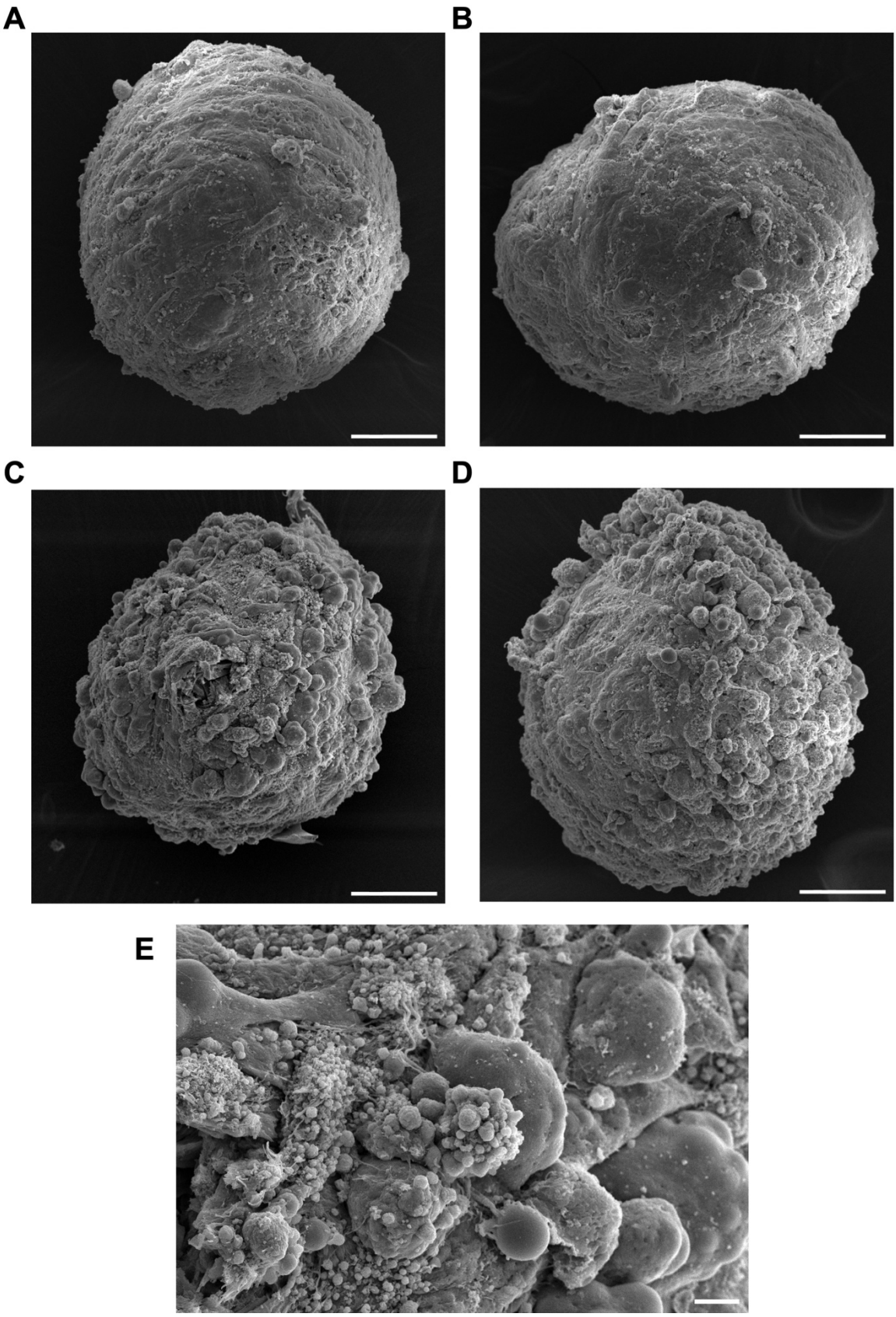

Figure 4.6 - Scanning Electron Microscopy (SEM) images of SGBS spheroids show an irregular surface on the surface of differentiated samples. Representative images of undifferentiated **(A-B)** or differentiated **(C-D)** spheroids which were processed for SEM and imaged at x350 magnification. Scale bar = 50 µm. **(E)** The differentiated spheroid shown in (C) at x2000 magnification. Scale bar = 5 µm.

4.4.3 Transmission Electron Microscopy allows visualisation of internal spheroid structures

Unlike the other techniques described so far, Transmission Electron Microscopy (TEM) requires ultrathin sectioning to examine the ultrastructure of cells within the spheroid. Using this technique, lipid droplets were again observed in the differentiated spheroids, appearing as circular structures with a uniform texture and pale grey colour, indicated by the red asterisks **(Figure 4.7A-C),** which were absent in the undifferentiated sections **(Figure 4.7D)**. Again, a mixed population of lipid droplet sizes was observed, with some very large droplets (~10 µm diameter) visible particularly in the outermost layer of cells around the spheroid periphery **(Figure 4.7)**.

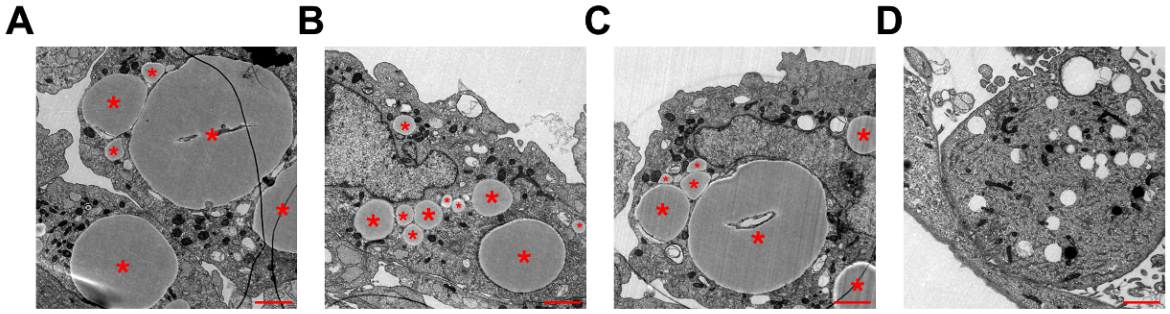

Figure 4.7 - Transmission Electron Microscopy (TEM) images of sectioned SGBS spheroids show large lipid droplets in differentiated samples. Differentiated **(A-C)** and undifferentiated **(D)** SGBS spheroids were processed and sectioned for TEM and images of the outermost cells around the spheroid periphery were taken at x2500 magnification. Lipid droplets are indicated by red *. Scale bar = 2 µm.

TEM also allowed visualisation of different regions of differentiated spheroids **(Figure 4.8).** The centre of the spheroids appeared to be fairly disordered with few visible lipid droplets **(Figure 4.8A)** with small lipid droplets appearing as the images move towards the outer surface of the spheroid **(Figure 4.8B)**. The lipid droplets gradually get bigger **(Figure 4.8C)** and eventually reach their largest size on the spheroid periphery **(Figure 4.8D).** Considering these spheroids are generated from a single cell type, these differences in cell phenotype based on location within the spheroid will require further investigation.

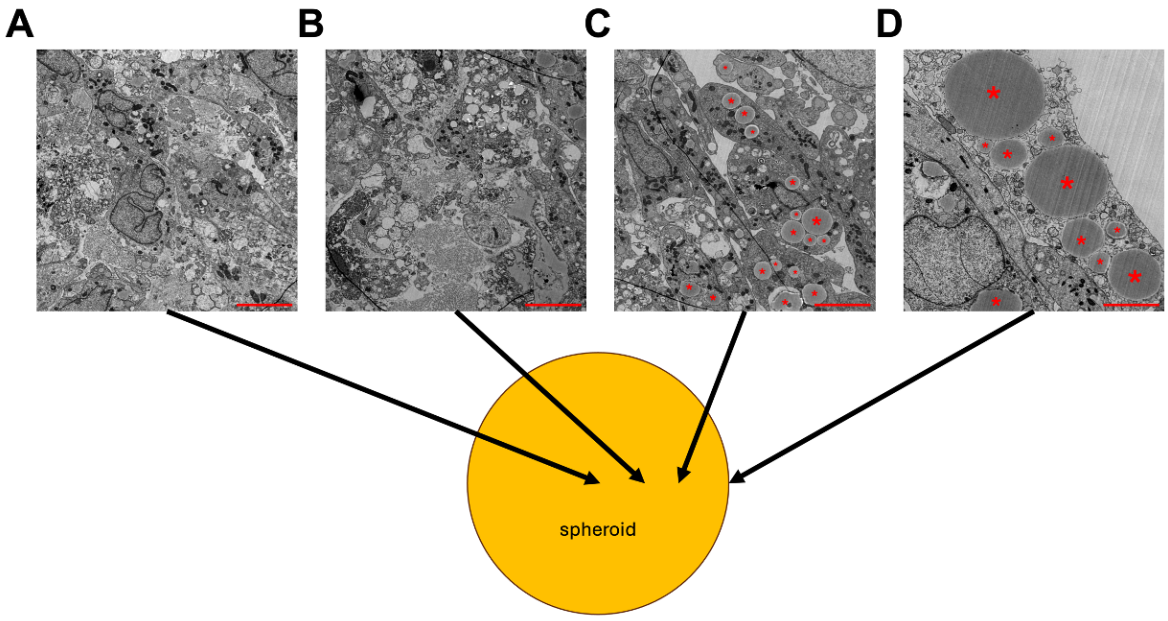

Figure 4.8 – TEM imaging at different regions of differentiated SGBS spheroids shows larger lipid droplets at spheroid periphery. Differentiated SGBS spheroids were processed and sectioned for TEM. Images were taken at x1500 magnification from regions moving from the centre **(A)** to the periphery **(D)** of the section, with arrows showing the approximate locations of image collection relative to a full spheroid section. Lipid droplets are indicated by red *. Scale bar = 5 µm.

4.4.4 Histological sectioning of spheroids

In order to better assess the internal structures of SGBS spheroids, a histological sectioning protocol would be useful to facilitate techniques such as immunohistochemistry. After significant optimisation, a traditional dehydration and paraffin-embedded sectioning protocol was developed, and sections were stained with Haematoxylin & Eosin (H&E) to visualise differentiation **(Figure 4.9).** Although the apparent presence of lipid droplets can be visualised in the later timepoints (indicated by arrows) **(Figure 4.9D-E)**, as the lipid itself is removed during sample processing, these are the spaces where the lipid would have been, and I hypothesised this was affecting the structural integrity of well-differentiated spheroids. Additionally, very few sections were obtained per block as the spheroids were difficult to see and therefore isolate on the slides. It was therefore not possible to determine where in the spheroid a section was from, which limited the usefulness of this approach.

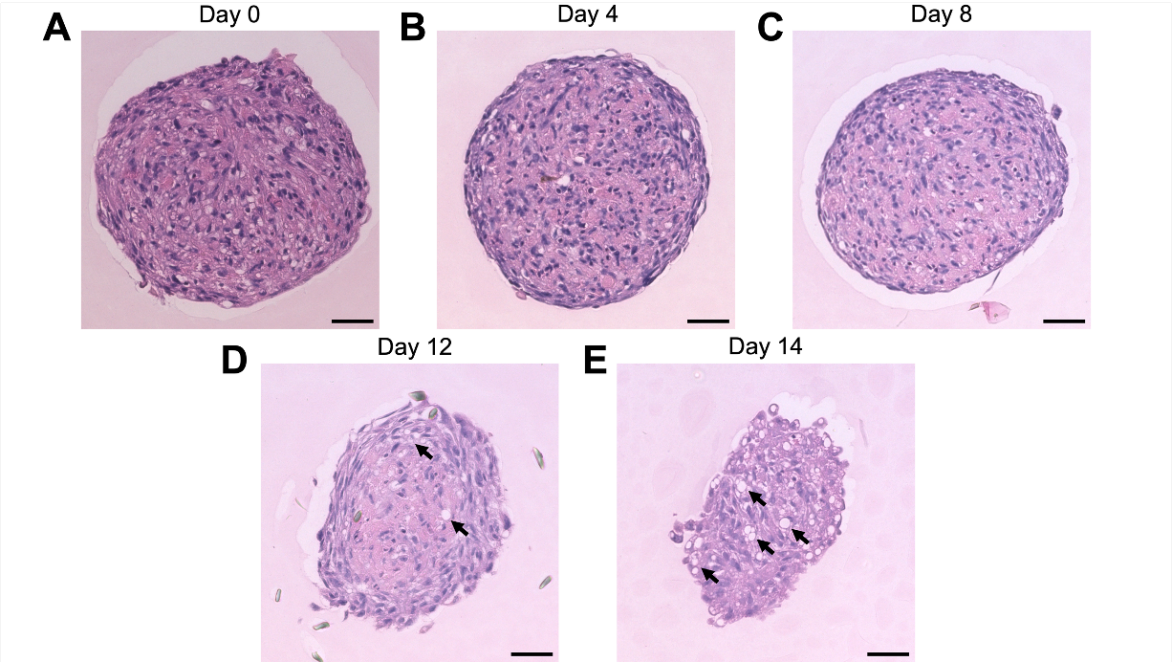

Figure 4.9 - Histological sections of SGBS spheroids throughout differentiation. SGBS spheroids were fixed at the indicated day of differentiation, embedded in paraffin and sectioned. Resulting sections were stained using Haematoxylin & Eosin (H&E) and imaged. Arrows indicate apparent presence of lipid droplets, visible as white spaces within the stained cell cytoplasm. Scale bar = 50 µm.

Cryosectioning – where fixed samples are snap-frozen in liquid nitrogen and sectioned – was investigated as an alternative to paraffin sectioning, as this technique allows lipid droplets to remain in the samples and therefore may better preserve the integrity of the differentiated spheroids. Using the cryostat, sequential sections were able to be isolated and imaged, allowing the relative position of a section within the spheroid to be inferred **(Figure 4.10).** These images again highlight the asymmetry of some differentiated spheroids, as well as the increased presence of lipid droplets appearing as lighter coloured 'bubbles' within the stained cytoplasm of cells around the spheroid periphery.

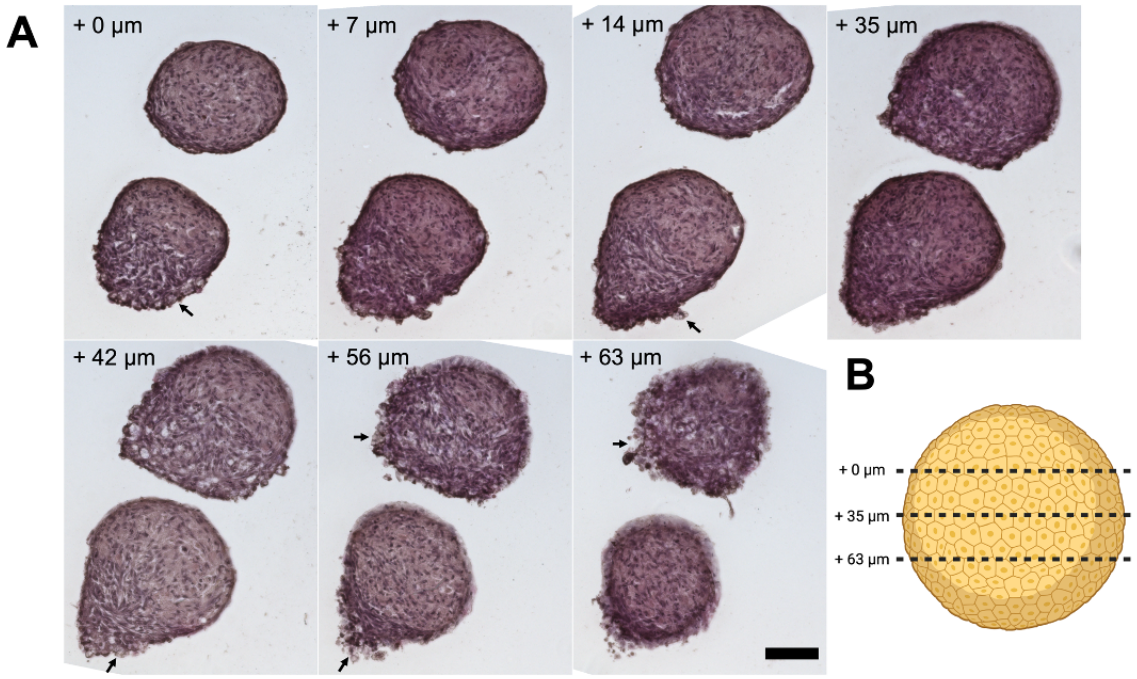

Figure 4.10 - Sequential cryosections of differentiated SGBS spheroids demonstrate asymmetric morphology and presence of lipid droplets. A) Differentiated SGBS spheroids were fixed, cryosectioned at 7 µm and sequential sections stained with H&E. Representative spheroids shown through the sequential sections, with distance from the first panel indicated. Arrows indicate apparent presence of lipid droplets, visible as lighter coloured 'bubbles' within the darker stained cell cytoplasm. Scale bar = 100 µm. **B)** Schematic showing approximate anticipated location of sections from an intact spheroid.

Overall, a series of imaging approaches have been developed to assess the morphology and phenotype of SGBS spheroids throughout differentiation. Each method is best suited to different purposes; however, all show the presence of lipid droplets in differentiated spheroids which are absent in undifferentiated spheroids. Together, these imaging approaches highlight that cells around the periphery of the spheroids appear to accumulate larger lipid droplets than the cells within the spheroid core, and that spheroids appear to differentiate asymmetrically, with more lipid droplets at one side of the spheroid than the other.

4.5 Changes in adipogenic gene and protein expression patterns can be measured in SGBS spheroids

4.5.1 SGBS spheroids undergo significant changes in gene expression during differentiation

To assess changes in gene expression across SGBS spheroid differentiation, RNA was isolated from pools of spheroids at different stages of differentiation – days 0, 4, 8, 12 and 14 – and expression of selected adipogenic markers was measured using RT-qPCR. C_T values were analysed using the $2^{-\Delta\Delta CT}$ method to show expression fold change relative to the day 0 sample using Sp1 as the housekeeping control **(Figure 4.11)**, with raw C_T values used to compare the relative expression levels of genes **(Table 4.2)**.

Several adipogenic markers are significantly upregulated during differentiation, with the key transcriptional regulator PPARG the first to be significantly upregulated after only 4 days **(Figure 4.11A)** alongside fatty acid binding protein 4 (FABP4) **(Figure 4.11B).** Next to be upregulated are the long chain fatty acid receptor FFA4 **(Figure 4.11C)**, the enzymes hormone-sensitive lipase (HSL) **(Figure 4.11D)** and lipoprotein lipase (LPL) **(Figure 4.11E)** and the adipokine adiponectin **(Figure 4.11F)**, where a significant increase is measured after 8 days (except FFA4 where the trend is not significant until day 12). Notably, the expression of FABP4, FFA4 and HSL **(Figure 4.11B-D)** appear to decrease between day 12 and 14, whereas expression of LPL and adiponectin **(Figure 4.11E-F)** continues to increase across the same time period, although these trends were not significant. Expression of the brown adipocyte marker uncoupling protein 1 (UCP1) was not reliably detected in differentiated or undifferentiated spheroids, with high C_T values >37 obtained for both.

Expression of the $ß_2$-adrenoceptor (ADRB2) is not significantly upregulated during differentiation **(Figure 4.11G)**, whereas the adipocyte-specific $ß_3$-adrenoceptor (ADRB3) appears to increase in expression during adipogenesis, although this was not significant **(Figure 4.11H).** However, the relative expression level of ADRB2 may be higher than ADRB3 throughout differentiation as indicated by the lower raw C_T values **(Table 4.2)**.

KRT19, the gene encoding cytoskeletal protein keratin 19, is significantly downregulated during differentiation **(Figure 4.11I)**, highlighting the transition of SGBS cells from a fibrobrast-like to adipocyte phenotype. Additionally, there is a significant upregulation of the GLUT4 insulin regulated glucose transporter coupled with a downregulation in the constitutively open GLUT1 transporter **(Figure 4.11J-K),** which may suggest a shift to an insulin-sensitive phenotype.

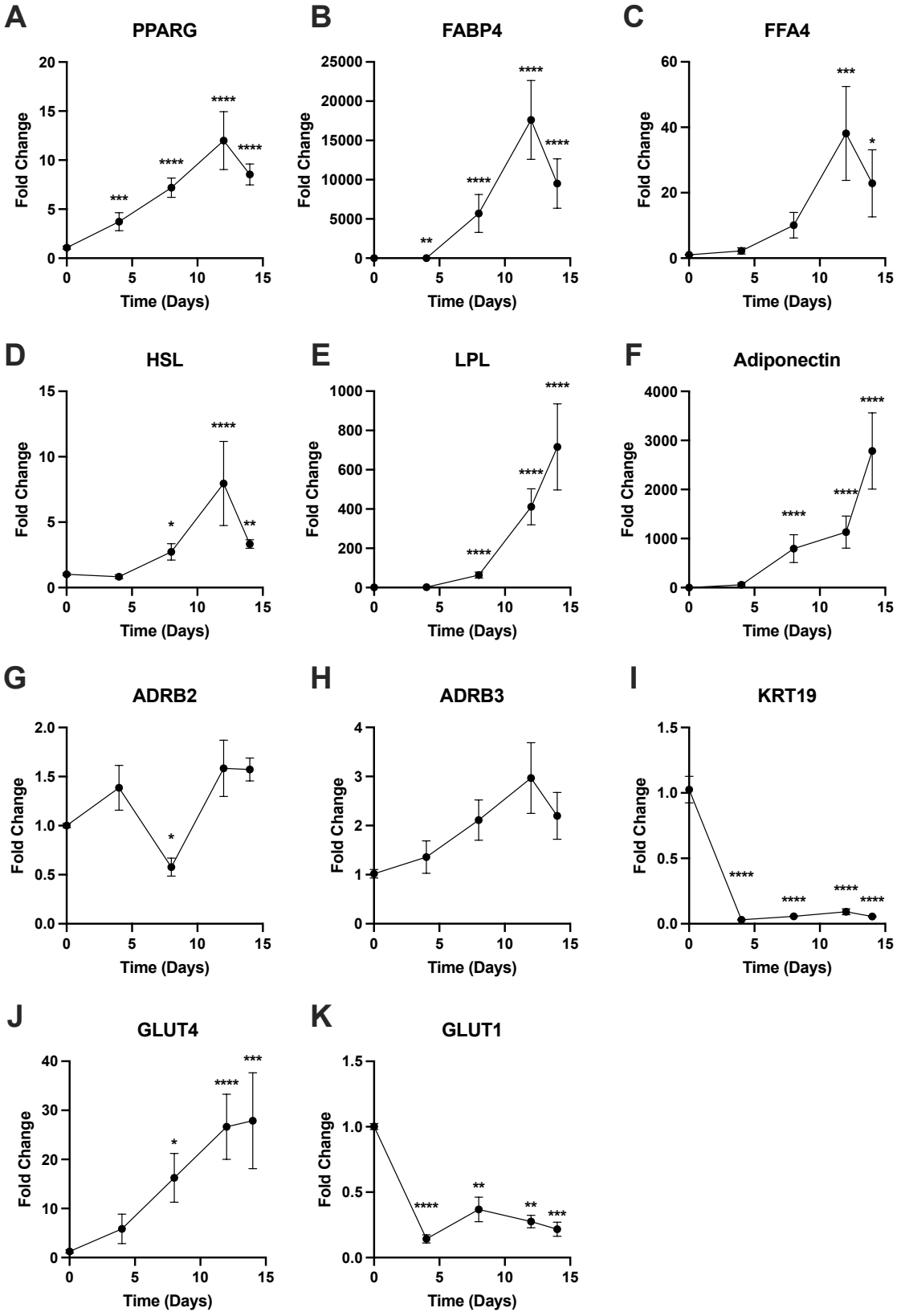

Figure 4.11 – Gene expression in SGBS spheroid changes during differentiation. RNA was isolated from spheroids at the indicated day of differentiation and RT-qPCR completed using primers for the indicated gene. C_T values were analysed using the $2^{-\Delta\Delta CT}$ method to show expression fold change relative to RNA isolated from day 0 cells, using primers for Sp1 as housekeeping control. Data are presented as mean ± SEM from N=3-5 independent experiments with n=2 technical replicates. Statistical comparisons are given to day 0 sample using lognormal one-way ANOVA with Dunnett's multiple comparisons test. *p < 0.05, **p < 0.01, ***p < 0.001, ****p < 0.0001.

Table 4.2 - Raw C_T values from qPCR experiments showing relative expression levels of genes. Heat map indicates magnitude of values where green indicates high expression and red indicates low expression. Presented as mean ± SEM of N=3-5 independent experiments with n=2 technical replicates.

Gene	Mean C_T ± SEM	
	Day 0	Day 14
PPARG	22.29 ± 0.28	20.16 ± 0.33
Adiponectin	27.47 ± 1.32	18.43 ± 0.86
FABP4	30.85 ± 0.57	19.5 ± 0.43
FFA4	24.05 ± 1.18	21.63 ± 0.43
HSL	31.68 ± 0.15	30.43 ± 0.36
LPL	27.78 ± 0.78	19.18 ± 0.71
ADRB2	26.74 ± 0.13	27.22 ± 0.36
ADRB3	32.62 ± 0.18	32.78 ± 0.40
KRT19	23.02 ± 0.15	27.66 ± 0.38
GLUT4	25.99 ± 0.23	23.43 ± 0.86
GLUT1	19.27 ± 0.17	22.88 ± 0.39
PLIN1	34.33 ± 0.54	19.85 ± 0.24
UCP1	37.68 ± 2.24	37.53 ± 1.34

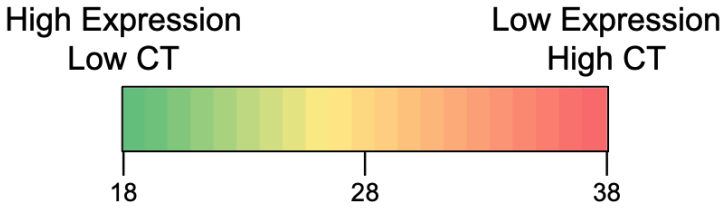

Overall, these qPCR data indicate that the gene expression of SGBS spheroids significantly changes during differentiation at the transcriptional level, with upregulation of classical adipogenic markers including PPARG, FABP4 and GLUT4 coupled with downregulation of fibroblast-like markers KRT19 and GLUT1.

4.5.2 Immunocytochemistry (ICC) shows changes in gene expression translate to protein level

Next, I investigated whether the changes in gene expression at the mRNA level translate to changes at the protein level. Perilipin 1 is a protein which coats the surface of lipid droplets and is involved in the regulation of lipolysis. In basal or fed conditions, perilipin 1 prevents lipase enzymes from accessing lipid droplets,

but in stimulated or fasted conditions, perilipin 1 is phosphorylated by PKA, allowing lipolysis to occur (Sztalryd and Brasaemle, 2017; Desgrouas et al., 2024).

In qPCR experiments, perilipin 1 is highly upregulated during differentiation **(Figure 4.12A)**. To compare whether this upregulation also occurs at the protein level, immunocytochemistry (ICC) was used to assess perilipin 1 protein expression. Differentiated or undifferentiated intact SGBS spheroids were fixed, permeabilised and stained with DAPI (nuclei, cyan) and antibody against perilipin 1 (magenta) and images taken of the surface of the spheroid using a confocal microscope **(Figure 4.12B)**.

Although some background staining is observed in the undifferentiated sample, there is a clear increase in specific staining observed in the differentiated sample. Perilipin 1 appears to be present in the cytoplasm of cell and around the outside of anticipated lipid droplets which appear as dark regions with no nuclear or perilipin 1 staining, indicated by the white arrows in the inset image **(Figure 4.12B)**. Use of a co-stain which directly labels lipid droplets such as BODIPY or LipidSpot **(Figure 4.5)** would help to confirm this finding.

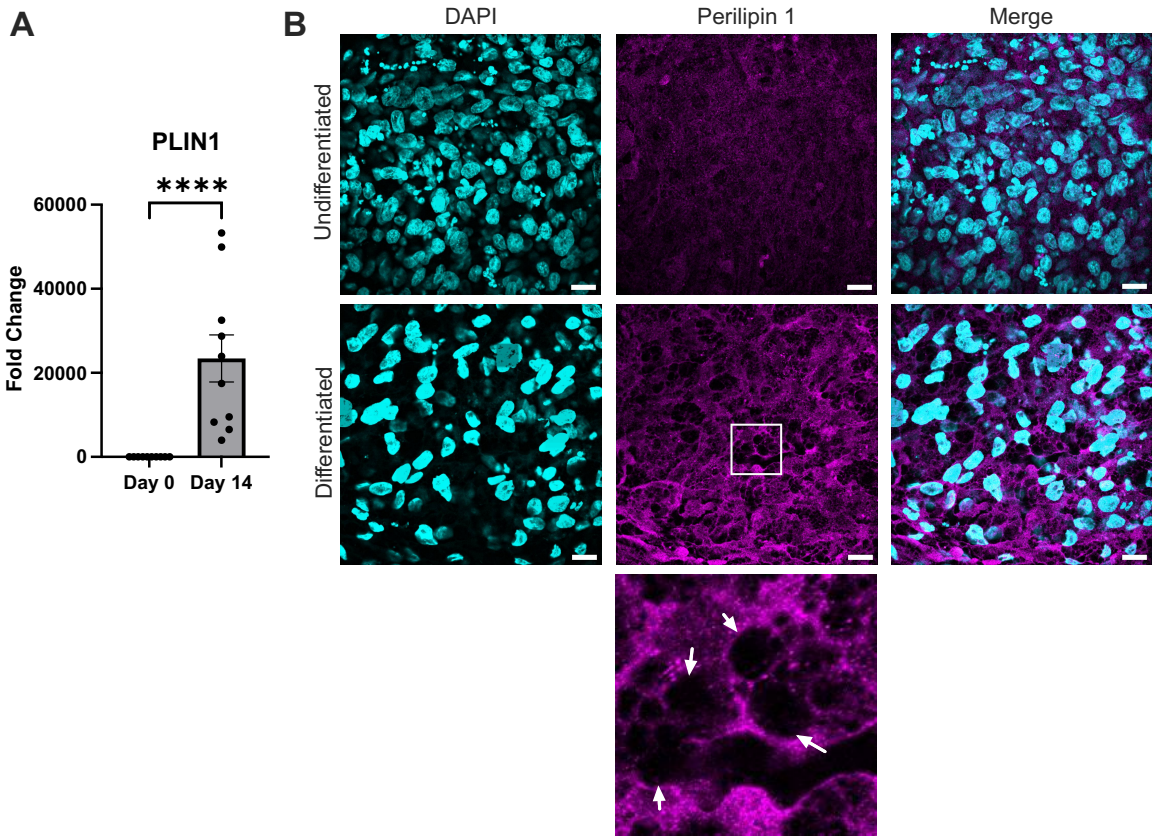

Figure 4.12 - Perilipin 1 is expressed at the gene and protein level in differentiated SGBS spheroids. A) Gene expression analysis of Perilpin 1 in SGBS spheroids before and after differentiation, determined by RT-qPCR. C_T values were analysed using the $2^{-\Delta\Delta CT}$ method to show expression fold change relative to RNA isolated from day 0 cells, using primers for Sp1 as housekeeping control. Data is presented as mean ± SEM from N=5 independent experiments with n=2 technical replicates. Statistical comparison was made using a lognormal t test, $p < 0.0001$. **B)** Undifferentiated or differentiated SGBS spheroids were fixed and expression of Perilipin 1 assessed using immunocytochemistry (ICC). Fixed spheroids were permeabilised and stained with DAPI (blue, nuclei) and anti-perilipin 1 antibody (magenta). Inset shows indicated region at higher magnification to show dark circles expected to be the location of lipid droplets, highlighted by white arrows. Scale bar = 20 µm.

Thus, there is evidence that the upregulation of adipogenic markers at the transcription level observed using qPCR is translated to the protein level. However, due to challenges with staining and imaging intact spheroids, ICC can only be used to visualise proteins expressed on the surface of the spheroids and additional approaches are needed to look at proteins in the spheroid core.

4.5.3 Immunohistochemistry (IHC) can be used to visualise protein expression in the centre of spheroids

To investigate protein expression in the centre of SGBS spheroids, differentiated or undifferentiated spheroids were fixed, cryosectioned and stained using immunohistochemistry (IHC) with primary antibody against the protein of interest and secondary antibody conjugated to horseradish peroxidase (HRP) enzyme which converts the 3,3'-diaminobenzidine (DAB) with nickel substrate to

a dark brown precipitate. Sequential sections were taken, with presented images taken towards the centre of the spheroid. Control conditions using differentiated spheroid sections were also prepared to assess non-specific staining with either an IgG control instead of primary antibody or secondary antibody only. Stained sections were counterstained with haematoxylin to identify cell nuclei in blue.

FABP4 was shown to be highly expressed in differentiated spheroids but absent in undifferentiated samples **(Figure 4.13)**. The staining is darkest around the spheroid periphery and close to cells where lipid droplets are visible as light-coloured circles (highlighted by arrows in inset), but is lighter towards the centre of the spheroid **(Figure 4.13A)**. An asymmetric distribution is again observed, with more differentiated cells and FABP4 staining on one side of the spheroid. No staining is observed in the undifferentiated **(Figure 4.13B)** or non-specific control samples **(Figure 4.13C-D)**.

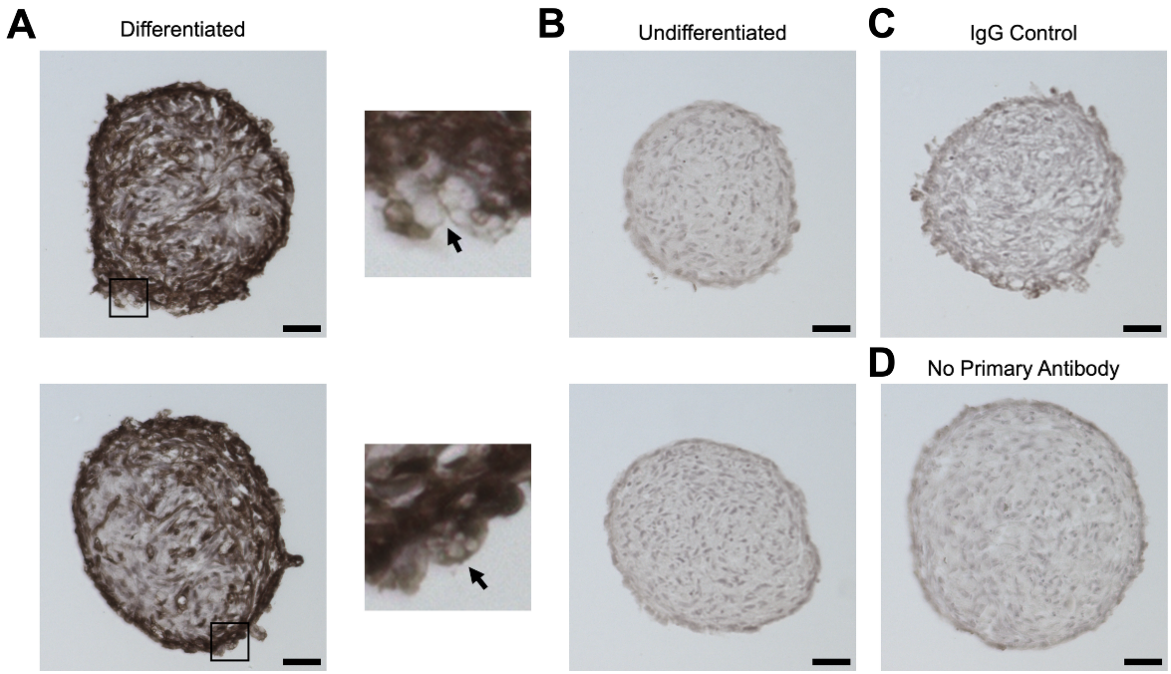

Figure 4.13 - FABP4 is highly expressed in differentiated SGBS spheroids. Differentiated **(A, C-D)** or undifferentiated **(B)** spheroids were fixed, cryosectioned at 7 µm and expression of FABP4 assessed using immunohistochemistry (IHC). Sections were probed using a rabbit primary antibody for FABP4 **(A-B)**, IgG control **(C)** or buffer only **(D)** and secondary anti-sera conjugated with HRP, with positive staining appearing as the dark brown precipitate of DAB/Ni substrate in the differentiated sample. Sections were counterstained with haematoxylin (nuclei, blue). Sequential sections were taken and stained with presented images taken from approximately the centre of spheroids. Insets show presence of lipid droplets as light-coloured circles, highlighted by arrows. Scale bar = 50 µm.

To test the hypothesis that the spheroids may be hypoxic in the centre, IHC was also used to assess the expression of hypoxia inducible factor 1 alpha (HIF-1α) in

differentiated and undifferentiated samples **(Figure 4.14)**. Again, sequential sections were taken and stained, with presented sections taken from towards the centre of the spheroid. No specific HIF-1α staining was observed anywhere within either the differentiated or undifferentiated sections **(Figure 4.14)**. However, the lack of positive control for HIF-1α staining in this experiment limits further interpretation, and a comparison to spheroids grown in low oxygen conditions is needed to confirm if this is result is due to no hypoxia or simply due to poor staining.

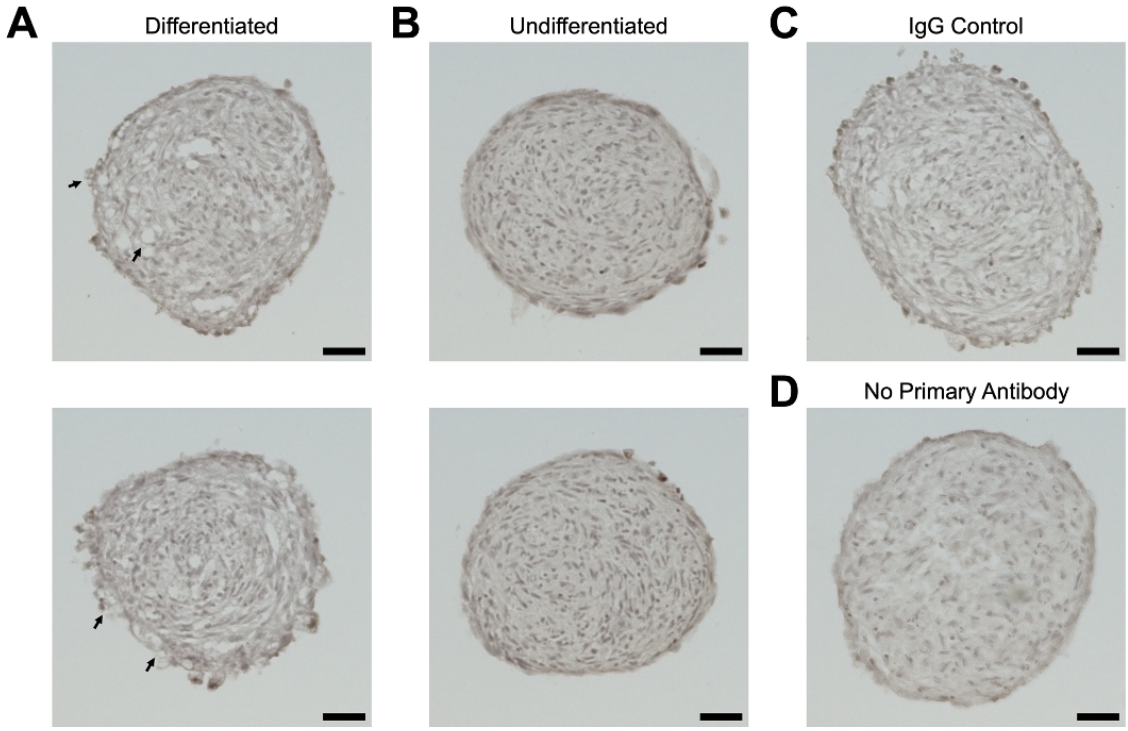

Figure 4.14 – HIF-1α is not detected in SGBS spheroids. Differentiated **(A, C-D)** or undifferentiated **(B)** spheroids were fixed, cryosectioned at 7 µm and expression of HIF1α assessed using immunohistochemistry (IHC). Sections were probed using a rabbit primary antibody for HIF-1α **(A-B)**, IgG control **(C)** or buffer only **(D)** and secondary anti-sera conjugated with HRP. Sections were counterstained with haematoxylin (nuclei, blue). Sequential sections were taken and stained, with presented images taken from approximately the centre of spheroids. Arrows indicate presence of lipid droplets. Scale bar = 50 µm.

Thus, IHC can be used to identify protein expression at different locations within the spheroids. Here, it has been shown that FABP4 is highly expressed within the differentiated cells present around the spheroid periphery but broadly absent in the spheroid centre and in undifferentiated spheroids. No evidence of HIF-1α expression was observed in differentiated or undifferentiated SGBS spheroids.

Together, these data demonstrate that differentiated SGBS spheroids upregulate key adipogenic markers at both gene and protein level. However, it appears that differentiation is not uniform throughout the spheroid, with cells on one side of

the spheroid expressing higher levels of FABP4 than the other, and cells around the spheroid periphery more highly differentiated than the cells towards the centre.

4.6 Changes in the mechanical properties of SGBS spheroids can be measured using nanoindentation

One advantage of spheroid models is that the cellular microenvironment better recapitulates the complexity *in vivo*, with cells maintaining the ability to interact with neighbouring cells and the ECM. This therefore means the mechanical and biophysical properties of spheroids may more closely resemble *in vivo* tissue compared to 2D cells grown on a stiff plastic surface (Baker and Chen, 2012).

The biophysical properties of differentiated or undifferentiated spheroids were investigated using nanoindentation (Ciccone et al., 2022), where the spheroids are positioned and pressed with the nanoindenter probe **(Figure 4.15A)**. The resulting deformation of the cantilever probe can be used to calculate the Young's Modulus *(E)* as a measure of spheroid stiffness. It was found that the stiffness of spheroids significantly increased during differentiation, from 0.68 kPa in undifferentiated spheroids to 1.01 kPa in differentiated spheroids **(Figure 4.15B)**.

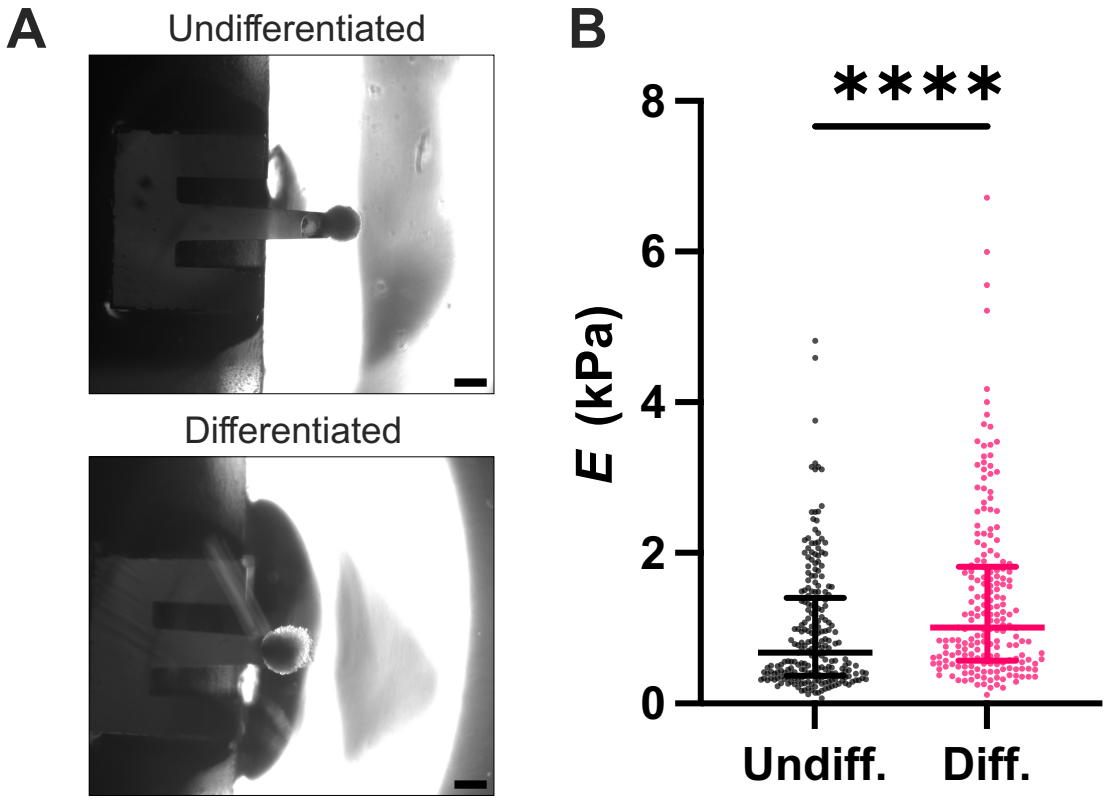

Figure 4.15 - Differentiated SGBS spheroids have higher stiffness than undifferentiated control. A) Representative images showing nanoindentation setup with undifferentiated (top) or differentiated (bottom) spheroid positioned underneath the nanoindenter cantilever probe. Scale

bar = 250 µm. **B)** Young's modulus determined by nanoindentation of undifferentiated and differentiated SGBS spheroids. Data is presented as median ± interquartile range from 195-225 individual measurements taken from 5 spheroids across two separate occasions. Statistical comparison was made using non-parametric Mann-Whitney test, $p < 0.0001$.

This demonstrates the possibility to use advanced biophysical techniques to measure the material properties of spheroids and indicates that lipid accumulation during adipogenesis increases the stiffness of SGBS spheroids.

4.7 Differentiated SGBS spheroids undergo lipolysis and glucose uptake

Next, it was critical to establish whether differentiated SGBS spheroids can function as adipocytes. To do this, assays were established to measure lipolysis and glucose uptake as examples of characteristic adipocyte function.

4.7.1 Differentiated SGBS spheroids undergo lipolysis in response to stimulation

Lipolysis is the metabolic process by which stored triglycerides are hydrolysed to glycerol and fatty acids. It is commonly measured *in vitro* by measuring the quantities of fatty acids or glycerol released by adipocytes in the basal or stimulated states (Schweiger et al., 2014).

Firstly, the Free Glycerol colorimetric reagent (Sigma) was used to quantify glycerol released by a pool of 20 spheroids in HBSS containing 1% Bovine Serum Albumin (BSA) to accept the released fatty acids and prevent their reuptake. After 10 minutes in buffer, a sample was removed and replaced with vehicle control or either the ß-adrenoceptor agonist isoprenaline or the adenyl cyclase activator forskolin, which are commonly used to stimulate lipolysis (Allen, 1985). Samples were taken at two-hour intervals and quantified using Free Glycerol reagent **(Figure 4.16)**.

At the baseline measurement, significantly more glycerol was released from the differentiated than undifferentiated spheroids, indicating a higher level of basal or unstimulated lipolysis **(Figure 4.16A)**. Furthermore, a measurable increase in glycerol released is observed in the differentiated spheroids in response to isoprenaline and forskolin, although only the forskolin response was statistically significant compared to vehicle control at the same time point **(Figure 4.16B)**. Additionally, this response occurs across a long incubation time, and requires many spheroids per sample with a large sample volume per measurement which limits throughput.

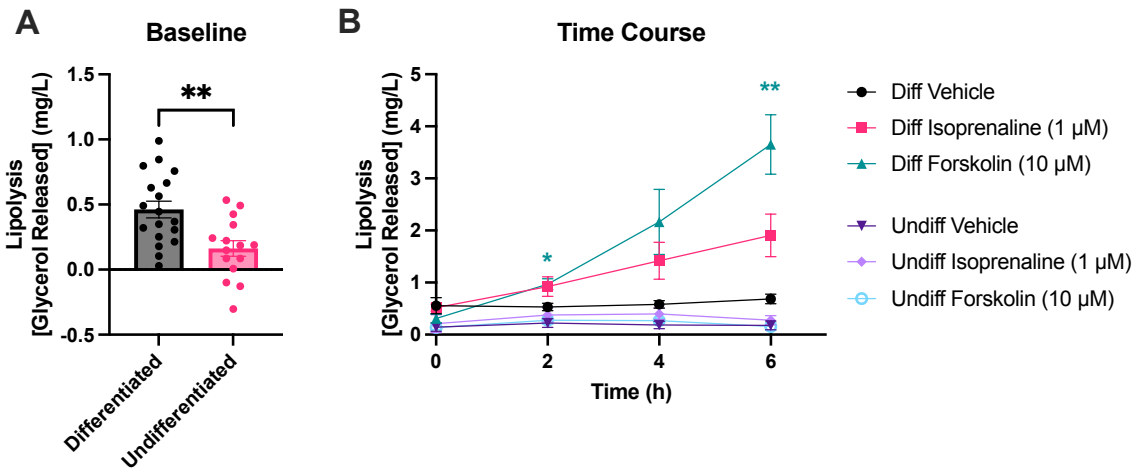

Figure 4.16 - Differentiated SGBS spheroids undergo lipolysis in response to stimulation. Differentiated or undifferentiated SGBS spheroids were pooled in HBSS + 1% BSA. After 10 minutes, a sample of buffer was removed (time 0) and replaced with 1 µM isoprenaline, 10 µM forskolin or vehicle control. Buffer samples were removed at two-hour intervals and released glycerol quantified using colorimetric Free Glycerol reagent. **A)** Glycerol released by differentiated or undifferentiated SGBS spheroids at time 0 showing baseline unstimulated lipolysis. Statistical comparison was made using an unpaired t test, **p < 0.01. **B)** Glycerol released by differentiated or undifferentiated SGBS spheroids in response to stimulation. Data presented as mean ± SEM from N=6 pools of 20 spheroids across 3 independent experiments with n=2 technical replicates. Statistical comparisons were made using repeated measures two-way ANOVA with Geisser-Greenhouse correction and Dunnett's multiple comparisons test. *p < 0.05, **p < 0.01 compared to Diff Vehicle response at each time point.

To overcome these obstacles, the Glycerol-Glo reagent (Promega) was identified as an alternative approach to quantify glycerol release. This kit is reported to be more sensitive and requires less sample volume than the Free Glycerol reagent, with the luminescent readout providing a linear detection range of 1-80 µM and sample volume of 5 µL, compared to 10-200 µM and 50 µL respectively with the Free Glycerol reagent.

To compare these reagents, the experiment in **Figure 4.16** was repeated with glycerol quantified from spheroid supernatant using both Free Glycerol and Glycerol-Glo reagents in parallel **(Figure 4.17)**. A significant increase in glycerol release can be measured after 4 hours following stimulation with 1 µM isoprenaline or 10 µM forskolin, with the trends observed appearing consistent between both kits **(Figure 4.17).** However, despite these measurements being taken from the same spheroid supernatant samples, the concentrations of glycerol measured appear higher with the Glycerol-Glo reagent compared to the Free Glycerol kit, perhaps indicating the sensitivity and detection range of the Glycerol-Glo reagent is better suited to this assay. This, combined with the fact that the smaller sample volumes required for the Glycerol-Glo kit can allow for a

more concentrated sample and therefore fewer required spheroids, meant that this kit was chosen as the preferred assay format for future studies.

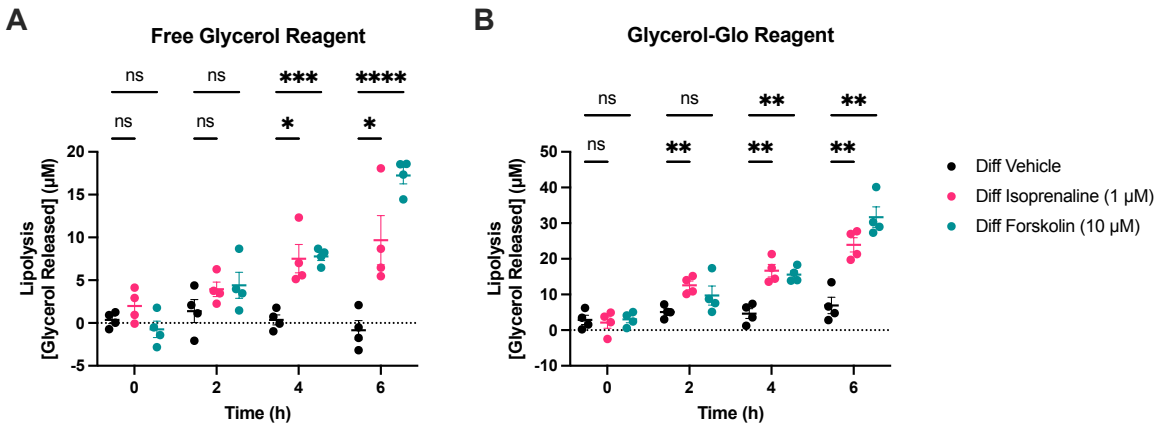

Figure 4.17 - Glycerol-Glo reagent allows more sensitive measurements of lipolysis. Experiment completed as Figure 4.16 with glycerol in supernatant quantified using both Free Glycerol **(A)** and Glycerol-Glo **(B)** reagents. Data presented as individual measurements with mean ± SEM indicated, from N=4 pools of 20 spheroids across 2 independent experiments with n=2 technical replicates. Statistical comparisons were made to vehicle using a repeated measures two-way ANOVA with Geisser-Greenhouse correction and Dunnett's multiple comparisons test. *p < 0.05, **p < 0.01, ***p < 0.001, ****p < 0.0001.

Thus, an assay has been developed to measure lipolysis in adipocyte spheroids and has been used to show that differentiated SGBS spheroids have higher basal lipolysis than undifferentiated spheroids and can increase lipolysis in response to isoprenaline and forskolin stimulation.

4.7.2 Differentiated SGBS spheroids undergo insulin-stimulated glucose uptake

Glucose uptake is a commonly used measurement of adipocyte function as it is a critical component of energy homeostasis in adipose tissue (Rosen and Spiegelman, 2006; Shi and Kandror, 2008). Typically, glucose uptake is measured using radiolabelled 2-deoxyglucose (2DG), however increasingly groups are transitioning to non-radioactive colorimetric, fluorescent or luminescent alternatives (Yamamoto et al., 2015). The Glucose Uptake-Glo assay (Promega) uses a bioluminescent detection reagent to quantify glucose uptake. Briefly, 2DG is added and taken up by cells where it is converted to 2-deoxyglucose-6-phosphate (2DG6P). The detection reagent contains glucose-6-phosphate dehydrogenase (G6PDH) which oxidises 2DG6P to 6-phosphodeoxygluconate (6PDG) while reducing NADP+ to NADPH, ultimately used by the Ultra-Glo Recombinant Luciferase to generate light.

Although this is a kit-based assay, no optimised protocol yet exists using the Glucose Uptake-Glo kit to measure glucose uptake into adipocyte spheroids. In this assay, adipocytes are treated for 1 hour with insulin to stimulate translocation of GLUT4 glucose transporters from intracellular vesicles to the cell membrane. Stimulated cells are then incubated with 2DG for a short period of uptake at room temperature before cells are lysed to stop the reaction. In 2D adipocyte cultures, a 2DG incubation time of 10 mins at room temperature is recommended. I hypothesised that a longer incubation time may be necessary to improve reagent penetration into the spheroid and increase the assay window **(Figure 4.18)**. Pools of differentiated spheroids were incubated in the presence or absence of 1 μM insulin to assess insulin sensitivity of the spheroids. 40 μM cytochalasin B was included as a small molecule inhibitor of glucose transporters and act as a baseline control (Ebstensen and Plagemann, 1972).

In the assay, it was shown that addition of insulin resulted in a ~75% increase in glucose uptake, which was blocked by addition of cytochalasin B. An increase in luminescent signal was observed with increasing 2DG incubation time in both vehicle and insulin-treated conditions **(Figure 4.18A).** When each timepoint was expressed as a fold change to its respective vehicle, no change in the insulin response was visible between timepoints **(Figure 4.18B)**. A 2DG incubation time of 20 minutes was selected for future experiments.

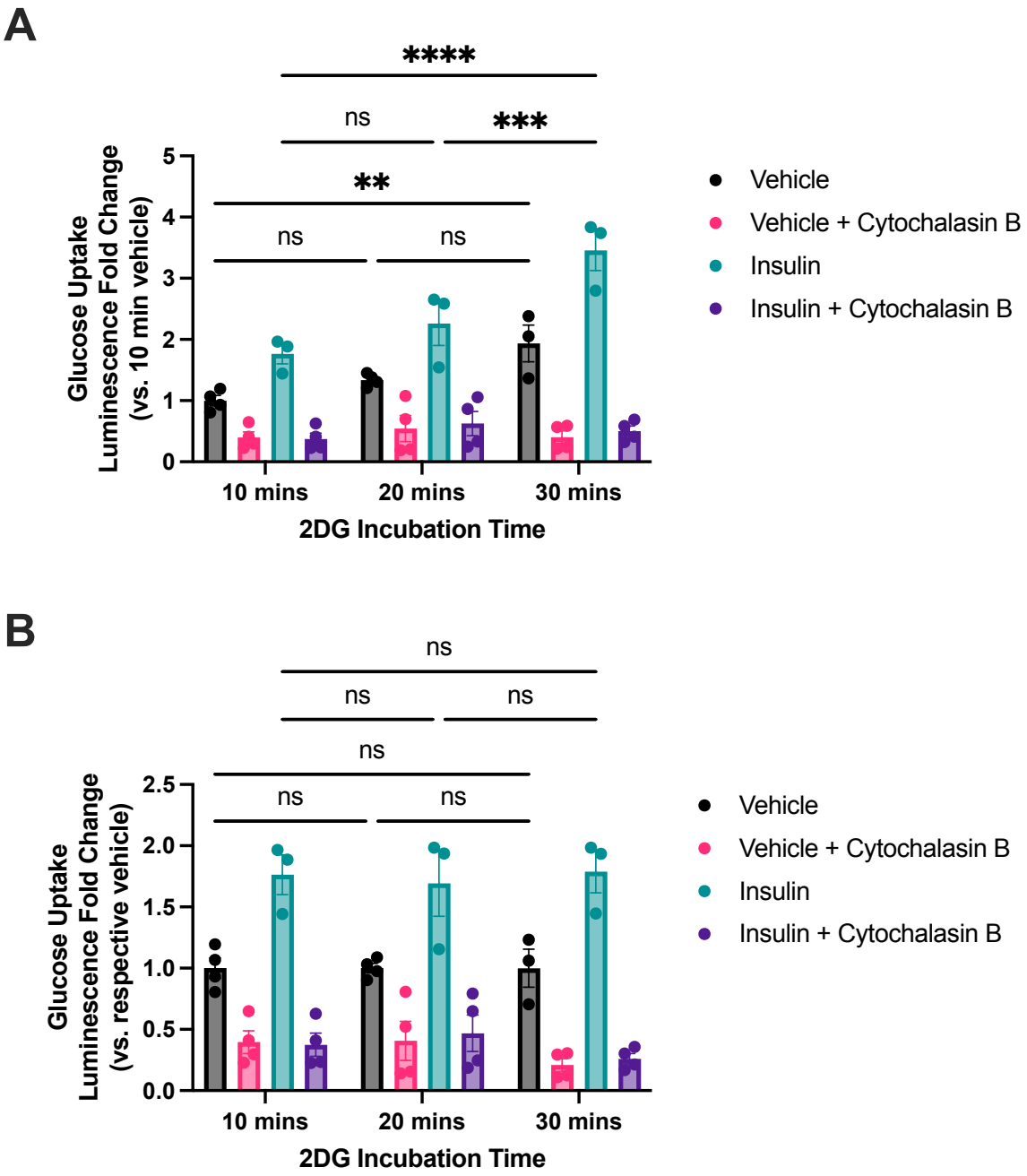

Figure 4.18 - 2DG incubation time does not affect baseline-corrected insulin-stimulated glucose uptake. Differentiated SGBS spheroids were pooled and treated with 1 µM insulin ± 40 µl cytochalasin B for one hour. 1 mM 2-deoxyglucose (2DG) was then added for the indicated time and glucose uptake quantified using the Glucose Uptake-Glo kit. Raw luminescence values were expressed as a fold change of the 10 mins vehicle **(A)** or as a fold change of each timepoint vehicle respectively **(B).** Data presented as mean ± SEM from N=4 pools of 8 spheroids across 2 independent experiments with n=2 technical replicates. Statistical comparisons were made using two-way ANOVA with Tukey's multiple comparisons test. **p < 0.01, ***p < 0.001.

Next, differentiated and undifferentiated spheroids were compared to determine whether insulin sensitivity develops during differentiation **(Figure 4.19)**. It was found that addition of insulin significantly increases (**p = 0.0011) glucose uptake by 83.1% in differentiated spheroids but has no effect in undifferentiated spheroids. In both differentiated and undifferentiated

spheroids, cytochalasin B significantly ($^{\#\#}p < 0.01$) inhibits the vehicle and insulin-stimulated responses **(Figure 4.19)**.

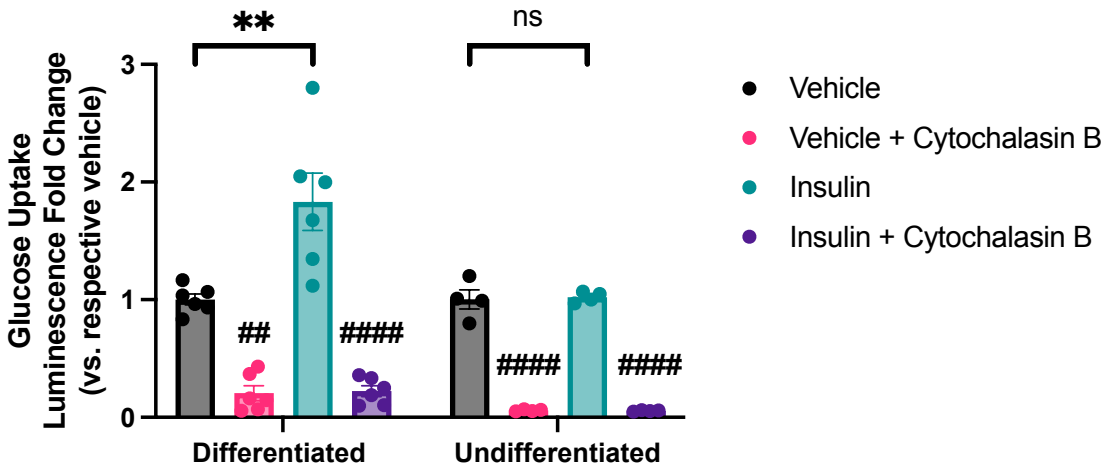

Figure 4.19 - Differentiated SGBS spheroids uptake glucose in response to insulin. Differentiated or undifferentiated SGBS spheroids were pooled and treated with 1 µM insulin ± 40 µl cytochalasin B for one hour. 1 mM 2DG was then added for 20 minutes and glucose uptake quantified using the Glucose Uptake-Glo kit. Raw luminescence values were expressed as a fold change of the respective vehicle. Data presented as mean ± SEM from N=4-6 pools of 8 spheroids across 3 independent experiments with n=2 technical replicates. Statistical comparisons were made using one-way ANOVA with Tukey's multiple comparisons test. **p < 0.01 (± insulin), $^{\#\#}p < 0.01$, $^{\#\#\#\#}p < 0.0001$ (± cytochalasin B).

I have therefore established a non-radioactive assay to assess glucose uptake in adipocyte spheroids and demonstrate that differentiated SGBS spheroids can increase glucose uptake in response to insulin.

Taken together, these data show that the function of SGBS spheroids can be determined in plate-based assays, and highlight that differentiated SGBS spheroids display characteristic adipocyte functions including ß-adrenoceptor-stimulated lipolysis and insulin-stimulated glucose uptake.

4.8 Discussion

In this chapter, I have developed and characterised a 3D *in vitro* adipocyte spheroid model using SGBS cells. I have optimised and validated several approaches to assess the appearance, expression profiles and function of these spheroids and have determined that differentiated SGBS spheroids accumulate lipid droplets, express adipogenic gene and protein markers, and show characteristic adipocyte functions including increased lipolysis in response to treatment with a ß-adrenoceptor agonist, and increased glucose uptake following insulin stimulation.

An initial aim of this project was to generate a completely animal-free spheroid system using human-derived SGBS cells rather than murine-derived 3T3-L1 cells, and replacing all animal-derived reagents with human-derived or synthetic alternatives to align with the Animal Free Research UK guidelines (Animal Free Research UK, 2021). This would therefore improve the human relevance and translational validity of this work by removing any effect of xenogeneic serum components on cell behaviour and physiology while also reducing the ethical concerns associated with use of animal-derived reagents (Nessar et al., 2025; Weber et al., 2025). Critically, as serum is an extremely complex mixture comprising several classes of proteins, carbohydrates, and lipids (Lee et al., 2022, 2023) with well-documented batch-to-batch variation (van der Valk et al., 2018; Weber et al., 2025), scientific reproducibility and reliability is likely to be improved when using defined medium.

Although the SGBS differentiation protocol was chemically defined, attempts to replace FBS in the SGBS growth medium proved challenging. Direct replacement of FBS with HS resulted in much slower growth, and although supplemented HS and hPL showed promising results, the optimisation required was not feasible within this project.

Unlike other animal-derived resources such as trypsin or collagen which can be directly replaced with - albeit costly - recombinant alternatives, chemically defined medium cannot fully recapitulate the complexity of FBS. Alternative medium formulations therefore tend to be specific to individual cell types, where significant optimisation has resulted in an optimal, but not universal

formulation. Alternatives for commonly used cell types can be found using the FCS-free database (Fetal Calf Serum Free Database, n.d.), however the cost of these products continues to be prohibitively expensive for many and there is a lack of validated and established protocols for lesser used cell types. The identification of a 'universal' serum alternative such as hPL or earthworm heat-inactivated coelomic fluid may address some of the ethical concerns of using FBS, but does not fully alleviate the batch dependency and need for defined composition for some purposes such as cell therapy or cultured meat (Chelladurai et al., 2021). These complexities require significantly more consideration and investment than is possible within a sub-project of a PhD thesis.

SGBS cells have been used since their identification in the early 2000s as an *in vitro* model of human adipocytes (Tews et al., 2022). The cells are not commercially available and can be obtained only through Material Transfer Agreement (MTA) from the Wabitsch group. Consequently, the uptake of SGBS cells in the field has been limited, with approximately 200 results on PubMed for the search term "SGBS adipocytes" compared to >10,000 for "3T3-L1 adipocytes". Nevertheless, SGBS cells have been well characterised by groups seeking a human-derived adipocyte cell strain with well-known gene expression and metabolic activity profiles (Wabitsch et al., 2001; Fischer-Posovszky et al., 2008; Tews et al., 2022). However, there are few studies directly comparing SGBS cells to other adipocyte types. Often SGBS cells generate similar results to other human-derived cell types including hMADS, LipPD1 or primary hADSCs in *in vitro* studies (Kässner et al., 2020; Wu et al., 2021). Conversely, marked differences have been recorded between SGBS cells and 3T3-L1 cells. Several studies have reported differences in adipogenic gene expression between the cell types (Allott et al., 2012; Li et al., 2023a; Takahashi et al., 2024) as well as differences in gene regulatory motifs (Schmidt et al., 2011) and post-translational modifications (Aldehoff et al., 2024). Critically, in a comprehensive study at AstraZeneca, Rossi et al. described significant differences between these two cell types following chronic insulin exposure to model insulin resistance, with gene expression between the cell lines suggesting differential responses to hyperinsulinemia, and SGBS cells showing a only a modest ~25% reduction in glucose uptake compared the ~75% reduction observed for 3T3-L1

cells, highlighting that selection of cell type is vital in studies of metabolic disease (Rossi et al., 2020).

Although it is known SGBS cells have limited differentiation potential, it was previously reported that the cells retain their capacity for differentiation for over 50 generations (Wabitsch et al., 2001). Thus, the observation that the SGBS cells in our lab could only be differentiated up to passage 5 was surprising. This may be due to confusion in terminology; the SGBS cells we received from the Wabitsch group (P1) were reportedly ‘generation 30’, and if ‘generation’ refers to population doublings, then each 1:5 cell passage split would be equivalent to 5 generations and thus ‘passage 5’ would in fact exceed the previously reported 50 generation limit. As publications in the literature do not typically report passage or generation number, it is not possible to know whether this observation is consistent with others. However, the limited differentiation capacity is a substantial disadvantage of these cells; as they were isolated from a single patient over 20 years ago, there is a finite global supply of these cells.

A further challenge with SGBS adipocyte differentiation is the batch-to-batch variation observed. In 2D cultures, differentiation was variable. Some batches saw near 100% of cells successfully differentiate, whereas others had small patches of differentiated cells. In 2D, differentiation is easy to assess by observing lipid droplet accumulation using a light microscope and can be quantified using oil red O staining (Kaczmarek et al., 2024). In 3D, it is much more challenging to assess differentiation using a microscope, although it was usually possible to infer whether a batch had differentiated well or poorly based on the size of the whole spheroid and any lipid-laden cells around the periphery. This is largely consistent with findings from other 3D cultured adipocytes, which also report a gradual increase in spheroid size and volume throughout the differentiation process associated with accumulation of lipid droplets (Turner et al., 2017; Klingelhutz et al., 2018; Shen et al., 2021). Interestingly, differentiation of human preadipocytes from primary (Shen et al., 2021) or immortalised (Klingelhutz et al., 2018) sources appear to differentiate more successfully than the SGBS spheroids, with a greater number and apparent size of lipid droplets observed in H&E, SEM and confocal images, albeit following a longer differentiation period of 3-7 weeks compared to the 14 days used here for SGBS spheroids (Klingelhutz et al., 2018; Shen et al., 2021). It is therefore

possible that extending the differentiation period may improve the differentiation success of SGBS spheroids.

A reliable quantitative method to assess differentiation success would be invaluable as a quality control parameter for spheroid assays. Although oil red O staining was possible with spheroids, the low signal acquired means large numbers of spheroids must be used to generate a reliable response. An alternative method, perhaps using a fluorescent neutral lipid staining dye such as BODIPY, NileRed, or LipidSpot (Fam et al., 2018) should be investigated. These fluorescent dyes may offer several potential advantages over oil red O; firstly, oil red O has poor solubility requiring the use of isopropanol for staining, which can disrupt the native morphology of lipid droplets, whereas fluorescent dyes are soluble in standard buffers (Fukumoto and Fujimoto, 2002). Additionally, these fluorescent dyes typically result in more specific staining due to their solvatochromic properties, meaning that they specifically fluoresce when in an organic or lipid-rich environment (Gocze and Freeman, 1994; Fam et al., 2018). Thus, unbound dye should not contribute to background signal and does not need to be washed off as thoroughly. Several imaging pipelines exist to quantify the number and size of BODIPY-stained lipid droplets in 2D adipocytes (Adomshick et al., 2020), and it is therefore likely that versions of these pipelines can be adapted for use in spheroid Z-stacks or cryosectioned slices (Garcia et al., 2023).

In this chapter, a series of imaging approaches including confocal microscopy, electron microscopy and histology were used to visualise the morphology of SGBS spheroids and understand how this changes during differentiation. These methods were challenging and required significant optimisation largely due to the size of the spheroids. The light scattering properties of intact spheroids are a major limitation to imaging depth (Diosdi et al., 2021), meaning traditional light and confocal microscopy approaches used in 2D are not suitable. However, the individual spheroids are very small compared to typical tissue samples, meaning sectioning protocols were difficult.

Imaging adipocytes and adipose tissue is known to be challenging due to the high lipid content of the samples which has high autofluorescence and light scattering properties (Richardson and Lichtman, 2015; Lai et al., 2017; Willows et al.,

2021). Therefore, using laser scanning confocal microscopy of intact spheroids, it was only possible to image the outer layers of the spheroid and not the internal core. Light sheet microscopy is likely to provide an improved method of imaging for intact 3D structures (Stelzer and Smyrek, 2017; Lazzari et al., 2019). Alternatively, optimisation of sample processing and inclusion of tissue clearing protocols may improve the images obtained using laser scanning confocal microscopy (Martinez-Santibañez et al., 2014; Chi et al., 2018; Diosdi et al., 2021).

Histological sectioning of spheroids is a common technique in the literature (Olsen et al., 2014; Klingelhutz et al., 2018; Jackisch, 2019), however very few publications report detailed protocols, particularly for small numbers of spheroids. The protocols reported here have combined features of previous methods and included adaptations to optimise sectioning of adipocyte spheroids. Firstly, a large pool of around 50 spheroids is preferred for reliable sectioning. Additionally, a pre-staining step – where fixed spheroids are stained with haematoxylin before sample processing – is helpful to improve visibility of the spheroids through subsequent steps. I have typically found that this haematoxylin stain fades through the processing stages and re-staining is required to view the nuclei on the final slides. Protocols for both paraffin-embedded and cryosectioned samples have been optimised. While paraffin embedding is reported to better preserve the morphology of sections and allows long term storage, cryosections better preserve the expression of antigens for downstream IHC (Hira et al., 2019). Critically, the solvents used when preparing paraffin-embedded sections dissolve lipids, whereas lipid droplets will remain intact during cryopreservation, meaning specific lipid stains can only be used with cryosections (Martinez-Santibañez et al., 2014).

For paraffin-embedded samples, an additional processing step was necessary to embed stained spheroids within a 2% (w/v) agarose gel ‘cell block’ which was then processed and sectioned as a ‘tissue’ sample. This approach resulted in modest success; although sections were obtained, only a small number of cut sections contained spheroid samples, and it was not possible to determine whereabouts in the spheroid a section was originally from. This may be due to poor structural integrity of the samples resulting from the removal of lipid during processing, or poor adherence between the spheroids and agarose

allowing the spheroid samples to float out of the section. The latter may be rectified by further optimisation of the agarose embedding process though altering the material properties or composition of the gel (Jones and Calabresi, 2007) or embedding the spheroids before fixation in the gel (Jain et al., 2014; Saharti, 2024). The cryosectioned samples were typically more reliable and sequential sections were obtained. This may be due to the lipid droplets remaining *in situ*, helping to preserve the structural integrity of the sample. Therefore, the cryosectioning protocol presented here is recommended for further use with adipocyte spheroids.

There are many distinct features in the morphology of SGBS adipocyte spheroids which can be concluded through the combination of imaging approaches used. Firstly, the SEM and sectioning images revealed the spheroids have an asymmetric morphology, where spheroids appear to differentiate more at one side than the other. This behaviour appears to be unusual for 3D cultures grown in ULA plates, with irregular morphologies more commonly reported for spheroids embedded within hydrogels (De Hoogt et al., 2017) or for cell types with specific invasive or protrusive functions (Leggett et al., 2017). However, there are also examples of some cell types which naturally form more irregular spheroids (Sargenti et al., 2020; Kulesza et al., 2021), and a recent study highlighted that the specific ULA plate type can also significantly affect the morphology of spheroids (Vitacolonna et al., 2024). The asymmetric differentiation of SGBS spheroids remains unexplained, but may be due to how spheroids sit in the ULA plates; although the cells do not adhere to the plate, they are still affected by gravity and settle against the base of the U-bottom well, and it may be that the cells touching the plate differentiate differently to those on the opposite face. It has previously been reported that the depth of cell culture medium can affect differentiation of adipocytes, with medium height inversely correlating with lipid content (Sheng et al., 2013). Therefore, the region of the spheroid which is closer to the surface of the medium (thus experiencing a shallower medium depth) could potentially differentiate better than the opposite face. This may be particularly pronounced with the 384-well ULA plates used in this study as a relatively high number of cells are seeded into narrow wells. It may be that the asymmetric morphology develops soon after the spheroids initially form and naturally settle in this orientation throughout

differentiation. Completing imaging studies at earlier time points would help to confirm this hypothesis. Furthermore, a comparison of SGBS spheroids prepared using alternative methods such as spinning flask (Hoefner et al., 2020), hanging drop (Klingelhutz et al., 2018) or magnetic levitation (Daquinag et al., 2013) or even compared to 96-well ULA plates would also help determine if this asymmetric phenotype is specific to the 384-well ULA plates used throughout this project or a more general feature of adipocyte spheroids.

Additionally, TEM images showed that larger lipid droplets were present around the outside of the spheroid and become smaller towards the centre, suggesting that adipogenesis is happening more at the outside of the spheroid. This is supported by the H&E sections also revealing more lipid droplets present around the spheroid periphery, and IHC confirming expression of FABP4 is lower in the centre of the spheroid. This phenomenon has been previously described for spheroids generated from primary ADSCs, where the authors use TEM to describe large unilocular adipocytes around the spheroid periphery which have a more mature phenotype than those observed in 2D culture, with undifferentiated or fibroblast-like cells in the centre (Robledo et al., 2023).

There are several plausible explanations for this observation. Firstly, the cells in the centre of the spheroids may be under physical pressure from the outer cells (Delarue et al., 2014; Dolega et al., 2017; Efremov et al., 2021), meaning the cells may be physically unable to expand to take up lipid, but may still receive the genetic cues to differentiate. This may be tested by using IHC to assess PPARG expression in the centre of the spheroid, as this is the key transcriptional regulator of adipogenesis (Rosen et al., 1999). Similarly, expression of adipogenic markers not directly associated with lipid accumulation, such as the adipokines leptin or adiponectin, could be assessed to determine whether the cells can express other mature adipocyte protein markers and are therefore only hindered in lipid accumulation, or whether differentiation has been completely inhibited. Use of spatial transcriptomics techniques (Williams et al., 2022) in spheroid sections could build a more complete picture of differences in gene expression across different regions of the spheroid. This hypothesis that cells in the centre of the spheroid have a physical restriction to lipid accumulation may also be supported by the observation that in well differentiated spheroids, some adipocytes appear to dissociate out of the spheroids. Adipocyte motility has not

been widely studied, with one report suggesting mature adipocytes are less motile than their preadipocyte progenitors (Lustig et al., 2019). However, as these measurements were completed with cells attached to glass, it is likely that the mechanical stimuli are vastly different to the spheroid microenvironment. Further investigation is required to determine whether these adipocytes are actively migrating outwards to give themselves more space to expand outwith the confines of the spheroid, or whether this observation is due to disruption of cell-cell contacts during differentiation and resulting in cells passively 'falling' out of the spheroid.

Alternatively, cells in the centre of the spheroid may not be receiving sufficient concentrations of the differentiation reagents, oxygen and nutrients leading to hypoxia and necrosis within the spheroid core. However, no expression of HIF-1α was observed in IHC staining, perhaps suggesting no hypoxia is occurring in the spheroid centre. This is consistent with a prior study in human mesenchymal stem cells (MSCs) demonstrating spheroids needed to be seeded with >$3x10^4$ cells/sphere and >500 μm diameter for hypoxia to be detected (Schmitz et al., 2021). The literature in this field is debated, with oxygen limitations predicted and observed for spheroids of 150-200 μm diameter (Curcio et al., 2007), although this is likely influenced by the cell type and spheroid formation methods (Schmitz et al., 2021). Furthermore, the HIF-1α IHC was lacking a positive control for staining. To confirm this finding, an additional control is needed where positive HIF-1α staining is observed after spheroids are grown in a hypoxia chamber.

In the qPCR experiments, gene expression trends were broadly as expected, with upregulation of key adipogenic markers occurring throughout differentiation. PPARG is the first to be upregulated as the master transcriptional factor regulating adipogenesis (Rosen et al., 1999), followed by traditional adipogenic markers associated with lipid accumulation and regulation of metabolism including adiponectin, FABP4, FFA4, HSL, LPL and ADRB3. Interestingly, the expression of many of these markers decreases between day 12 and day 14 of differentiation, although this was not significant. Previous studies have investigated the mRNA expression dynamics in adipogenesis, and although mRNA expression of early differentiation markers such as PPARG tend to decrease in mature adipocytes, it is somewhat surprising that expression of FABP4 and HSL

appear to decrease, as these would typically be considered as markers of mature adipocytes (Schouwink et al., 2025). The transcript expression trends in this study are broadly consistent with a previous 2D culture RNA microarray transcriptomics study of differentiation in SGBS cells (Galhardo et al., 2014), although as this previous data set was only continued to day 12 of differentiation, it is not possible to compare the drop observed at day 14.

The upregulation of GLUT4 coupled to the downregulation of GLUT1 is similar to observations from primary human (Hauner et al., 1998) and 3T3-L1 adipocytes (Alshammari et al., 2025), and this transition to an insulin-sensitive phenotype is reflected in the glucose uptake functional assays. However, while protein expression of GLUT1 is downregulated to an almost undetectable level in human adipocytes (Hauner et al., 1998), 3T3-L1 cells maintain a relatively high expression level of GLUT1 at both the transcript and protein level, particularly when troglitazone is added to the differentiation cocktail, leading to a higher basal glucose uptake level (Tafuri, 1996; Alshammari et al., 2025). This demonstrates a further difference between human and murine adipocytes and highlights the requirement to use human-relevant models to study human disease.

The nanoindentation data presented in this chapter showed that stiffness of SGBS spheroids increased with differentiation. There is conflicting literature in this field, with studies reporting stiffness decreases in 3T3-L1 or SGBS cells (Kwon et al., 2011; Abuhattum et al., 2022), does not change in ADSCs (Labriola and Darling, 2015) or increases in 3T3-L1 cells (Shoham et al., 2014) during adipogenesis. Recent studies have highlighted the role that nutrition and metabolic disease may play in the mechanical properties of adipose tissue (Naftaly et al., 2022; Tsai et al., 2022), with one study suggesting that non-diabetic adipocytes become softer during differentiation but diabetic adipocytes become stiffer during adipogenesis (Abuhattum et al., 2022). Broadly, the literature suggests that accumulation of lipid leads to stiffening of cells and tissues, with excessive lipid accumulation leading to the stiffening of adipose tissue observed in obesity (Blade et al., 2024).

It is well known that cells can alter their behaviour in response to the mechanical properties of their microenvironment (Baker and Chen, 2012;

Chaudhuri et al., 2020). Thus, a major advantage of 3D cell culture should be that the mechanical properties of spheroids better match measurements *in vivo* than 2D cell cultures grown on plastic. Although this is widely accepted, the literature is lacking in studies measuring the stiffness of the same cell types grown in 2D vs 3D and compared to *in vivo* or *ex vivo* tissue. Differences in study methodology and parameters including indentation depth and the subcellular location of the probe (i.e. nucleus vs lipid droplet) can impact the stiffness measurement, making it difficult to compare between studies.

The data presented in this thesis concluded differentiated spheroids had a Young's modulus of around 1 kPa. This is broadly in line with the stiffness of adipose tissue reported in other studies (Blade et al., 2024), although methods and cell types vary. One study has reported the stiffness of SGBS cells in 2D as 0.46 kPa (Abuhattum et al., 2022), although this paper did not report any statistical analyses. There are no published studies measuring the mechanical properties of adipocyte spheroids. It is clear there are several unanswered questions around the mechanical properties of differentiating adipocytes, and thus the development of novel 3D model systems and experimental approaches to assess their biomechanical properties will be valuable in working towards answers. Furthermore, it will be interesting to investigate how the mechanical properties of the SGBS spheroids may change with drug treatments or the addition of inflammatory stimuli.

In functional assays, differentiated SGBS spheroids were shown to increase lipolysis in response to isoprenaline and increase glucose uptake in response to insulin. These characteristic adipocyte behaviours have been widely reported and previously confirmed in differentiated SGBS 2D monolayers (Wabitsch et al., 2001). Although there have been several examples of adipocyte spheroids reported in the literature, relatively few reports describe functional assays and rely instead on imaging and qPCR methodologies (Daquinag et al., 2013; Klingelhutz et al., 2018; Dufau et al., 2021; Shen et al., 2021; Mandl et al., 2022; Robledo et al., 2023; Dariolli et al., 2025; Wagner et al., 2025). This is likely due to handling challenges with adipocyte spheroids; not only are these samples free-floating in the medium, but the high lipid content also means these spheroids are buoyant and prone to accidental loss during differentiation medium changes and during assay wash steps. Functional assays therefore often

rely on quantifying metabolites in the assay buffer, e.g. glycerol or fatty acids released by lipolysis, or adipokines such as adiponectin. One example of a glucose uptake assay in a spheroid system was identified, however this involved quantifying the reduction in glucose in the assay buffer over a defined time period (Kemas et al., 2021; Shen et al., 2021; Avelino et al., 2024). Therefore, to my knowledge, this thesis presents the first direct glucose uptake assay in an adipocyte spheroid.

The magnitude of responses from the SGBS adipocyte spheroids in the functional assays somewhat differs from previous reported values. In the Glycerol-Glo lipolysis assay, 1 µM isoprenaline resulted in an approximately 3.5-fold increase in glycerol released over vehicle after 6 hours, which is in line with the values of 2.5-3-fold obtained by SGBS cells in 2D (Wabitsch et al., 2001; Fischer-Posovszky et al., 2008; Kässner et al., 2020) and primary human white adipocytes in 3D (Shen et al., 2021), although with differing incubation times of 3-22 hours. Conversely, the ~70% increase in glucose uptake obtained in SGBS adipocyte spheroids following treatment with 1 µM insulin is markedly smaller than the 2.5-3-fold increase reported for SGBS monolayers following 5–15-minute incubation with ^{14}C-2DG (Wabitsch et al., 2001; Kässner et al., 2020; Tews et al., 2022). The SGBS spheroids did appear to show an increased glucose uptake window compared to 3T3-L1 adipocyte spheroids (Avelino et al., 2024), however this study used quantification of glucose in the supernatant to infer glucose uptake and therefore is not an ideal comparison. No studies were identified which investigated insulin-stimulated glucose uptake in adipocyte spheroids directly using labelled 2DG.

In the literature, two examples of SGBS adipocyte spheroids have been previously reported (Jackisch, 2019; Kässner et al., 2020). In the thesis by Jackisch (2019), SGBS spheroids are generated by the hanging drop method, accumulation of lipid droplets is observed in H&E staining and qPCR shows upregulation of FABP4 (aP2), the lipid transferase CIDEC, and FFA4 (GPR120) during differentiation (Jackisch, 2019). In the research paper by Kässner et al. (2020), SGBS spheroids are generated with ULA plates as a comparison to the novel lipoma-derived cell strain LipPD1 and show an increase in NileRed lipid staining and upregulation of adiponectin and PPARG expression. In both, spheroid characterisation is limited to a single imaging approach and RNA

isolation for qPCR. Thus, this thesis represents the first comprehensive characterisation of SGBS adipocyte spheroids using a range of imaging approaches, gene and protein expression analyses and functional assays.

Further development of this platform would ultimately depend on the intended experimental application. Liquid handling was a significant practical challenge throughout this work, with slow and manual approaches required to minimise spheroid loss. This must be addressed to improve the throughput of the spheroid assays, for example to facilitate high-throughput screening for drug discovery approaches. One option may be to use a magnetic levitation method to generate adipocyte spheroids, where cells are loaded with magnetic nanoparticles and a magnetic field is used to guide cells to form spheroids (Daquinag et al., 2013; Tseng et al., 2018; Dariolli et al., 2025). Consequently, magnets can be used at the base of tissue culture plates to restrain the spheroids, reducing the risk of spheroid loss during manipulation and facilitating automation (Baillargeon et al., 2019; Dariolli et al., 2025).

A further technical challenge was the requirement to pool many individual spheroids to generate sufficient sample for each experiment. This laborious process involved manually picking individual spheroids out of the 384-well plate and transferring them into eppendorf tubes. To improve the throughput and reliability of these assays, further miniaturisation of the assays may ensure fewer spheroids are required to obtain a signal. Alternatively, different methods of spheroid preparation which generate large batches of uniform spheroids could be considered, such as microwell arrays (Lee et al., 2018) or rotating bioreactors (Wrzesinski et al., 2021). Spheroid pooling is commonly used in the literature to obtain enough cellular material for western blotting, imaging or invasion assays (Berens et al., 2015; Maritan et al., 2017; Madsen et al., 2025), however many studies do not report the number of spheroids pooled for each application (Klingelhutz et al., 2018; Shen et al., 2021; Ioannidou et al., 2022), making it challenging to reproduce previously published methods.

For lower throughput studies, introducing macrophages or endothelial cells into the spheroid model would increase its complexity and likely better recapitulate a metabolic disease phenotype. SGBS cells have previously been used in co-culture studies with macrophages, however there are significant limitations to

the practicality of this system, including the inhibition of adipocyte differentiation and induction of adipocyte apoptosis (Keuper et al., 2011b, 2011a). Thus, this experiment must be carefully optimised with appropriate controls to ensure relevant conclusions are drawn. In parallel to this work, our lab group has also generated adipocyte spheroids from 3T3-L1 cells in both their native form and expressing genetically encoded biosensors (Vita et al., unpublished). Considering the previously discussed differences in the behaviour of these cell lines, a direct comparison of 3T3-L1 and SGBS spheroids with primary adipose tissue would be hugely beneficial in validating these models.

Of course, the purpose of any model system is to address a specific research question. The use of this SGBS adipocyte spheroid model to better understand the role of metabolite-sensing GPCRs in metabolic disease will be described in Chapter 5.

5 Investigating the role of metabolite-sensing GPCRs in metabolic disease using adipocyte spheroids

5.1 Introduction

Metabolic disorders including obesity, T2D and MASLD are characterised by low-level chronic inflammation of metabolic tissues, leading to disruption in energy homeostasis through development of insulin resistance (IR) and subsequent complications driven by the resulting hyperglycaemia (Olefsky and Glass, 2010; World Health Organisation, 2021; Institute for Health Metrics and Evaluation, 2024). The relationship between metabolic disorders and adipose tissue inflammation has been reviewed extensively in the literature and discussed elsewhere in this thesis (de Luca and Olefsky, 2008; Olefsky and Glass, 2010; Artemniak-Wojtowicz et al., 2020), and largely stems from the discovery that macrophage infiltration of adipose tissue is elevated in metabolic disease and subsequent release of pro-inflammatory cytokines can drive development of IR (Weisberg et al., 2003; Harman-Boehm et al., 2007; Gasmi et al., 2020). However, despite significant effort in this field, much of the mechanistic detail of these metabolic-immune interactions remain unknown.

Recently, a group of metabolite-sensing GPCRs (m-GPCRs) have emerged whose endogenous ligands are metabolic intermediates obtained from nutrients, the gut microbiota or released by endocrine and metabolic tissues (Husted et al., 2017). Critically, several of these metabolite molecules are released by adipocytes, and are therefore thought to facilitate communication to infiltrating macrophages in the context of metabolic disease through m-GPCR signalling pathways (Duncan et al., 2023). Three m-GPCRs are of particular interest to this project – the FFA4 long chain fatty acid receptor, the SUCNR1 succinate receptor and the HCA_2 hydroxycarboxylic acid receptor – as these receptors are expressed in both adipocytes and macrophages, and their respective ligands have the potential to act in autocrine or paracrine signalling loops in adipose tissue.

The free fatty acid receptor family (FFA1-4) respond to either long chain fatty acids derived from dietary fats or by *de novo* synthesis in the liver (FFA1 and FFA4), or short chain fatty acids primarily derived through fermentation of dietary fibre by the gut microbiota (FFA2 and FFA3) (Milligan et al., 2017b). FFA2 and FFA4 are both highly expressed in adipocytes, where they have both been shown to negatively regulate ß-adrenoceptor-stimulated lipolysis through a Gi-coupled mechanism (Brown et al., 2003; Satapati et al., 2017; Husted et al.,

2020; Alshammari et al., 2025). Additionally, FFA4 has been shown to enhance adipogenesis in *in vitro* and *in vivo* systems (Gotoh et al., 2007; Song et al., 2016; Alshammari et al., 2025), and dysfunction of this receptor can lead to obesity in both murine and human contexts (Ichimura et al., 2012). Unlike FFA2, FFA4 is also highly expressed in macrophages, where its activation has been shown to attenuate the pro-inflammatory response and reduce macrophage chemotaxis and infiltration to adipose tissue (Oh et al., 2010, 2014). FFA4 has therefore been proposed to be part of autocrine, paracrine, or more recently, intracrine (O'Brien et al., 2025) signalling loops to regulate key adipose tissue functions (Husted et al., 2020; Duncan et al., 2023).

The succinate receptor, SUCNR1, is also expressed in adipocytes and is activated by the metabolic intermediate of the citric acid cycle (He et al., 2004; Regard et al., 2008). Although succinate is typically localised within the mitochondria, during periods of hypoxia, such as those associated with metabolic disorders (Engin, 2017; Mirabelli et al., 2024), the activity of the enzyme succinate dehydrogenase can reverse, leading to a build-up of succinate within the mitochondria which is subsequently transported out of cells where it is able to activate SUCNR1 on the plasma membrane (Ariza et al., 2012; de Castro Fonseca et al., 2016). $SUCNR1^{-/-}$ mice have been shown to have abnormal metabolic phenotypes when on a high fat diet (McCreath et al., 2015; Keiran et al., 2019) and SUCNR1 has been shown to inhibit lipolysis in *in vitro* and *in vivo* studies (Regard et al., 2008; McCreath et al., 2015), suggesting succinate may be another key regulator of adipose tissue in the context of metabolic disease.

The hydroxycarboxylic acid family of receptors are also highly expressed in adipocytes, where they can be activated by lactate (HCA_1), ß-hydroxybutyrate (BHB) (HCA_2) and 3-hydroxyoctanoate (HCA_3) to also negatively regulate ß-adrenoceptor-stimulated lipolysis through a Gi-coupled mechanism (Tunaru et al., 2003; Taggart et al., 2005; Husted et al., 2017). HCA_2 and HCA_3 are also expressed in macrophages, however as the gene for HCA_3 is only present in hominids with no equivalent in rodent species (Peters et al., 2019), studies have focused on the HCA_2 receptor. BHB is produced in the liver through oxidation of fatty acids released by adipocytes during fasting (Newman and Verdin, 2017), and both BHB and niacin, another potent agonist of HCA_2, demonstrate anti-lipolytic effects (Offermanns and Schwaninger, 2015). In fact, niacin has

previously been used therapeutically to control dyslipidaemia (Boden et al., 2014). In macrophages, HCA_2 is thought to play an immunomodulatory role through supressing pro-inflammatory cytokine and chemoattractant chemokine production, thus suggesting a further role for HCA_2 in mediating metabolic-immune communication (Shi et al., 2017; Mandrika et al., 2018).

Taken together, it is clear that FFA4, SUCNR1 and HCA_2 play critical roles in the regulation of energy homeostasis in adipocytes, particularly through inhibition of lipolysis, and their respective ligands may act as autocrine and paracrine signalling molecules between adipocytes and infiltrating macrophages. Confirming these proposed signalling mechanisms in a physiologically relevant system is vital to understanding the role of m-GPCRs in the development, and ultimately treatment, of metabolic disorders.

In this chapter, I aimed to use the genetically encoded biosensors and SGBS adipocyte spheroids developed earlier in this thesis to investigate the role of m-GPCRs in metabolic disorders. First, the expression of key m-GPCRs was confirmed in adipocyte spheroids, and specific ligands were used in differentiation and lipolysis assays to assess the role of m-GPCRs in adipogenesis and adipocyte function. Next, the cytokine Tumor Necrosis Factor (TNF) was added to SGBS spheroids to investigate the effect of a pro-inflammatory microenvironment in spheroid differentiation and functional assays. Finally, a range of transfection approaches were tested with the aim of incorporating genetically encoded biosensors into adipocytes to directly measure the activation and signalling of m-GPCRs in SGBS spheroids.

5.2 Metabolite-sensing GPCRs are upregulated during SGBS spheroid differentiation

First, it was important to establish whether m-GPCRs were expressed in SGBS adipocyte spheroids. RNA was extracted from undifferentiated (day 0) and differentiated (day 14) spheroids and RT-qPCR was used to measure expression of receptors for free fatty acids **(Figure 5.1A)**, hydroxycarboxylic acids **(Figure 5.1B)** and succinate **(Figure 5.1C)**. As before, C_T values were analysed using the $2^{-\Delta\Delta CT}$ method to show expression fold change relative to the undifferentiated sample, with raw C_T values used to compare the relative expression levels of genes **(Table 5.1).**

The expression of all m-GPCR genes measured was significantly upregulated during differentiation, with the largest fold increases observed for the short chain fatty acid receptors FFA2 and FFA3, and the hydroxycarboxylic acid receptor family, particularly HCA_2 **(Figure 5.1)**.

Although all genes were upregulated, they are not all expressed at the same levels, as determined by raw C_T values in the undifferentiated or differentiated samples **(Table 5.1).** In the undifferentiated samples, the C_T values would suggest that FFA4 and SUCNR1 are the most highly expressed, with C_T values of 24.8 and 28.7 respectively, while all other genes tested show low expression levels with C_T values >30. In differentiated samples, raw C_T values suggest that FFA4, HCA_1 and HCA_2 are the most highly expressed with C_T values <26, followed by FFA2, FFA3, HCA_3 and SUCNR1 with C_T values in the range of 28-30. Notably, expression levels of the long chain fatty acid receptor FFA1 remain very low in the differentiated samples with a C_T value of 34.9.

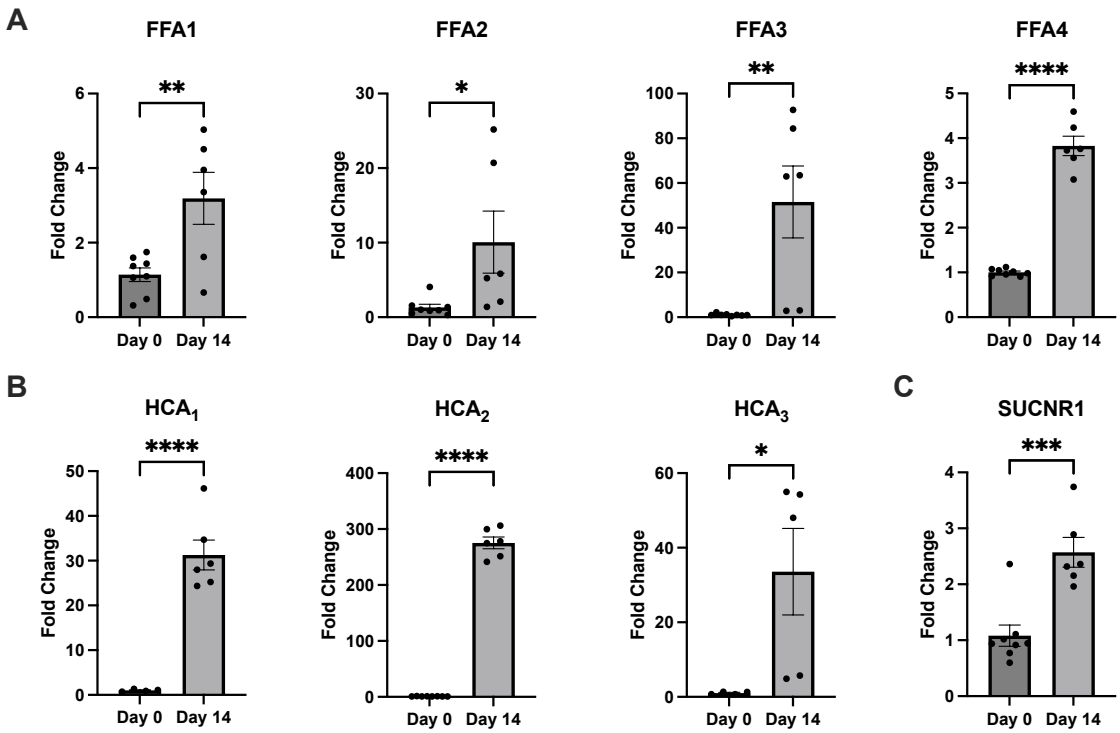

Figure 5.1 - m-GPCR gene expression is upregulated during differentiation of SGBS spheroids. Gene expression analysis of free fatty acid **(A)**, hydroxycarboxylic acid **(B)** and succinate **(C)** receptors in SGBS spheroids before and after differentiation, determined by RT-qPCR. C_T values were analysed using the $2^{-\Delta\Delta CT}$ method to show expression fold change relative to RNA isolated from day 0 cells, using primers for Sp1 as housekeeping control. Data is presented as mean ± SEM from N=2-4 independent experiments with n=2 technical replicates. Statistical comparisons were made using an unpaired t test. *p < 0.05, **p < 0.01, ***p < 0.001, ****p < 0.0001.

Table 5.1 - Raw C_T values from qPCR experiments showing relative expression levels of genes. Heat map indicates magnitude of values where green indicates high expression and red indicates low expression. Presented as mean ± SEM of N=2-4 independent experiments with n=2 technical replicates.

Gene	Mean C_T ± SEM	
	Day 0	Day 14
FFA1	35.14 ± 0.53	34.86 ± 0.23
FFA2	32.45 ± 0.52	30.92 ± 0.39
FFA3	32.68 ± 0.51	29.13 ± 0.43
FFA4	24.8 ± 0.11	23.52 ± 0.06
HCA_1	31.03 ± 0.6	25.58 ± 0.29
HCA_2	30.84 ± 0.11	23.47 ± 0.11
HCA_3	32.82 ± 0.39	28.03 ± 0.43
SUCNR1	28.73 ± 0.28	27.97 ± 0.22

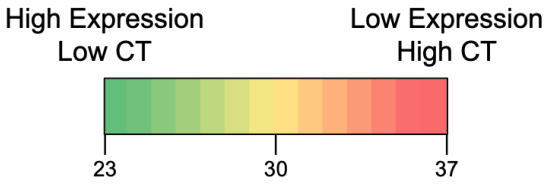

It has therefore been confirmed that the key m-GPCRs of interest – FFA4, HCA_2 and SUCNR1 alongside other members of their respective families – are indeed expressed in SGBS adipocyte spheroids, thus validating this as a model system for studying these receptors.

5.3 Metabolite-sensing GPCRs play a role in adipogenesis of SGBS cells and spheroids

Next, I set out to investigate any potential involvement of m-GPCRs in adipogenesis by incorporating specific pharmacological tool compounds for m-GPCRs to the SGBS differentiation cocktail throughout the differentiation process.

5.3.1 Inverse agonism of FFA4 reduces adipogenesis of SGBS cells in 2D

Genetic knockdown of FFA4 in adipocytes has previously been shown to inhibit adipogenesis (Gotoh et al., 2007; Song et al., 2016), and recent work in our lab group has expanded this finding by using an inverse agonist for FFA4, AH7614 (Sparks et al., 2014), to inhibit adipogenesis in 3T3-L1 adipocytes (Alshammari et al., 2025). I first wished to confirm this finding in the human-derived SGBS adipocytes **(Figure 5.2).**

SGBS cells were seeded on collagen-coated plates and cultured for 14 days in normal growth medium (undifferentiated) or differentiation cocktail containing 10 μM AH7614 or 0.1% DMSO vehicle control. Cells were fixed and stained with Oil Red O (ORO) for imaging **(Figure 5.2A)** and quantification **(Figure 5.2B)**. A significant increase in lipid droplet accumulation was observed between undifferentiated and vehicle samples (****$p < 0.0001$), which was then significantly reduced to approximately 65% of control with addition of AH7614 (**$p < 0.01$).

RNA was also isolated from SGBS cells differentiated in the presence of AH7614 and used to measure changes in gene expression of adipogenic markers **(Figure 5.2C)**. As expected, expression of adiponectin, PPARG and GLUT4 is significantly upregulated following differentiation, however only GLUT4 expression appeared to decrease following AH7614 treatment, although this was not statistically significant. In this experiment, FFA4 expression did not appear to increase following differentiation with vehicle treatment, however this is likely due to an already high expression level in undifferentiated cells with a mean C_T value of 17.94 ± 0.23 in this experiment.

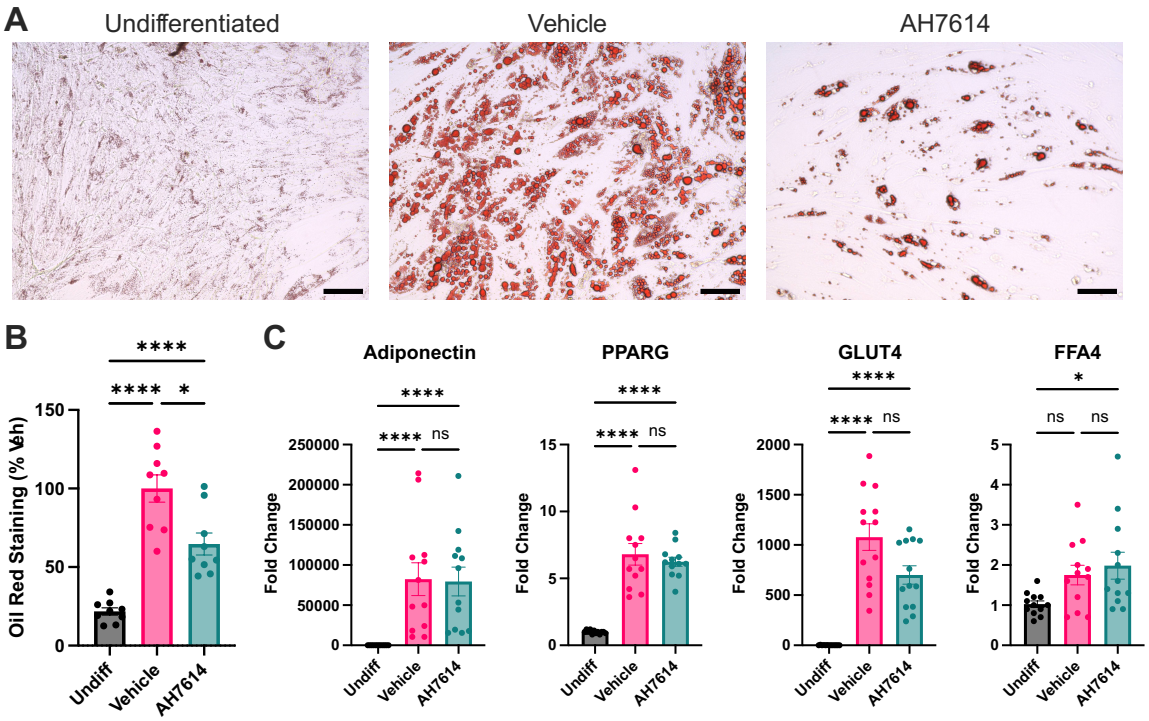

Figure 5.2 – Adipogenesis of SGBS cells in 2D is reduced by inverse agonism of FFA4. A) Representative brightfield images of Oil Red O (ORO) stained SGBS cells which were undifferentiated or differentiated in the presence of 0.1% DMSO (vehicle) or 10 μM AH7614. Scale bar = 100 μM. **B)** Quantification of ORO staining from (A). ORO absorbance was corrected for cell number and expressed as a percentage of vehicle treatment. Data presented as mean ± SEM from N=3 independent experiments with n=3 technical replicates. **C)** Gene expression analysis of adipogenic markers and FFA4 following SGBS cell differentiation in the presence of vehicle or 10 μM AH7614, determined by RT-qPCR. C_T values were analysed using the $2^{-\Delta\Delta CT}$ method to show expression fold change relative to RNA isolated from undiff cells, using primers for Sp1 as housekeeping control. Data is presented as mean ± SEM from N=3 independent experiments with n=4 technical replicates. Throughout, statistical comparisons were made using lognormal one-way ANOVA with Tukey's multiple comparisons test. *p < 0.05, ****p < 0.0001.

Overall, these data show that inverse agonism of FFA4 significantly reduces lipid accumulation during adipogenesis of SGBS adipocytes, but has only a limited effect on gene expression.

5.3.2 m-GPCR activation affects adipogenesis in SGBS spheroids

To further develop this finding, a similar experiment was carried out where agonists of m-GPCRs (or FFA4 inverse agonist AH7614) were added to the differentiation cocktail of SGBS spheroids throughout differentiation. After 14 days, spheroids were fixed and lipid accumulation measured through staining and quantification of Oil Red O **(Figure 5.3).**

In this experiment, modulation of m-GPCR activity was shown to significantly affect lipid accumulation of SGBS spheroids (one-way ANOVA, **p = 0.0028). However, due to the technical challenges with this protocol resulting in low

absorbance measurements obtained (discussed in **Chapter 4**), no individual treatments were found to be significantly different from vehicle (Šídák's multiple comparisons test, $p > 0.05$). Nevertheless, some general trends were observed. To investigate FFA4, 10 µM agonist TUG-891 or 10 µM inverse agonist AH7614 were used. TUG-891 appeared to reduce lipid accumulation by ~50% compared to vehicle whereas no change was observed with AH7614. Conversely, addition of 10 µM niacin or 1 mM succinate, agonists for the HCA_2 and SUCNR1 receptors respectively, appeared to increase lipid accumulation during differentiation by ~50% compared to vehicle.

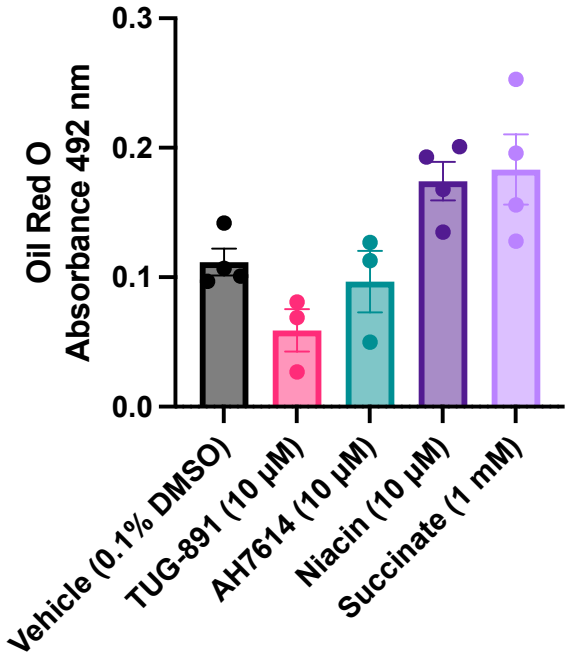

Figure 5.3 - m-GPCR activation affects adipogenesis of SGBS spheroids. Quantification of ORO staining from SGBS spheroids differentiated in the presence of the indicated compound or vehicle control. Data presented as mean ± SEM from N=2 independent experiments with n=1-2 technical replicates.

These data therefore suggest that m-GPCRs play a role in modulating adipogenesis in SGBS spheroids, however the specific mechanistic details remain to be determined.

5.4 m-GPCR activation inhibits lipolysis in SGBS adipocyte spheroids

FFA4, HCA_2 and SUCNR1 have well established anti-lipolytic effects in adipocytes primarily through Gi-mediated signalling pathways (Tunaru et al., 2003; McCreath et al., 2015; Satapati et al., 2017). I therefore wished to determine whether these findings are consistent in SGBS adipocyte spheroids by incorporating agonists for these receptors in the previously established spheroid lipolysis assay **(Chapter 4)**. However, some initial optimisation was first required to facilitate use of these ligands in the assay **(Figure 5.4)**.

Lipolysis assays require addition of bovine serum albumin (BSA) in the assay buffer in order to accept the release of fatty acids from the cells and prevent their immediate reuptake (Viswanadha and Londos, 2006; Bridge-Comer and Reilly, 2023). This was confirmed in a spheroid lipolysis assay, demonstrating that the fold increase in glycerol released following stimulation with 10 μM forskolin is increased in a concentration dependent manner with increasing concentrations of BSA included in the buffer **(Figure 5.4A).** This increase was significant for 0.5% (*p = 0.16) and 1% (***p = 0.0004) BSA compared to 0% BSA, and between 0.1% and 1% BSA (*p = 0.017).

FFA4 is a receptor for long chain fatty acids, and as a result, orthosteric agonists for this receptor typically have similar physical and chemical properties to fatty acids, including a negatively charged acid group combined with an extended hydrophobic structure, which often results in high plasma protein binding (Sparks et al., 2014; Milligan et al., 2017a; Carullo et al., 2021). When BSA is added to buffers alongside FFA4 agonists, the agonists bind to the BSA, resulting in a much lower free compound concentration available to act on the receptor (Spector, 1975; Hirasawa et al., 2005; Oliveira et al., 2015). This was confirmed in an arrestin recruitment assay where addition of BSA significantly reduced the potency of TUG-891 in a concentration-dependent manner, from a pEC_{50} of 6.41 ± 0.07 in the absence of BSA to a pEC_{50} of 5.20 ± 0.18 with 0.1% BSA (**p = 0.007), 4.82 ± 0.26 with 0.5% BSA (**p = 0.001), and 4.47 ± 0.18 with 1% BSA (***p = 0.0004) **(Figure 5.4B).**

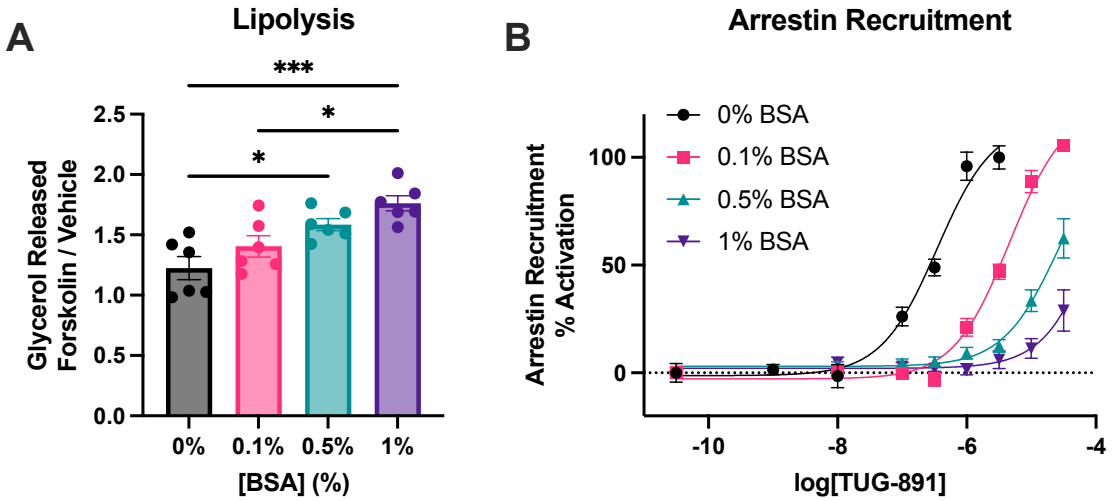

Figure 5.4 - BSA is required in the assay buffer for lipolysis but reduces the potency of TUG-891 at FFA4. A) SGBS spheroids were assessed for response to 10 μM forskolin in Glycerol-Glo lipolysis assay with different concentrations of Bovine Serum Albumin (BSA) included in assay buffer. Glycerol was quantified in spheroid supernatant at basal state and following 3-hour treatment with 10 μM forskolin or vehicle control. Measurements were first expressed as a fold change relative to basal sample, then as fold change of forskolin response over vehicle. Data presented as mean ± SEM from N=2 independent experiments with n=3 technical replicates. Statistical comparisons were made using one-way ANOVA with Tukey's multiple comparisons test. *$p < 0.05$, ***$p < 0.001$. **B)** NBA bystander assay in HEK293-T cells measuring arrestin recruitment to FFA4 following activation with TUG-891, with different concentrations of BSA included in assay buffer. Data presented as mean ± SEM from N=3 independent experiments with n=3 technical replicates.

It is critical therefore to identify a BSA concentration which will enable lipolysis to be measured while allowing enough free TUG-891 concentration to act on FFA4. A BSA concentration of 0.5% and a TUG-891 concentration of 30 μM were selected for future lipolysis assays.

As the m-GPCRs under investigation are known to inhibit lipolysis, next an appropriate lipolysis stimulation condition needed to be identified. To do this, an isoprenaline concentration response curve was generated in the spheroid lipolysis assay **(Figure 5.5A)**. In these experiments, a pEC_{50} of 9.48 ± 0.26 was obtained for isoprenaline. A submaximal (~EC_{80}) concentration of 3 nM isoprenaline was selected for m-GPCR studies.

Finally, the lipolysis assay was completed where spheroids were simultaneously treated with 3 nM isoprenaline and agonists for FFA4, HCA_2 and SUCNR1 receptors **(Figure 5.5B)**. Activation of FFA4 using 30 μM TUG-891 agonist appeared to reduce lipolysis to around 75% of isoprenaline control, although this was not significant. Treating with 10 μM inverse agonist AH7614 trended towards a very slight increase in lipolysis. Activation of HCA_2 and SUCNR1 receptors both

significantly inhibited isoprenaline-stimulated lipolysis, with 10 μM niacin reducing glycerol release to ~45% of control, and 1 mM succinate almost completely returning lipolysis to basal conditions.

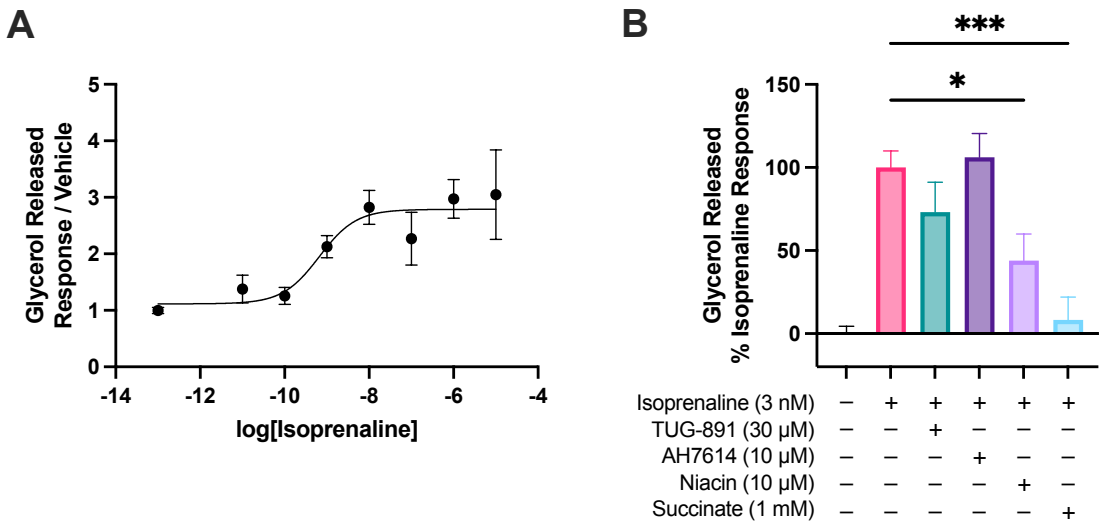

Figure 5.5 - m-GPCR activity affects lipolysis in SGBS spheroids. A) Concentration response curve of isoprenaline measured in Glycerol-Glo lipolysis assay. Spheroids were pooled and glycerol in supernatant quantified at basal state and following 3-hour treatment with the indicated concentration of isoprenaline. Measurements were first expressed as a fold change relative to basal sample, then as fold change over vehicle. Data presented as mean ± SEM from n=8 spheroid pools across N=3 independent experiments. **B)** Effect of m-GPCR specific compounds in Glycerol-Glo lipolysis assay. Spheroids were pooled and glycerol in supernatant quantified at basal state and following 3-hour treatment with an EC80 concentration of isoprenaline (3 nM) and the indicated m-GPCR compound. Measurements were first expressed as a fold change relative to basal sample, then as a % of isoprenaline response. Data presented as mean ± SEM from n=9-12 spheroid pools across N=3-4 independent experiments. Statistical comparisons were made using one-way ANOVA with Tukey's multiple comparisons test. *p < 0.05, ***p < 0.001.

These experiments therefore confirm that activation of the m-GPCRs FFA4, HCA_2 and SUCNR1 can inhibit lipolysis in SGBS adipocyte spheroids, showing this model system can be used to determine the functional consequences of m-GPCR signalling. This highlights the potential for complex *in vitro* systems to help deepen our mechanistic understanding of biological pathways.

5.5 Addition of TNF to SGBS spheroids mimics a pro-inflammatory microenvironment for investigation of metabolic disease

A key motivation for studying m-GPCRs in adipocytes is to better understand the interaction between adipocytes and infiltrating macrophages in the low-level chronic adipose tissue inflammation observed in metabolic diseases. I therefore wished to investigate how a pro-inflammatory microenvironment may affect the phenotype of SGBS adipocyte spheroids. Addition of the pro-inflammatory cytokine Tumor Necrosis Factor (TNF) is a common technique in the literature to investigate inflammation-driven insulin resistance in adipocytes using simple *in vitro* cell models including SGBS and 3T3-L1 cells (Stephens et al., 1997; Ruan et al., 2002; Massaro et al., 2016; Quarta et al., 2021) and was chosen as a starting point for this work.

SGBS spheroids were generated and differentiated following the standard 14-day protocol with 10 ng/mL recombinant human TNF added to the differentiation cocktail, either for 24 hours on the final day of differentiation (i.e. added on day 13 of differentiation) or added throughout differentiation (i.e. for the full 14 days) to mimic acute and chronic inflammation respectively. This concentration of TNF was selected for consistency with other reported studies in SGBS cells (Massaro et al., 2016; Quarta et al., 2021). After 14 days, spheroids were analysed using imaging, gene expression, and functional assay approaches to determine whether a pro-inflammatory microenvironment alters the phenotype of adipocyte spheroids.

To establish if the 10 ng/mL TNF treatment had any cytotoxic effect, spheroids were imaged and viability quantified using the CellTitre-Glo 3D reagent **(Figure 5.6)**. Phase contrast microscopy images suggested that addition of TNF affects spheroid morphology, with TNF treatment appearing to reduce the number of adipocytes migrating from the spheroid, and an uneven spheroid surface was observed following 14-day treatment **(Figure 5.6A).** Despite a slight downward trend, TNF treatment did not significantly reduce the viability of SGBS adipocyte spheroids in the CellTitre-Glo assay (one-way ANOVA, $p = 0.22$) **(Figure 5.6B)**.

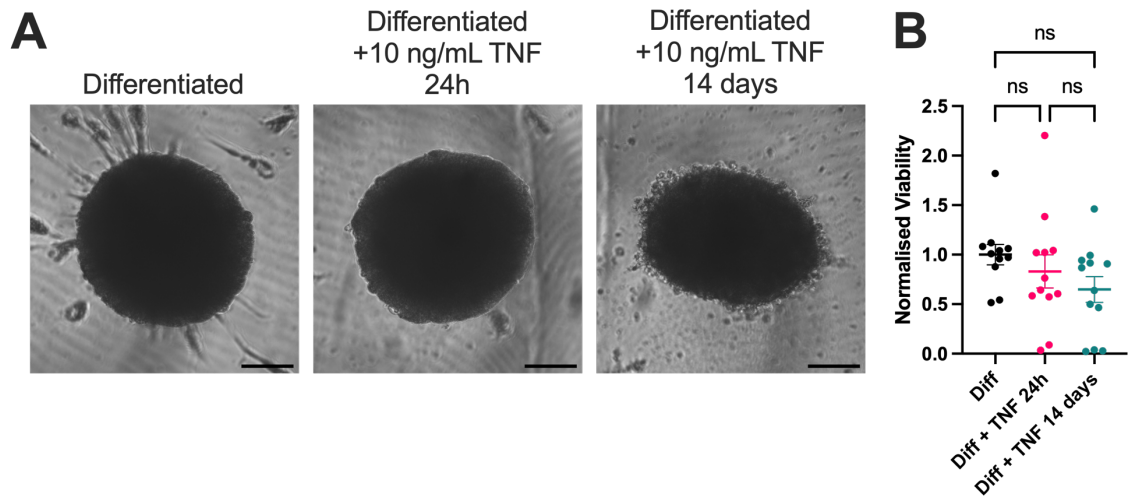

Figure 5.6 - Addition of TNF affects SGBS spheroid morphology but not viability. A) Representative phase contrast images of differentiated SGBS spheroids following treatment with 10 ng/mL Tumor Necrosis Factor (TNF) for the final 24 hours or full 14 days during differentiation. Scale bar = 100 µm. **B)** CellTitre-Glo viability assay of TNF-treated SGBS spheroids. Measurements were expressed as a fold change relative to untreated condition and are presented as individual replicates with mean ± SEM indicated from n=11-12 spheroid pools across N=3 independent experiments. Statistical comparisons were made using one-way ANOVA with Tukey's multiple comparisons test.

Next, RNA was isolated from SGBS spheroids following TNF treatment, and gene expression of adipogenic and inflammatory markers was determined by RT-qPCR **(Figure 5.7).** No significant differences in the expression of FABP4 transcript were measured following either 24h or 14-day TNF treatment **(Figure 5.7A)**. The expression of the adipokine adiponectin is not affected by 24h treatment of TNF, but is significantly downregulated to ~40% of the control level after chronic TNF treatment **(Figure 5.7B).** The insulin-sensitive glucose transporter GLUT4 is significantly downregulated compared to control after both acute 24h and chronic 14-day TNF treatments, reducing to ~75% and ~40% of control levels respectively **(Figure 5.7C).** Together these data suggest that while TNF treatment may not significantly affect differentiation of adipocyte spheroids, the reduction in adiponectin and GLUT4 expression suggest that TNF treatment may impair metabolic function through reduced adipokine signalling and glucose uptake.

The expression of the pro-inflammatory cytokine interleukin-1 beta (IL-1ß) was slightly elevated following TNF addition to ~1.5 fold control levels, although this was not significant **(Figure 5.7D).** The chemokine C-C motif ligand 2 (CCL2), also known as monocyte chemoattractant protein 1 (MCP1), is significantly upregulated by ~7-fold following acute and chronic TNF treatment **(Figure**

5.7E). Thus, addition of TNF appears to stimulate upregulation of pro-inflammatory markers in adipocyte spheroids.

Interestingly, expression of FFA4 receptor transcript was significantly upregulated by ~50% following 24h TNF treatment. However, chronic TNF treatment showed a non-significant decrease of ~30% expression compared to untreated control **(Figure 5.7F).** This finding may suggest that FFA4 could play differential roles in acute vs. chronic inflammation of adipose tissue and warrants further investigation.

It can therefore be concluded that a pro-inflammatory microenvironment affects the gene expression of adipogenic and inflammatory markers in SGBS adipocyte spheroids, with the specific magnitude and direction of these effects dependent on the specific gene and length of TNF treatment.

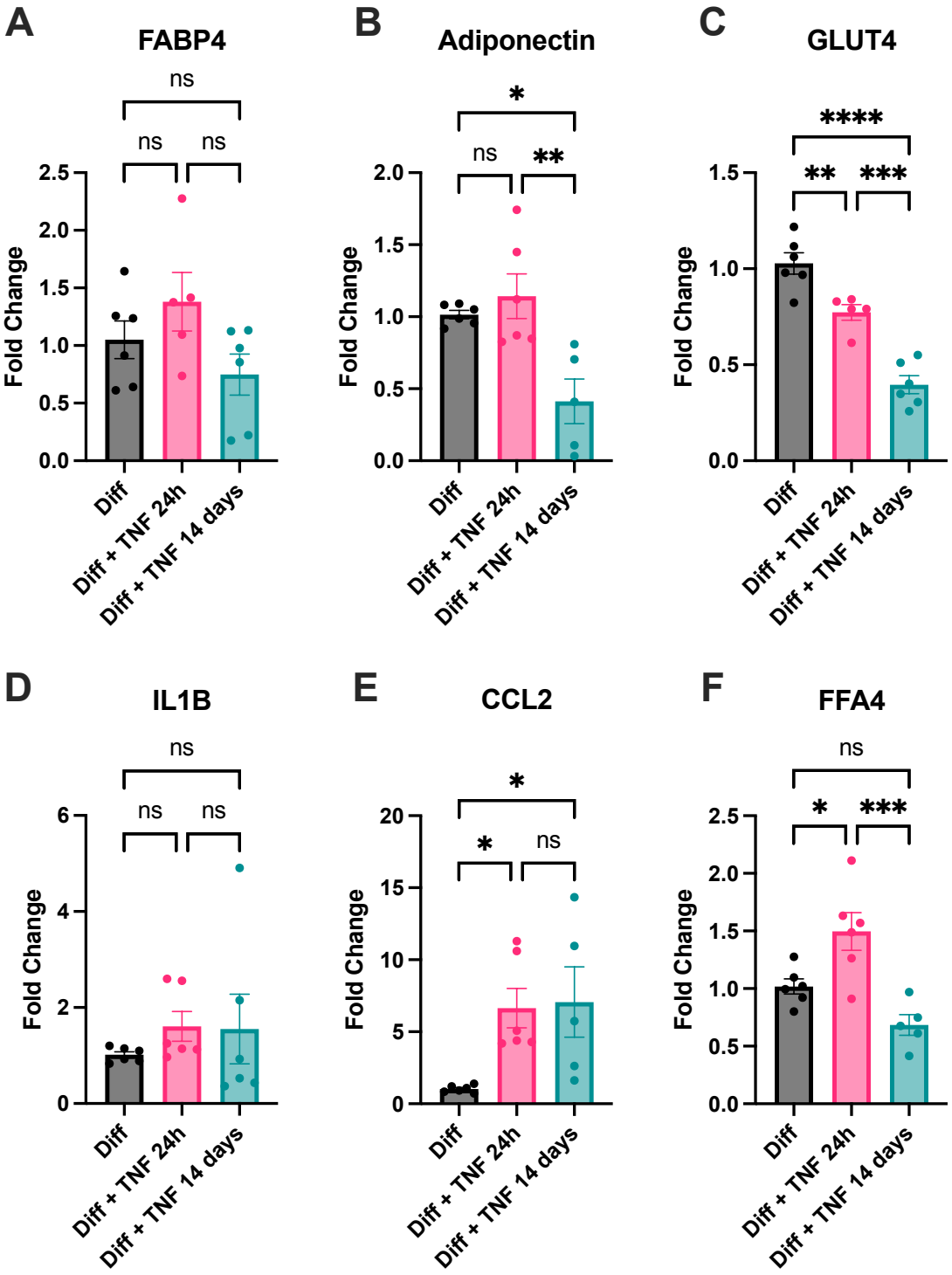

Figure 5.7 - Addition of TNF affects gene expression of adipogenic and inflammatory markers in SGBS spheroids. Gene expression analysis of adipogenic **(A-C)** and inflammatory **(D-E)** markers and FFA4 **(F)** in differentiated SGBS spheroids following treatment with 10 ng/mL TNF for 24 hours or 14 days, determined by RT-qPCR. C_T values were analysed using the $2^{-\Delta\Delta CT}$ method to show expression fold change relative to RNA isolated from untreated spheroids using primers for Sp1 as housekeeping control. Data presented as mean ± SEM from n=6 spheroid pools from N=3 independent experiments. Statistical comparisons were made using one-way ANOVA with Tukey's multiple comparisons test. *p < 0.05, **p < 0.01, ***p < 0.001, ****p < 0.0001.

Finally, to determine whether the gene expression changes observed following TNF treatment translate into functional effects, TNF-treated spheroids were

assessed for insulin response in the previously developed glucose uptake assay **(Figure 5.8).**

In untreated spheroids, a clear concentration-dependent insulin response is observed, with 1 µM and 100 nM insulin concentrations resulting in significant increases in glucose uptake over vehicle. Similar concentration-dependent trends are observed for both 24h and 14-day TNF treatments, where these responses are dampened when compared to untreated control. This attenuation is more pronounced for the acute TNF treatment where no significant increase in glucose uptake is measured above vehicle control at any insulin concentration tested. A significant decrease in glucose uptake compared to the non-TNF-treated control is measured following treatment with 1 µM insulin (*p = 0.037). Chronic TNF treatment also shows a reduced level of glucose uptake compared to the non-TNF-treated control observed at 1 µM insulin, although this is not significant (p = 0.16). At lower insulin concentrations, glucose uptake is comparable between untreated and chronic TNF treated samples.

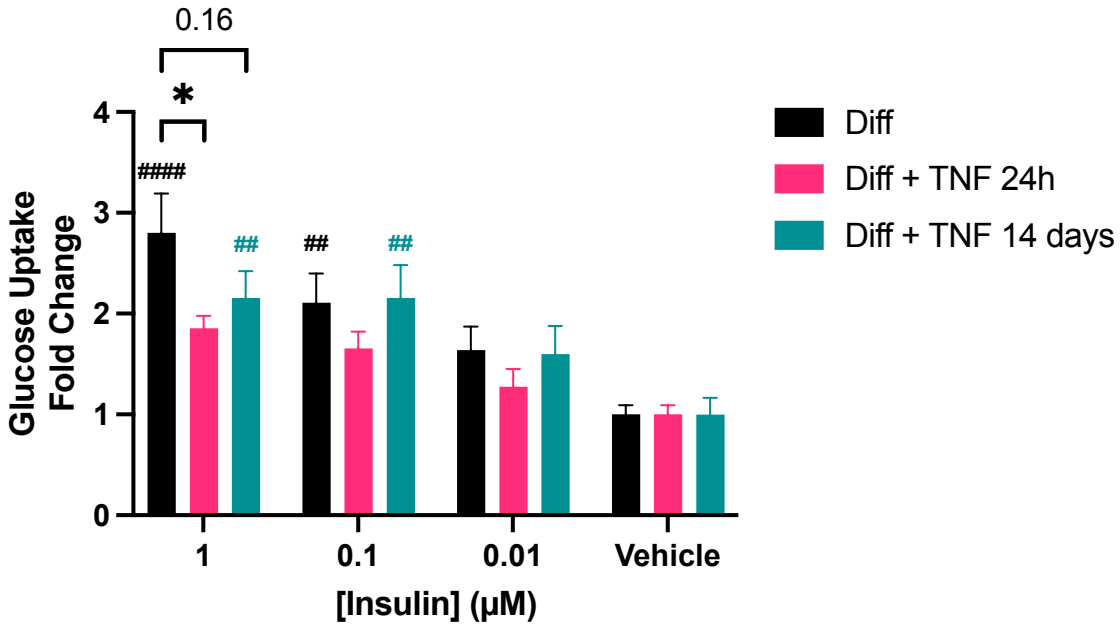

Figure 5.8 - Addition of TNF reduces insulin-stimulated glucose uptake in SGBS spheroids. Glucose uptake of differentiated SGBS spheroids following treatment with 10 ng/mL TNF for 24 hours or 14 days during differentiation in response to the indicated concentration of insulin. Glucose uptake was quantified using Glucose Uptake-Glo kit and raw luminescence values expressed as a fold change of the respective vehicle. Data presented as mean ± SEM from n=5-10 spheroid pools across N=3-4 independent experiments. Statistical comparisons were made using two-way ANOVA with Tukey's multiple comparisons test. *p < 0.05 (comparison as indicated), $^{\#\#}$p < 0.01, $^{\#\#\#\#}$p < 0.0001 (comparison to respective vehicle).

Taken together, these data show that introduction of a pro-inflammatory microenvironment through addition of TNF affects gene expression and glucose

uptake of SGBS adipocyte spheroids and suggests a transition towards a more insulin-resistant phenotype. This therefore indicates the potential for this spheroid platform to be used in deeper mechanistic studies of metabolism and inflammation in metabolic disorders.

5.6 Optimising transfection methods to express biosensors in spheroids

The data presented thus far in this chapter has indicated that m-GPCRs play a role in the regulation of energy homeostasis in adipocytes through modulation of adipogenesis and inhibition of lipolysis. Furthermore, FFA4 is upregulated in a pro-inflammatory spheroid microenvironment and therefore may support the hypothesis that FFA4 is a key mediator of communication between metabolic and inflammatory cells in metabolic disease. However, these conclusions are based on the use of pharmacological tool compounds for these receptors in functional assays and not direct readouts of GPCR signalling. Therefore, I wished to express the genetically encoded biosensors generated in **Chapter 3** in the SGBS adipocyte spheroids to allow a more direct measurement of GPCR signalling. However, adipocytes and preadipocytes are known to be particularly challenging to transfect (Dugail, 2001; Park et al., 2015; Romanelli and Macdougald, 2020), and therefore several transfection methods were investigated to incorporate genetic material into SGBS cells.

5.6.1 A single plasmid NBA biosensor shows a reduced assay window compared to two-component sensor

Firstly, I hypothesised that transfection of fewer plasmids would improve the transfection efficiency of SGBS cells. The NBA biosensor requires co-transfection of two plasmids expressing Lyn11-LgBiT and SmBiT-Arr, however if transfection efficiency is low, there is no guarantee that both plasmids required for the assay are successfully transfected into the same cell. Thus, a single plasmid was designed which separated the Lyn11-LgBiT and SmBiT-Arr components using a self-cleaving 2A peptide sequence from porcine teschovirus-1 (P2A), allowing transcription of a single mRNA strand but translation of two individual proteins (Szymczak et al., 2004; Liu et al., 2017; Zhu et al., 2023). This new construct, termed the 'NBA Plasmid', was transfected into HEK293-T cells with FFA4 or pcDNA control to validate its function and compare performance to the original two-component biosensor **(Figure 5.9).**

Firstly, it was noticed that the baseline luminescence signal of the NBA plasmid biosensor was approximately 6-fold higher than the two-component biosensor

(*p < 0.05) when 10 ng/well total biosensor DNA was transfected **(Figure 5.9A).** As a result, following addition of 10 µM TUG-891, the single plasmid biosensor resulted in a significantly reduced peak signal increase of 0.7 – 1.0 fold compared to a peak fold increase of 6.1 with the original two-component biosensor (****p < 0.0001). There was no significant difference in the peak response between the 10 ng and 30 ng amounts of NBA plasmid transfected (p = 0.98) **(Figure 5.9B-C).** It is not possible to know from these data whether the baseline signal is higher due to greater transfection efficiency than the two-component biosensor, or whether there is an increased baseline signal caused by incomplete cleavage of the P2A sequence. Transfecting lower amounts of the NBA plasmid than tested here may help to reduce the baseline response and therefore improve the assay window. However, the NBA plasmid biosensor is still able to measure arrestin recruitment to the FFA4 receptor in HEK293-T cells at both amounts of transfected plasmid tested, with a significant peak response over vehicle (****p < 0.0001), albeit with a lower signal window than its two-component counterpart. Co-transfection of FFA4 is required to measure this response in HEK293-T cells but may not be required in differentiated SGBS cells which endogenously express the FFA4 receptor.

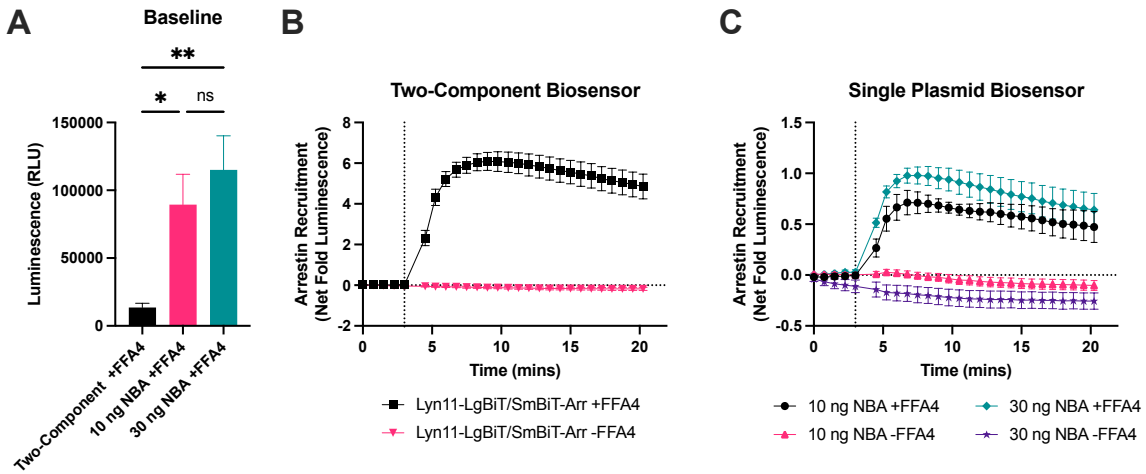

Figure 5.9 - Single plasmid NBA biosensor reduces assay window compared to two-component biosensor. 5 ng/well of each plasmid in two-component NBA biosensor (Lyn11-LgBiT/SmBiT-Arr) or the indicated amount of single NBA plasmid biosensor were transfected into HEK-293T cells with 30 ng/well FFA4 plasmid (+FFA4) or pcDNA control (-FFA4). **A)** Baseline luminescence measurements from biosensor combinations +FFA4 are given as raw luminescence values from the final measurement before compound addition and are presented as mean ± SEM from N=2 independent experiments with n=8 technical replicates. Statistical comparisons were made using one-way ANOVA with Tukey's multiple comparisons test. *p < 0.05, **p < 0.01. **B-C)** Kinetic measurements of luminescent signal recorded when two-component **(B)** or single plasmid **(C)** biosensors are activated by 10 µM TUG-891 at 3 minutes (indicated by the dotted line). Raw luminescence values were divided by baseline signal (average of 5 measurements before compound addition) and vehicle response subtracted. Data presented as mean ± SEM from N=2 independent experiments with n=3-4 technical replicates.

Therefore, while the two-component biosensor shows a higher assay window than the single plasmid version, a significant increase in arrestin recruitment is recorded using both biosensor designs following TUG-891 treatment. The single plasmid biosensor may therefore be a useful tool for transfection optimisation of SGBS cells.

5.6.2 Chemical transfection methods do not allow measurement of arrestin recruitment in SGBS cells

Several methods exist to introduce genetic material into mammalian cell types. Chemical-based transfection methods are perhaps the most commonly used, as reagents are commercially available and do not require any specialist equipment or viral vectors (Kim and Eberwine, 2010). In these methods, negatively charged DNA or RNA molecules bind to cationic polymers or lipids to facilitate their uptake into cells (Kim and Eberwine, 2010). Cationic polymers such as polyethylenimine (PEI) are internalised into cells through endocytosis, where the genetic material is released and transcription can occur (Chesnoy and Huang, 2000). Conversely, cationic lipid reagents such as Lipofectamine 3000 (L3000) (ThermoFisher) can fuse directly with the cell membrane before endocytosis and deliver nucleic acid cargo to the cytoplasm (Dalby et al., 2004; Cardarelli et al., 2016).

Adipocytes are a notoriously challenging cell type to transfect using standard methods (Dugail, 2001; Romanelli and Macdougald, 2020), and although some reports indicate success with introducing genetic material into SGBS cells using lipofectamine-based approaches, these are typically limited to small cargoes (e.g. siRNAs) which do not require translocation to the nucleus, rather than DNA plasmids (Enlund et al., 2014; Landgraf et al., 2020). Nevertheless, as these reagents are easily accessible, I initially investigated these methods to transfect SGBS cells. A reporter plasmid expressing a mNeonGreen-NanoLuciferase (mNG-NLuc) fusion protein was used for transfection optimisation as expression of this construct would allow both visualisation using fluorescence microscopy and sensitive measurement of luminescence following addition of NanoGlo furimazine substrate. Additionally, messenger RNA (mRNA) transfection has emerged as an alternative to DNA plasmids in hard-to-transfect cell lines as the genetic material does not require entry to the nucleus for effective translation

(Conry et al., 1995; Qin et al., 2022). Therefore, *in vitro* transcription of mNG-NLuc mRNA was carried out and used to investigate whether this is a more effective transfection method for SGBS cells.

First, transfection of undifferentiated SGBS preadipocytes with plasmid expressing mNG-NLuc or empty vector control (pcDNA) was attempted using PEI and L3000 reagents, and mRNA transfection completed using Lipofectamine MessengerMAX reagent (**Figure 5.10**). Luminescence signal was measured from transfected cells 10 minutes after addition of NanoGlo substrate, with transfection of mNG-NLuc constructs showing a significant increase in luminescent signal over pcDNA control for all methods tested (**Figure 5.10A**). For the mRNA transfection, it was noted that a high level of luminescence signal was still measured in the 'empty' control, potentially indicating some level of RNA contamination, although the comparison with mNG-NLuc was still significant. Although the luminescence measured for mNG-NLuc transfected using L3000 was statistically higher than PEI and mRNA methods, PEI was progressed for future work as it is the cheapest reagent and still resulted in successful transfection.

Although these results suggest it is possible to transfect undifferentiated SGBS cells using lipofection or PEI, it is important to note that the transfection efficiency of SGBS cells remains poor compared to easier to transfect cells like HEK293-T cells. Fluorescent microscopy of cells transfected with mNG-NLuc using PEI showed that a very small number of SGBS cells were transfected compared to the majority of HEK293-T cells (**Figure 5.10B**). However, as a measurable luminescence signal was observed, I attempted transfection of the NBA biosensor components to measure arrestin recruitment in undifferentiated SGBS cells.

SGBS or HEK293-T cells were co-transfected using PEI with 5 ng/well with plasmids expressing the NBA biosensor components (Lyn11-LgBiT and SmBiT-Arr) with 30 ng/well FFA4 plasmid (+FFA4) or pcDNA control (-FFA4) and assessed for response to TUG-891. The baseline luminescence signal measured was ~200-fold higher for HEK293-T cells compared to SGBS cells, again highlighting the poor transfection efficiency in these cells (**Figure 5.10C**). In the arrestin recruitment assay, no measurable response to TUG-891 was observed for SGBS cells whether

FFA4 was transfected or not (**Figure 5.10D**), indicating that further optimisation is required. In contrast, a robust response was observed when constructs were transfected using PEI in HEK293-T cells, as previously observed in **Chapter 3**.

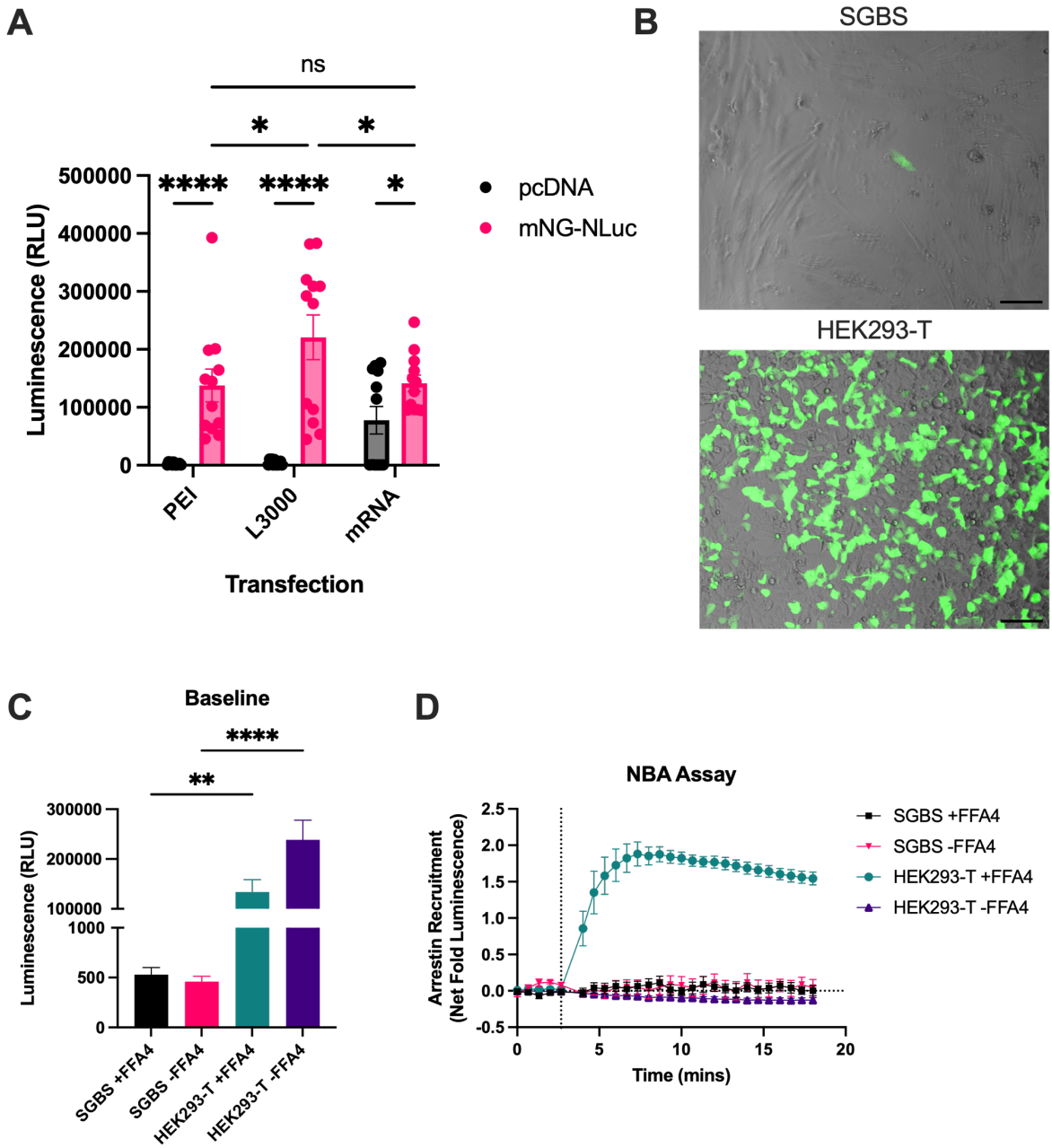

Figure 5.10 - Chemical-based techniques demonstrate limited capacity to transfect undifferentiated SGBS cells in 2D. A) Undifferentiated SGBS cells were transfected with plasmids or mRNA expressing an mNG-NLuc fusion protein or empty pcDNA control using the indicated transfection method, and luminescence signal measured 10 mins after addition of NanoGlo substrate. Data presented as individual replicates with mean ± SEM indicated from N=2 independent experiments with n=6 technical replicates. Statistical comparisons were made using two-way ANOVA with Tukey's multiple comparisons test. **B)** Representative brightfield and green fluorescence images of SGBS cells (top) or HEK cells (bottom) expressing mNG-NLuc following transfection with PEI. Scale bar = 100 µm. **C-D)** SGBS or HEK293-T cells were transfected with 5 ng/well NBA plasmids expressing Lyn11-LgBiT and SmBiT-Arr with 30 ng/well FFA4 plasmid (+FFA4) or pcDNA control (-FFA4) and assessed for response to TUG-891. **C)** Baseline luminescence measurements are given as raw luminescence values from the final measurement before compound addition and are presented as mean ± SEM from N=2 independent experiments with n=6 technical replicates. Statistical comparisons were made using one-way ANOVA with

Tukey's multiple comparisons test. **D)** Kinetic measurements of luminescent signal recorded when transfected SGBS or HEK293-T cells are activated by 10 μM TUG-891 at 2.67 minutes (indicated by the dotted line). Raw luminescence values were divided by baseline signal (average of 5 measurements before compound addition) and vehicle response subtracted. Data presented as mean ± SEM from N=2 independent experiments with n=3 technical replicates. Throughout, *p < 0.05, **p < 0.01, ****p < 0.0001.

Next, transfection of differentiated SGBS cells was investigated again using mNG-NLuc plasmid DNA or mRNA, or pcDNA empty vector control. In addition to the PEI and L3000 reagents tested for undifferentiated cells, additional broad-spectrum DNA transfection reagents were obtained (TransIT-LT1, TransIT-2020 and TransIT-X2, all Mirus Bio) as reports suggested these reagents were effective at transfecting a brown preadipocyte cell line (O'Brien et al., 2025). Luminescence signal from transfected cells was again measured 10 minutes after NanoGlo substrate addition **(Figure 5.11A).** In these experiments, only mRNA transfection of mNG-NLuc showed a significant increase in luminescence signal over the pcDNA control and therefore was selected for progression to the NBA assay.

mRNA from the single-component NBA plasmid was then generated by *in vitro* transcription and transfected into differentiated SGBS cells or HEK293-T cells using Lipofectamine MessengerMAX reagent, and cells assessed for response to TUG-891 in a NBA assay **(Figure 5.11B-C).** The baseline luminescence signal for transfected HEK293-T cells was approximately 2-fold higher than SGBS adipocytes (*p < 0.05), with no significant difference observed in the baseline between untransfected and transfected SGBS cells **(Figure 5.11B).** No measurable response to TUG-891 was observed in the arrestin recruitment assay in SGBS cells **(Figure 5.11C),** demonstrating that chemical-based approaches are not sufficient for transfection of genetically-encoded biosensors into differentiated SGBS cells. Additionally, no response to TUG-891 was observed in the HEK293-T cells, although this is likely because these cells were only transfected with mRNA of the biosensor and not FFA4 receptor. As shown throughout **Chapter 3** and in **Figure 5.9B,** an arrestin recruitment response cannot be measured in HEK293-T without co-transfection of exogenous receptor.

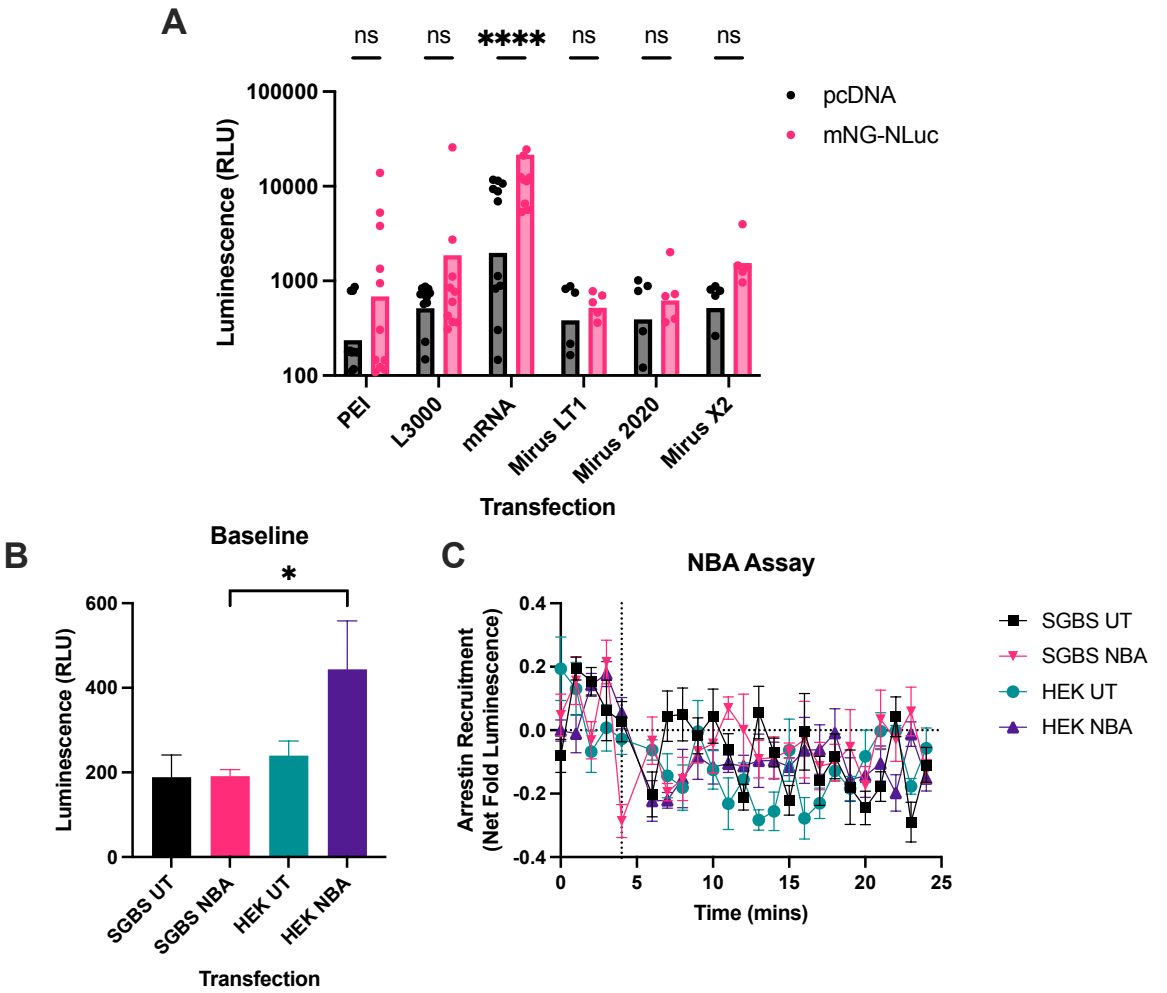

Figure 5.11 - mRNA is transfected into differentiated SGBS cells but is not sufficient to measure arrestin recruitment. A) Differentiated SGBS cells were transfected with plasmids or mRNA expressing an mNG-NLuc fusion protein or empty pcDNA control using the indicated transfection method, and luminescence signal measured 10 mins after addition of NanoGlo substrate. Data presented as individual replicates with mean ± SEM indicated from N=2-3 independent experiments with n=3-6 technical replicates. Statistical comparisons were made using two-way ANOVA with Tukey's multiple comparisons test. ****p < 0.0001. **B-C)** SGBS or HEK293-T cells were transfected with 100 ng/well mRNA expressing the single component NBA biosensor (NBA) or untransfected control (UT) and assessed for response to TUG-891. **B)** Baseline luminescence measurements are given as raw luminescence values from the final measurement before compound addition and are presented as mean ± SEM from N=2 independent experiments with n=6 technical replicates. Statistical comparisons were made using one-way ANOVA with Tukey's multiple comparisons test. *p < 0.05. **C)** Kinetic measurements of luminescent signal recorded when transfected SGBS or HEK293-T cells are activated by 10 µM TUG-891 at 4 minutes (indicated by the dotted line). Raw luminescence values were divided by baseline signal (average of 5 measurements before compound addition) and vehicle response subtracted. Data presented as mean ± SEM from N=2 independent experiments with n=3 technical replicates.

Finally, some preliminary experiments were completed to investigate chemical transfection of SGBS spheroids **(Figure 5.12).** Undifferentiated SGBS spheroids were transfected again using DNA or mRNA for mNG-NLuc or empty vector control, and luminescence signal measured 10 minutes after addition of NanoGlo substrate. As a control, spheroids were also prepared using HEK293-T cells seeded at 10,000 cells/well in 384-well ULA plates. Spheroids were transfected

directly in the ULA plates and transferred to white 96-well assay plates either individually or in pools of four spheroids for luminescence measurements.

In these experiments, transfection of SGBS spheroids appeared to be largely unsuccessful. A significant increase in luminescence signal for mNG-NLuc constructs above pcDNA was only measured for L3000 transfection in single spheroids (*p = 0.048) **(Figure 5.12A).** In pooled spheroids, both L3000 and mRNA transfection appeared to show increased luminescent signal compared to pcDNA, although this was not significant (p = 0.10 and 0.12 respectively) **(Figure 5.12B).** In contrast, in single spheroids generated from HEK293-T cells, the increase over pcDNA control was significant for both L3000 and mRNA transfections (****p < 0.0001 and **p = 0.007 respectively), with L3000 mNG-NLuc transfection also showing a significant increase over the mNG-NLuc transfection with PEI and mRNA (****p < 0.0001) **(Figure 5.12C)**. Similarly, in pooled HEK293-T spheroids, a significant increase was measured for PEI and L3000 transfection over pcDNA control, with a non-significant trend also observed for mRNA **(Figure 5.12D).** Again, L3000 transfection resulted in significantly higher luminescent signal compared to PEI and mRNA. Comparatively, transfection of HEK spheroids with mNG-NLuc resulted in markedly higher luminescence measurements in the region of ~10^6 RLU compared to SGBS spheroids with measurements around 10^4 RLU **(Figure 5.12C-D)**.

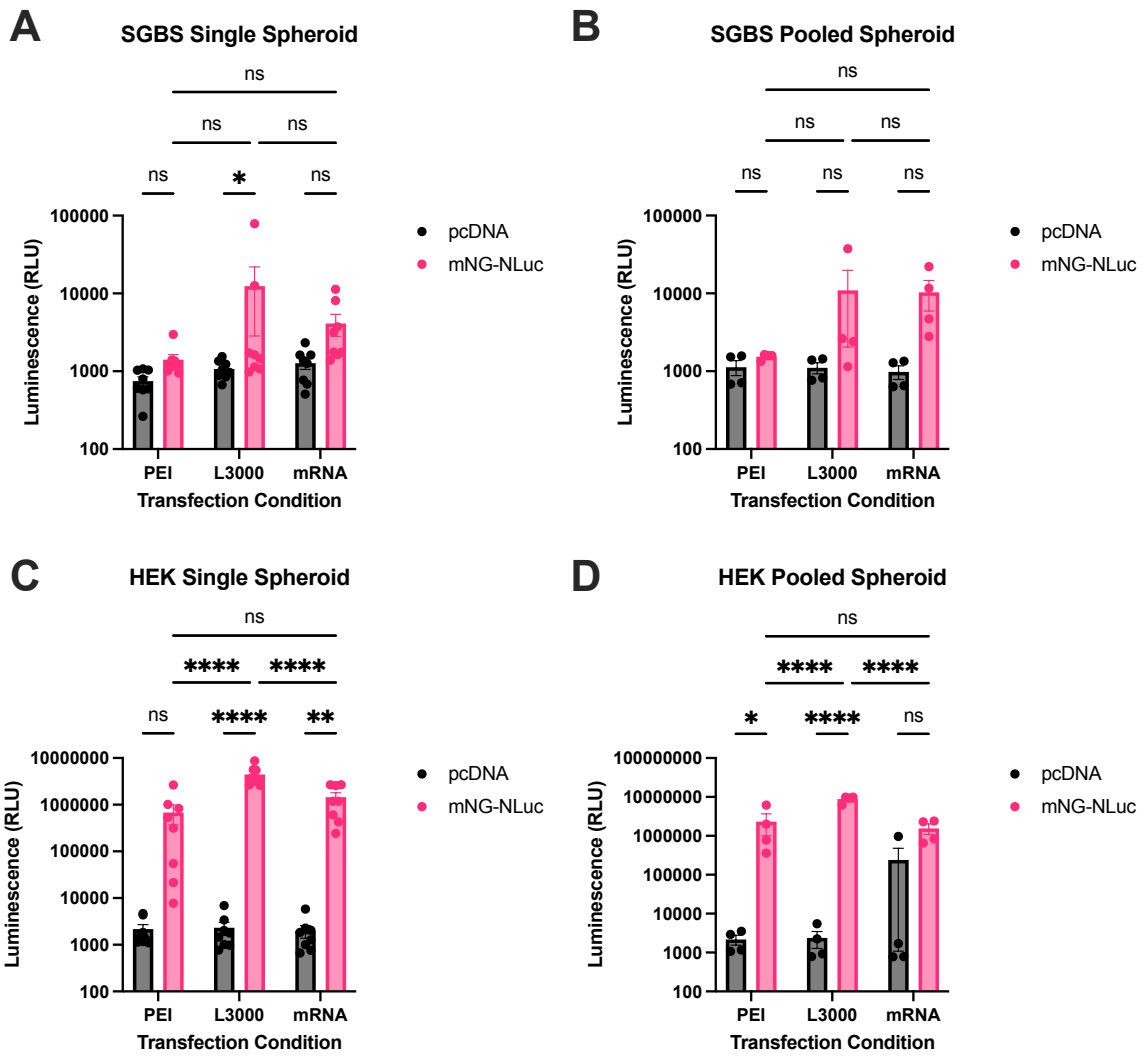

Figure 5.12 - Lipofectamine approaches are not effective at transfecting undifferentiated SGBS spheroids. A-B) Undifferentiated SGBS spheroids were transfected with plasmids or mRNA expressing an mNG-NLuc fusion protein or empty pcDNA control using the indicated transfection method, and luminescence signal measured from individual **(A)** or pools of 4 **(B)** spheroids 10 mins after addition of NanoGlo substrate. **C-D)** As (A-B) using spheroids generated with HEK293-T cells. Data presented as individual replicates with mean ± SEM indicated from N=2 independent experiments with n=4 (single spheroids) or n=2 (pooled spheroids) technical replicates. Statistical comparisons were made using two-way ANOVA with Tukey's multiple comparisons test. *p < 0.05, **p < 0.01, ****p < 0.0001.

Overall, it was determined that lipofection-based transfection methods are not suitable for expression of genetically encoded biosensors and subsequent measurement of GPCR signalling in undifferentiated or differentiated SGBS cells and spheroids. Thus, an alternative transfection strategy was evaluated.

5.6.3 Electroporation methods allow measurement of arrestin recruitment in 2D SGBS cells but not spheroids

Electroporation is an alternative transfection method where electrical pulses are thought to generate transient pores in the cell membrane thus allowing delivery of genetic material (Inoue and Krumlauf, 2001; Kim and Eberwine, 2010).

Electroporation has been widely used to introduce DNA and RNA into adipocytes *in vitro* and *in vivo* (Dugail, 2001; Okada et al., 2003; Granneman et al., 2004; Granneman, 2008; Schweiger et al., 2012), and thus was investigated as a possible transfection approach for SGBS adipocytes.

To establish an initial electroporation protocol using the Neon™ Transfection System (Invitrogen), the pre-programmed optimisation protocol for DNA was followed where undifferentiated SGBS cells were electroporated with mNG-NLuc plasmid using different electroporation parameters for each well of a 24-well plate **(Table 5.2).** Luminescence signal was measured following incubation with NanoGlo substrate and the two most successful conditions with the highest luminescence signal – wells C4 and D3 – were progressed for further optimisation **(Figure 5.13A).**

Subsequently, a further round of optimisation was completed by narrowing the pulse voltage around the most successful optimisation conditions from the initial experiment **(Table 5.3).** Luminescent signal was again measured following incubation with NanoGlo substrate and the most successful parameters – 1275 V, 10 ms, 3 pulses – selected for future work **(Figure 5.13B).** Notably, epifluorescence microscopy imaging indicates that electroporation appears to be more successful than lipofection for SGBS cells, as more transfected cells are visible within a given field of view **(Figure 5.10C, Figure 5.13C).**

Table 5.2 - List of electroporation conditions used for Neon Optimisation Day 1.

Well	Pulse voltage (V)	Pulse width (ms)	Pulse number
A1	0	0	0
A2	1400	20	1
A3	1500	20	1
A4	1600	20	1
A5	1700	20	1
A6	1100	30	1
B1	1200	30	1
B2	1300	30	1
B3	1400	30	1
B4	1000	40	1
B5	1100	40	1

B6	1200	40	1
C1	1100	20	2
C2	1200	20	2
C3	1300	20	2
C4	1400	20	2
C5	850	30	2
C6	950	30	2
D1	1050	30	2
D2	1150	30	2
D3	1300	10	3
D4	1400	10	3
D5	1500	10	3
D6	1600	10	3

Table 5.3 - List of electroporation parameters used for Neon Optimisation Day 2. Original conditions identified from Day 1 are underlined.

Well	Pulse voltage (V)	Pulse width (ms)	Pulse number	Plasmid
A1	1350	20	2	mNG-NLuc
A2	1375	20	2	mNG-NLuc
A3	1400	20	2	mNG-NLuc
A4	1425	20	2	mNG-NLuc
A5	1450	20	2	mNG-NLuc
A6	1400	20	2	pcDNA
B1	1250	10	3	mNG-NLuc
B2	1275	10	3	mNG-NLuc
B3	1300	10	3	mNG-NLuc
B4	1325	10	3	mNG-NLuc
B5	1350	10	3	mNG-NLuc
B6	1300	10	3	pcDNA

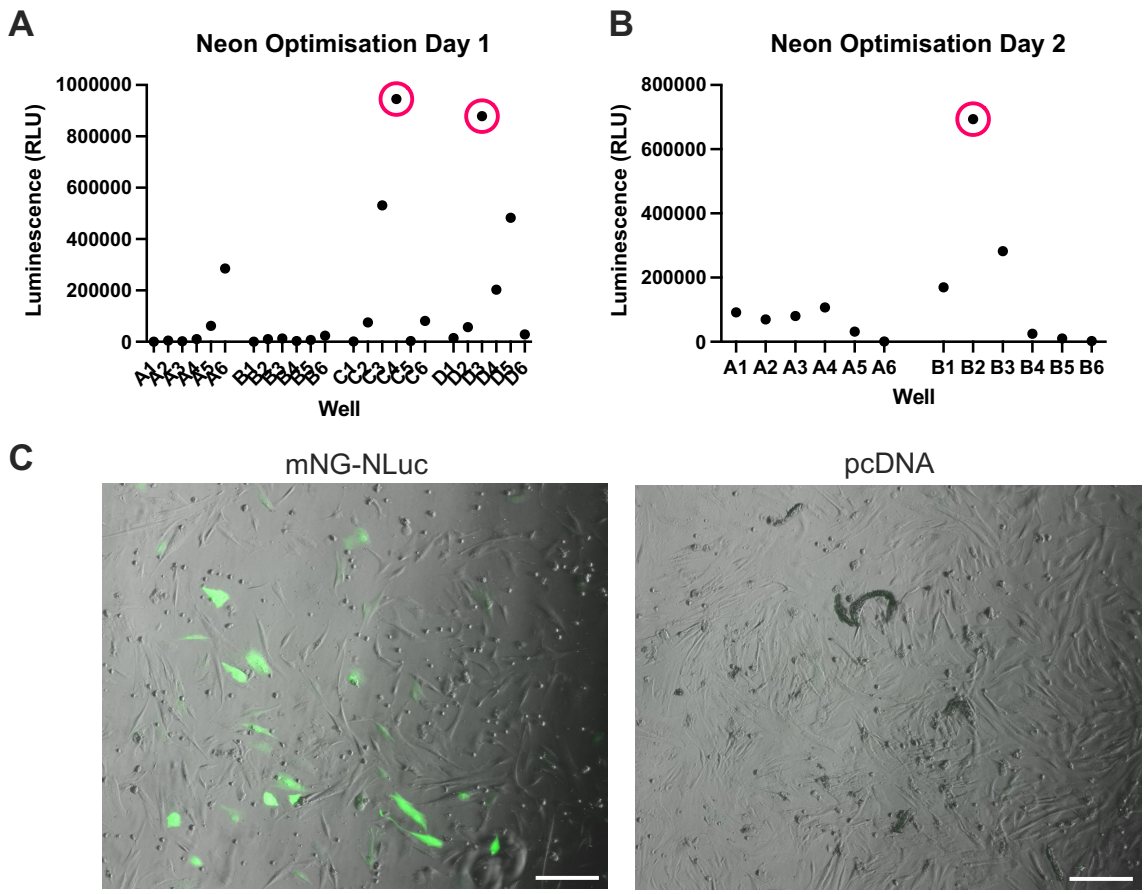

Figure 5.13 - Optimisation of electroporation protocols allows transfection of undifferentiated SGBS cells with mNG-NLuc. A) Undifferentiated SGBS cells were mixed with plasmid DNA expressing mNG-NLuc fusion protein and electroporated using the protocol indicated in Table 5.2. Luminescence values were measured following 10-minute incubation with NanoGlo substrate. Circled conditions were progressed for further optimisation. **B)** As (A), with electroporation protocols indicated in Table 5.3. Circled condition was selected for future work. **C)** Representative brightfield and green fluorescence images of SGBS cells electroporated with mNG-NLuc or pcDNA using 1275 V / 10 ms / 3 pulse protocol selected from (B). Scale bar = 100 µm.

Next, the optimised electroporation parameters were used to transfect a genetically encoded biosensor with FFA4 receptor or pcDNA control into undifferentiated SGBS cells and measure arrestin recruitment **(Figure 5.14).** As the signal window for the NBA plasmid was low, an equivalent BRET-based biosensor was used which allows bystander measurement of arrestin recruitment from a single plasmid where Lyn11-mNeonGreen and NLuc-Arrestin are separated by an Internal Ribosome Entry Site, termed pIRES (Marsango et al., 2022).

Undifferentiated SGBS cells were co-electroporated with 1 µg pIRES biosensor plasmid and 1 µg FFA4 receptor plasmid or pcDNA control. Control samples were electroporated with no DNA added or with the mNG-NLuc plasmid. Luminescence signal was measured from transfected cells 10 mins after addition of NanoGlo substrate **(Figure 5.14A).** The average luminescence signal was ~100,000 RLU for both the pIRES + FFA4 and pIRES + pcDNA conditions, with no DNA control

reaching 3100 RLU and mNG-NLuc showing significantly higher luminescent signal at over 500,000 RLU (****$p < 0.0001$) **(Figure 5.14A)**.

Visualisation of electroporated SGBS cells appeared to show many floating, likely dead cells **(Figure 5.13C).** This observation was confirmed in a CellTitre-Glo viability assay; electroporation with DNA constructs significantly reduced the viability of SGBS cells compared to electroporation alone **(Figure 5.14B).** The viability of pIRES + FFA4 was lower than pIRES + pcDNA, although non-significant ($p = 0.32$), perhaps suggesting that the amount of transcribed DNA is more important than the total amount of DNA transfected, and highlighting that optimisation of DNA amount is critical in maintaining viability of electroporated cells.

In the bystander BRET arrestin recruitment assay, activation of FFA4 using 10 μM TUG-891 resulted in a significant increase in net fold BRET over vehicle in the + FFA4 condition, whereas no response was observed when FFA4 was not transfected **(Figure 5.14C-D).** This indicates that it is possible to use electroporation to transfect genetically encoded biosensors into undifferentiated SGBS cells and measure arrestin recruitment, but the endogenous expression of FFA4 in this cell type is not sufficient to generate a measurable response to TUG-891.

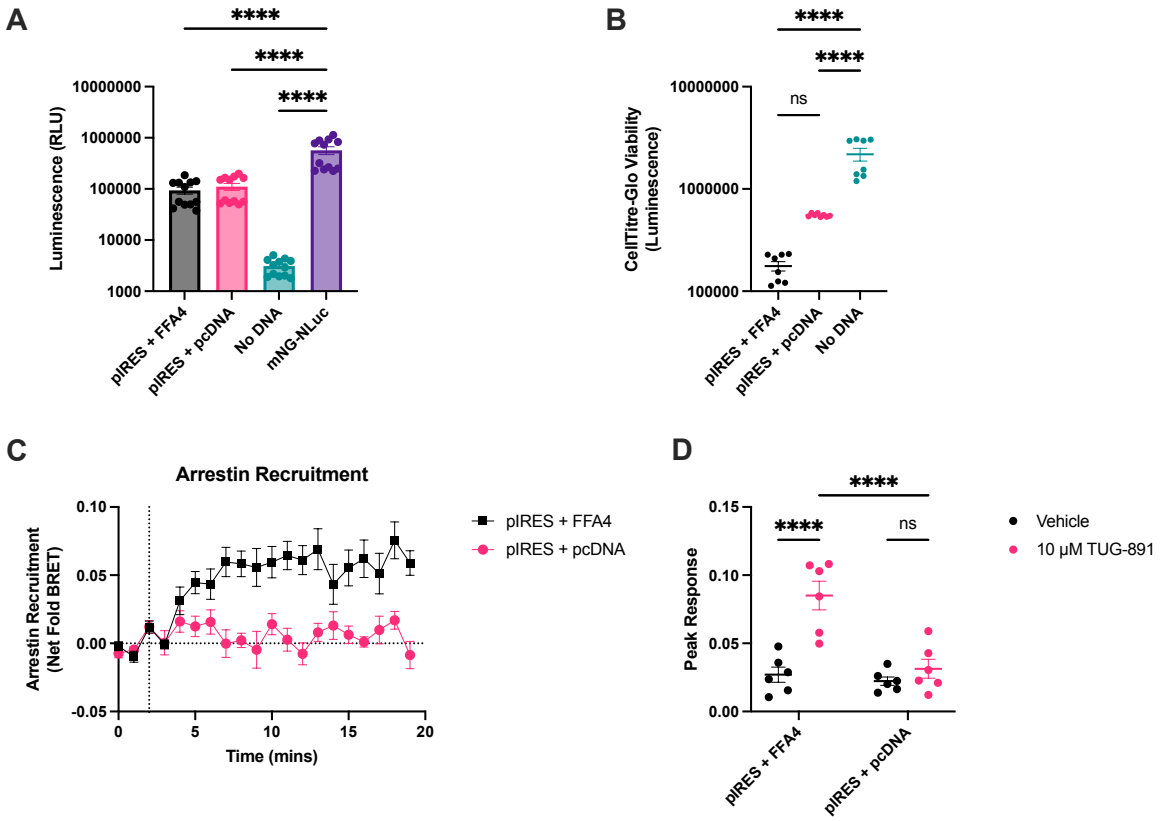

Figure 5.14 - Electroporation of SGBS cells allows measurement of arrestin recruitment using a BRET-based biosensor. A) Undifferentiated SGBS cells were electroporated with plasmids expressing a BRET-based bystander arrestin recruitment biosensor (pIRES) and FFA4 receptor or pcDNA control. Control cells were electroporated with no DNA or mNG-NLuc fusion protein. Luminescence signal was measured 10 mins after addition of NG substrate. Data presented as individual replicates with mean ± SEM indicated from N=2 independent experiments with n=6 technical replicates. Statistical comparisons were made using one-way ANOVA with Tukey's multiple comparisons test. ****p < 0.0001. **B)** CellTitre-Glo viability measurements of electroporated SGBS cells. Data presented as individual replicates with mean ± SEM indicated from N=2 independent experiments with n=4 technical replicates. Statistical comparisons were made using one-way ANOVA with Tukey's multiple comparisons test. ****p < 0.0001. **C)** Kinetic measurements of BRET signal recorded when pIRES biosensor is activated by 10 µM TUG-891 at 2 minutes (indicated by the dotted line). BRET ratios were divided by baseline signal (average of 3 measurements before compound addition) and vehicle response subtracted. Data presented as mean ± SEM from N=2 independent experiments with n=3 technical replicates. **D)** Quantification of peak response from kinetic curves shown in (C). Data presented as individual replicates with mean ± SEM indicated from N=2 independent experiments with n=3 technical replicates. Statistical comparisons were made using two-way ANOVA with Tukey's multiple comparisons test. ****p < 0.0001.

Next, electroporation was used to transfect undifferentiated SGBS spheroids **(Figure 5.15)**. Electroporation is typically carried out using cells in suspension, with a fixed number of cells and amount of DNA per electrical stimulation. For spheroid electroporation, 12-18 spheroids were pooled per stimulation, and the amount of plasmid DNA was optimised. Luminescence signal was then measured from individual or pools of 3 transfected spheroids following incubation with NanoGlo substrate **(Figure 5.15A-B)**. For both individual and pooled spheroids, 1 µg mNG-NLuc plasmid resulted in a significant increase in luminescence compared to no DNA or pcDNA control, and this was taken forward for further

work. Fluorescence microscopy images showed a small number of successfully transfected cells around the periphery of the spheroids, although visualisation is likely hindered due to the challenges of observing 3D structures using an epifluorescence microscope **(Figure 5.15C).**

As with the 2D samples, spheroids were co-electroporated with 0.5 µg pIRES biosensor plasmid and 0.5 µg FFA4 receptor or pcDNA control per 12-18 spheroids, or 1 µg pcDNA control. Luminescence signal was measured from pools of 4 transfected spheroids 10 minutes after addition of NanoGlo substrate, with average luminescence measurements of 3695, 7305 and 341 RLU after 10 minutes for the pIRES + FFA4, pIRES + pcDNA and pcDNA conditions respectively **(Figure 5.15D).** However, despite increasing the measurement read time to 15 s per well, no significant changes in BRET were detected following addition of 10 µM TUG-891, suggesting that transfection efficiency is still too low to facilitate measurement of arrestin recruitment in undifferentiated SGBS spheroids **(Figure 5.15E).**

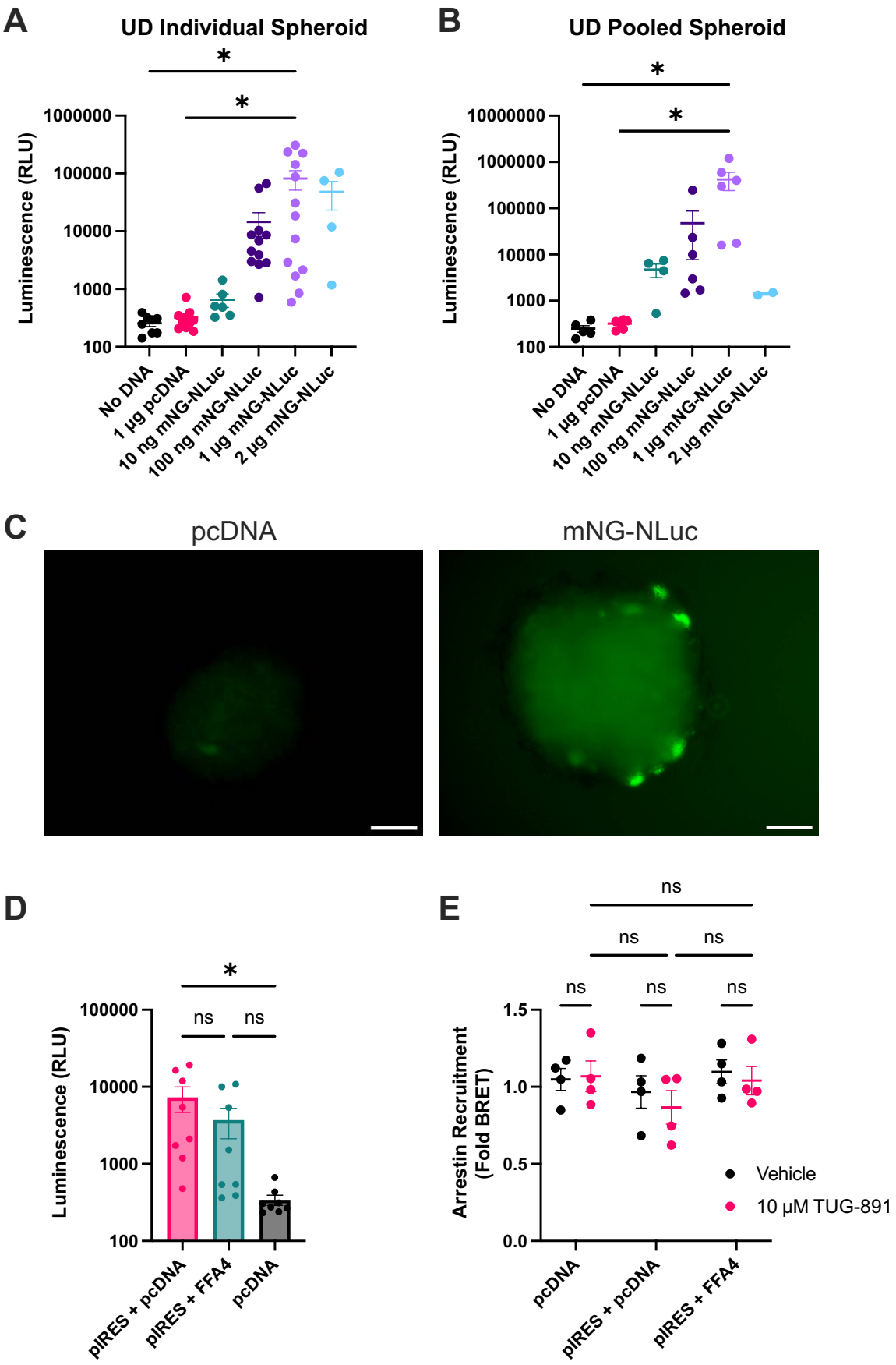

Figure 5.15 - Electroporation can transfect undifferentiated SGBS spheroids but is not sufficient to measure arrestin recruitment. A) Undifferentiated SGBS spheroids were pooled and electroporated with the indicated amount of plasmid expressing mNG-NLuc fusion protein or pcDNA control. Luminescence values were measured from individual spheroids following 10-minute incubation with NanoGlo substrate. Data presented as individual replicates with mean ± SEM indicated from n=2-4 pools of electroporated spheroids across N=1-2 independent

experiments with n=2-4 technical replicates. Statistical comparisons were made using one-way ANOVA with Tukey's multiple comparisons test. *p < 0.05. **B)** As (A) with 3 transfected spheroids pooled before luminescence measurement. Data presented as individual replicates with mean ± SEM indicated from n=2-4 pools of electroporated spheroids across N=1-2 independent experiments with n=1-2 technical replicates. **C)** Representative green fluorescence images of undifferentiated SGBS spheroids electroporated with mNG-NLuc or pcDNA. Scale bar = 100 µm. **D)** Undifferentiated SGBS spheroids were electroporated with plasmids expressing a BRET-based bystander arrestin recruitment biosensor (pIRES) and FFA4 receptor or pcDNA control. 4 spheroids were pooled per well and luminescence signal was measured 10 mins after addition of NanoGlo substrate. Data presented as individual replicates with mean ± SEM indicated from a single experiment with n=8 technical replicates. Statistical comparisons were made using way ANOVA with Tukey's multiple comparisons test. *p < 0.05. **E)** Endpoint BRET measurements were made with 15 s read time per well before and after addition of 10 µM TUG-891 or vehicle control and expressed as fold change of baseline measurement. Data presented as individual replicates with mean ± SEM indicated from a single experiment with n=4 technical replicates. Statistical comparisons were made using two-way ANOVA with Tukey's multiple comparisons test.

Finally, electroporation was used to transfect differentiated SGBS spheroids **(Figure 5.16).** A literature search suggested adipocytes may be better electroporated using a low voltage of 50-200 V (Dugail, 2001; Okada et al., 2003; Granneman et al., 2004), however lowest voltage possible on the Neon device is 500 V. Therefore, an initial comparison of the preadipocyte electroporation parameters (1275 V, 10 ms, 3 pulses) was made with two low-voltage protocols (500 V, 2 ms, 7 pulses or 500 V, 20 ms, 1 pulse) again using the mNG-NLuc plasmid or pcDNA control. As previously, luminescence signal was measured from pools of 4 transfected spheroids 10 minutes after addition of NanoGlo substrate **(Figure 5.16A).** It was found that the preadipocyte protocol remained effective in differentiated SGBS spheroids, with a significant increase over pcDNA control measured (****p < 0.0001). The lower voltage protocols appeared ineffective at transfecting the mNG-NLuc plasmid with no significant difference between mNG-NLuc and pcDNA control.

In an equivalent experiment to the undifferentiated condition, differentiated spheroids were co-electroporated with 0.5 µg pIRES biosensor plasmid and 0.5 µg FFA4 receptor or pcDNA control per 12-18 spheroids, or 1 µg pcDNA or mNG-NLuc control. Luminescence signal was again measured from pools of 4 transfected spheroids resulting in a trending but non-significant increase in signal for the pIRES + FFA4, pIRES + pcDNA and mNG-NLuc conditions compared to pcDNA **(Figure 5.16B).** No changes in BRET response were observed following addition of 10 µM TUG-891 for any of the transfection conditions **(Figure 5.16C).**

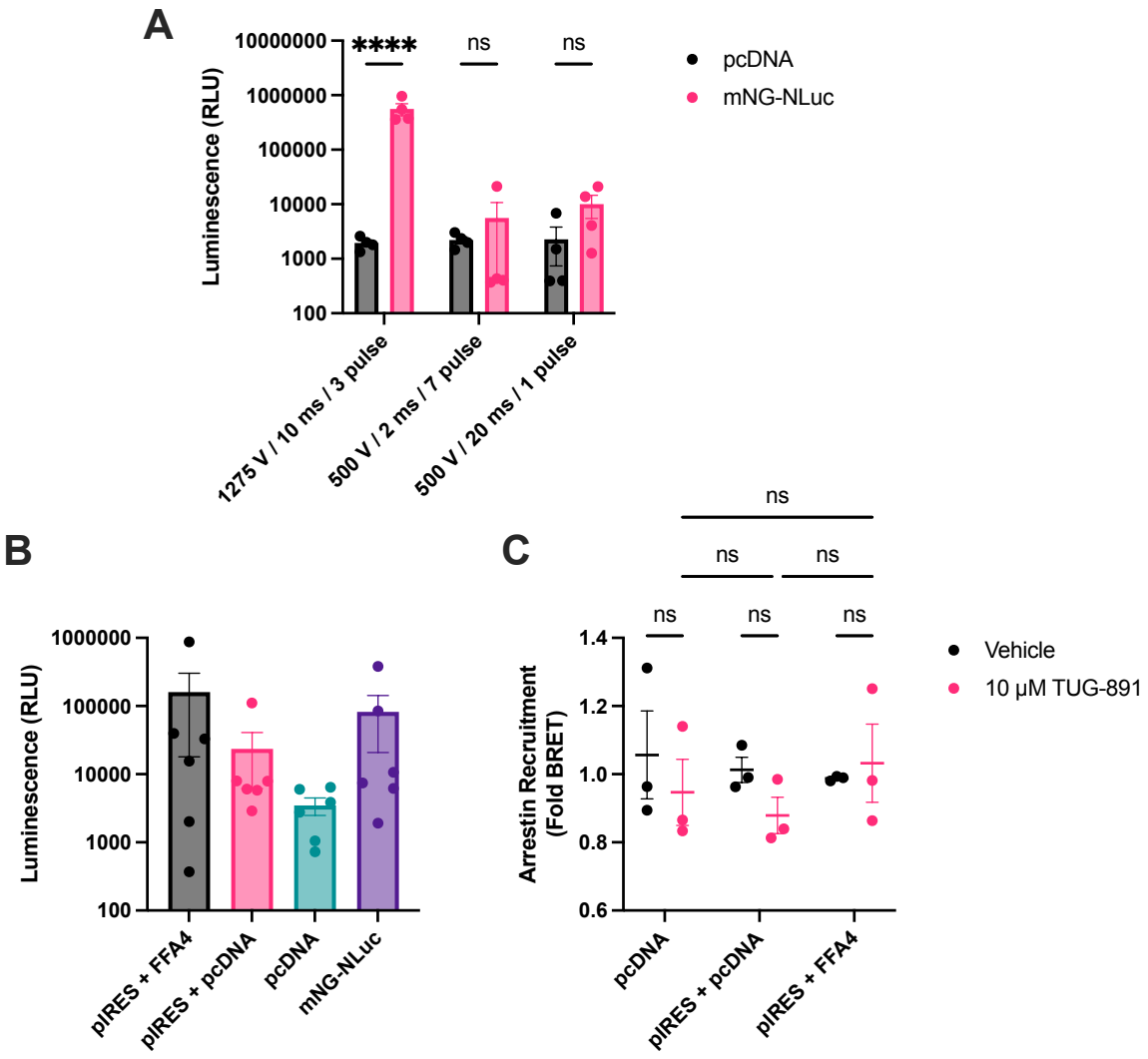

Figure 5.16 - Differentiated SGBS spheroids can be electroporated, but transfection is not sufficient to measure arrestin recruitment. A) Differentiated SGBS spheroids were pooled and electroporated with plasmid DNA expressing mNG-NLuc fusion protein or pcDNA control using the indicated protocol. 4 spheroids were pooled per well and luminescence signal was measured 10 mins after addition of NanoGlo substrate. Data presented as individual replicates with mean ± SEM indicated from a single experiment with n=4 technical replicates. Statistical comparisons were made using two-way ANOVA with Tukey's multiple comparisons test. ****p < 0.0001. **B)** Differentiated SGBS spheroids were electroporated with plasmids expressing a BRET-based bystander arrestin recruitment biosensor (pIRES) and FFA4 receptor or pcDNA control. Control spheroids were electroporated with mNG-NLuc. 4 spheroids were pooled per well and luminescence signal was measured 10 mins after addition of NanoGlo substrate. Data presented as individual replicates with mean ± SEM indicated from a single experiment with n=6 technical replicates. **C)** Endpoint BRET measurements were made with 15 s read time per well before and after addition of 10 µM TUG-891 or vehicle control and expressed as fold change of baseline measurement. Data presented as individual replicates with mean ± SEM indicated from a single experiment with n=3 technical replicates. Statistical comparisons were made using two-way ANOVA with Tukey's multiple comparisons test.

In conclusion, these experiments demonstrated that electroporation is more successful than chemical-based methods for transfection of SGBS cells, and allowed measurement of arrestin recruitment by a genetically encoded BRET biosensor in undifferentiated 2D samples with overexpression of FFA4. Both undifferentiated and differentiated SGBS spheroids were also able to be successfully electroporated with expression of the mNG-NLuc control plasmid

detected. However, the transfection efficiency was still too low to facilitate measurement of arrestin recruitment using pooled samples in a plate reader, and therefore further optimisation or an alternative transfection method is necessary to continue this work.

5.7 Discussion

In this chapter, I endeavoured to use the genetically encoded biosensors and adipocyte spheroids developed earlier in this thesis as tools to investigate the role of m-GPCRs in metabolic disorders. After confirming the expression of these m-GPCRs in the SGBS spheroids, pharmacological tool compounds were used to investigate the functional effect of FFA4, HCA_2 and SUCNR1 activation in adipogenesis and lipolysis. Addition of the cytokine TNF to adipocyte spheroids demonstrated that a pro-inflammatory microenvironment alters the gene expression profile and insulin sensitivity of SGBS spheroids. Finally, several transfection approaches were evaluated to express genetically encoded biosensors in SGBS spheroids for direct measurement of GPCR signalling, however this was not fully achieved within the constraints of this project.

RT-qPCR data demonstrated that expression of all members of the free fatty acid and hydroxycarboxylic acid receptor families, as well as the succinate receptor, are upregulated following differentiation of SGBS spheroids. However, the relative expression levels of these receptors vary, as determined by raw C_T values from qPCR experiments. FFA1 had the lowest expression level, consistent with literature reports that this receptor has low to no expression in adipose tissue and is instead highly expressed in pancreatic islets (Briscoe et al., 2003; Itoh et al., 2003). The short chain fatty acid receptors FFA2 and FFA3 had a modest expression level in this experiment. The literature around expression of these receptors in adipose tissue is somewhat controversial (Bolognini et al., 2016; Ikeda et al., 2022). FFA2 is widely accepted to be expressed in adipocytes (Le Poul et al., 2003; Hong et al., 2005; Ge et al., 2008) but FFA3 expression appears to vary between cell models and species (Brown et al., 2003; Xiong et al., 2004; Hong et al., 2005). The high expression of FFA4, HCA_1 and HCA_2 in adipocytes is well reported and consistent with the qPCR data presented here (Tunaru et al., 2003; Wise et al., 2003; Gotoh et al., 2007). HCA_3 is also reported to be expressed in adipose tissue but at perhaps a lower abundance than HCA_2, again demonstrating consistency with the findings presented here (Soga et al., 2003; Wise et al., 2003). Finally, the succinate receptor is also reported to be highly expressed in adipocytes (Regard et al., 2008; McCreath et al., 2015), however it is not thought to be expressed in the commonly used adipocyte cell line, 3T3-L1 (Regard et al., 2008; Sun et al., 2020). As SUCNR1

was expressed in differentiated SGBS adipocyte spheroids, this platform may provide an alternative and useful model for *in vitro* studies of the SUCNR1 receptor.

Next, pharmacological tool compounds were used to investigate the role of m-GPCRs during adipogenesis. In 2D adipocytes, inverse agonism of FFA4 by AH7614 appeared to inhibit lipid droplet accumulation, although only modest changes in gene expression were observed. This is largely consistent with comparable experiments in 3T3-L1 cells (Alshammari et al., 2025) and with studies in the wider literature linking FFA4 genetic knockdown and pharmacological inhibition to inhibition of adipogenesis (Gotoh et al., 2007; Song et al., 2016; Watterson et al., 2017). Interestingly, this finding appeared to be reversed in the spheroid experiment, where FFA4 agonism using TUG-891 appeared to reduce lipid accumulation, and AH7614 showed no effect. This may indicate an unexpected and crucial difference between the mechanisms of adipogenesis between 2D and 3D microenvironments. However, as discussed in **Chapter 4**, the Oil Red O staining method is perhaps not the most reliable for the quantification of differentiation in spheroid models. An alternative approach may be to use a live-cell imaging or high-content analysis pipeline using an instrument such as the Incucyte (Sartorius) to measure parameters such as increased spheroid diameter observed during differentiation **(Chapter 4)** or quantification of a fluorescent neutral lipid stain in a high-throughput, automated manner, and thus allowing validation of these findings.

These data suggested that activation of the HCA_2 and SUCNR1 receptors resulted in a modest enhancement of lipid accumulation in SGBS spheroids. There is very limited literature available investigating these receptors in adipogenesis, with a single study suggesting that addition of 50 μM niacin to differentiating 3T3-L1 cells shows no change in lipid accumulation or gene expression (Mandrika et al., 2018). These findings may however be indicative of the well-reported anti-lipolytic effects of these receptors preventing baseline lipolysis (Tunaru et al., 2003; Regard et al., 2008). Unlike FFA4, where the endogenous long chain fatty acid ligands are released directly from adipocytes and able to signal in an autocrine and/or intracrine manner (Husted et al., 2020; O'Brien et al., 2025), the endogenous ligands for HCA_2 and SUCNR1 require additional stages which may not be modelled in this system; fatty acids require oxidation in the liver to

form the HCA_2 ligand BHB (Newman and Verdin, 2017) and succinate is only released from adipocytes during periods of metabolic stress (Ariza et al., 2012; de Castro Fonseca et al., 2016), although the high glucose levels in cell culture medium may also induce elevated succinate levels (Tanis et al., 2015). This further highlights the requirement to investigate m-GPCRs and their ligands in physiologically relevant systems to better understand their complex signalling pathways.

In the lipolysis assay, activation of FFA4, HCA_2 and SUCNR1, using TUG-891, niacin, and succinate respectively, were able to inhibit isoprenaline-stimulated glycerol release. Both niacin and succinate significantly inhibited the measured response, whereas TUG-891 resulted in a more modest trend. The limited FFA4 effect may be a consequence of TUG-891 binding to BSA in the buffer; a 30 μM TUG-891 concentration in 0.5% BSA is only demonstrating around 50% efficacy in an arrestin recruitment assay **(Figure 5.4B)** whereas the 10 μM niacin and 1 mM succinate used are likely reaching maximal efficacy (Zhang et al., 2005; Regard et al., 2008). As mentioned, the anti-lipolytic effects of these receptors are well documented and thus the results obtained were expected. However, this is the first demonstration of these effects in a 3D adipocyte spheroid platform, thus providing additional validation of the spheroid model and highlighting its potential for use in further studies of m-GPCRs. Future work should focus on understanding the endogenous ligands of these receptors *in situ*, i.e. through stimulation of lipolysis releasing fatty acids or triggering succinate release by hypoxia, rather than exogenous application of artificial ligand concentrations.

The incorporation of inflammation to the SGBS spheroids through supplementation with TNF changed the gene expression profile of select adipogenic and inflammatory markers, and affected adipocyte function by reduction of insulin-stimulated glucose uptake. Although non-significant, a clear trend was observed that addition of TNF reduced the viability of SGBS spheroids. The concentration of TNF used here was selected based on literature reports from *in vitro* studies using TNF to induce insulin resistance in SGBS or 3T3-L1 adipocytes (Stephens et al., 1997; Ruan et al., 2002; Massaro et al., 2016; Quarta et al., 2021). It is likely that these conditions could be further optimised for example by reducing TNF concentration, using a low-glucose medium, or

addition of hypoxia (Lo et al., 2013; Odeniyi et al., 2024) to achieve the desired inflammatory phenotype while maintaining spheroid viability.

A further consideration in these studies is whether the concentration of TNF used is appropriate to model the chronic low-level inflammation associated with metabolic disorders. It is well known that levels of circulating TNF are increased in obese and diabetic individuals (Pfeiffer et al., 1997; Katsuki et al., 1998; Tsigos et al., 1999; Zahorska-Markiewicz et al., 2000; Bruun et al., 2003; Olszanecka-Glinianowicz et al., 2004; Eswar et al., 2024). However, the specific concentrations of TNF measured can vary dramatically between studies, with values ranging from 1.6 to 21.7 pg/mL in lean individuals, and 2.9 to 238.6 pg/mL in obesity, with differences dependent on sex, ethnicity, and distribution of adipose tissue (Pfeiffer et al., 1997; Tsigos et al., 1999; Eswar et al., 2024). Consequently, the concentration of TNF used in *in vitro* studies using adipocytes can also vary considerably, with concentrations ranging from 100 pg/mL to 20 µg/mL and concentration dependent effects reported for inhibition of adipogenesis (Chae and Kwak, 2003; Cawthorn et al., 2007), reduced insulin sensitivity (Stephens et al., 1997), and enhanced lipolysis (Kawakami et al., 1987). It may therefore be valuable to determine whether the TNF-mediated effects recorded here are also concentration-dependent.

In this study, RT-qPCR was used to assess changes in gene expression caused by addition of TNF. It was found that expression of the pro-inflammatory chemokine CCL2 was significantly upregulated, with a modest, non-significant increase in IL-1ß expression. A logical next step would therefore be to quantify the levels of these released cytokines in the spheroid supernatant using ELISA or similar kits. Expression of adiponectin and GLUT4 were significantly downregulated after 14-day TNF treatment. Adiponectin is a hormone secreted by adipocytes which is thought to improve insulin sensitivity by a series of mechanisms (Fang and Judd, 2018), and GLUT4 is the primary glucose transporter responsible for insulin-sensitive glucose uptake in adipose tissue (Bryant et al., 2002). Together, therefore, this may suggest that TNF treatment would result in an insulin-resistant phenotype. This is indeed observed in the glucose uptake assay. Interestingly, the downregulation of these markers is less pronounced after 24h TNF treatment compared to the 14-day treatment, however the reduction in glucose uptake is greater with the shorter treatment. In the literature, there are

limited studies investigating prolonged TNF exposure over several days, with most studies tending to compare TNF treatments at shorter time courses of 1-24h (Massaro et al., 2016; Avelino et al., 2024; Odeniyi et al., 2024). In 3T3-L1 cells, it has been reported that 13-day incubation with TNF reduces insulin-stimulated glucose uptake compared to 24h treatment, driven through an increased basal glucose uptake level and reduced GLUT4 expression (Stephens and Pekala, 1991), with subsequent studies suggesting that no further reduction in insulin-stimulated glucose uptake is achieved with TNF treatments longer than 96h (Stephens et al., 1997). It is therefore unclear why the glucose uptake response measured here in 3D human adipocyte spheroids was further reduced in adipocyte spheroids treated with TNF for 24h compared to 14 days. One possible explanation may be that 24h treated spheroids may have a slightly elevated basal glucose uptake level (Stephens and Pekala, 1991), thus resulting in a reduced fold increase in glucose uptake measured compared to 14 day TNF-treated spheroids. Alternatively, compensatory mechanisms may develop following prolonged TNF treatment, for example upregulation of other components of the insulin signalling cascade, which improve insulin sensitivity in this system.

Perhaps the most intriguing finding was the observation that the FFA4 receptor is upregulated following acute TNF exposure. This could support the hypothesis that FFA4 is a key mediator of communication between adipocytes and macrophages (Duncan et al., 2023); the presence of TNF may indicate to the adipocytes that infiltrating macrophages are near, and FFA4 is upregulated to prepare for long chain fatty acid signalling loops promoting anti-inflammatory and anti-lipolytic effects. Macrophages may also provide their own source of long chain fatty acids, including arachidonic acid, through hydrolysis of phospholipids by phospholipase A2 (PLA_2), which could feasibly activate FFA4 on adipocytes (Christiansen et al., 2015) although this has not yet been fully investigated (Duncan et al., 2023). This again highlights the critical need for better methods to study complex m-GPCR signalling dynamics in physiologically relevant systems. Expression of HCA_2 and SUCNR1 were not measured in this experiment but should be investigated in future work.

This initial study of a pro-inflammatory microenvironment in adipocyte spheroids also indicates how much additional work is required in this field to build from

the effects of a single cytokine to complex multicellular systems. As a follow up to these experiments, I would first progress to studying the effects of a conditioned medium from human macrophages such as PMA-differentiated THP-1 cells (Tsuchiya et al., 1980, 1982). From there, it may be possible to build to a transwell model where adipocytes are cultured in close proximity to macrophages before progressing to a direct co-culture model.

Beyond the technical challenges with completing such complex experimental setups, such as identifying a suitable culture medium for co-culture studies, there are also significant biological challenges to address. Inflammation throughout differentiation of preadipocytes has been shown to inhibit adipogenesis in 3T3-L1, SGBS and primary human cells (Constant et al., 2006; Yarmo et al., 2010; Keuper et al., 2011b). It is therefore possible that conclusions drawn from these studies are not due to comparisons between inflamed and non-inflamed adipocytes, but comparisons of mature adipocytes to preadipocytes. Although it is possible that development of insulin resistance *in vivo* is driven by reduced adipogenesis (Gustafson et al., 2015; Moreno-Indias and Tinahones, 2015), it would be valuable to assess the relative contribution of reduced preadipocyte differentiation to the effect from mature adipocytes. Therefore, the time at which inflammation is incorporated must be carefully considered to ensure conclusions are valid. In this work, the adipogenic markers assessed in the RT-qPCR experiment were slightly downregulated in the 14-day TNF treatment compared to control, although this was only significant for adiponectin and GLUT4 already discussed. The expression of FABP4 and FFA4 were not significantly reduced, however it is possible that their modest reduction is due to the TNF-treated spheroids not differentiating as effectively in the presence of inflammation. Again, an improved quantitative measure of lipid accumulation would aid in answering this pertinent question by clearly separating this aspect of differentiation from expression of adipogenic markers.

Several studies have investigated the effect of inflammation on SGBS cells in 2D using various methods. Addition of 10 ng/mL TNF for 18-24 hours was shown to reduce GLUT4 and adiponectin transcription, increase expression of inflammatory markers CCL2, CXCL-10 and ICAM-1 and inhibit insulin stimulated glucose uptake (Massaro et al., 2016; Quarta et al., 2021), consistent with the findings presented here and with earlier work investigating similar responses in

3T3-L1 adipocytes (Stephens et al., 1997; Ruan et al., 2002). Treatment of SGBS cells with macrophage conditioned medium followed by direct co-culture with THP-1 macrophages resulted in impaired adipogenesis when treated throughout differentiation, but also demonstrated impaired glucose uptake, lipogenesis and insulin signalling after only 24 hours of treatment (Keuper et al., 2011b, 2011a). There has been less reported on the effects of inflammation on adipocyte spheroids, although one study reported impaired metabolic function of 3T3-L1 spheroids when treated with TNF (Turner et al., 2015) and a further investigated the interaction between macrophages and adipocyte spheroids from primary human sources, although did not report the effects on adipocytes (Shen et al., 2020). A more recent study also showed that 3T3-L1 spheroids treated with 2.5 nM TNF for 24h somewhat mimicked the proteomic signatures of primary white adipose tissue obtained from diet-induced obese mice (Avelino et al., 2024). There is therefore clear scope for further investigation of the pro-inflammatory microenvironment within complex 3D adipocyte systems.

In this chapter, a series of optimisation experiments were carried out to facilitate transfection of adipocytes with genetically encoded biosensors to measure m-GPCR signalling. Although expression of a mNG-NLuc reporter construct was possible using the lipofection and PEI methods, these approaches were not sufficient to allow measurement of arrestin recruitment in undifferentiated or differentiated SGBS monolayers using a plate reader. This is consistent with literature reports where lipofection is typically used only for expression of small constructs such as micro or short interfering RNAs in SGBS cells (Enlund et al., 2014; Landgraf et al., 2020), rather than large DNA constructs such as those that encode fluorescent proteins. To overcome these issues and maintain the advantages of lipofection approaches over other transfection methods (notably cost, accessibility and safety), one group has conjugated PEI to nuclear localisation peptide sequences and showed this improved transfection efficiency in 3T3-L1 and primary human ADSCs (Park et al., 2015), offering a novel solution to this challenge. The apparent improvement when using mRNA transfection in differentiated SGBS adipocytes is perhaps unsurprising. It is thought that the lipid droplets present in adipocytes act as a barrier preventing effective translocation of genetic material into the nucleus; this step is not required with mRNA transfection (Conry et al., 1995;

Qin et al., 2022). mRNA transfection has therefore been proposed as an effective alternative to DNA transfection in difficult to transfect cell types including macrophages (Van De Parre et al., 2005; Chandra and Philips, 2018), neural stem cells (McLenachan et al., 2013) and several cancer cell lines (Juncker et al., 2023), consistently achieving higher transfection efficiencies and viability than DNA transfection controls (Van De Parre et al., 2005; McLenachan et al., 2013; Juncker et al., 2023). It has also been reported that electroporation with mRNA constructs leads to higher transfection efficiencies than chemical transfection methods (McLenachan et al., 2013; Juncker et al., 2023), suggesting this may be a promising direction for future transfection optimisation of SGBS spheroids.

The polycistronic NBA biosensor, where the Lyn11-LgBiT and SmBiT-Arr constructs were separated by a self-cleaving P2A peptide sequence, was designed to improve the NBA assay in adipocytes by only requiring a single plasmid to be transfected. However, the performance of this biosensor was poor in HEK293-T cells, with a smaller fold response following addition of TUG-891 than the original two component biosensor, likely driven by an increase in the baseline signal. It was not determined whether the increased baseline signal was due to incomplete cleavage of the biosensor peptide or simply a higher transfection efficiency of this plasmid. This may be tested by using a western blot to establish whether transfection of the NBA plasmid results in a protein band of appropriate size to be a fusion of Lyn11-LgBiT and SmBiT-Arr as well as the individual components, alongside further optimisation of DNA transfection amounts and comparison to other polycistronic separation motifs. mRNA transfection of the biosensor was unable to measure arrestin recruitment in differentiated SGBS cells, although this experiment was missing a key control in that the HEK293-T cells did not express the FFA4 receptor and therefore a response to TUG-891 could not be observed. If progressed, these experiments could be repeated in Flp-In 293 cells stably expressing the FFA4 receptor to confirm that mRNA transfection of the NBA biosensor can measure arrestin recruitment.

The electroporation transfection method was more successful, with expression of mNG-NLuc obtained in both undifferentiated and differentiated SGBS cells and spheroids. Arrestin recruitment measurements were possible in undifferentiated SGBS monolayers with overexpression of FFA4 but have not yet

been obtained with endogenous FFA4 expression in adipocytes, or in spheroid cultures. Again, this is consistent with literature reports where electroporation and/or nucleofection approaches have shown success in transfection of SGBS cells (Schweiger et al., 2012; Kässner et al., 2020) and in other adipocyte cell models (Dugail, 2001; Okada et al., 2003; Zaragosi et al., 2007; Granneman, 2008). However, the transfection efficiency was still low. This may be due to non-optimal electroporation parameters; electroporation of differentiated adipocytes typically uses a lower voltage than is possible using the Neon transfection system (Dugail, 2001; Okada et al., 2003; Granneman et al., 2004). No literature protocols were found which used the Neon for electroporation of differentiated adipocytes, potentially as this method requires cells in suspension and adipocytes are notorious for poor re-adhesion once harvested (Strnadová et al., 2024). The work presented in this thesis therefore likely represents the first successful protocol to electroporate differentiated adipocytes using the Neon system, with the advantage that the spheroids are maintained in suspension. Furthermore, although there are examples of spheroid electroporation in the literature, these typically involve custom or modified instruments including microfluidic chips and have largely been used to model delivery of chemotherapeutic drugs (Gibot et al., 2013, 2020; Bregigeon et al., 2022). This is therefore also likely to be the first example of spheroid electroporation using a widely available, unmodified device.

While the transfection efficiency achieved for SGBS adipocyte spheroids was too low to successfully investigate GPCR signalling in plate-based assays, there are examples of single-cell and microscopy-based applications where genetically encoded biosensors may still be used despite this low transfection efficiency. Genetically encoded BRET and NanoBiT biosensors have been studied at single-cell or subcellular resolution using microscopy to measure aspects of GPCR signalling, including arrestin recruitment, internalisation and intracellular trafficking (Namkung et al., 2016; Hattori et al., 2025). It may therefore be feasible to use the traditional or colour-shifted NBA biosensors developed in **Chapter 3** to measure arrestin recruitment in the small population of successfully transfected cells using BRET microscopy in 2D SGBS cultures. While BRET microscopy is likely to be technically challenging in 3D spheroids due to the requirement for confocal or light sheet microscopy to obtain high resolution

images of intact spheroids, there are examples of genetically encoded FRET biosensors used to measure glucose concentration (Maioli et al., 2016), apoptosis (Anand et al., 2015; Weber et al., 2015) and AMPK activity (Chennell et al., 2016) in spheroid cultures. It may therefore be possible to combine a FRET-based GPCR biosensor such as the SPASM (Malik et al., 2013) or G protein dissociation (Janetopoulos et al., 2001) with the spheroid transfection protocols developed here to measure m-GPCR signalling in single cells within the SGBS adipocyte spheroids. This would therefore allow further investigation into the function of these receptors within a complex *in vitro* model system.

Ultimately, the best approach for expressing the biosensor constructs in adipocytes is likely by viral transduction, which has been successful in SGBS cells (Fischer-Posovszky et al., 2012; Iwata et al., 2012) and adipocyte spheroids (Shen et al., 2021). Briefly, these methods involve packaging of the desired construct in a non-replicating DNA virus which can infect the target cell, allowing effective expression of the construct in a transient or stable manner depending on the specific viral vector used (Glover et al., 2005). Typically, adenoviruses are used for transient expression of constructs whereas lentiviral vectors facilitate stable integration of the gene of interest into the host cell genome (Yudaeva et al., 2024). In the case of adipocyte spheroids, it is possible that stable integration of the construct is preferred, as this would allow transduction of the SGBS preadipocytes before spheroid formation and allow expression to be maintained throughout differentiation (Collon et al., 2022). Unfortunately, it was not possible to set up the requisite safety approvals for viral transduction experiments within the timescale of this project. It is possible to generate cell lines stably expressing a gene of interest through transfection with PEI and following a traditional single-cell clonal selection protocol (Longo et al., 2014). However, given the limited differentiation capacity of SGBS cells discussed in **Chapter 4**, it is likely that by the time a clonal cell line is obtained, the SGBS cells would no longer be able to undergo adipogenesis.

Overall, in this chapter I have demonstrated that SGBS adipocyte spheroids represent a novel platform for studies into m-GPCRs in a physiologically relevant microenvironment, through pharmacological modulation of adipocyte function and incorporation of inflammation through treatment with TNF. I have also highlighted the challenges with expressing genetically encoded biosensors in this

system, but demonstrated that electroporation can introduce fluorescent proteins into preadipocyte and adipocyte spheroids, thus offering a potential avenue for further optimisation.

6 Final Discussion

Metabolic diseases including obesity and T2D are a major global healthcare and economic burden affecting over 1 billion people worldwide (World Obesity Federation, 2025). These diseases are typically caused by excessive accumulation and subsequent dysfunction of adipose tissue, leading to impaired metabolic regulation and severe downstream consequences for patients (World Health Organisation, 2021, 2025; Institute for Health Metrics and Evaluation, 2024). Low-level chronic inflammation of adipose tissue is an important hallmark of metabolic disease and is thought to be a key driver in the development of insulin resistance (Artemniak-Wojtowicz et al., 2020; Rohm et al., 2022). m-GPCRs responding to metabolites released from autocrine and paracrine sources may facilitate communication between adipocytes and infiltrating macrophages (Husted et al., 2017), and therefore targeting these receptors may be a promising strategy to develop novel treatments for metabolic disease (Duncan et al., 2023). However, there is a pressing need to develop new tools and experimental models to better understand these complex metabolic signalling networks in physiologically relevant cell systems. In this thesis, I aimed to develop and characterise a novel 3D human adipocyte spheroid model, incorporating features of the *in vivo* adipose tissue microenvironment, while maintaining the benefits of *in vitro* systems. Furthermore, I endeavoured to design and integrate a genetically encoded biosensor which would allow real-time measurement of m-GPCR signalling and therefore improve our understanding of m-GPCRs in adipose tissue function.

In **Chapter 3**, a series of genetically encoded biosensors were developed to measure different aspects of the GPCR signalling cascade using the FFA4 long chain fatty acid receptor as a model. By using bystander NanoBiT split luciferase technology (Dixon et al., 2015), these biosensors could measure real time mG protein binding and arrestin recruitment of unmodified receptors with a single wavelength measurement. Furthermore, preliminary experiments using colour-shifted NanoBiT biosensors demonstrated the potential of these biosensors to be used in multiplexed assays to simultaneously measure GPCR activation in co-cultured cell types or from different cellular compartments (Lan et al., 2012; O'Brien et al., 2025). However, attempts to express these biosensors in SGBS adipocytes reported in **Chapter 5** proved to be challenging. Poor transfection

efficiencies were achieved despite extensive optimisation in undifferentiated or differentiated adipocytes using PEI, lipofectamine and electroporation approaches using DNA or mRNA cargoes, in either monolayer or spheroid formats. This therefore prevented the use of these biosensors to measure the activity of endogenous GPCRs in more physiologically relevant cell types during this project.

This technical difficulty was perhaps unsurprising, as pre-adipocytes and mature white adipocytes are notoriously challenging to transfect, in part due to their high lipid content hindering access of transfected DNA to the nucleus (Dugail, 2001; Park et al., 2015; Romanelli and Macdougald, 2020). Ultimately, viral transduction methods are likely required to achieve higher efficiency when expressing biosensor constructs in adipocytes, although questions remain about the optimal timing of transduction. Adenoviral transduction would likely improve expression of constructs in differentiated adipocytes (Bérériat et al., 2005; Bates et al., 2020), however the transient nature of this expression would therefore require transduction of intact, differentiated spheroids. It remains to be seen whether this would only facilitate expression in the outermost cell layer of the spheroids or penetrate deeper within the spheroid core, and what impact this may have on any results. Conversely, lentiviral transduction facilitates stable integration of the construct into the genome of cells (Yudaeva et al., 2024). This would therefore allow transduction of cell monolayers which could then be used to form spheroids expressing biosensors through their entire structure and throughout the differentiation process (Collon et al., 2022). This strategy would therefore allow investigation of how m-GPCR signalling dynamics may change during adipogenesis, and provide further mechanistic insight to the role of these receptors in adipocyte function.

If suitable transfection efficiencies are achieved, genetically encoded biosensors could be used to answer pertinent questions about FFA4-mediated long chain fatty acid signalling loops in adipose tissue. For example, to assess autocrine signalling of long chain FFAs in adipocyte spheroids, the NBA or mG biosensors could be used to measure FFA4 activation in response to exogenous application of individual or combinations of FFAs, or FFAs released following stimulation of lipolysis. Similarly, to investigate whether FFAs released from macrophages could signal to adipocytes in a paracrine manner, FFA4 activation could be

measured in response to conditioned medium from e.g. THP1 macrophages, both with and without PLA_2 stimulation triggering release of long chain FFAs through hydrolysis of phospholipids (Murawska et al., 2024). These experiments could be completed at different stages of adipogenesis and with incorporation of inflammatory mediators (or activation of macrophages using e.g. LPS) to assess differences in signalling due to phenotypic changes in the spheroids.

Some success has been achieved generating 3T3-L1 adipocyte cell lines which stably express genetically encoded biosensor constructs to measure GPCR signalling (Vita, unpublished). However, to create clonal cell lines where the biosensor is integrated into the same genomic location across the entire cell population, the cell line must be generated following isolation of a single expressing cell (Longo et al., 2014). As discussed in **Chapter 4**, SGBS cells have a limited capacity for differentiation above a certain number of population doublings (Wabitsch et al., 2001). It is therefore likely that SGBS cell lines would have reduced differentiation capacity following single cell isolation and expansion, therefore limiting their utility as a model of mature adipocytes. However, as discussed in **Chapter 5**, the transfection efficiency already achieved by spheroid electroporation may be sufficient to measure m-GPCR signalling using FRET biosensors in single cell microscopy experiments.

In this thesis, SGBS cells were the only adipocyte model used for transfection studies. As discussed in **Chapter 5**, the limited use of these cells in the wider literature meant no published protocols were identified which reported efficient transfection of DNA into these cells using chemical or electroporation-mediated methods. It would therefore be pertinent to attempt transfection of alternative adipocyte models such as 3T3-L1 cells (Okada et al., 2003), ADSCs (Park et al., 2015), or immortalised brown adipocytes (O'Brien et al., 2025) for which successful transient DNA transfection protocols have been reported, to validate whether these biosensors are effective in measuring m-GPCR activation in adipocytes. It is also important to note that the bystander biosensors designed in **Chapter 3** are not specific to the FFA4 receptor, and therefore have the potential to measure signalling of other GPCRs in physiologically relevant cell types which may be easier to transfect. Indeed, these biosensors have already been used to investigate the pharmacology of the FFA1 receptor (Valentini et al., 2025) in HEK293-T cells, and this work could be expanded to insulinoma cell

lines (e.g. MIN-6 or INS-1), which have higher transfection efficiencies (Ohsugi et al., 2005; Gong et al., 2015) to investigate FFA1 signalling.

In **Chapter 4**, a 3D adipocyte spheroid model was generated by seeding human SGBS pre-adipocyte cells in ULA plates and differentiating them into mature adipocytes. Characterisation of this model system using a range of imaging approaches, analysis of gene and protein expression, and functional assays demonstrated that SGBS spheroids undergo adipogenesis, demonstrated by accumulation of lipid droplets and expression of adipogenic markers at both the gene and protein levels. Additionally, differentiated SGBS adipocyte spheroids could complete characteristic adipocyte functions including ß-adrenoceptor-stimulated lipolysis and insulin-stimulated glucose uptake. Critically, throughout this project, several experimental protocols were generated and optimised; these may now be employed when using 3D adipocyte models to answer pertinent questions about adipocyte function and dysfunction in metabolic disease.

Biologically, SGBS adipocyte spheroids appeared to have an asymmetric differentiation pattern, where cells around the outside of the spheroid accumulated larger lipid droplets and express higher levels of adipogenic protein markers than those in the spheroid core. No evidence of hypoxia was found in the centre of spheroid structures, although this conclusion may be confirmed by comparing HIF-1α expression to spheroids cultured in low oxygen conditions. Furthermore, more lipid droplets were observed on one side of the spheroid than the other, possibly thought to be a consequence of spheroid differentiation in the 384-well ULA plates. Comparison of these findings to alternative methods of spheroid generation such as magnetic levitation (Daquinag et al., 2013) or hanging droplet (Klingelhutz et al., 2018) techniques may address this unanswered question. Expansion of these findings may include use of -omics approaches such as single cell RNA sequencing (Tang et al., 2009; Jovic et al., 2022) to investigate broader transcriptomic changes occurring during adipogenesis, as well as clustering of cell populations which may express different genes based on their position within the spheroid.

In **Chapter 5**, it was shown that m-GPCRs affect the lipolytic function of SGBS adipocyte spheroids, with addition of succinate and niacin as agonists for the

SUCNR1 and HCA_2 receptors respectively leading to a significant inhibition of isoprenaline-stimulated lipolysis, consistent with previous reports (Zhang et al., 2005; Regard et al., 2008). It was also shown that addition of the FFA4 inverse agonist AH7614 reduced lipid accumulation of SGBS adipocytes in 2D consistent with results in 3T3-L1 cells (Alshammari et al., 2025), however attempts to repeat this finding in spheroids were not conclusive. Advancement of this work may require further technical development of spheroid assays, for example a quantitative measure of differentiation based on lipid accumulation or spheroid size, to identify more nuanced changes in adipogenesis following treatment with m-GPCR compounds. The contribution of m-GPCRs to adipocyte function may also be investigated by using siRNA knockdown or CRISPR-mediated knockout of these receptors in SGBS cells (Lee et al., 2013a; Tews et al., 2013; Chen et al., 2020; Kamble et al., 2020) and measuring the resulting effect on lipolysis, adipogenesis and other adipocyte functions such as glucose uptake and adipokine secretion.

Finally, addition of the cytokine TNF to adipocyte spheroids demonstrated altered gene expression profiles as well as a reduction in insulin-stimulated glucose uptake, perhaps modelling a pro-inflammatory phenotype more representative of metabolic disease. It was found that expression of the FFA4 receptor was significantly elevated following an acute treatment with TNF, perhaps supporting the hypothesis that paracrine signalling of fatty acids through the FFA4 receptor may play a role in communication between adipocytes and infiltrating immune cells in metabolic disease (Duncan et al., 2023). The functional implication of this finding is yet to be elucidated, but in the first instance it may be interesting to determine whether the limited effects of FFA4 compounds observed in the lipolysis assay are enhanced if spheroids are first treated with TNF. Taken together, the SGBS spheroids developed and characterised here have allowed the function of m-GPCRs to be assessed in adipocytes, but further work is required to more clearly define the specific mechanistic contribution of these receptors in metabolic disease.

The SGBS adipocyte spheroid platform developed here has many potential applications to address unanswered questions about adipogenesis and adipocyte function. For example, it would be interesting to determine whether currently approved obesity therapeutics such as GLP-1 receptor agonists have any effect

on gene expression, glucose uptake or lipolytic function of adipocyte spheroids. Similarly, the model could be used to measure the effects of other substances such as chemicals, drugs, or nutrients on adipocyte differentiation. There is some current literature suggesting microplastics may act as human 'obesogens', with exposure to these particles potentially driving the increasing prevalence of obesity (Kannan and Vimalkumar, 2021). The SGBS adipocyte spheroids could therefore provide an opportunity to investigate the effects of microplastics on adipogenesis in a physiologically relevant human cell system.

3D cell culture models incorporate more features of the *in vivo* microenvironment than traditional 2D monolayers with more physiologically relevant cell-cell contacts, nutrient and oxygen diffusion gradients and physical forces than traditional cell culture on plastic or glass substrates (Baker and Chen, 2012; Jensen and Teng, 2020). A major limitation to this work is therefore the lack of comparison between the 3D cell models with either 2D cultured adipocytes or *ex vivo* adipose tissue samples to validate that this 3D model does in fact better recapitulate features of primary adipose tissue than monolayer cultures. Similarly, it would be beneficial to compare spheroids generated from SGBS cells, 3T3-L1 cells and human primary adipocytes to assess whether the human SGBS cells do behave more like the primary human cells than the murine-derived 3T3-L1 cells. Although literature reports have suggested 3D adipocyte culture more closely resembles *in vivo* tissue morphology, gene expression and lipid composition than 2D alternatives (Turner et al., 2018; Shen et al., 2021; Wolff et al., 2022; Umetsu et al., 2024), this finding has not been confirmed for SGBS cells and should therefore be validated for this particular model system. Similarly, although differences between 3T3-L1 cells and human adipocytes including SGBS cells have been widely reported (Soukas et al., 2001; Wang et al., 2014; Morrison and McGee, 2015; Rossi et al., 2020), these have not yet been investigated in 3D systems. That said, these experiments are likely to be technically challenging due to the inherent differences in culture conditions and assay protocols between the different samples, making it difficult to avoid confounding variables. For example, the adipocyte differentiation cocktail for SGBS cells is chemically defined whereas differentiation of 3T3-L1 cells requires supplementation with FBS containing an undefined combination of bioactive molecules (Dufau et al., 2021). Furthermore, differences in functional responses

between 2D monolayers, 3D spheroids, and tissue biopsies in e.g. lipolysis assays will be difficult to compare directly and will likely need normalisation to a parameter such as (viable) cell number, DNA content, or protein concentrations, thus introducing further complications to the experimental conclusions.

Further development to this adipocyte spheroid model will ultimately depend on the specific research question being posed. To achieve a more complex *in vitro* adipose model that better recapitulates the complete adipose tissue microenvironment, additional cell types could be incorporated into the current spheroids to generate more complex organoid systems. For example, addition of endothelial cells could facilitate formation of vascularised networks between adipocytes (Muller et al., 2019), neuronal cells could be used to investigate innervation (Saarimaa et al., 2025) and co-culture with macrophages would incorporate more aspects of the immune system (Taylor et al., 2020). Furthermore, these organoids could be grown in microfluidic devices to research the effect of fluid dynamics on the model (Brooks et al., 2017; Loskill et al., 2017; McCarthy et al., 2020) or be embedded into tuneable hydrogels to better understand the role of the extracellular matrix in adipogenesis or mature adipocyte function (Muller et al., 2019; Pieters et al., 2022; Ky et al., 2023). Additionally, organoids could be incorporated into multiorgan-on-a-chip devices to investigate crosstalk between adipose tissue and distant organs such as the liver, intestines, or brain (Viravaidya and Shuler, 2004; McCarthy et al., 2020; Picollet-D'hahan et al., 2021). Thus, there is clear scope to expand this work into more complex bioengineered systems to address more varied questions about adipose tissue dysfunction in metabolic disease.

Conversely, for higher throughput applications such as compound screening in a drug discovery cascade, significant effort is required to overcome the technical challenges encountered during this project. The availability of cellular material was a concern throughout this work, with the slow growth of SGBS cells coupled with their inability to differentiate at higher passages limiting the potential throughput of experiments. It may be that an alternative, better characterised cell model such as 3T3-L1 cells are better suited to high throughput studies (Hino et al., 2011; Tsui, 2022). Furthermore, large numbers of spheroids were required to be pooled for many of the experimental approaches used, and therefore a method of spheroid generation where large numbers of spheroids are

formed in bulk, such as hanging droplet (Klingelhutz et al., 2018) or spinning flask cultures (Wrzesinski et al., 2021), may be more appropriate for subsequent studies. Finally, the long and laborious manual spheroid handling processes may be addressed through incorporation of automated liquid handling approaches, with or without inclusion of a hydrogel matrix to reduce spheroid loss (Graham et al., 2019). Therefore, although there is potential for adipocyte spheroid models to be used in high throughput drug screens, this is likely to require significant optimisation and reworking of the findings presented in this thesis.

Finally, if the intended purpose of the research is to translate any findings more directly to clinical samples, it may be sensible to transition from the SGBS cell strain to spheroids generated from patient-derived primary cells. Within this project, it was possible to obtain primary human ADSCs from a female patient undergoing breast reconstruction surgery. These cells could be grown as spheroids and differentiated using the same protocol as SGBS cells, except with a reduced number of 2000 cells/spheroid due to the limited total number of cells available **(Figure 6.1).** Using phase contrast microscopy, an increase in spheroid size was observed during differentiation with some cells appearing to move out of the spheroid, analogous to observations with SGBS cells **(Figure 6.1A, Figure 4.4).** Confocal microscopy using a BODIPY fluorescent lipid stain indicated the presence of lipid droplets in differentiated ADSC spheroids which are absent in undifferentiated samples **(Figure 6.1B).** Again, this is consistent with SGBS spheroids **(Figure 4.5)**, with ADSC spheroids perhaps showing larger lipid droplets, although it is not clear whether this is due to the different cell type or differences in spheroid size. Ideally, these preliminary findings should be expanded to further studies comparing gene and protein expression as well as spheroid function between ADSC and SGBS spheroids. This therefore demonstrates that the experimental approaches optimised for SGBS spheroids can be directly applied to primary human ADSCs, highlighting the translational potential of this project.

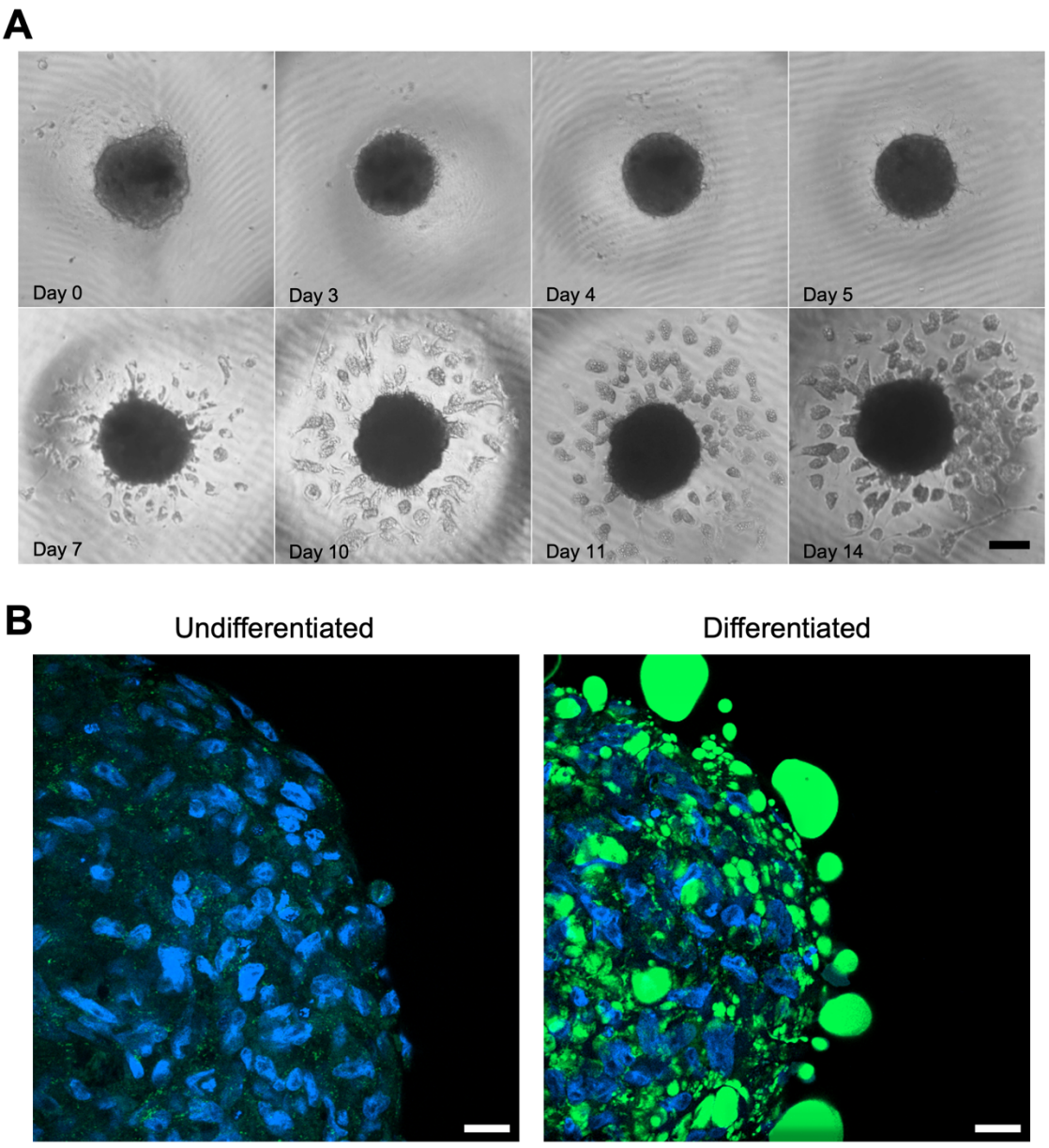

Figure 6.1 - SGBS cell protocols also enable generation and differentiation of primary human adipocyte spheroids. Primary human adipose-derived stromal cells (ADSCs) were isolated from donor adipose tissue, plated in ultra-low adhesion plates to form spheroids, and differentiated according to established SGBS cell protocol. **A)** Phase contrast images of ADSC spheroids at the indicated day of differentiation. Scale bar = 100 µm. **B)** Representative images of undifferentiated (left) or differentiated (right) ADSC spheroids which were fixed, stained with Hoescht (blue, nuclei) and BODIPY (green, lipid) fluorescent dyes and imaged using a Zeiss LSM980 confocal microscope with 40X oil-immersion objective. Scale bar = 20 µm.

In conclusion, the data presented here describes the development and characterisation of a novel human 3D adipocyte spheroid model generated from SGBS cells. This platform has allowed the investigation of m-GPCR function in a more physiologically relevant microenvironment than traditional 2D cell culture, and future incorporation of genetically encoded biosensors will allow further dissection of the complex GPCR signalling networks within adipocytes. Overall, this work provides a strong foundation for future studies investigating the

mechanistic interactions between metabolic and immune cells in metabolic disease, ultimately leading to the development of novel therapeutics to ease the global burden of these diseases.

List of References

Abuhattum, S., Kotzbeck, P., Schlüßler, R., Harger, A., Ariza de Schellenberger, A., Kim, K., et al. (2022). Adipose cells and tissues soften with lipid accumulation while in diabetes adipose tissue stiffens. *Sci Rep* 12, 1–17. doi: 10.1038/s41598-022-13324-9

Adomshick, V., Pu, Y., and Veiga-Lopez, A. (2020). Automated Lipid Droplet Quantification System for Phenotypic Analysis of Adipocytes using CellProfiler. *Toxicol Mech Methods* 30, 378. doi: 10.1080/15376516.2020.1747124

Akinjiyan, F. A., Fazal, A., Hild, M., Beckwith, R. E. J., Ross, N. T., Paulk, J., et al. (2020). A Novel Luminescence-Based High-Throughput Approach for Cellular Resolution of Protein Ubiquitination Using Tandem Ubiquitin Binding Entities (TUBEs). *SLAS Discovery* 25, 350–360. doi: 10.1177/2472555219901261

Albrecht, F. B., Schmidt, F. F., Volz, A. C., and Kluger, P. J. (2022). Bioprinting of 3D Adipose Tissue Models Using a GelMA-Bioink with Human Mature Adipocytes or Human Adipose-Derived Stem Cells. *Gels* 8. doi: 10.3390/GELS8100611

Aldehoff, A. S., Karkossa, I., Goerdeler, C., Krieg, L., Schor, J., Engelmann, B., et al. (2024). Unveiling the dynamics of acetylation and phosphorylation in SGBS and 3T3-L1 adipogenesis. *iScience* 27, 109711. doi: 10.1016/J.ISCI.2024.109711

Alexander, S. P. H., Christopoulos, A., Davenport, A. P., Kelly, E., Mathie, A. A., Peters, J. A., et al. (2023). The Concise Guide to PHARMACOLOGY 2023/24: G protein-coupled receptors. *Br J Pharmacol* 180, S23–S144. doi: 10.1111/BPH.16177

Ali, R., Ramadurai, S., Barry, F., and Nasheuer, H. P. (2018). Optimizing fluorescent protein expression for quantitative fluorescence microscopy and spectroscopy using herpes simplex thymidine kinase promoter sequences. *FEBS Open Bio* 8, 1043. doi: 10.1002/2211-5463.12432

Allen, D. O. (1985). Rate-limiting steps in isoproterenol and forskolin stimulated lipolysis. *Biochem Pharmacol* 34, 843–846. doi: 10.1016/0006-2952(85)90765-8

Allott, E. H., Oliver, E., Lysaght, J., Gray, S. G., Reynolds, J. V., Roche, H. M., et al. (2012). The SGBS cell strain as a model for the in vitro study of obesity and cancer. *Clinical & Translational Oncology* 14, 774–782. doi: 10.1007/S12094-012-0863-6

Alshammari, W. S., Duncan, E. M., Vita, L., Kenawy, M., Dibnah, B., Wabitsch, M., et al. (2025). Inverse agonism of the FFA4 free fatty acid receptor controls both adipogenesis and mature adipocyte function. *Cell Signal* 131, 111714. doi: 10.1016/J.CELLSIG.2025.111714

Anand, P., Fu, A., Teoh, S. H., and Luo, K. Q. (2015). Application of a fluorescence resonance energy transfer (FRET)-based biosensor for detection of drug-induced apoptosis in a 3D breast tumor model. *Biotechnol Bioeng* 112, 1673–1682. doi: 10.1002/BIT.25572

Angers, S., Salahpour, A., Joly, E., Hilairet, S., Chelsky, D., Dennis, M., et al. (2000). Detection of β2-adrenergic receptor dimerization in living cells using bioluminescence resonance energy transfer (BRET). *Proc Natl Acad Sci U S A* 97, 3684. doi: 10.1073/PNAS.060590697

Animal Free Research UK (2021). Animal Derived Biomaterials. *AFRUK Principles*. Available at: https://www.animalfreeresearchuk.org/animal-derived-biomaterials/ (Accessed December 14, 2021).

Ariza, A. C., Deen, P. M., and Robben, J. H. (2012). The succinate receptor as a novel therapeutic target for oxidative and metabolic stress-related conditions. *Front Endocrinol (Lausanne)* 3, 22. doi: 10.3389/fendo.2012.00022

Artemniak-Wojtowicz, D., Pyrżak, B., and Kucharska, A. M. (2020). Obesity and chronic inflammation crosslinking. *Cent Eur J Immunol* 45, 461. doi: 10.5114/CEJI.2020.103418

Atwood, B. K., Lopez, J., Wager-Miller, J., Mackie, K., and Straiker, A. (2011). Expression of G protein-coupled receptors and related proteins in HEK293, AtT20, BV2, and N18 cell lines as revealed by microarray analysis. *BMC Genomics* 12. doi: 10.1186/1471-2164-12-14

Avelino, T. M., Provencio, M. G. A., Peroni, L. A., Domingues, R. R., Torres, F. R., de Oliveira, P. S. L., et al. (2024). Improving obesity research: Unveiling metabolic pathways through a 3D In vitro model of adipocytes using 3T3-L1 cells. *PLoS One* 19, e0303612. doi: 10.1371/JOURNAL.PONE.0303612

Avet, C., Mancini, A., Breton, B., Gouill, C. Le, Hauser, A. S., Normand, C., et al. (2022). Effector membrane translocation biosensors reveal G protein and Parrestin coupling profiles of 100 therapeutically relevant GPCRs. *Elife* 11. doi: 10.7554/ELIFE.74101

Azad, A. K., Zhabyeyev, P., Vanhaesebroeck, B., Eitzen, G., Oudit, G. Y., Moore, R. B., et al. (2020). Inactivation of endothelial cell phosphoinositide 3-kinase ß inhibits tumor angiogenesis and tumor growth. *Oncogene* 39, 6480–6492. doi: 10.1038/S41388-020-01444-3

Azevedo, C. M. G., Watterson, K. R., Wargent, E. T., Hansen, S. V. F., Hudson, B. D., Kępczyńska, M. A., et al. (2016). Non-Acidic Free Fatty Acid Receptor 4 Agonists with Antidiabetic Activity. *J Med Chem* 59, 8868–8878. doi: 10.1021/ACS.JMEDCHEM.6B00685

Baganha, F., Schipper, R., and Hagberg, C. E. (2022). Towards better models for studying human adipocytes in vitro. *Adipocyte* 11, 413–419. doi: 10.1080/21623945.2022.2104514

Baillargeon, P., Shumate, J., Hou, S., Fernandez-Vega, V., Marques, N., Souza, G., et al. (2019). Automating a Magnetic 3D Spheroid Model Technology for High-Throughput Screening. *SLAS Technol* 24, 420–428. doi: 10.1177/2472630319854337

Baker, B. M., and Chen, C. S. (2012). Deconstructing the third dimension-how 3D culture microenvironments alter cellular cues. *J Cell Sci* 125, 3015–3024. doi: 10.1242/JCS.079509

Baliga, U. K., Gurunian, A., Nogales, A., Martinez-Sobrido, L., and Dean, D. A. (2025). Electroporation- and Liposome-Mediated Co-Transfection of Single and Multiple Plasmids. *Pharmaceutics* 17, 905. doi: 10.3390/PHARMACEUTICS17070905

Barbazán, J., Majellaro, M., Martínez, A. L., Brea, J. M., Sotelo, E., and Abal, M. (2022). Identification of A2BAR as a potential target in colorectal cancer using novel fluorescent GPCR ligands. *Biomedicine & Pharmacotherapy* 153. doi: 10.1016/j.biopha.2022.113408

Barreto, C. A. V., Baptista, S. J., Bueschbell, B., Magalhães, P. R., Preto, A. J., Lemos, A., et al. (2021). "Arrestin and G Protein Interactions with GPCRs: A Structural Perspective," in *GPCRs as Therapeutic Targets*, (wiley), 109–179. doi: 10.1002/9781119564782.CH5

Bates, R., Huang, W., and Cao, L. (2020). Adipose Tissue: An Emerging Target for Adeno-associated Viral Vectors. *Mol Ther Methods Clin Dev* 19, 236–249. doi: 10.1016/j.omtm.2020.09.009

Benyó, Z., Gille, A., Kero, J., Csiky, M., Suchánková, M. C., Nüsing, R. M., et al. (2005). GPR109A (PUMA-G/HM74A) mediates nicotinic acid–induced flushing. *J Clin Invest* 115, 3634–3640. doi: 10.1172/JCI23626

Berens, E. B., Holy, J. M., Riegel, A. T., and Wellstein, A. (2015). A Cancer Cell Spheroid Assay to Assess Invasion in a 3D Setting. *Journal of Visualized Experiments* 2015, 53409. doi: 10.3791/53409

Béréziat, V., Moritz, S., Klonjkowski, B., Decaudain, A., Auclair, M., Eloit, M., et al. (2005). Efficient adenoviral transduction of 3T3-F442A preadipocytes without affecting adipocyte differentiation. *Biochimie* 87, 951–958. doi: 10.1016/j.biochi.2005.05.010

Bertrand, L., Parent, S., Caron, M., Legault, M., Joly, E., Angers, S., et al. (2002). The BRET2/arrestin assay in stable recombinant cells: a platform to screen for compounds that interact with G protein-coupled receptors (GPCRS). *Journal of Receptors and Signal Transduction* 22, 533–541. doi: 10.1081/RRS-120014619

Beyer, H. M., Gonschorek, P., Samodelov, S. L., Meier, M., Weber, W., and Zurbriggen, M. D. (2015). AQUA Cloning: A Versatile and Simple Enzyme-Free Cloning Approach. *PLoS One* 10, e0137652. doi: 10.1371/JOURNAL.PONE.0137652

Blad, C. C., Tang, C., and Offermanns, S. (2012). G protein-coupled receptors for energy metabolites as new therapeutic targets. *Nat Rev Drug Discov* 11, 603–619. doi: 10.1038/nrd3777

Blade, S. P., Falkowski, D. J., Bachand, S. N., Pagano, S. J., and Chin, L. K. (2024). Mechanobiology of Adipocytes. *Biology (Basel)* 13, 434. doi: 10.3390/BIOLOGY13060434

Blüher, M. (2024). Understanding Adipose Tissue Dysfunction. *J Obes Metab Syndr* 33, 275–288. doi: 10.7570/JOMES24013

Blyth, R. R. R., Laversin, S. A., Foxall, R. B., Savva, C., Copson, E., Cutress, R. I., et al. (2025). Development and characterisation of a novel 3D in vitro model of obesity-associated breast cancer as a tool for drug testing. *NPJ Breast Cancer* 11, 1–16. doi: 10.1038/S41523-025-00766-3

Boden, W. E., Sidhu, M. S., and Toth, P. P. (2014). The therapeutic role of niacin in dyslipidemia management. *J Cardiovasc Pharmacol Ther* 19, 141–158. doi: 10.1177/1074248413514481

Bolognini, D., Barki, N., Butcher, A. J., Hudson, B. D., Sergeev, E., Molloy, C., et al. (2019). Chemogenetics defines receptor-mediated functions of short chain free fatty acids. *Nat Chem Biol* 15, 489–498. doi: 10.1038/s41589-019-0270-1

Bolognini, D., Tobin, A. B., Milligan, G., and Hodge, D. (2016). The Pharmacology and Function of Receptors for Short-Chain Fatty Acids. *Mol Pharmacol* 89, 388–398. doi: 10.1124/MOL.115.102301

Bone, J., Barber, J., Bunting, T., Leunig, T., Harper, H., Tudor, K., et al. (2025). The economic and productivity costs of obesity and excess weight in the UK | Nesta. Available at: https://www.nesta.org.uk/report/the-economic-and-productivity-costs-of-obesity-and-overweight-in-the-uk/ (Accessed October 5, 2025).

Börgeson, E., Boucher, J., and Hagberg, C. E. (2022). Of mice and men: Pinpointing species differences in adipose tissue biology. *Front Cell Dev Biol* 10, 1003118. doi: 10.3389/FCELL.2022.1003118

Boshart, M., Weber, F., Jahn, G., Dorsch-Hler, K., Fleckenstein, B., and Schaffner, W. (1985). A very strong enhancer is located upstream of an immediate early gene of human cytomegalovirus. *Cell* 41, 521–530. doi: 10.1016/S0092-8674(85)80025-8

Boulton, A. J. M., Vinik, A. I., Arezzo, J. C., Bril, V., Feldman, E. L., Freeman, R., et al. (2005). Diabetic NeuropathiesA statement by the American Diabetes Association. *Diabetes Care* 28, 956–962. doi: 10.2337/DIACARE.28.4.956

Boussif, O., LezoualC'H, F., Zanta, M. A., Mergny, M. D., Scherman, D., Demeneix, B., et al. (1995). A versatile vector for gene and oligonucleotide transfer into cells in culture and in vivo: polyethylenimine. *Proc Natl Acad Sci U S A* 92, 7297–7301. doi: 10.1073/PNAS.92.16.7297

Boute, N., Jockers, R., and Issad, T. (2002). The use of resonance energy transfer in high-throughput screening: BRET versus FRET. *Trends Pharmacol Sci* 23, 351–354. doi: 10.1016/S0165-6147(02)02062-X

Bregigeon, P., Rivière, C., Franqueville, L., Vollaire, C., Marchalot, J., and Frénéa-Robin, M. (2022). Integrated platform for culture, observation, and parallelized electroporation of spheroids. *Lab Chip* 22, 2489–2501. doi: 10.1039/D2LC00074A

Bridge-Comer, P. E., and Reilly, S. M. (2023). Measuring the Rate of Lipolysis in Ex Vivo Murine Adipose Tissue and Primary Preadipocytes Differentiated In Vitro. *Journal of Visualized Experiments* 2023, 10.3791/65106. doi: 10.3791/65106

Briscoe, C. P., Tadayyon, M., Andrews, J. L., Benson, W. G., Chambers, J. K., Eilert, M. M., et al. (2003). The Orphan G Protein-coupled Receptor GPR40 Is Activated by Medium and Long Chain Fatty Acids. *Journal of Biological Chemistry* 278, 11303–11311. doi: 10.1074/JBC.M211495200

Brooks, J. C., Judd, R. L., and Easley, C. J. (2017). Culture and sampling of primary adipose tissue in practical microfluidic systems. *Methods in Molecular Biology* 1566, 185–201. doi: 10.1007/978-1-4939-6820-6_18

Brown, A. J., Goldsworthy, S. M., Barnes, A. A., Eilert, M. M., Tcheang, L., Daniels, D., et al. (2003). The orphan G protein-coupled receptors GPR41 and GPR43 are activated by propionate and other short chain carboxylic acids. *Journal of Biological Chemistry* 278, 11312–11319. doi: 10.1074/jbc.M211609200

Bruun, J. M., Lihn, A. S., Verdich, C., Pedersen, S. B., Toubro, S., Astrup, A., et al. (2003). Regulation of adiponectin by adipose tissue-derived cytokines: in vivo and in vitro investigations in humans. *Am J Physiol Endocrinol Metab* 285, 527–533. doi: 10.1152/AJPENDO.00110.2003

Bryant, N. J., Govers, R., and James, D. E. (2002). Regulated transport of the glucose transporter GLUT4. *Nat Rev Mol Cell Biol* 3, 267–277. doi: 10.1038/NRM782;KWRD

Butcher, A. J., Hudson, B. D., Shimpukade, B., Alvarez-Curto, E., Prihandoko, R., Ulven, T., et al. (2014). Concomitant action of structural elements and receptor phosphorylation determines arrestin-3 interaction with the free fatty acid receptor FFA4. *Journal of Biological Chemistry* 289, 18451–18465. doi: 10.1074/jbc.M114.568816

Cacciamali, A., Villa, R., and Dotti, S. (2022). 3D Cell Cultures: Evolution of an Ancient Tool for New Applications. *Front Physiol* 13, 836480. doi: 10.3389/FPHYS.2022.836480

Calebiro, D., Miljus, T., and O'Brien, S. (2024). Endomembrane GPCR signaling: 15 years on, the quest continues. *Trends Biochem Sci* 50, 46–60. doi: 10.1016/J.TIBS.2024.10.006

Calebiro, D., Nikolaev, V. O., Gagliani, M. C., De Filippis, T., Dees, C., Tacchetti, C., et al. (2009). Persistent cAMP-Signals Triggered by Internalized G-Protein–Coupled Receptors. *PLoS Biol* 7, e1000172. doi: 10.1371/JOURNAL.PBIO.1000172

Cannon, B., and Nedergaard, J. (2004). Brown Adipose Tissue: Function and Physiological Significance. *Physiol Rev* 84, 277–359. doi: 10.1152/PHYSREV.00015.2003

Cardarelli, F., Digiacomo, L., Marchini, C., Amici, A., Salomone, F., Fiume, G., et al. (2016). The intracellular trafficking mechanism of Lipofectamine-based transfection reagents and its implication for gene delivery. *Sci Rep* 6, 25879-. doi: 10.1038/srep25879

Caroli, J., Mamyrbekov, A., Harpsøe, K., Gardizi, S., Dörries, L., Ghosh, E., et al. (2023). A community Biased Signaling Atlas. *Nat Chem Biol* 19, 531–535. doi: 10.1038/s41589-023-01292-8

Carpenter, B., and Tate, C. G. (2016). Engineering a minimal G protein to facilitate crystallisation of G protein-coupled receptors in their active conformation. *Protein Engineering, Design and Selection* 29, 583–594. doi: 10.1093/PROTEIN/GZW049

Carullo, G., Mazzotta, S., Vega-Holm, M., Iglesias-Guerra, F., Vega-Perez, J. M., Aiello, F., et al. (2021). GPR120/FFAR4 Pharmacology: Focus on Agonists in Type 2 Diabetes Mellitus Drug Discovery. *J Med Chem* 64, 4312–4332. doi: 10.1021/ACS.JMEDCHEM.0C01002

Cawthorn, W. P., Heyd, F., Hegyi, K., and Sethi, J. K. (2007). Tumour necrosis factor-α inhibits adipogenesis via a β-catenin/TCF4(TCF7L2)-dependent pathway. *Cell Death Differ* 14, 1361–1373. doi: 10.1038/sj.cdd.4402127

Celebi, L. E., Ketchum, F., Bozkaya, D. N., and Zorlutuna, P. (2025). Tissue Engineered Models of Adipose Tissue Dysfunction to Investigate Obesity-Related Comorbidities. *Progress in Biomedical Engineering*. doi: 10.1088/2516-1091/AE1CFE

Chae, G. N., and Kwak, S. J. (2003). NF-κB is involved in the TNF-α induced inhibition of the differentiation of 3T3-L1 cells by reducing PPARγ expression. *Exp Mol Med* 35, 431–437. doi: 10.1038/EMM.2003.56

Chandra, P., and Philips, J. A. (2018). Ectopic Gene Expression in Macrophages Using in vitro Transcribed mRNA. *Bio Protoc* 8. doi: 10.21769/BIOPROTOC.2857

Charest, P. G., Terrillon, S., and Bouvier, M. (2005). Monitoring agonist-promoted conformational changes of β-arrestin in living cells by intramolecular BRET. *EMBO Rep* 6, 334–340. doi: 10.1038/SJ.EMBOR.7400373

Chaudhuri, O., Cooper-White, J., Janmey, P. A., Mooney, D. J., and Shenoy, V. B. (2020). Effects of extracellular matrix viscoelasticity on cellular behaviour. *Nature* 584, 535–546. doi: 10.1038/s41586-020-2612-2

Chelladurai, K. S., Selvan Christyraj, J. D., Rajagopalan, K., Yesudhason, B. V., Venkatachalam, S., Mohan, M., et al. (2021). Alternative to FBS in animal cell culture - An overview and future perspective. *Heliyon* 7, e07686. doi: 10.1016/j.heliyon.2021.e07686

Chen, Z., Yu, H., Shi, X., Warren, C. R., Lotta, L. A., Friesen, M., et al. (2020). Functional Screening of Candidate Causal Genes for Insulin Resistance in Human Preadipocytes and Adipocytes. *Circ Res* 126, 330–346. doi: 10.1161/CIRCRESAHA.119.315246

Cheng, L., Wang, J., Dai, H., Duan, Y., An, Y., Shi, L., et al. (2021). Brown and beige adipose tissue: a novel therapeutic strategy for obesity and type 2 diabetes mellitus. *Adipocyte* 10, 48–65. doi: 10.1080/21623945.2020.1870060

Chennell, G., Willows, R. J. W., Warren, S. C., Carling, D., French, P. M. W., Dunsby, C., et al. (2016). Imaging of Metabolic Status in 3D Cultures with an Improved AMPK FRET Biosensor for FLIM. *Sensors* 16, 1312. doi: 10.3390/S16081312

Chesnoy, S., and Huang, L. (2000). Structure and function of lipid-DNA complexes for gene delivery. *Annu Rev Biophys Biomol Struct* 29, 27–47. doi: 10.1146/ANNUREV.BIOPHYS.29.1.27

Chi, J., Wu, Z., Choi, C. H. J., Nguyen, L., Tegegne, S., Ackerman, S. E., et al. (2018). Three-Dimensional Adipose Tissue Imaging Reveals Regional Variation in Beige Fat Biogenesis and PRDM16-Dependent Sympathetic Neurite Density. *Cell Metab* 27, 226-236.e3. doi: 10.1016/j.cmet.2017.12.011

Chouchani, E. T., and Kajimura, S. (2019). Metabolic adaptation and maladaptation in adipose tissue. *Nat Metab* 1, 189–200. doi: 10.1038/S42255-018-0021-8

Christiansen, E., Hudson, B. D., Hansen, A. H., Milligan, G., and Ulven, T. (2016). Development and Characterization of a Potent Free Fatty Acid Receptor 1 (FFA1) Fluorescent Tracer. *J Med Chem* 59, 4849–4858. doi: 10.1021/ACS.JMEDCHEM.6B00202

Christiansen, E., Watterson, K. R., Stocker, C. J., Sokol, E., Jenkins, L., Simon, K., et al. (2015). Activity of dietary fatty acids on FFA1 and FFA4 and characterisation of pinolenic acid as a dual FFA1/FFA4 agonist with potential effect against metabolic diseases. *British Journal of Nutrition* 113, 1677–1688. doi: 10.1017/S000711451500118X

Christoffers, S., Seiler, L., Wiebe, E., and Blume, C. (2024). Possibilities and efficiency of MSC co-transfection for gene therapy. *Stem Cell Res Ther* 15, 1–17. doi: 10.1186/S13287-024-03757-6

Ciba, M., Dibnah, B., Hudson, B. D., and Rexen Ulven, E. (2023). Development and Characterization of Potent Succinate Receptor Fluorescent Tracers. *J Med Chem* 66, 8951–8974. doi: 10.1021/ACS.JMEDCHEM.3C00552

Ciccone, G., Gonzalez Oliva, M. A., Antonovaite, N., Lüchtefeld, I., Sanchez, M. S., and Vassalli, M. (2022). Experimental and Data Analysis Workflow for Soft Matter Nanoindentation. *Journal of Visualized Experiments* 2022. doi: 10.3791/63401

Clemente-Suárez, V. J., Redondo-Flórez, L., Beltrán-Velasco, A. I., Martín-Rodríguez, A., Martínez-Guardado, I., Navarro-Jiménez, E., et al. (2023). The Role of Adipokines in Health and Disease. *Biomedicines* 11, 1290. doi: 10.3390/BIOMEDICINES11051290

Collon, K., Gallo, M. C., Bell, J. A., Chang, S. W., Rodman, J. C. S., Sugiyama, O., et al. (2022). Improving Lentiviral Transduction of Human Adipose-Derived Mesenchymal Stem Cells. *Hum Gene Ther* 33, 1260. doi: 10.1089/HUM.2022.117

Conflitti, P., Lyman, E., Sansom, M. S. P., Hildebrand, P. W., Gutiérrez-de-Terán, H., Carloni, P., et al. (2025). Functional dynamics of G protein-coupled receptors reveal new routes for drug discovery. *Nat Rev Drug Discov* 24, 251–275. doi: 10.1038/S41573-024-01083-3

Conry, R. M., Lobuglio, A. F., Wright, M., Sumerel, L., Pike, M. J., Johanning, F., et al. (1995). Characterization of a Messenger RNA Polynucleotide Vaccine Vector. *Cancer Res* 55, 1397–1400. Available at: http://aacrjournals.org/cancerres/article-pdf/55/7/1397/2460061/cr0550071397.pdf (Accessed September 24, 2025).

Constant, V. A., Gagnon, A., Landry, A., and Sorisky, A. (2006). Macrophage-conditioned medium inhibits the differentiation of 3T3-L1 and human

abdominal preadipocytes. *Diabetologia* 49, 1402–1411. doi: 10.1007/S00125-006-0253-0/FIGURES/5

Contessi Negrini, N., Pellegrinelli, V., Salem, V., Celiz, A., and Vidal-Puig, A. (2025). Breaking barriers in obesity research: 3D models of dysfunctional adipose tissue. *Trends Biotechnol* 43, 1079–1093. doi: 10.1016/J.TIBTECH.2024.09.017

Cosín-Roger, J., Ortiz-Masia, D., Barrachina, M. D., and Calatayud, S. (2020). Metabolite Sensing GPCRs: Promising Therapeutic Targets for Cancer Treatment? *Cells* 9, 2345. doi: 10.3390/CELLS9112345

Crewe, C., An, Y. A., and Scherer, P. E. (2017). The ominous triad of adipose tissue dysfunction: inflammation, fibrosis, and impaired angiogenesis. *J Clin Invest* 127, 74–82. doi: 10.1172/JCI88883

Curcio, E., Salerno, S., Barbieri, G., De Bartolo, L., Drioli, E., and Bader, A. (2007). Mass transfer and metabolic reactions in hepatocyte spheroids cultured in rotating wall gas-permeable membrane system. *Biomaterials* 28, 5487–5497. doi: 10.1016/J.BIOMATERIALS.2007.08.033

Cvetkovic, C., Patel, R., Shetty, A., Hogan, M. K., Anderson, M., Basu, N., et al. (2022). Assessing Gq-GPCR-induced human astrocyte reactivity using bioengineered neural organoids. *Journal of Cell Biology* 221. doi: 10.1083/JCB.202107135

Czech, M. P., Tencerova, M., Pedersen, D. J., and Aouadi, M. (2013). Insulin signalling mechanisms for triacylglycerol storage. *Diabetologia* 56, 949. doi: 10.1007/S00125-013-2869-1

Dalby, B., Cates, S., Harris, A., Ohki, E. C., Tilkins, M. L., Price, P. J., et al. (2004). Advanced transfection with Lipofectamine 2000 reagent: primary neurons, siRNA, and high-throughput applications. *Methods* 33, 95–103. doi: 10.1016/J.YMETH.2003.11.023

Daly, C., Guseinov, A. A., Hahn, H., Wright, A., Tikhonova, I. G., Thomsen, A. R. B., et al. (2023). ß-Arrestin-dependent and -independent endosomal G protein activation by the vasopressin type 2 receptor. *Elife* 12, 87754. doi: 10.7554/ELIFE.87754

Daquinag, A. C., Souza, G. R., and Kolonin, M. G. (2013). Adipose tissue engineering in three-dimensional levitation tissue culture system based on magnetic nanoparticles. *Tissue Eng Part C Methods* 19, 336–344. doi: 10.1089/ten.tec.2012.0198

Darimont, C., Zbinden, I., Avanti, O., Leone-Vautravers, P., Giusti, V., Burckhardt, P., et al. (2003). Reconstitution of telomerase activity combined with HPV-E7 expression allow human preadipocytes to preserve their differentiation capacity after immortalization. *Cell Death & Differentiation 2003 10:9* 10, 1025–1031. doi: 10.1038/sj.cdd.4401273

Dariolli, R., Nir, R., Mushlam, T., Souza, G. R., Farmer, S. R., and Batista, M. L. (2025). Optimized scaffold-free human 3D adipose tissue organoid culture for obesity and disease modeling. *SLAS Discovery* 31, 100218. doi: 10.1016/j.slasd.2025.100218

Davenport, A. P., Alexander, S. P. H., Sharman, J. L., Pawson, A. J., Benson, H. E., Monaghan, A. E., et al. (2013). International Union of Basic and Clinical Pharmacology. LXXXVIII. G Protein-Coupled Receptor List: Recommendations for New Pairings with Cognate Ligands. *Pharmacol Rev* 65, 967–986. doi: 10.1124/PR.112.007179

de Castro Fonseca, M., Aguiar, C. J., da Rocha Franco, J. A., Gingold, R. N., and Leite, M. F. (2016). GPR91: expanding the frontiers of Krebs cycle intermediates. *Cell Communication and Signaling* 14, 3. doi: 10.1186/s12964-016-0126-1

De Groof, T. W. M., Bergkamp, N. D., Heukers, R., Giap, T., Bebelman, M. P., Goeij-de Haas, R., et al. (2021). Selective targeting of ligand-dependent and -independent signaling by GPCR conformation-specific anti-US28 intrabodies. *Nat Commun* 12. doi: 10.1038/S41467-021-24574-Y

De Hoogt, R., Estrada, M. F., Vidic, S., Davies, E. J., Osswald, A., Barbier, M., et al. (2017). Data descriptor: Protocols and characterization data for 2d, 3d, and slice-based tumor models from the predect project. *Sci Data* 4, 170170-. doi: 10.1038/SDATA.2017.170

de Luca, C., and Olefsky, J. M. (2008). Inflammation and Insulin Resistance. *FEBS Lett* 582, 97. doi: 10.1016/J.FEBSLET.2007.11.057

de Moura e Dias, M., dos Reis, S. A., da Conceição, L. L., Sediyama, C. M. N. de O., Pereira, S. S., de Oliveira, L. L., et al. (2021). Diet-induced obesity in animal models: points to consider and influence on metabolic markers. *Diabetol Metab Syndr* 13, 1–14. doi: 10.1186/S13098-021-00647-2

Delarue, M., Montel, F., Vignjevic, D., Prost, J., Joanny, J. F., and Cappello, G. (2014). Compressive stress inhibits proliferation in tumor spheroids through a volume limitation. *Biophys J* 107, 1821–1828. doi: 10.1016/j.bpj.2014.08.031

Demby, A., and Zaccolo, M. (2024). Investigating G-protein coupled receptor signalling with light-emitting biosensors. *Front Physiol* 14, 1310197. doi: 10.3389/FPHYS.2023.1310197

Desgrouas, C., Thalheim, T., Cerino, M., Badens, C., and Bonello-Palot, N. (2024). Perilipin 1: a systematic review on its functions on lipid metabolism and atherosclerosis in mice and humans. *Cardiovasc Res* 120, 237–248. doi: 10.1093/CVR/CVAE005

Di Blasi, R., Marbiah, M. M., Siciliano, V., Polizzi, K., and Ceroni, F. (2021). A call for caution in analysing mammalian co-transfection experiments and implications of resource competition in data misinterpretation. *Nat Commun* 12, 2545. doi: 10.1038/S41467-021-22795-9

Di Stefano, A. B., Urrata, V., Trapani, M., Moschella, F., Cordova, A., and Toia, F. (2022). Systematic review on spheroids from adipose-derived stem cells: Spontaneous or artefact state? *J Cell Physiol* 237, 4397. doi: 10.1002/JCP.30892

Diabetes UK (2025). Complications of Diabetes. *Diabetes UK*. Available at: https://www.diabetes.org.uk/about-diabetes/looking-after-diabetes/complications (Accessed October 12, 2025).

Diosdi, A., Hirling, D., Kovacs, M., Toth, T., Harmati, M., Koos, K., et al. (2021). A quantitative metric for the comparative evaluation of optical clearing protocols for 3D multicellular spheroids. *Comput Struct Biotechnol J* 19, 1233–1243. doi: 10.1016/J.CSBJ.2021.01.040

Dixon, A. S., Schwinn, M. K., Hall, M. P., Zimmerman, K., Otto, P., Lubben, T. H., et al. (2015). NanoLuc Complementation Reporter Optimized for Accurate Measurement of Protein Interactions in Cells. *ACS Chem Biol* 11, 400–408. doi: 10.1021/ACSCHEMBIO.5B00753

Dolega, M. E., Delarue, M., Ingremeau, F., Prost, J., Delon, A., and Cappello, G. (2017). Cell-like pressure sensors reveal increase of mechanical stress towards the core of multicellular spheroids under compression. *Nat Commun* 8, 14056-. doi: 10.1038/ncomms14056

Donthamsetti, P., Quejada, J. R., Javitch, J. A., Gurevich, V. V., and Lambert, N. A. (2015). Using Bioluminescence Resonance Energy Transfer (BRET) to Characterize Agonist-Induced Arrestin Recruitment to Modified and Unmodified G Protein-Coupled Receptors. *Curr Protoc Pharmacol* 70, 2.14.1-2.14.14. doi: 10.1002/0471141755.PH0214S70

Dragulescu-Andrasi, A., Chan, C. T., De, A., Massoud, T. F., and Gambhir, S. S. (2011). Bioluminescence resonance energy transfer (BRET) imaging of protein-protein interactions within deep tissues of living subjects. *Proc Natl Acad Sci U S A* 108, 12060–12065. doi: 10.1073/PNAS.1100923108

Dufau, J., Shen, J. X., Couchet, M., Barbosa, T. D. C., Mejhert, N., Massier, L., et al. (2021). In vitro and ex vivo models of adipocytes. *Am J Physiol Cell Physiol* 320, C822–C841. doi: 10.1152/AJPCELL.00519.2020

Dugail, I. (2001). Transfection of Adipocytes and Preparation of Nuclear Extracts. *Adipose Tissue Protocols*, 141–146. doi: 10.1385/1-59259-231-7:141

Duncan, E. M., Vita, L., Dibnah, B., and Hudson, B. D. (2023). Metabolite-sensing GPCRs controlling interactions between adipose tissue and inflammation. *Front Endocrinol (Lausanne)* 14, 1197102. doi: 10.3389/FENDO.2023.1197102

Ebstensen, R. D., and Plagemann, P. G. (1972). Cytochalasin B: Inhibition of Glucose and Glucosamine Transport. *Proc Natl Acad Sci U S A* 69, 1430. doi: 10.1073/PNAS.69.6.1430

Efremov, Y. M., Zurina, I. M., Presniakova, V. S., Kosheleva, N. V., Butnaru, D. V., Svistunov, A. A., et al. (2021). Mechanical properties of cell sheets and spheroids: the link between single cells and complex tissues. *Biophys Rev* 13, 541–561. doi: 10.1007/S12551-021-00821-W

Eizirik, D. L., Pasquali, L., and Cnop, M. (2020). Pancreatic β-cells in type 1 and type 2 diabetes mellitus: different pathways to failure. *Nat Rev Endocrinol* 16, 349–362. doi: 10.1038/S41574-020-0355-7

Engin, A. (2017). Adipose Tissue Hypoxia in Obesity and Its Impact on Preadipocytes and Macrophages: Hypoxia Hypothesis. *Adv Exp Med Biol* 960, 305–326. doi: 10.1007/978-3-319-48382-5_13

Enlund, E., Fischer, S., Handrick, R., Otte, K., Debatin, K. M., Wabitsch, M., et al. (2014). Establishment of Lipofection for Studying miRNA Function in Human Adipocytes. *PLoS One* 9. doi: 10.1371/JOURNAL.PONE.0098023

Eswar, S., Rajagopalan, B., Ete, K., and Gattem, S. N. R. (2024). Serum Tumor Necrosis Factor Alpha (TNF-α) Levels in Obese and Overweight Adults: Correlations With Metabolic Syndrome and Inflammatory Markers. *Cureus* 16, e64619. doi: 10.7759/CUREUS.64619

Fam, T. K., Klymchenko, A. S., and Collot, M. (2018). Recent Advances in Fluorescent Probes for Lipid Droplets. *Materials* 11, 1768. doi: 10.3390/MA11091768

Fang, H., and Judd, R. L. (2018). Adiponectin Regulation and Function. *Compr Physiol* 8, 1031–1063. doi: 10.1002/J.2040-4603.2018.TB00036.X

Fazel, Y., Koenig, A. B., Sayiner, M., Goodman, Z. D., and Younossi, Z. M. (2016). Epidemiology and natural history of non-alcoholic fatty liver disease. *Metabolism* 65, 1017–1025. doi: 10.1016/j.metabol.2016.01.012

Fedorenko, A., Lishko, P. V., and Kirichok, Y. (2012). Mechanism of fatty-acid-dependent UCP1 uncoupling in brown fat mitochondria. *Cell* 151, 400–413. doi: 10.1016/j.cell.2012.09.010

Ferrandon, S., Feinstein, T. N., Castro, M., Wang, B., Bouley, R., Potts, J. T., et al. (2009). Sustained cyclic AMP production by parathyroid hormone receptor endocytosis. *Nat Chem Biol* 5, 734–742. doi: 10.1038/NCHEMBIO.206

Fetal Calf Serum Free Database (n.d.). Available at: https://fcs-free.org/ (Accessed June 17, 2022).

Fischer-Posovszky, P., Newell, F. S., Wabitsch, M., and Tornqvist, H. E. (2008). Human SGBS Cells – a Unique Tool for Studies of Human Fat Cell Biology. *Obes Facts* 1, 184. doi: 10.1159/000145784

Fischer-Posovszky, P., Tews, D., Horenburg, S., Debatin, K. M., and Wabitsch, M. (2012). Differential function of Akt1 and Akt2 in human adipocytes. *Mol Cell Endocrinol* 358, 135–143. doi: 10.1016/J.MCE.2012.03.018

Foord, S. M., Bonner, T. I., Neubig, R. R., Rosser, E. M., Pin, J. P., Davenport, A. P., et al. (2005). International Union of Pharmacology. XLVI. G Protein-Coupled Receptor List. *Pharmacol Rev* 57, 279–288. doi: 10.1124/PR.57.2.5

Frederich, R. C., Hamann, A., Anderson, S., Löllmann, B., Lowell, B. B., and Flier, J. S. (1995). Leptin levels reflect body lipid content in mice: Evidence for diet-induced resistance to leptin action. *Nat Med* 1, 1311–1314. doi: 10.1038/NM1295-1311

Fredriksson, R., Lagerström, M. C., Lundin, L. G., and Schiöth, H. B. (2003). The G-Protein-Coupled Receptors in the Human Genome Form Five Main Families. Phylogenetic Analysis, Paralogon Groups, and Fingerprints. *Mol Pharmacol* 63, 1256–1272. doi: 10.1124/MOL.63.6.1256

Fukumoto, S., and Fujimoto, T. (2002). Deformation of lipid droplets in fixed samples. *Histochem Cell Biol* 118, 423–428. doi: 10.1007/S00418-002-0462-7/METRICS

Galhardo, M., Sinkkonen, L., Berninger, P., Lin, J., Sauter, T., and Heinäniemi, M. (2014). Transcriptomics profiling of human SGBS adipogenesis. *Genom Data* 2, 246–248. doi: 10.1016/J.GDATA.2014.07.004

Garcia, K., Alves, A., Ribeiro-Rodrigues, T. M., Reis, F., and Viana, S. (2023). Analysis of Fluorescent-Stained Lipid Droplets with 3D Reconstruction for Hepatic Steatosis Assessment. *Journal of Visualized Experiments* 2023, e65206. doi: 10.3791/65206

Gasmi, A., Noor, S., Menzel, A., Doşa, A., Pivina, L., and Bjørklund, G. (2020). Obesity and Insulin Resistance: Associations with Chronic Inflammation, Genetic and Epigenetic Factors. *Curr Med Chem* 28, 800–826. doi: 10.2174/0929867327666200824112056

The GBD 2015 Obesity Collaborators (2017). Health Effects of Overweight and Obesity in 195 Countries over 25 Years. *New England Journal of Medicine* 377, 13–27. doi: 10.1056/NEJMOA1614362

Ge, H., Li, X., Weiszmann, J., Wang, P., Baribault, H., Chen, J. L., et al. (2008). Activation of G Protein-Coupled Receptor 43 in Adipocytes Leads to Inhibition of Lipolysis and Suppression of Plasma Free Fatty Acids. *Endocrinology* 149, 4519–4526. doi: 10.1210/EN.2008-0059

Gibot, L., Montigny, A., Baaziz, H., Fourquaux, I., Audebert, M., and Rols, M. P. (2020). Calcium Delivery by Electroporation Induces In Vitro Cell Death through Mitochondrial Dysfunction without DNA Damages. *Cancers (Basel)* 12, 425. doi: 10.3390/CANCERS12020425

Gibot, L., Wasungu, L., Teissié, J., and Rols, M. P. (2013). Antitumor drug delivery in multicellular spheroids by electropermeabilization. *Journal of Controlled Release* 167, 138–147. doi: 10.1016/J.JCONREL.2013.01.021

Glover, D. J., Lipps, H. J., and Jans, D. A. (2005). Towards safe, non-viral therapeutic gene expression in humans. *Nat Rev Genet* 6, 299–310. doi: 10.1038/NRG1577

Gocze, P. M., and Freeman, D. A. (1994). Factors underlying the variability of lipid droplet fluorescence in MA-10 leydig tumor cells. *Cytometry* 17, 151–158. doi: 10.1002/CYTO.990170207

Goedeke, L., Perry, R. J., and Shulman, G. I. (2016). Emerging Pharmacological Targets for the Treatment of Nonalcoholic Fatty Liver Disease, Insulin

Resistance, and Type 2 Diabetes. *https://doi.org/10.1146/annurev-pharmtox-010716-104727* 59, 65–87. doi: 10.1146/ANNUREV-PHARMTOX-010716-104727

Gomes, A. A. S., Di Michele, M., Roessner, R. A., Damian, M., Bisch, P. M., Sibille, N., et al. (2025). Lipids modulate the dynamics of GPCR:ß-arrestin interaction. *Nat Commun* 16, 1–16. doi: 10.1038/s41467-025-59842-8

Gong, G. C., Fan, W. Z., Li, D. Z., Tian, X., Chen, S. J., Fu, Y. C., et al. (2015). Increased Specific Labeling of INS-1 Pancreatic Beta-Cell by Using RIP-Driven Cre Mutants with Reduced Activity. *PLoS One* 10, e0129092. doi: 10.1371/JOURNAL.PONE.0129092

Gotoh, C., Hong, Y.-H., Iga, T., Hishikawa, D., Suzuki, Y., Song, S.-H., et al. (2007). The regulation of adipogenesis through GPR120. *Biochem Biophys Res Commun* 354, 591–597. doi: 10.1016/J.BBRC.2007.01.028

Grabner, G. F., Xie, H., Schweiger, M., and Zechner, R. (2021). Lipolysis: cellular mechanisms for lipid mobilization from fat stores. *Nat Metab* 3, 1445–1465. doi: 10.1038/S42255-021-00493-6

Graham, A. D., Pandey, R., Tsancheva, V. S., Candeo, A., Botchway, S. W., Allan, A. J., et al. (2019). The development of a high throughput drug-responsive model of white adipose tissue comprising adipogenic 3T3-L1 cells in a 3D matrix. *Biofabrication* 12, 015018. doi: 10.1088/1758-5090/AB56FE

Granneman, J. G. (2008). Delivery of DNA into adipocytes within adipose tissue. *Methods in Molecular Biology* 423, 191–195. doi: 10.1007/978-1-59745-194-9_13

Granneman, J. G., Li, P., Lu, Y., and Tilak, J. (2004). Seeing the trees in the forest: selective electroporation of adipocytes within adipose tissue. *Am J Physiol Endocrinol Metab* 287, 574–582. doi: 10.1152/AJPENDO.00567.2003

Green, H., and Meuth, M. (1974). An established pre-adipose cell line and its differentiation in culture. *Cell* 3, 127–133. doi: 10.1016/0092-8674(74)90116-0

Gregory, E. L. M. (1989). Thermoregulatory aspects of adipose tissue. *Clin Dermatol* 7, 78–92. doi: 10.1016/0738-081X(89)90044-8

Gstraunthaler, G., Lindl, T., and Van Der Valk, J. (2013). A plea to reduce or replace fetal bovine serum in cell culture media. *Cytotechnology* 65, 791. doi: 10.1007/S10616-013-9633-8

Guh, D. P., Zhang, W., Bansback, N., Amarsi, Z., Birmingham, C. L., and Anis, A. H. (2009). The incidence of co-morbidities related to obesity and overweight: A systematic review and meta-analysis. *BMC Public Health* 9, 1–20. doi: 10.1186/1471-2458-9-88

Gupta, S., and Chen, M. (2023). Medical management of obesity. *Clinical Medicine* 23, 323–329. doi: 10.7861/CLINMED.2023-0183

Gurevich, V. V., and Gurevich, E. V. (2019). The structural basis of the arrestin binding to GPCRs. *Mol Cell Endocrinol* 484, 34. doi: 10.1016/J.MCE.2019.01.019

Gustafson, B., Hedjazifar, S., Gogg, S., Hammarstedt, A., and Smith, U. (2015). Insulin resistance and impaired adipogenesis. *Trends in Endocrinology & Metabolism* 26, 193–200. doi: 10.1016/j.tem.2015.01.006

Haider, R. S., Reichel, M., Matthees, E. S. F., and Hoffmann, C. (2023). Conformational flexibility of ß-arrestins – How these scaffolding proteins guide and transform the functionality of GPCRs. *BioEssays* 45, 2300053. doi: 10.1002/BIES.202300053

Hanif, S. Z., Au, C. C., Torregroza, I., Kutz, C., Jannath, S. Y., Fabiha, T., et al. (2025). The Orphan G Protein-Coupled Receptor GPR52 is a Novel Regulator

of Breast Cancer Multicellular Organization. *bioRxiv*. doi: 10.1101/2024.07.22.604482

Harman-Boehm, I., Blüher, M., Redel, H., Sion-Vardy, N., Ovadia, S., Avinoach, E., et al. (2007). Macrophage Infiltration into Omental Versus Subcutaneous Fat across Different Populations: Effect of Regional Adiposity and the Comorbidities of Obesity. *J Clin Endocrinol Metab* 92, 2240–2247. doi: 10.1210/JC.2006-1811

Hattori, M., Wazawa, T., Orioka, M., Hiruta, Y., and Nagai, T. (2025). Creating coveted bioluminescence colors for simultaneous multi-color bioimaging. *Sci Adv* 11, 4750. doi: 10.1126/SCIADV.ADP4750

Hauge, M., Vestmar, M. A., Husted, A. S., Ekberg, J. P., Wright, M. J., Di Salvo, J., et al. (2015). GPR40 (FFAR1) – Combined Gs and Gq signaling in vitro is associated with robust incretin secretagogue action ex vivo and in vivo. *Mol Metab* 4, 3–14. doi: 10.1016/J.MOLMET.2014.10.002

Hauner, H., Röhrig, K., Spelleken, M., Liu, L. S., and Eckel, J. (1998). Development of insulin-responsive glucose uptake and GLUT4 expression in differentiating human adipocyte precursor cells. *Int J Obes* 22, 448–453. doi: 10.1038/sj.ijo.0800606

Hauser, A. S., Attwood, M. M., Rask-Andersen, M., Schiöth, H. B., and Gloriam, D. E. (2017). Trends in GPCR drug discovery: new agents, targets and indications. *Nat Rev Drug Discov* 16, 829. doi: 10.1038/NRD.2017.178

He, W., Miao, F. J., Lin, D. C., Schwandner, R. T., Wang, Z., Gao, J., et al. (2004). Citric acid cycle intermediates as ligands for orphan G-protein-coupled receptors. *Nature* 429, 188–193. doi: 10.1038/nature02488

Heath, N. G., O'Geen, H., Halmai, N. B., Corn, J. E., and Segal, D. J. (2022). Imaging Unique DNA Sequences in Individual Cells Using a CRISPR-Cas9-Based, Split Luciferase Biosensor. *Front Genome Ed* 4, 867390. doi: 10.3389/FGEED.2022.867390

Hebert, T. L., Wu, X., Yu, G., Goh, B. C., Halvorsen, Y. D. C., Wang, Z., et al. (2009). Culture effects of epidermal growth factor (EGF) and basic fibroblast growth factor (bFGF) on cryopreserved human adipose-derived stromal/stem cell proliferation and adipogenesis. *Journal of Tissue Tngineering and Regenerative Medicine* 3, 553. doi: 10.1002/TERM.198

Heilbronn, L., Smith, S. R., and Ravussin, E. (2004). Failure of fat cell proliferation, mitochondrial function and fat oxidation results in ectopic fat storage, insulin resistance and type II diabetes mellitus. *Int J Obes* 28, S12–S21. doi: 10.1038/SJ.IJO.0802853

Henning, R. J. (2021). Obesity and obesity-induced inflammatory disease contribute to atherosclerosis: a review of the pathophysiology and treatment of obesity. *Am J Cardiovasc Dis* 11, 504. Available at: https://pmc.ncbi.nlm.nih.gov/articles/PMC8449192/ (Accessed October 11, 2025).

Herenbrink, C. K., Sykes, D. A., Donthamsetti, P., Canals, M., Coudrat, T., Shonberg, J., et al. (2016). The role of kinetic context in apparent biased agonism at GPCRs. *Nat Commun* 7, 1–14. doi: 10.1038/ncomms10842

Herrera, L. P. T., Andreassen, S. N., Caroli, J., Rodríguez-Espigares, I., Kermani, A. A., Keseru, G. M., et al. (2025). GPCRdb in 2025: adding odorant receptors, data mapper, structure similarity search and models of physiological ligand complexes. *Nucleic Acids Res* 53, D425–D435. doi: 10.1093/NAR/GKAE1065

Hino, K., Nagata, H., Shimonishi, M., and Ido, M. (2011). High-throughput screening for small-molecule adiponectin secretion modulators. *J Biomol Screen* 16, 628–636. doi: 10.1177/1087057111403474

Hira, V. V. V., de Jong, A. L., Ferro, K., Khurshed, M., Molenaar, R. J., and Van Noorden, C. J. F. (2019). Comparison of different methodologies and cryostat versus paraffin sections for chromogenic immunohistochemistry. *Acta Histochem* 121, 125–134. doi: 10.1016/J.ACTHIS.2018.10.011

Hirasawa, A., Tsumaya, K., Awaji, T., Katsuma, S., Adachi, T., Yamada, M., et al. (2005). Free fatty acids regulate gut incretin glucagon-like peptide-1 secretion through GPR120. *Nat Med* 11, 90–94. doi: 10.1038/nm1168

Hires, S. A., Zhu, Y., and Tsien, R. Y. (2008). Optical measurement of synaptic glutamate spillover and reuptake by linker optimized glutamate-sensitive fluorescent reporters. *Proc Natl Acad Sci U S A* 105, 4411–4416. doi: 10.1073/PNAS.0712008105

Hoefner, C., Muhr, C., Horder, H., Wiesner, M., Wittmann, K., Lukaszyk, D., et al. (2020). Human Adipose-Derived Mesenchymal Stromal/Stem Cell Spheroids Possess High Adipogenic Capacity and Acquire an Adipose Tissue-like Extracellular Matrix Pattern. *Tissue Engineering - Part A: Research Advances* 26, 915–926. doi: 10.1089/TEN.TEA.2019.0206

Hoffmann, C., Gaietta, G., Bünemann, M., Adams, S. R., Oberdorff-Maass, S., Behr, B., et al. (2005). A FlAsH-based FRET approach to determine G protein–coupled receptor activation in living cells. *Nat Methods* 2, 171–176. doi: 10.1038/nmeth742

Hollins, B., Kuravi, S., Digby, G. J., and Lambert, N. A. (2009). The c-terminus of GRK3 indicates rapid dissociation of G protein heterotrimers. *Cell Signal* 21, 1015–1021. doi: 10.1016/J.CELLSIG.2009.02.017

Hong, Y. H., Nishimura, Y., Hishikawa, D., Tsuzuki, H., Miyahara, H., Gotoh, C., et al. (2005). Acetate and Propionate Short Chain Fatty Acids Stimulate Adipogenesis via GPCR43. *Endocrinology* 146, 5092–5099. doi: 10.1210/EN.2005-0545

Hoshino, H., Nakajima, Y., and Ohmiya, Y. (2007). Luciferase-YFP fusion tag with enhanced emission for single-cell luminescence imaging. *Nat Methods* 4, 637–639. doi: 10.1038/nmeth1069

Hotamisligil, G. S., Shargill, N. S., and Spiegelman, B. M. (1993). Adipose Expression of Tumor Necrosis Factor-α: Direct Role in Obesity-Linked Insulin Resistance. *Science (1979)* 259, 87–91. doi: 10.1126/SCIENCE.7678183

Hu, E., Liang, P., and Spiegelman, B. M. (1996). AdipoQ Is a Novel Adipose-specific Gene Dysregulated in Obesity. *Journal of Biological Chemistry* 271, 10697–10703. doi: 10.1074/JBC.271.18.10697

Hudson, B. D. (2017). "Using biosensors to study free fatty acid receptor pharmacology and function," in *Handbook of Experimental Pharmacology*, (Springer New York LLC), 79–100. doi: 10.1007/164_2016_58

Hudson, B. D., Shimpukade, B., Mackenzie, A. E., Butcher, A. J., Pediani, J. D., Christiansen, E., et al. (2013). The Pharmacology of TUG-891, a Potent and Selective Agonist of the Free Fatty Acid Receptor 4 (FFA4/GPR120), Demonstrates Both Potential Opportunity and Possible Challenges to Therapeutic Agonism. *Mol Pharmacol* 84, 710–725. doi: 10.1124/MOL.113.087783

Hudson, B. D., Smith, N. J., and Milligan, G. (2011). Experimental Challenges to Targeting Poorly Characterized GPCRs: Uncovering the Therapeutic Potential for Free Fatty Acid Receptors. *Adv Pharmacol* 62, 175–218. doi: 10.1016/B978-0-12-385952-5.00006-3

Husted, A. S., Ekberg, J. H., Tripp, E., Nissen, T. A. D., Meijnikman, S., O'Brien, S. L., et al. (2020). Autocrine negative feedback regulation of lipolysis through sensing of NEFAs by FFAR4/GPR120 in WAT. *Mol Metab* 42, 101103. doi: 10.1016/J.MOLMET.2020.101103

Husted, A. S., Trauelsen, M., Rudenko, O., Hjorth, S. A., and Schwartz, T. W. (2017). GPCR-Mediated Signaling of Metabolites. *Cell Metab* 25, 777–796. doi: 10.1016/J.CMET.2017.03.008

Ibay, I. C., and Gilchrist, A. (2021). An Overview of G Protein Coupled Receptors and Their Signaling Partners. *GPCRs as Therapeutic Targets* 1, 3–19. doi: 10.1002/9781119564782.CH1

Ichimura, A., Hirasawa, A., Poulain-Godefroy, O., Bonnefond, A., Hara, T., Yengo, L., et al. (2012). Dysfunction of lipid sensor GPR120 leads to obesity in both mouse and human. *Nature* 483, 350–354. doi: 10.1038/nature10798

Ikeda, T., Nishida, A., Yamano, M., and Kimura, I. (2022). Short-chain fatty acid receptors and gut microbiota as therapeutic targets in metabolic, immune, and neurological diseases. *Pharmacol Ther* 239, 108273. doi: 10.1016/J.PHARMTHERA.2022.108273

Inoue, A., Raimondi, F., Kadji, F. M. N., Singh, G., Kishi, T., Uwamizu, A., et al. (2019). Illuminating G-Protein-Coupling Selectivity of GPCRs. *Cell* 177, 1933-1947.e25. doi: 10.1016/J.CELL.2019.04.044

Inoue, T., Heo, W. Do, Grimley, J. S., Wandless, T. J., and Meyer, T. (2005). An inducible translocation strategy to rapidly activate and inhibit small GTPase signaling pathways. *Nat Methods* 2, 415–418. doi: 10.1038/NMETH763;KWRD=LIFE+SCIENCES

Inoue, T., and Krumlauf, R. (2001). An Impulse to the brain—using in vivo electroporation. *Nat Neurosci* 4, 1156–1158. doi: 10.1038/NN1101-1156

Institute for Health Metrics and Evaluation (2024). Global Burden of Disease 2021: Findings from the GBD 2021 Study. Seattle, WA. Available at: https://www.healthdata.org/research-analysis/library/global-burden-disease-2021-findings-gbd-2021-study (Accessed October 5, 2025).

International Diabetes Federation (2025). IDF Diabetes Atlas 2025. *IDF Diabetes Atlas, 11th edn*. Available at: https://diabetesatlas.org/resources/idf-diabetes-atlas-2025/ (Accessed October 12, 2025).

Ioannidou, A., Alatar, S., Schipper, R., Baganha, F., Åhlander, M., Hornell, A., et al. (2022). Hypertrophied human adipocyte spheroids as in vitro model of weight gain and adipose tissue dysfunction. *Journal of Physiology* 600, 869–883. doi: 10.1113/JP281445

Itoh, Y., Kawamata, Y., Harada, M., Kobayashi, M., Fujii, R., Fukusumi, S., et al. (2003). Free fatty acids regulate insulin secretion from pancreatic ß cells through GPR40. *Nature* 422, 173–176. doi: 10.1038/nature01478

Iwata, T., Taniguchi, H., Kuwajima, M., Taniguchi, T., Okuda, Y., Sukeno, A., et al. (2012). The Action of D-Dopachrome Tautomerase as an Adipokine in Adipocyte Lipid Metabolism. *PLoS One* 7, e33402. doi: 10.1371/JOURNAL.PONE.0033402

Jackisch, L. (2019). Molecular mechanisms of adipose tissue mitochondrial (mal)adaptation in obesity. University of Warwick. Available at: http://webcat.warwick.ac.uk/record=b3736170 (Accessed May 29, 2023).

Jain, D., Mathur, S. R., and Iyer, V. K. (2014). Cell blocks in cytopathology: A review of preparative methods, utility in diagnosis and role in ancillary studies. *Cytopathology* 25, 356–371. doi: 10.1111/CYT.12174

Janetopoulos, C., Jin, T., and Devreotes, P. (2001). Receptor-Mediated Activation of Heterotrimeric G-Proteins in Living Cells. *Science (1979)* 291, 2408–2411. doi: 10.1126/SCIENCE.1055835

Janicot, R., Maziarz, M., Park, J. C., Zhao, J., Luebbers, A., Green, E., et al. (2024). Direct interrogation of context-dependent GPCR activity with a universal biosensor platform. *Cell* 187, 1527-1546.e25. doi: 10.1016/J.CELL.2024.01.028

Jean-Charles, P. Y., Kaur, S., and Shenoy, S. K. (2017). G Protein-Coupled Receptor Signaling Through ß-Arrestin-Dependent Mechanisms. *J Cardiovasc Pharmacol* 70, 142–158. doi: 10.1097/FJC.0000000000000482

Jenkins, L., Harries, N., Lappin, J. E., MacKenzie, A. E., Neetoo-Isseljee, Z., Southern, C., et al. (2012). Antagonists of GPR35 Display High Species Ortholog Selectivity and Varying Modes of Action. *J Pharmacol Exp Ther* 343, 683. doi: 10.1124/JPET.112.198945

Jenkins, L., Marsango, S., Mancini, S., Mahmud, Z. Al, Morrison, A., McElroy, S. P., et al. (2021). Discovery and Characterization of Novel Antagonists of the Proinflammatory Orphan Receptor GPR84. *ACS Pharmacol Transl Sci* 4, 1598–1613. doi: 10.1021/ACSPTSCI.1C00151

Jensen, C., and Teng, Y. (2020). Is It Time to Start Transitioning From 2D to 3D Cell Culture? *Front Mol Biosci* 7, 33. doi: 10.3389/fmolb.2020.00033

Jeon, Y. G., Kim, Y. Y., Lee, G., and Kim, J. B. (2023). Physiological and pathological roles of lipogenesis. *Nat Metab* 5, 735–759. doi: 10.1038/S42255-023-00786-Y

Jones, M. V., and Calabresi, P. A. (2007). Agar-gelatin for embedding tissues prior to paraffin processing. *Biotechniques* 42, 569–570. doi: 10.2144/000112456

Jorand, R., Biswas, S., Wakefield, D. L., Tobin, S. J., Golfetto, O., Hilton, K., et al. (2016). Molecular signatures of mu opioid receptor and somatostatin receptor 2 in pancreatic cancer. *Mol Biol Cell* 27, 3659–3672. doi: 10.1091/MBC.E16-06-0427

Jovic, D., Liang, X., Zeng, H., Lin, L., Xu, F., and Luo, Y. (2022). Single-cell RNA sequencing technologies and applications: A brief overview. *Clin Transl Med* 12, e694. doi: 10.1002/CTM2.694

Juncker, T., Chatton, B., and Donzeau, M. (2023). The Prodigious Potential of mRNA Electrotransfer as a Substitute to Conventional DNA-Based Transient Transfection. *Cells* 12, 1591. doi: 10.3390/CELLS12121591

Kaczmarek, I., Suchý, T., Strnadová, M., and Thor, D. (2024). Qualitative and quantitative analysis of lipid droplets in mature 3T3-L1 adipocytes using oil red O. *STAR Protoc* 5, 102977. doi: 10.1016/J.XPRO.2024.102977

Kamble, P. G., Hetty, S., Vranic, M., Almby, K., Castillejo-López, C., Abalo, X. M., et al. (2020). Proof-of-concept for CRISPR/Cas9 gene editing in human preadipocytes: Deletion of FKBP5 and PPARG and effects on adipocyte differentiation and metabolism. *Sci Rep* 10, 10565-. doi: 10.1038/s41598-020-67293-y

Kannan, K., and Vimalkumar, K. (2021). A Review of Human Exposure to Microplastics and Insights Into Microplastics as Obesogens. *Front Endocrinol (Lausanne)* 12, 724989. doi: 10.3389/FENDO.2021.724989/BIBTEX

Karnieli, O., Friedner, O. M., Allickson, J. G., Zhang, N., Jung, S., Fiorentini, D., et al. (2017). A consensus introduction to serum replacements and serum-free media for cellular therapies. *Cytotherapy* 19, 155–169. doi: 10.1016/J.JCYT.2016.11.011

Kässner, F., Kirstein, A., Händel, N., Schmid, G. L., Landgraf, K., Berthold, A., et al. (2020). A new human adipocyte model with PTEN haploinsufficiency. *Adipocyte* 9, 290. doi: 10.1080/21623945.2020.1785083

Katsuki, A., Sumida, Y., Murashima, S., Murata, K., Takarada, Y., Ito, K., et al. (1998). Serum Levels of Tumor Necrosis Factor-α Are Increased in Obese Patients with Noninsulin-Dependent Diabetes Mellitus. *J Clin Endocrinol Metab* 83, 859–862. doi: 10.1210/JCEM.83.3.4618

Kawai, T., Autieri, M. V., and Scalia, R. (2021). Adipose tissue inflammation and metabolic dysfunction in obesity. *Am J Physiol Cell Physiol* 320, C375–C391. doi: 10.1152/AJPCELL.00379.2020

Kawakami, M., Murase, T., Ogama, H., Ishibashi, S., Mori, N., Takaku, F., et al. (1987). Human Recombinant TNF Suppresses Lipoprotein Lipase Activity and Stimulates Lipolysis in 3T3-L1 Cells. *The Journal of Biochemistry* 101, 331–338. doi: 10.1093/OXFORDJOURNALS.JBCHEM.A121917

Keiran, N., Ceperuelo-Mallafre, V., Calvo, E., Hernandez-Alvarez, M. I., Ejarque, M., Nunez-Roa, C., et al. (2019). SUCNR1 controls an anti-inflammatory program in macrophages to regulate the metabolic response to obesity. *Nat Immunol* 20, 581–592. doi: 10.1038/s41590-019-0372-7

Kemas, A. M., Youhanna, S., Zandi Shafagh, R., and Lauschke, V. M. (2021). Insulin-dependent glucose consumption dynamics in 3D primary human liver cultures measured by a sensitive and specific glucose sensor with nanoliter input volume. *The FASEB Journal* 35, e21305. doi: 10.1096/FJ.202001989RR

Kershaw, E. E., and Flier, J. S. (2004). Adipose Tissue as an Endocrine Organ. *J Clin Endocrinol Metab* 89, 2548–2556. doi: 10.1210/JC.2004-0395

Kersten, S. (2001). Mechanisms of nutritional and hormonal regulation of lipogenesis. *EMBO Rep* 2, 282–286. doi: 10.1093/EMBO-REPORTS/KVE071

Keuper, M., Blüher, M., Schön, M. R., Möller, P., Dzyakanchuk, A., Amrein, K., et al. (2011a). An inflammatory micro-environment promotes human adipocyte apoptosis. *Mol Cell Endocrinol* 339, 105–113. doi: 10.1016/J.MCE.2011.04.004

Keuper, M., Dzyakanchuk, A., Amrein, K. E., Wabitsch, M., and Fischer-Posovszky, P. (2011b). THP-1 macrophages and SGBS adipocytes - a new human in vitro model system of inflamed adipose tissue. *Front Endocrinol (Lausanne)* 2, 15170. doi: 10.3389/FENDO.2011.00089/BIBTEX

Kim, H., Baek, I. Y., and Seong, J. (2022). Genetically encoded fluorescent biosensors for GPCR research. *Front Cell Dev Biol* 10, 1007893. doi: 10.3389/FCELL.2022.1007893

Kim, J. (2023). The pathophysiology of diabetic foot: a narrative review. *Journal of Yeungnam Medical Science* 40, 328–334. doi: 10.12701/JYMS.2023.00731

Kim, T. K., and Eberwine, J. H. (2010). Mammalian cell transfection: The present and the future. *Anal Bioanal Chem* 397, 3173–3178. doi: 10.1007/S00216-010-3821-6

Kingham, P. J., Kalbermatten, D. F., Mahay, D., Armstrong, S. J., Wiberg, M., and Terenghi, G. (2007). Adipose-derived stem cells differentiate into a Schwann cell phenotype and promote neurite outgrowth in vitro. *Exp Neurol* 207, 267–274. doi: 10.1016/J.EXPNEUROL.2007.06.029

Kitahara, C. M., Flint, A. J., Berrington de Gonzalez, A., Bernstein, L., Brotzman, M., MacInnis, R. J., et al. (2014). Association between Class III Obesity (BMI of 40–59 kg/m2) and Mortality: A Pooled Analysis of 20 Prospective Studies. *PLoS Med* 11, e1001673. doi: 10.1371/JOURNAL.PMED.1001673

Kivimäki, M., Strandberg, T., Pentti, J., Nyberg, S. T., Frank, P., Jokela, M., et al. (2022). Body-mass index and risk of obesity-related complex multimorbidity: an observational multicohort study. *Lancet Diabetes Endocrinol* 10, 253–263. doi: 10.1016/S2213-8587(22)00033-X

Klingelhutz, A. J., Gourronc, F. A., Chaly, A., Wadkins, D. A., Burand, A. J., Markan, K. R., et al. (2018). Scaffold-free generation of uniform adipose spheroids for metabolism research and drug discovery. *Sci Rep* 8. doi: 10.1038/S41598-017-19024-Z

Klip, A., McGraw, T. E., and James, D. E. (2019). Thirty sweet years of GLUT4. *Journal of Biological Chemistry* 294, 11369–11381. doi: 10.1074/JBC.REV119.008351

Koh, Y. J., Koh, B. I., Kim, H., Joo, H. J., Jin, H. K., Jeon, J., et al. (2011). Stromal Vascular Fraction From Adipose Tissue Forms Profound Vascular Network Through the Dynamic Reassembly of Blood Endothelial Cells. *Arterioscler Thromb Vasc Biol* 31, 1141–1150. doi: 10.1161/ATVBAHA.110.218206

Kolb, P., Kenakin, T., Alexander, S. P. H., Bermudez, M., Bohn, L. M., Breinholt, C. S., et al. (2022). Community guidelines for GPCR ligand bias: IUPHAR review 32. *Br J Pharmacol* 179, 3651–3674. doi: 10.1111/BPH.15811

Kulesza, J., Pawłowska, M., and Augustin, E. (2021). The Influence of Antitumor Unsymmetrical Bisacridines on 3D Cancer Spheroids Growth and Viability. *Molecules* 26, 6262. doi: 10.3390/MOLECULES26206262

Kwon, Y. N., Kim, W. K., Lee, S. H., Kim, K., Kim, E. Y., Ha, T. H., et al. (2011). Monitoring of adipogenic differentiation at the single-cell level using atomic force microscopic analysis. *Journal of Spectroscopy* 26, 329–335. doi: 10.3233/SPE-2012-0566

Ky, A., McCoy, A. J., Flesher, C. G., Friend, N. E., Li, J., Akinleye, K., et al. (2023). Matrix density regulates adipocyte phenotype. *Adipocyte* 12. doi: 10.1080/21623945.2023.2268261

Labriola, N. R., and Darling, E. M. (2015). Temporal heterogeneity in single-cell gene expression and mechanical properties during adipogenic differentiation. *J Biomech* 48, 1058–1066. doi: 10.1016/J.JBIOMECH.2015.01.033

Lai, M., Li, X., Li, J., Hu, Y., Czajkowsky, D. M., and Shao, Z. (2017). Improved clearing of lipid droplet-rich tissues for three-dimensional structural elucidation. *Acta Biochim Biophys Sin (Shanghai)* 49, 465–467. doi: 10.1093/ABBS/GMX018

Lan, T. H., Liu, Q., Li, C., Wu, G., and Lambert, N. A. (2012). Sensitive and High Resolution Localization and Tracking of Membrane Proteins in Live Cells with BRET. *Traffic* 13, 1450–1456. doi: 10.1111/J.1600-0854.2012.01401.X

Landgraf, K., Klöting, N., Gericke, M., Maixner, N., Guiu-Jurado, E., Scholz, M., et al. (2020). The Obesity-Susceptibility Gene TMEM18 Promotes Adipogenesis through Activation of PPARG. *Cell Rep* 33, 108295. doi: 10.1016/j.celrep.2020.108295

Lane, S. W., Williams, D. A., and Watt, F. M. (2014). Modulating the stem cell niche for tissue regeneration. *Nat Biotechnol* 32, 795. doi: 10.1038/NBT.2978

Langhans, S. A. (2018). Three-dimensional in vitro cell culture models in drug discovery and drug repositioning. *Front Pharmacol* 9, 6. doi: 10.3389/fphar.2018.00006

Lauschke, V. M., and Hagberg, C. E. (2023). Next-generation human adipose tissue culture methods. *Curr Opin Genet Dev* 80, 102057. doi: 10.1016/J.GDE.2023.102057

Lazzari, G., Vinciguerra, D., Balasso, A., Nicolas, V., Goudin, N., Garfa-Traore, M., et al. (2019). Light sheet fluorescence microscopy versus confocal microscopy: in quest of a suitable tool to assess drug and nanomedicine penetration into multicellular tumor spheroids. *European Journal of Pharmaceutics and Biopharmaceutics* 142, 195–203. doi: 10.1016/J.EJPB.2019.06.019

Le, P., Tatar, M., Dasarathy, S., Alkhouri, N., Herman, W. H., Taksler, G. B., et al. (2025). Estimated Burden of Metabolic Dysfunction–Associated Steatotic

Liver Disease in US Adults, 2020 to 2050. *JAMA Netw Open* 8, e2454707. doi: 10.1001/JAMANETWORKOPEN.2024.54707

Le Poul, E., Loison, C., Struyf, S., Springael, J. Y., Lannoy, V., Decobecq, M. E., et al. (2003). Functional Characterization of Human Receptors for Short Chain Fatty Acids and Their Role in Polymorphonuclear Cell Activation. *Journal of Biological Chemistry* 278, 25481–25489. doi: 10.1074/JBC.M301403200

Lee, D. Y., Lee, S. Y., Yun, S. H., Jeong, J. W., Kim, J. H., Kim, H. W., et al. (2022). Review of the Current Research on Fetal Bovine Serum and the Development of Cultured Meat. *Food Sci Anim Resour* 42, 775. doi: 10.5851/KOSFA.2022.E46

Lee, D. Y., Yun, S. H., Lee, S. Y., Lee, J., Mariano, E., Joo, S. T., et al. (2023). Analysis of commercial fetal bovine serum (FBS) and its substitutes in the development of cultured meat. *Food Research International* 174, 113617. doi: 10.1016/J.FOODRES.2023.113617

Lee, J. M., Park, D. Y., Yang, L., Kim, E. J., Ahrberg, C. D., Lee, K. B., et al. (2018). Generation of uniform-sized multicellular tumor spheroids using hydrogel microwells for advanced drug screening. *Sci Rep* 8, 1–10. doi: 10.1038/S41598-018-35216-7

Lee, M. H., Appleton, K. M., Strungs, E. G., Kwon, J. Y., Morinelli, T. A., Peterson, Y. K., et al. (2016). The conformational signature of ß-arrestin2 predicts its trafficking and signalling functions. *Nature* 531, 665–668. doi: 10.1038/nature17154

Lee, M. J., and Fried, S. K. (2014). Optimal Protocol for the Differentiation and Metabolic Analysis of Human Adipose Stromal Cells. *Methods Enzymol* 538, 49. doi: 10.1016/B978-0-12-800280-3.00004-9

Lee, M. J., Pickering, R. T., and Puri, V. (2013a). Prolonged efficiency of siRNA-mediated gene silencing in primary cultures of human preadipocytes and adipocytes. *Obesity* 22, 1064. doi: 10.1002/OBY.20641

Lee, M. J., Wu, Y., and Fried, S. K. (2013b). Adipose tissue heterogeneity: Implication of depot differences in adipose tissue for obesity complications. *Mol Aspects Med* 34, 1–11. doi: 10.1016/J.MAM.2012.10.001

Leggett, S. E., Khoo, A. S., and Wong, I. Y. (2017). Multicellular tumor invasion and plasticity in biomimetic materials. *Biomater Sci* 5, 1460–1479. doi: 10.1039/C7BM00272F

Lehr, S., Hartwig, S., and Sell, H. (2012). Adipokines: A treasure trove for the discovery of biomarkers for metabolic disorders. *Proteomics Clin Appl* 6, 91–101. doi: 10.1002/PRCA.201100052

Li, J., Jin, C., Gustafsson, S., Rao, A., Wabitsch, M., Park, C. Y., et al. (2023a). Single-cell transcriptome dataset of human and mouse in vitro adipogenesis models. *Sci Data* 10, 1–10. doi: 10.1038/S41597-023-02293-X

Li, X., Ren, Y., Chang, K., Wu, W., Griffiths, H. R., Lu, S., et al. (2023b). Adipose tissue macrophages as potential targets for obesity and metabolic diseases. *Front Immunol* 14, 1153915. doi: 10.3389/FIMMU.2023.1153915

Lim, S., and Meigs, J. B. (2014). Links Between Ectopic Fat and Vascular Disease in Humans. *Arterioscler Thromb Vasc Biol* 34, 1820–1826. doi: 10.1161/ATVBAHA.114.303035

Lin, Y., and Smrcka, A. V. (2011). Understanding molecular recognition by G protein ßγ subunits on the path to pharmacological targeting. *Mol Pharmacol* 80, 551–557. doi: 10.1124/mol.111.073072

Littmann, T., Buschauer, A., and Bernhardt, G. (2019). Split luciferase-based assay for simultaneous analyses of the ligand concentration- and time-

dependent recruitment of ß-arrestin2. *Anal Biochem* 573, 8–16. doi: 10.1016/J.AB.2019.02.023

Liu, S., Su, Y., Lin, M. Z., and Ronald, J. A. (2021). Brightening up Biology: Advances in Luciferase Systems for in Vivo Imaging. *ACS Chem Biol* 16, 2707. doi: 10.1021/ACSCHEMBIO.1C00549

Liu, Z., Chen, O., Wall, J. B. J., Zheng, M., Zhou, Y., Wang, L., et al. (2017). Systematic comparison of 2A peptides for cloning multi-genes in a polycistronic vector. *Sci Rep* 7, 1–9. doi: 10.1038/S41598-017-02460-2

Lo, K. A., Labadorf, A., Kennedy, N. J., Han, M. S., Yap, Y. S., Matthews, B., et al. (2013). Analysis of in vitro insulin resistance models and their physiological relevance to in vivo diet-induced adipose insulin resistance. *Cell Rep* 5, 259–270. doi: 10.1016/J.CELREP.2013.08.039

Longo, P. A., Kavran, J. M., Kim, M. S., and Leahy, D. J. (2014). Single Cell Cloning of a Stable Mammalian Cell Line. *Methods Enzymol* 536, 165–172. doi: 10.1016/B978-0-12-420070-8.00014-3

Loos, R. J. F., and Yeo, G. S. H. (2022). The genetics of obesity: from discovery to biology. *Nat Rev Genet* 23, 120–133. doi: 10.1038/S41576-021-00414-Z

Lopez-Jimenez, F., Almahmeed, W., Bays, H., Cuevas, A., Di Angelantonio, E., le Roux, C. W., et al. (2022). Obesity and cardiovascular disease: mechanistic insights and management strategies. A joint position paper by the World Heart Federation and World Obesity Federation. *Eur J Prev Cardiol* 29, 2218–2237. doi: 10.1093/EURJPC/ZWAC187

Lorente, J. S., Sokolov, A. V., Ferguson, G., Schiöth, H. B., Hauser, A. S., and Gloriam, D. E. (2025). GPCR drug discovery: new agents, targets and indications. *Nat Rev Drug Discov* 24, 458–479. doi: 10.1038/s41573-025-01139-y

Loskill, P., Sezhian, T., Tharp, K. M., Lee-Montiel, F. T., Jeeawoody, S., Reese, W. M., et al. (2017). WAT-on-a-chip: a physiologically relevant microfluidic system incorporating white adipose tissue. *Lab Chip* 17, 1645–1654. doi: 10.1039/C6LC01590E

Louis, F., Piantino, M., Liu, H., Kang, D. H., Sowa, Y., Kitano, S., et al. (2021). Bioprinted Vascularized Mature Adipose Tissue with Collagen Microfibers for Soft Tissue Regeneration. *Cyborg and Bionic Systems* 2021, 1412542. doi: 10.34133/2021/1412542

Luca, T., Pezzino, S., Puleo, S., and Castorina, S. (2024). Lesson on obesity and anatomy of adipose tissue: new models of study in the era of clinical and translational research. *J Transl Med* 22, 1–18. doi: 10.1186/S12967-024-05547-3

Lung, T., Jan, S., Tan, E. J., Killedar, A., and Hayes, A. (2019). Impact of overweight, obesity and severe obesity on life expectancy of Australian adults. *Int J Obes* 43, 782–789. doi: 10.1038/S41366-018-0210-2

Luo, H., Ruan, H., Ye, C., Jiang, W., Wang, X., Chen, S., et al. (2024). Plant-derived leaf vein scaffolds for the sustainable production of dog cell-cultured meat. *Food Chem X* 23, 101603. doi: 10.1016/J.FOCHX.2024.101603

Lustig, M., Zadka, Y., Levitsky, I., Gefen, A., and Benayahu, D. (2019). Adipocytes Migration is Altered Through Differentiation. *Microscopy and Microanalysis* 25, 1195–1200. doi: 10.1017/S1431927619014727

MacKenzie, A. E., Caltabiano, G., Kent, T. C., Jenkins, L., McCallum, J. E., Hudson, B. D., et al. (2014). The Antiallergic Mast Cell Stabilizers Lodoxamide and Bufrolin as the First High and Equipotent Agonists of Human and Rat GPR35. *Mol Pharmacol* 85, 91. doi: 10.1124/MOL.113.089482

Mackenzie, A. E., Quon, T., Lin, L. C., Hauser, A. S., Jenkins, L., Inoue, A., et al. (2019). Receptor selectivity between the G proteins Gα12 and Gα13 is defined by a single leucine-to-isoleucine variation. *The FASEB Journal* 33, 5005–5017. doi: 10.1096/FJ.201801956R

Madsen, N. H., Nielsen, B. S., Skandorff, I., Rodriguez-Pardo, C., Hadrup, S. R., Ormhøj, M., et al. (2025). Novel approaches to 3D cancer heterospheroid culture and assay development for immunotherapy screening. *Exp Cell Res* 449, 114604. doi: 10.1016/J.YEXCR.2025.114604

Maffei, M., Halaas, J., Ravussin, E., Pratley, R. E., Lee, G. H., Zhang, Y., et al. (1995). Leptin levels in human and rodent: Measurement of plasma leptin and ob RNA in obese and weight-reduced subjects. *Nat Med* 1, 1155–1161. doi: 10.1038/NM1195-1155

Maioli, V., Chennell, G., Sparks, H., Lana, T., Kumar, S., Carling, D., et al. (2016). Time-lapse 3-D measurements of a glucose biosensor in multicellular spheroids by light sheet fluorescence microscopy in commercial 96-well plates. *Sci Rep* 6, 37777-. doi: 10.1038/srep37777

Malik, R. U., Dysthe, M., Ritt, M., Sunahara, R. K., and Sivaramakrishnan, S. (2017). ER/K linked GPCR-G protein fusions systematically modulate second messenger response in cells. *Sci Rep* 7, 1–13. doi: 10.1038/s41598-017-08029-3

Malik, R. U., Ritt, M., DeVree, B. T., Neubig, R. R., Sunahara, R. K., and Sivaramakrishnan, S. (2013). Detection of G Protein-selective G Protein-coupled Receptor (GPCR) Conformations in Live Cells. *Journal of Biological Chemistry* 288, 17167–17178. doi: 10.1074/JBC.M113.464065

Mamouni, K., Kim, J., Lokeshwar, B. L., and Kallifatidis, G. (2021). ARRB1 Regulates Metabolic Reprogramming to Promote Glycolysis in Stem Cell-Like Bladder Cancer Cells. *Cancers (Basel)* 13. doi: 10.3390/CANCERS13081809

Mancini, S. J., Mahmud, Z. Al, Jenkins, L., Bolognini, D., Newman, R., Barnes, M., et al. (2019). On-target and off-target effects of novel orthosteric and allosteric activators of GPR84. *Sci Rep* 9. doi: 10.1038/S41598-019-38539-1

Mandl, M., Viertler, H. P., Hatzmann, F. M., Brucker, C., Großmann, S., Waldegger, P., et al. (2022). An organoid model derived from human adipose stem/progenitor cells to study adipose tissue physiology. *Adipocyte* 11, 164–174. doi: 10.1080/21623945.2022.2044601

Mandrika, I., Tilgase, A., Petrovska, R., and Klovins, J. (2018). Hydroxycarboxylic Acid Receptor Ligands Modulate Proinflammatory Cytokine Expression in Human Macrophages and Adipocytes without Affecting Adipose Differentiation. *Biol Pharm Bull* 41, 1574–1580. doi: 10.1248/BPB.B18-00301

Marcelin, G., Gautier, E. L., and Clement, K. (2022). Adipose Tissue Fibrosis in Obesity: Etiology and Challenges. *Annu Rev Physiol* 84, 135–155. doi: 10.1146/ANNUREV-PHYSIOL-060721-092930

Mariman, E. C. M., and Wang, P. (2010). Adipocyte extracellular matrix composition, dynamics and role in obesity. *Cellular and Molecular Life Sciences* 67, 1277–1292. doi: 10.1007/S00018-010-0263-4

Marín-Peñalver, J. J., Martín-Timón, I., Sevillano-Collantes, C., and Cañizo-Gómez, F. J. del (2016). Update on the treatment of type 2 diabetes mellitus. *World J Diabetes* 7, 354. doi: 10.4239/WJD.V7.I17.354

Maritan, S. M., Lian, E. Y., and Mulligan, L. M. (2017). An Efficient and Flexible Cell Aggregation Method for 3D Spheroid Production. *Journal of Visualized Experiments* 2017, 55544. doi: 10.3791/55544

Markussen, L., Isidor, M., Breining, P., Andersen, E., Rasmussen, N., LI, P. L., et al. (2017). Characterization of immortalized human brown and white pre-

adipocyte cell models from a single donor. *PLoS One* 12. doi: 10.1371/JOURNAL.PONE.0185624

Marsango, S., Ward, R. J., Jenkins, L., Butcher, A. J., Mahmud, Z. Al, Dwomoh, L., et al. (2022). Selective phosphorylation of threonine residues defines GPR84–arrestin interactions of biased ligands. *Journal of Biological Chemistry* 298. doi: 10.1016/j.jbc.2022.101932

Martinez-Santibañez, G., Cho, K. W., and Lumeng, C. N. (2014). Imaging White Adipose Tissue with Confocal Microscopy. *Methods Enzymol* 537, 17–30. doi: 10.1016/B978-0-12-411619-1.00002-1

Marvin, J. S., Borghuis, B. G., Tian, L., Cichon, J., Harnett, M. T., Akerboom, J., et al. (2013). An optimized fluorescent probe for visualizing glutamate neurotransmission. *Nature Methods 2013 10:2* 10, 162–170. doi: 10.1038/nmeth.2333

Massaro, M., Scoditti, E., Pellegrino, M., Carluccio, M. A., Calabriso, N., Wabitsch, M., et al. (2016). Therapeutic potential of the dual peroxisome proliferator activated receptor (PPAR)α/γ agonist aleglitazar in attenuating TNF-α-mediated inflammation and insulin resistance in human adipocytes. *Pharmacol Res* 107, 125–136. doi: 10.1016/J.PHRS.2016.02.027

Masuho, I., Martemyanov, K. A., and Lambert, N. A. (2015a). Monitoring G protein activation in cells with BRET. *Methods in Molecular Biology* 1335, 107. doi: 10.1007/978-1-4939-2914-6_8

Masuho, I., Ostrovskaya, O., Kramer, G. M., Jones, C. D., Xie, K., and Martemyanov, K. A. (2015b). Distinct profiles of functional discrimination among G proteins determine the actions of G protein-coupled receptors. *Sci Signal* 8. doi: 10.1126/SCISIGNAL.AAB4068

Maziarz, M., Park, J., Leyme, A., Marivin, A., Garcia-Lopez, A., Patel, P., et al. (2020). Revealing the Activity of Trimeric G-proteins in Live Cells with a Versatile Biosensor Design. *Cell* 182, 770-785.e16. doi: 10.1016/J.CELL.2020.06.020

Mazini, L., Ezzoubi, M., and Malka, G. (2021). Overview of current adipose-derived stem cell (ADSCs) processing involved in therapeutic advancements: flow chart and regulation updates before and after COVID-19. *Stem Cell Res Ther* 12, 1. doi: 10.1186/S13287-020-02006-W

McCaffrey, M. W., and Lindsay, A. J. (2013). Rab Family. *Encyclopedia of Biological Chemistry: Second Edition*, 1–6. doi: 10.1016/B978-0-12-378630-2.00404-7

McCarthy, M., Brown, T., Alarcon, A., Williams, C., Wu, X., Abbott, R. D., et al. (2020). Fat-On-A-Chip Models for Research and Discovery in Obesity and Its Metabolic Comorbidities. *Tissue Eng Part B Rev* 26, 586. doi: 10.1089/TEN.TEB.2019.0261

McCreath, K. J., Espada, S., Galvez, B. G., Benito, M., de Molina, A., Sepulveda, P., et al. (2015). Targeted disruption of the SUCNR1 metabolic receptor leads to dichotomous effects on obesity. *Diabetes* 64, 1154–1167. doi: 10.2337/db14-0346

McLenachan, S., Zhang, D., Palomo, A. B. A., Edel, M. J., and Chen, F. K. (2013). mRNA Transfection of Mouse and Human Neural Stem Cell Cultures. *PLoS One* 8, e83596. doi: 10.1371/JOURNAL.PONE.0083596

Milligan, G., Alvarez-Curto, E., Hudson, B. D., Prihandoko, R., and Tobin, A. B. (2017a). FFA4/GPR120: Pharmacology and Therapeutic Opportunities. *Trends Pharmacol Sci* 38, 809–821. doi: 10.1016/j.tips.2017.06.006

Milligan, G., Shimpukade, B., Ulven, T., and Hudson, B. D. (2017b). Complex pharmacology of free fatty acid receptors. *Chem Rev* 117, 67–110. doi: 10.1021/acs.chemrev.6b00056

Mirabelli, M., Misiti, R., Sicilia, L., Brunetti, F. S., Chiefari, E., Brunetti, A., et al. (2024). Hypoxia in Human Obesity: New Insights from Inflammation towards Insulin Resistance—A Narrative Review. *Int J Mol Sci* 25, 9802. doi: 10.3390/IJMS25189802

Miyawaki, A., Llopis, J., Heim, R., Michael McCaffery, J., Adams, J. A., Ikura, M., et al. (1997). Fluorescent indicators for Ca2+based on green fluorescent proteins and calmodulin. *Nature* 388, 882–887. doi: 10.1038/42264

Moffett, J. R., Puthillathu, N., Vengilote, R., Jaworski, D. M., and Namboodiri, A. M. (2020). Acetate Revisited: A Key Biomolecule at the Nexus of Metabolism, Epigenetics and Oncogenesis—Part 1: Acetyl-CoA, Acetogenesis and Acyl-CoA Short-Chain Synthetases. *Front Physiol* 11, 580167. doi: 10.3389/FPHYS.2020.580167

Moreno-Indias, I., and Tinahones, F. J. (2015). Impaired Adipose Tissue Expandability and Lipogenic Capacities as Ones of the Main Causes of Metabolic Disorders. *J Diabetes Res* 2015, 970375. doi: 10.1155/2015/970375

Morgan, A., Hartmanis, S., Tsochatzis, E., Newsome, P. N., Ryder, S. D., Elliott, R., et al. (2021). Disease burden and economic impact of diagnosed non-alcoholic steatohepatitis (NASH) in the United Kingdom (UK) in 2018. *The European Journal of Health Economics* 22, 505. doi: 10.1007/S10198-020-01256-Y

Morrison, S., and McGee, S. L. (2015). 3T3-L1 adipocytes display phenotypic characteristics of multiple adipocyte lineages. *Adipocyte* 4, 295. doi: 10.1080/21623945.2015.1040612

Muller, S., Ader, I., Creff, J., Leménager, H., Achard, P., Casteilla, L., et al. (2019). Human adipose stromal-vascular fraction self-organizes to form vascularized adipose tissue in 3D cultures. *Sci Rep* 9, 7250-. doi: 10.1038/s41598-019-43624-6

Muniyappa, R., Chen, H., Muzumdar, R. H., Einstein, F. H., Yan, X., Yue, L. Q., et al. (2009). Comparison between surrogate indexes of insulin sensitivity/resistance and hyperinsulinemic euglycemic clamp estimates in rats. *Am J Physiol Endocrinol Metab* 297, 1023–1029. doi: 10.1152/AJPENDO.00397.2009

Muniyappa, R., Lee, S., Chen, H., and Quon, M. J. (2008). Current approaches for assessing insulin sensitivity and resistance in vivo: advantages, limitations, and appropriate usage. *Am J Physiol Endocrinol Metab* 294, 15–26. doi: 10.1152/AJPENDO.00645.2007

Muniyappa, R., Tella, S. H., Sortur, S., Mszar, R., Grewal, S., Abel, B. S., et al. (2019). Predictive Accuracy of Surrogate Indices for Hepatic and Skeletal Muscle Insulin Sensitivity. *J Endocr Soc* 3, 108–118. doi: 10.1210/JS.2018-00206

Murawska, G. M., Armando, A. M., and Dennis, E. A. (2024). Lipidomics of phospholipase A2 reveals exquisite specificity in macrophages. *J Lipid Res* 65, 100571. doi: 10.1016/J.JLR.2024.100571

Nadel, C. M., Ran, X., and Gestwicki, J. E. (2020). Luminescence complementation assay for measurement of binding to protein C-termini in live cells. *Anal Biochem* 611, 113947. doi: 10.1016/J.AB.2020.113947

Naftaly, A., Kislev, N., Izgilov, R., Adler, R., Silber, M., Shalgi, R., et al. (2022). Nutrition Alters the Stiffness of Adipose Tissue and Cell Signaling. *Int J Mol Sci* 23, 15237. doi: 10.3390/IJMS232315237

Nakai, J., Ohkura, M., and Imoto, K. (2001). A high signal-to-noise Ca2+ probe composed of a single green fluorescent protein. *Nat Biotechnol* 19, 137–141. doi: 10.1038/84397

Nam, Y. H., Rodriguez, I., Shin, S. W., Shim, J. H., Kim, N. W., Kim, M. C., et al. (2021). Characteristics of the New Insulin-Resistant Zebrafish Model. *Pharmaceuticals* 14, 642. doi: 10.3390/PH14070642

Namkung, Y., Le Gouill, C., Lukashova, V., Kobayashi, H., Hogue, M., Khoury, E., et al. (2016). Monitoring G protein-coupled receptor and ß-arrestin trafficking in live cells using enhanced bystander BRET. *Nat Commun* 7, 1–12. doi: 10.1038/ncomms12178

Nandi, A., Kitamura, Y., Kahn, C. R., and Accili, D. (2004). Mouse Models of Insulin Resistance. *Physiol Rev* 84, 623–647. doi: 10.1152/PHYSREV.00032.2003

National Institute for Health and Care Excellence (2025). Overweight and obesity management (NG246). *NICE Guideline*. Available at: https://www.nice.org.uk/guidance/ng246/ (Accessed October 13, 2025).

National Institute of Health and Care Excellence (2022). Type 2 diabetes in adults: management (NG28). *NICE Guideline*. Available at: https://www.nice.org.uk/guidance/ng28 (Accessed October 13, 2025).

Neeland, I. J., Poirier, P., and Després, J. P. (2018). Cardiovascular and Metabolic Heterogeneity of Obesity: Clinical Challenges and Implications for Management. *Circulation* 137, 1391–1406. doi: 10.1161/CIRCULATIONAHA.117.029617

Neeland, I. J., Ross, R., Després, J. P., Matsuzawa, Y., Yamashita, S., Shai, I., et al. (2019). Visceral and ectopic fat, atherosclerosis, and cardiometabolic disease: a position statement. *Lancet Diabetes Endocrinol* 7, 715–725. doi: 10.1016/S2213-8587(19)30084-1

Nehmea, R., Carpenter, B., Singhal, A., Strege, A., Edwards, P. C., White, C. F., et al. (2017). Mini-G proteins: Novel tools for studying GPCRs in their active conformation. *PLoS One* 12, e0175642. doi: 10.1371/JOURNAL.PONE.0175642

Nessar, A., Röhrs, V., Ziersch, M., Ali, A. S. M., Moradi, J., Kurreck, A., et al. (2025). Promoting ethical and reproducible cell culture: implementing animal-free alternatives to teaching in molecular and cell biology. *Frontiers in Toxicology* 7, 1670513. doi: 10.3389/FTOX.2025.1670513

Newman, J. C., and Verdin, E. (2017). ß-Hydroxybutyrate: A Signaling Metabolite. *Annu Rev Nutr* 37, 51–76. doi: 10.1146/ANNUREV-NUTR-071816-064916

Nicolaidis, S. (2019). Environment and obesity. *Metabolism* 100. doi: 10.1016/j.metabol.2019.07.006

Nikolaev, V. O., Bünemann, M., Hein, L., Hannawacker, A., and Lohse, M. J. (2004). Novel single chain cAMP sensors for receptor-induced signal propagation. *Journal of Biological Chemistry* 279, 37215–37218. doi: 10.1074/jbc.C400302200

Obaseki, E., Adebayo, D., Bandyopadhyay, S., and Hariri, H. (2024). Lipid droplets and fatty acid-induced lipotoxicity: in a nutshell. *FEBS Lett* 598, 1207–1214. doi: 10.1002/1873-3468.14808

O'Brien, S. L., Tripp, E., Barki, N., Blondel-Tepaz, E., Smith, G., Boufersaoui, A., et al. (2025). Intracrine FFA4 signaling controls lipolysis at lipid droplets. *Nat Chem Biol*, 1–11. doi: 10.1038/S41589-025-01982-5

Odeniyi, I. A., Ahmed, B., Anbiah, B., Hester, G., Abraham, P. T., Lipke, E. A., et al. (2024). An improved in vitro 3T3-L1 adipocyte model of inflammation and insulin resistance. *Adipocyte* 13, 2414919. doi: 10.1080/21623945.2024.2414919

Odoemelam, C. S., Percival, B., Wallis, H., Chang, M. W., Ahmad, Z., Scholey, D., et al. (2020). G-Protein coupled receptors: structure and function in drug discovery. *RSC Adv* 10, 36337–36348. doi: 10.1039/D0RA08003A

Offermanns, S., and Schwaninger, M. (2015). Nutritional or pharmacological activation of HCA2 ameliorates neuroinflammation. *Trends Mol Med* 21, 245–255. doi: 10.1016/J.MOLMED.2015.02.002

Oh, D. Y., Talukdar, S., Bae, E. J., Imamura, T., Morinaga, H., Fan, W. Q., et al. (2010). GPR120 Is an Omega-3 Fatty Acid Receptor Mediating Potent Anti-inflammatory and Insulin-Sensitizing Effects. *Cell* 142, 687–698. doi: 10.1016/j.cell.2010.07.041

Oh, D. Y., Walenta, E., Akiyama, T. E., Lagakos, W. S., Lackey, D., Pessentheiner, A. R., et al. (2014). A Gpr120-selective agonist improves insulin resistance and chronic inflammation in obese mice. *Nat Med* 20, 942–947. doi: 10.1038/nm.3614

Oh, Y., Park, Y., Cho, J. H., Wu, H., Paulk, N. K., Liu, L. X., et al. (2019). An orange calcium-modulated bioluminescent indicator for non-invasive activity imaging. *Nat Chem Biol* 15, 433–436. doi: 10.1038/s41589-019-0256-z

Ohsugi, M., Gras-Méneur, C., Zhou, Y., Bernal-Mizrachi, E., Johnson, J. D., Luciani, D. S., et al. (2005). Reduced Expression of the Insulin Receptor in Mouse Insulinoma (MIN6) Cells Reveals Multiple Roles of Insulin Signaling in Gene Expression, Proliferation, Insulin Content, and Secretion. *Journal of Biological Chemistry* 280, 4992–5003. doi: 10.1074/JBC.M411727200

Okada, S., Mori, M., and Pessin, J. E. (2003). Introduction of DNA into 3T3-L1 Adipocytes by Electroporation. *Methods Mol Med* 83, 93–96. doi: 10.1385/1-59259-377-1:093

Olefsky, J. M., and Glass, C. K. (2010). Macrophages, Inflammation, and Insulin Resistance. *Annu Rev Physiol* 72, 219–246. doi: 10.1146/ANNUREV-PHYSIOL-021909-135846

Oliveira, A. F., Cunha, D. A., Ladriere, L., Igoillo-Esteve, M., Bugliani, M., Marchetti, P., et al. (2015). In vitro use of free fatty acids bound to albumin: A comparison of protocols. *Biotechniques* 58, 228–233. doi: 10.2144/000114285

Olsen, R. H. J., DiBerto, J. F., English, J. G., Glaudin, A. M., Krumm, B. E., Slocum, S. T., et al. (2020). TRUPATH, an open-source biosensor platform for interrogating the GPCR transducerome. *Nat Chem Biol* 16, 841–849. doi: 10.1038/S41589-020-0535-8

Olsen, R. H. J., and English, J. G. (2023). Advancements in G protein-coupled receptor biosensors to study GPCR-G protein coupling. *Br J Pharmacol* 180, 1433–1443. doi: 10.1111/BPH.15962

Olsen, T. R., Mattix, B., Casco, M., Herbst, A., Williams, C., Tarasidis, A., et al. (2014). Processing cellular spheroids for histological examination. *J Histotechnol* 37, 138–142. doi: 10.1179/2046023614Y.0000000047

Olszanecka-Glinianowicz, M., Zahorska-Markiewicz, B., Janowska, J., and Zurakowski, A. (2004). Serum concentrations of nitric oxide, tumor necrosis factor (TNF)-α and TNF soluble receptors in women with overweight and obesity. *Metabolism* 53, 1268–1273. doi: 10.1016/J.METABOL.2004.07.001

Palombella, S., Guiotto, M., Higgins, G. C., Applegate, L. L., Raffoul, W., Cherubino, M., et al. (2020). Human platelet lysate as a potential clinical-Translatable supplement to support the neurotrophic properties of human adipose-derived stem cells. *Stem Cell Res Ther* 11, 1–14. doi: 10.1186/S13287-020-01949-4

Park, E., Cho, H. B., and Takimoto, K. (2015). Effective gene delivery into adipose-derived stem cells: transfection of cells in suspension with the use

of a nuclear localization signal peptide–conjugated polyethylenimine. *Cytotherapy* 17, 536–542. doi: 10.1016/J.JCYT.2014.11.008

Patriarchi, T., Cho, J. R., Merten, K., Howe, M. W., Marley, A., Xiong, W. H., et al. (2018). Ultrafast neuronal imaging of dopamine dynamics with designed genetically encoded sensors. *Science (1979)* 360. doi: 10.1126/SCIENCE.AAT4422

Pearce, A., Redfern-Nichols, T., Wills, E., Rosa, M., Manulak, I., Sisk, C., et al. (2025). Quantitative approaches for studying G protein-coupled receptor signalling and pharmacology. *J Cell Sci* 138. doi: 10.1242/JCS.263434/365010

Pedersen, M. H., Pham, J., Mancebo, H., Inoue, A., Asher, W. B., and Javitch, J. A. (2021). A novel luminescence-based ß-arrestin recruitment assay for unmodified receptors. *Journal of Biological Chemistry* 296. doi: 10.1016/J.JBC.2021.100503

Peri, K., and Eisenberg, M. (2024a). Review on obesity management: diet, exercise and pharmacotherapy. *BMJ Public Health* 2, e000246. doi: 10.1136/BMJPH-2023-000246

Peri, K., and Eisenberg, M. (2024b). Review on the update in obesity management: epidemiology. *BMJ Public Health* 2, e000247. doi: 10.1136/BMJPH-2023-000247

Persaud, S. J., and Jones, P. M. (2022). Physiology of Glucose Homeostasis. *Oxford Textbook of Endocrinology and Diabetes*, 1918–1922. doi: 10.1093/MED/9780198870197.003.0241

Peters, A., Krumbholz, P., Jäger, E., Heintz-Buschart, A., Çakir, M. V., Rothemund, S., et al. (2019). Metabolites of lactic acid bacteria present in fermented foods are highly potent agonists of human hydroxycarboxylic acid receptor 3. *PLoS Genet* 15, e1008145. doi: 10.1371/JOURNAL.PGEN.1008145

Petersen, M. C., and Shulman, G. I. (2018). Mechanisms of Insulin Action and Insulin Resistance. *Physiol Rev* 98, 2133–2223. doi: 10.1152/PHYSREV.00063.2017

Pfeiffer, A., Janott, J., Möhlig, M., Ristow, M., Rochlitz, H., Busch, K., et al. (1997). Circulating tumor necrosis factor α is elevated in male but not in female patients with type II diabetes mellitus. *Hormone and Metabolic Research* 29, 111–114. doi: 10.1055/S-2007-979001

Pfleger, K. D. G., and Eidne, K. A. (2006). Illuminating insights into protein-protein interactions using bioluminescence resonance energy transfer (BRET). *Nat Methods* 3, 165–174. doi: 10.1038/nmeth841

Pham, D. H., Moretti, P. A. B., Goodall, G. J., and Pitson, S. M. (2008). Attenuation of leakiness in doxycycline-inducible expression via incorporation of 3′ AU-rich mRNA destabilizing elements. *Biotechniques* 45, 155–162. doi: 10.2144/000112896

Picollet-D'hahan, N., Zuchowska, A., Lemeunier, I., and Le Gac, S. (2021). Multiorgan-on-a-Chip: A Systemic Approach To Model and Decipher Inter-Organ Communication. *Trends Biotechnol* 39, 788–810. doi: 10.1016/J.TIBTECH.2020.11.014

Pierce, K. L., Premont, R. T., and Lefkowitz, R. J. (2002). Seven-transmembrane receptors. *Nat Rev Mol Cell Biol* 3, 639–650. doi: 10.1038/NRM908

Pieters, V. M., Rjaibi, S. T., Singh, K., Li, N. T., Khan, S. T., Nunes, S. S., et al. (2022). A three-dimensional human adipocyte model of fatty acid-induced obesity. *Biofabrication* 14, 045009. doi: 10.1088/1758-5090/AC84B1

Powell-Wiley, T. M., Poirier, P., Burke, L. E., Després, J. P., Gordon-Larsen, P., Lavie, C. J., et al. (2021). Obesity and Cardiovascular Disease: A Scientific

Statement From the American Heart Association. *Circulation* 143, E984–E1010. doi: 10.1161/CIR.0000000000000973

Pradhan, A. D., Manson, J. E., Rifai, N., Buring, J. E., and Ridker, P. M. (2001). C-Reactive Protein, Interleukin 6, and Risk of Developing Type 2 Diabetes Mellitus. *JAMA* 286, 327–334. doi: 10.1001/JAMA.286.3.327

Promega Corporation (n.d.). NanoBiT ® Protein:Protein Interaction System Instructions for Use of Products N2014 and N2015. Available at: www.promega.com (Accessed September 1, 2025).

Pușcașu, C., Andrei, C., Olaru, O. T., and Zanfirescu, A. (2025). Metabolite-Sensing Receptors: Emerging Targets for Modulating Chronic Pain Pathways. *Curr Issues Mol Biol* 47. doi: 10.3390/CIMB47010063

Qian, J., Gu, Y., Wu, C., Yu, F., Chen, Y., Zhu, J., et al. (2017). Agonist-induced activation of human FFA1 receptor signals to extracellular signal-regulated kinase 1 and 2 through Gq- and Gi-coupled signaling cascades. *Cell Mol Biol Lett* 22, 1–12. doi: 10.1186/S11658-017-0043-3

Qin, J. Y., Zhang, L., Clift, K. L., Hulur, I., Xiang, A. P., Ren, B. Z., et al. (2010). Systematic Comparison of Constitutive Promoters and the Doxycycline-Inducible Promoter. *PLoS One* 5, e10611. doi: 10.1371/JOURNAL.PONE.0010611

Qin, S., Tang, X., Chen, Y., Chen, K., Fan, N., Xiao, W., et al. (2022). mRNA-based therapeutics: powerful and versatile tools to combat diseases. *Signal Transduct Target Ther* 7, 1–35. doi: 10.1038/S41392-022-01007-W

Quarta, S., Scoditti, E., Carluccio, M. A., Calabriso, N., Santarpino, G., Damiano, F., et al. (2021). Coffee Bioactive N-Methylpyridinium Attenuates Tumor Necrosis Factor (TNF)-α-Mediated Insulin Resistance and Inflammation in Human Adipocytes. *Biomolecules* 11, 1545. doi: 10.3390/BIOM11101545

Rajangam, T., Park, M. H., and Kim, S. H. (2016). 3D Human Adipose-Derived Stem Cell Clusters as a Model for In Vitro Fibrosis. *Tissue Eng Part C Methods* 22, 679–690. doi: 10.1089/TEN.TEC.2016.0037

Ramakrishnan, V. M., and Boyd, N. L. (2018). The Adipose Stromal Vascular Fraction as a Complex Cellular Source for Tissue Engineering Applications. *Tissue Eng Part B Rev* 24, 289. doi: 10.1089/TEN.TEB.2017.0061

Rashki, S., Haddadi, M. H., Marzhoseyni, Z., Khaledi, M., Yekani, M., Shooraj, M., et al. (2025). Challenges and Solutions in Advanced Management of Diabetic Foot Infections: A Review of Recent Studies. *J Diabetes Res* 2025, 6715157. doi: 10.1155/JDR/6715157

Rask-Madsen, C., and King, G. L. (2013). Vascular complications of diabetes: mechanisms of injury and protective factors. *Cell Metab* 17, 20. doi: 10.1016/J.CMET.2012.11.012

Rasmussen, S. G. F., Devree, B. T., Zou, Y., Kruse, A. C., Chung, K. Y., Kobilka, T. S., et al. (2011). Crystal structure of the β2 adrenergic receptor–Gs protein complex. *Nature* 477, 549–555. doi: 10.1038/nature10361

Regard, J. B., Sato, I. T., and Coughlin, S. R. (2008). Anatomical profiling of G protein-coupled receptor expression. *Cell* 135, 561–571. doi: 10.1016/j.cell.2008.08.040

Richard, A. J., White, U., Elks, C. M., and Stephens, J. M. (2020). *Adipose Tissue: Physiology to Metabolic Dysfunction*. MDText.com, Inc. Available at: https://www.ncbi.nlm.nih.gov/books/NBK555602/ (Accessed August 23, 2021).

Richardson, D. S., and Lichtman, J. W. (2015). Clarifying Tissue Clearing. *Cell* 162, 246–257. doi: 10.1016/J.CELL.2015.06.067

Roberts, L. D., Virtue, S., Vidal-Puig, A., Nicholls, A. W., and Griffin, J. L. (2009). Metabolic phenotyping of a model of adipocyte differentiation. *Physiol Genomics* 39, 109. doi: 10.1152/PHYSIOLGENOMICS.90365.2008

Robledo, F., González-Hodar, L., Tapia, P., Figueroa, A. M., Ezquer, F., and Cortés, V. (2023). Spheroids derived from the stromal vascular fraction of adipose tissue self-organize in complex adipose organoids and secrete leptin. *Stem Cell Res Ther* 14, 70. doi: 10.1186/S13287-023-03262-2

Rodrigues, D. B., Reis, R. L., and Pirraco, R. P. (2024). Modelling the complex nature of the tumor microenvironment: 3D tumor spheroids as an evolving tool. *J Biomed Sci* 31, 1–22. doi: 10.1186/S12929-024-00997-9

Rodriguez, A. M., Elabd, C., Delteil, F., Astier, J., Vernochet, C., Saint-Marc, P., et al. (2004). Adipocyte differentiation of multipotent cells established from human adipose tissue. *Biochem Biophys Res Commun* 315, 255–263. doi: 10.1016/J.BBRC.2004.01.053

Rodriguez, A. M., Pisani, D., Dechesne, C. A., Turc-Carel, C., Kurzenne, J. Y., Wdziekonski, B., et al. (2005). Transplantation of a multipotent cell population from human adipose tissue induces dystrophin expression in the immunocompetent mdx mouse. *Journal of Experimental Medicine* 201, 1397–1405. doi: 10.1084/JEM.20042224

Rohm, T. V., Meier, D. T., Olefsky, J. M., and Donath, M. Y. (2022). Inflammation in obesity, diabetes, and related disorders. *Immunity* 55, 31–55. doi: 10.1016/J.IMMUNI.2021.12.013

Romanelli, S. M., and Macdougald, O. A. (2020). Viral and Nonviral Transfer of Genetic Materials to Adipose Tissues: Toward a Gold Standard Approach. *Diabetes* 69, 2581. doi: 10.2337/DBI20-0036

Rosen, E. D., Sarraf, P., Troy, A. E., Bradwin, G., Moore, K., Milstone, D. S., et al. (1999). PPAR gamma is required for the differentiation of adipose tissue in vivo and in vitro. *Mol Cell* 4, 611–617. doi: 10.1016/S1097-2765(00)80211-7

Rosen, E. D., and Spiegelman, B. M. (2006). Adipocytes as regulators of energy balance and glucose homeostasis. *Nature* 444, 847–853. doi: 10.1038/nature05483

Rosen, E. D., and Spiegelman, B. M. (2014). What we talk about when we talk about fat. *Cell* 156, 20–44. doi: 10.1016/J.CELL.2013.12.012

Rossi, A., Eid, M., Dodgson, J., Davies, G., Musial, B., Wabitsch, M., et al. (2020). In vitro characterization of the effects of chronic insulin stimulation in mouse 3T3-L1 and human SGBS adipocytes. *Adipocyte* 9, 415–426. doi: 10.1080/21623945.2020.1798613

Ruan, H., Hacohen, N., Golub, T. R., Van Parijs, L., and Lodish, H. F. (2002). Tumor Necrosis Factor-α Suppresses Adipocyte-Specific Genes and Activates Expression of Preadipocyte Genes in 3T3-L1 AdipocytesNuclear Factor-κB Activation by TNF-α Is Obligatory. *Diabetes* 51, 1319–1336. doi: 10.2337/DIABETES.51.5.1319

Ruiz-Ojeda, F. J., Méndez-Gutiérrez, A., Aguilera, C. M., and Plaza-Díaz, J. (2019). Extracellular Matrix Remodeling of Adipose Tissue in Obesity and Metabolic Diseases. *Int J Mol Sci* 20, 4888. doi: 10.3390/IJMS20194888

Ruiz-Ojeda, F. J., Rupérez, A. I., Gomez-Llorente, C., Gil, A., and Aguilera, C. M. (2016). Cell Models and Their Application for Studying Adipogenic Differentiation in Relation to Obesity: A Review. *Int J Mol Sci* 17, 1040. doi: 10.3390/IJMS17071040

Saarimaa, S., Juntunen, M., Isosaari, L., Autio, R., Kuuskeri, M., Narkilahti, S., et al. (2025). Human induced pluripotent stem cell-derived neurons and coculture conditions regulate the adipogenic differentiation and

functionality of human adipose stromal/stem cells. *Cell Communication and Signaling*. doi: 10.1186/S12964-025-02544-X

Saharti, S. (2024). Contemporary art of cell-block preparation: Overview. *Cytojournal* 21, 5. doi: 10.25259/CYTOJOURNAL_56_2023

Saito, M., Matsushita, M., Yoneshiro, T., and Okamatsu-Ogura, Y. (2020). Brown Adipose Tissue, Diet-Induced Thermogenesis, and Thermogenic Food Ingredients: From Mice to Men. *Front Endocrinol (Lausanne)* 11, 533838. doi: 10.3389/FENDO.2020.00222/FULL

Sakers, A., De Siqueira, M. K., Seale, P., and Villanueva, C. J. (2022). Adipose-tissue plasticity in health and disease. *Cell* 185, 419–446. doi: 10.1016/J.CELL.2021.12.016

Salahpour, A., Espinoza, S., Masri, B., Lam, V., Barak, L. S., and Gainetdinov, R. R. (2012). BRET biosensors to study GPCR biology, pharmacology, and signal transduction. *Front Endocrinol (Lausanne)* 3, 30991. doi: 10.3389/FENDO.2012.00105

Sargenti, A., Musmeci, F., Bacchi, F., Delprete, C., Cristaldi, D. A., Cannas, F., et al. (2020). Physical Characterization of Colorectal Cancer Spheroids and Evaluation of NK Cell Infiltration Through a Flow-Based Analysis. *Front Immunol* 11, 564887. doi: 10.3389/FIMMU.2020.564887

Satapati, S., Qian, Y., Wu, M. S., Petrov, A., Dai, G., Wang, S. P., et al. (2017). GPR120 suppresses adipose tissue lipolysis and synergizes with GPR40 in antidiabetic efficacy. *J Lipid Res* 58, 1561–1578. doi: 10.1194/jlr.M075044

Sato, M., Ueda, Y., and Umezawa, Y. (2006). Imaging diacylglycerol dynamics at organelle membranes. *Nat Methods* 3, 797–799. doi: 10.1038/nmeth930

Schmidt, S. F., Jørgensen, M., Chen, Y., Nielsen, R., Sandelin, A., and Mandrup, S. (2011). Cross species comparison of C/EBPα and PPARγ profiles in mouse and human adipocytes reveals interdependent retention of binding sites. *BMC Genomics* 12, 1–16. doi: 10.1186/1471-2164-12-152

Schmitz, C., Potekhina, E., Belousov, V. V., and Lavrentieva, A. (2021). Hypoxia Onset in Mesenchymal Stem Cell Spheroids: Monitoring With Hypoxia Reporter Cells. *Front Bioeng Biotechnol* 9, 611837. doi: 10.3389/FBIOE.2021.611837

Schouwink, M., Öner-Sieben, S., and Ensenauer, R. (2025). Longitudinal expression profiles of key markers during stages of adipogenic differentiation of 3T3-L1 cells using the PPARG agonist rosiglitazone. *Biochem Biophys Res Commun* 770, 151850. doi: 10.1016/J.BBRC.2025.151850

Schröder, R., Janssen, N., Schmidt, J., Kebig, A., Merten, N., Hennen, S., et al. (2010). Deconvolution of complex G protein–coupled receptor signaling in live cells using dynamic mass redistribution measurements. *Nat Biotechnol* 28, 943–949. doi: 10.1038/nbt.1671

Schweiger, M., Eichmann, T. O., Taschler, U., Zimmermann, R., Zechner, R., and Lass, A. (2014). Measurement of Lipolysis. *Methods Enzymol* 538, 171. doi: 10.1016/B978-0-12-800280-3.00010-4

Schweiger, M., Paar, M., Eder, C., Brandis, J., Moser, E., Gorkiewicz, G., et al. (2012). G0/G1 switch gene-2 regulates human adipocyte lipolysis by affecting activity and localization of adipose triglyceride lipase. *J Lipid Res* 53, 2307. doi: 10.1194/JLR.M027409

Schweiger, M., Schreiber, R., Haemmerle, G., Lass, A., Fledelius, C., Jacobsen, P., et al. (2006). Adipose Triglyceride Lipase and Hormone-sensitive Lipase Are the Major Enzymes in Adipose Tissue Triacylglycerol Catabolism. *Journal of Biological Chemistry* 281, 40236–40241. doi: 10.1074/JBC.M608048200

Sekar, R. B., and Periasamy, A. (2003). Fluorescence resonance energy transfer (FRET) microscopy imaging of live cell protein localizations. *Journal of Cell Biology* 160, 629. doi: 10.1083/JCB.200210140

Semple, G., Skinner, P. J., Gharbaoui, T., Shin, Y. J., Jung, J. K., Cherrier, M. C., et al. (2008). 3-(1H-tetrazol-5-yl)-1,4,5,6-tetrahydro-cyclopentapyrazole (MK-0354): A partial agonist of the nicotinic acid receptor, G-protein coupled receptor 109a, with antilipolytic but no vasodilatory activity in mice. *J Med Chem* 51, 5101–5108. doi: 10.1021/JM800258P

Senkel, S., Waldner, C., Ryffel, G., and Thomas, H. (2009). Improved conditional expression systems resulting in physiological level of HNF4α expression confirm HNF4α induced apoptosis in the pancreatic ß-cell line INS-1. *BMC Res Notes* 2, 210. doi: 10.1186/1756-0500-2-210

Sewter, C. P., Digby, J. E., Blows, F., Prins, J., and O'Rahilly, S. (1999). Regulation of tumour necrosis factor-alpha release from human adipose tissue in vitro. *Journal of Endocrinology* 163, 33–38. doi: 10.1677/JOE.0.1630033

Shah, R. V., Murthy, V. L., Abbasi, S. A., Blankstein, R., Kwong, R. Y., Goldfine, A. B., et al. (2014). Visceral Adiposity and the Risk of Metabolic Syndrome Across Body Mass Index: The MESA Study. *JACC Cardiovasc Imaging* 7, 1221–1235. doi: 10.1016/J.JCMG.2014.07.017

Shakhmin, A., Hall, M. P., Machleidt, T., Walker, J. R., Wood, K. V., and Kirkland, T. A. (2017). Coelenterazine analogues emit red-shifted bioluminescence with NanoLuc. *Org Biomol Chem* 15, 8559–8567. doi: 10.1039/C7OB01985H

Shapiro, H., Shachar, S., Sekler, I., Hershfinkel, M., and Walker, M. D. (2005). Role of GPR40 in fatty acid action on the ß cell line INS-1E. *Biochem Biophys Res Commun* 335, 97–104. doi: 10.1016/J.BBRC.2005.07.042

Shen, J. X., Couchet, M., Dufau, J., Barbosa, T. de C., Ulbrich, M. H., Helmstädter, M., et al. (2021). 3D Adipose Tissue Culture Links the Organotypic Microenvironment to Improved Adipogenesis. *Advanced Science* 8, 2100106. doi: 10.1002/ADVS.202100106

Shen, K., Vesey, D. A., Hasnain, S. Z., Zhao, K. N., Wang, H., Johnson, D. W., et al. (2020). A cost-effective three-dimensional culture platform functionally mimics the adipose tissue microenvironment surrounding the kidney. *Biochem Biophys Res Commun* 522, 736–742. doi: 10.1016/J.BBRC.2019.11.119

Sheng, X., Tucci, J., Malvar, J., and Mittelman, S. D. (2013). Adipocyte differentiation is affected by media height above the cell layer. *Int J Obes* 38, 315. doi: 10.1038/IJO.2013.96

Shi, J., and Kandror, K. V. (2008). Study of glucose uptake in adipose cells. *Methods in Molecular Biology* 456, 307–315. doi: 10.1007/978-1-59745-245-8_23

Shi, Y., Lai, X., Ye, L., Chen, K., Cao, Z., Gong, W., et al. (2017). Activated niacin receptor HCA2 inhibits chemoattractant-mediated macrophage migration via Gßγ/PKC/ERK1/2 pathway and heterologous receptor desensitization. *Sci Rep* 7, 1–14. doi: 10.1038/srep42279

Shimpukade, B., Hudson, B. D., Hovgaard, C. K., Milligan, G., and Ulven, T. (2012). Discovery of a potent and selective GPR120 agonist. *J Med Chem* 55, 4511–4515. doi: 10.1021/JM300215X

Shoham, N., Girshovitz, P., Katzengold, R., Shaked, N. T., Benayahu, D., and Gefen, A. (2014). Adipocyte Stiffness Increases with Accumulation of Lipid Droplets. *Biophys J* 106, 1421. doi: 10.1016/J.BPJ.2014.01.045

Singh, R., Barrios, A., Dirakvand, G., and Pervin, S. (2021). Human Brown Adipose Tissue and Metabolic Health: Potential for Therapeutic Avenues. *Cells* 10, 3030. doi: 10.3390/CELLS10113030

Sivaramakrishnan, S., and Spudich, J. A. (2011). Systematic control of protein interaction using a modular ER/K α-helix linker. *Proc Natl Acad Sci U S A* 108, 20467–20472. doi: 10.1073/PNAS.1116066108

Soccio, R. E., Chen, E. R., and Lazar, M. A. (2014). Thiazolidinediones and the Promise of Insulin Sensitization in Type 2 Diabetes. *Cell Metab* 20, 573–591. doi: 10.1016/J.CMET.2014.08.005

Soga, T., Kamohara, M., Takasaki, J., Matsumoto, S. I., Saito, T., Ohishi, T., et al. (2003). Molecular identification of nicotinic acid receptor. *Biochem Biophys Res Commun* 303, 364–369. doi: 10.1016/S0006-291X(03)00342-5

Soltis, R. D., Hasz, D., Morris, M. J., and Wilson, I. D. (1979). The effect of heat inactivation of serum on aggregation of immunoglobulins. *Immunology* 36, 37–45.

Song, T., Zhou, Y., Peng, J., Tao, Y. X., Yang, Y., Xu, T., et al. (2016). GPR120 promotes adipogenesis through intracellular calcium and extracellular signal-regulated kinase 1/2 signal pathway. *Mol Cell Endocrinol* 434, 1–13. doi: 10.1016/J.MCE.2016.06.009

Soukas, A., Socci, N. D., Saatkamp, B. D., Novelli, S., and Friedman, J. M. (2001). Distinct Transcriptional Profiles of Adipogenesis in Vivo and in Vitro. *Journal of Biological Chemistry* 276, 34167–34174. doi: 10.1074/jbc.M104421200

Sparks, S. M., Chen, G., Collins, J. L., Danger, D., Dock, S. T., Jayawickreme, C., et al. (2014). Identification of diarylsulfonamides as agonists of the free fatty acid receptor 4 (FFA4/GPR120). *Bioorg Med Chem Lett* 24, 3100–3103. doi: 10.1016/J.BMCL.2014.05.012

Spector, A. A. (1975). Fatty acid binding to plasma albumin. *J Lipid Res* 16, 165–179. doi: 10.1016/S0022-2275(20)36723-7

Spillmann, M., Thurner, L., Romantini, N., Zimmermann, M., Meger, B., Behe, M., et al. (2020). New Insights into Arrestin Recruitment to GPCRs. *Int J Mol Sci* 21, 4949. doi: 10.3390/IJMS21144949

Stelzer, E. H. K., and Smyrek, I. (2017). Quantitative three-dimensional evaluation of immunofluorescence staining for large whole mount spheroids with light sheet microscopy. *Biomed Opt Express* 8, 484–499. doi: 10.1364/BOE.8.000484

Stephens, J. M., Lee, J., and Pilch, P. F. (1997). Tumor necrosis factor-α-induced insulin resistance in 3T3-L1 adipocytes is accompanied by a loss of insulin receptor substrate-1 and GLUT4 expression without a loss of insulin receptor-mediated signal transduction. *Journal of Biological Chemistry* 272, 971–976. doi: 10.1074/jbc.272.2.971

Stephens, J. M., and Pekala, P. H. (1991). Transcriptional repression of the GLUT4 and C/EBP genes in 3T3-L1 adipocytes by tumor necrosis factor-alpha - PubMed. *Journal of Biological Chemistry* 266, 21839–21845. Available at: https://pubmed.ncbi.nlm.nih.gov/1939208/ (Accessed November 30, 2025).

Stoddart, L. A., Johnstone, E. K. M., Wheal, A. J., Goulding, J., Robers, M. B., MacHleidt, T., et al. (2015). Application of BRET to monitor ligand binding to GPCRs. *Nat Methods* 12, 661–663. doi: 10.1038/nmeth.3398

Strnadová, M., Thor, D., and Kaczmarek, I. (2024). Protocol for changing gene expression in 3T3-L1 (pre)adipocytes using siRNA-mediated knockdown. *STAR Protoc* 5, 103075. doi: 10.1016/J.XPRO.2024.103075

Suganami, T., Nishida, J., and Ogawa, Y. (2005). A paracrine loop between adipocytes and macrophages aggravates inflammatory changes: Role of free

fatty acids and tumor necrosis factor α. *Arterioscler Thromb Vasc Biol* 25, 2062–2068. doi: 10.1161/01.ATV.0000183883.72263.13

Suleiman, J. B., Mohamed, M., and Bakar, A. B. A. (2019). A systematic review on different models of inducing obesity in animals: Advantages and limitations. *J Adv Vet Anim Res* 7, 103. doi: 10.5455/JAVAR.2020.G399

Sum, C. S., Murphy, B. J., Li, Z., Wang, T., Zhang, L., and Cvijic, M. E. (2019). Pharmacological Characterization of GPCR Agonists, Antagonists, Allosteric Modulators and Biased Ligands from HTS Hits to Lead Optimization. *Assay Guidance Manual*. Available at: https://www.ncbi.nlm.nih.gov/books/NBK549462/ (Accessed December 2, 2025).

Sun, F., Zeng, J., Jing, M., Zhou, J., Feng, J., Owen, S. F., et al. (2018). A Genetically Encoded Fluorescent Sensor Enables Rapid and Specific Detection of Dopamine in Flies, Fish, and Mice. *Cell* 174, 481–496.e19. doi: 10.1016/j.cell.2018.06.042

Sun, W., Yu, Z., Yang, S., Jiang, C., Kou, Y., Xiao, L., et al. (2020). A Transcriptomic Analysis Reveals Novel Patterns of Gene Expression During 3T3-L1 Adipocyte Differentiation. *Front Mol Biosci* 7, 564339. doi: 10.3389/FMOLB.2020.564339

Sutherland, R. M., McCredie, J. A., and Inch, W. R. (1971). Growth of Multicell Spheroids in Tissue Culture as a Model of Nodular Carcinomas. *JNCI: Journal of the National Cancer Institute* 46, 113–120. doi: 10.1093/JNCI/46.1.113

Suzuki, K., Kimura, T., Shinoda, H., Bai, G., Daniels, M. J., Arai, Y., et al. (2016). Five colour variants of bright luminescent protein for real-time multicolour bioimaging. *Nat Commun* 7, 1–10. doi: 10.1038/ncomms13718

Syed-Abdul, M. M. (2023). Lipid Metabolism in Metabolic-Associated Steatotic Liver Disease (MASLD). *Metabolites* 14, 12. doi: 10.3390/METABO14010012

Sztalryd, C., and Brasaemle, D. L. (2017). The perilipin family of lipid droplet proteins: Gatekeepers of intracellular lipolysis. *Biochimica et Biophysica Acta (BBA) - Molecular and Cell Biology of Lipids* 1862, 1221–1232. doi: 10.1016/J.BBALIP.2017.07.009

Szymczak, A. L., Workman, C. J., Wang, Y., Vignali, K. M., Dilioglou, S., Vanin, E. F., et al. (2004). Correction of multi-gene deficiency in vivo using a single "self-cleaving" 2A peptide-based retroviral vector. *Nat Biotechnol* 22, 589–594. doi: 10.1038/NBT957

Tafuri, S. R. (1996). Troglitazone enhances differentiation, basal glucose uptake, and Glut1 protein levels in 3T3-L1 adipocytes. *Endocrinology* 137, 4706–4712. doi: 10.1210/ENDO.137.11.8895337

Taggart, A. K. P., Kero, J., Gan, X., Cai, T. Q., Cheng, K., Ippolito, M., et al. (2005). (D)-ß-hydroxybutyrate inhibits adipocyte lipolysis via the nicotinic acid receptor PUMA-G. *Journal of Biological Chemistry* 280, 26649–26652. doi: 10.1074/jbc.C500213200

Takahashi, A., Koike, R., Watanabe, S., Kuribayashi, K., Wabitsch, M., Miyamoto, M., et al. (2024). Polypeptide N-acetylgalactosaminyltransferase-15 regulates adipogenesis in human SGBS cells. *Sci Rep* 14, 20049. doi: 10.1038/S41598-024-70930-5

Tang, C., Ahmed, K., Gille, A., Lu, S., Gröne, H. J., Tunaru, S., et al. (2015). Loss of FFA2 and FFA3 increases insulin secretion and improves glucose tolerance in type 2 diabetes. *Nature Medicine 2015* 21, 173–177. doi: 10.1038/nm.3779

Tang, F., Barbacioru, C., Wang, Y., Nordman, E., Lee, C., Xu, N., et al. (2009). mRNA-Seq whole-transcriptome analysis of a single cell. *Nat Methods* 6, 377–382. doi: 10.1038/nmeth.1315

Tanimura, A., Nezu, A., Morita, T., Turner, R. J., and Tojyo, Y. (2004). Fluorescent biosensor for quantitative real-time measurements of inositol 1,4,5-trisphosphate in single living cells. *Journal of Biological Chemistry* 279, 38095–38098. doi: 10.1074/jbc.C400312200

Tanis, R. M., Piroli, G. G., Day, S. D., and Frizzell, N. (2015). The effect of glucose concentration and sodium phenylbutyrate treatment on mitochondrial bioenergetics and ER stress in 3T3-L1 adipocytes. *Biochimica et Biophysica Acta (BBA) - Molecular Cell Research* 1853, 213–221. doi: 10.1016/J.BBAMCR.2014.10.012

Tartaglia, L. A., Dembski, M., Weng, X., Deng, N., Culpepper, J., Devos, R., et al. (1995). Identification and expression cloning of a leptin receptor, OB-R. *Cell* 83, 1263–1271. doi: 10.1016/0092-8674(95)90151-5

Taylor, J., Sellin, J., Kuerschner, L., Krähl, L., Majlesain, Y., Förster, I., et al. (2020). Generation of immune cell containing adipose organoids for in vitro analysis of immune metabolism. *Sci Rep* 10, 21104-. doi: 10.1038/s41598-020-78015-9

Tchang, B. G., Aras, M., Kumar, R. B., and Aronne, L. J. (2024). Pharmacologic Treatment of Overweight and Obesity in Adults. *Endotext*. Available at: https://www.ncbi.nlm.nih.gov/books/NBK279038/ (Accessed October 13, 2025).

Tennakoon, M., Senarath, K., Kankanamge, D., Ratnayake, K., Wijayaratna, D., Olupothage, K., et al. (2021). Subtype-dependent regulation of Gβγ signalling. *Cell Signal* 82, 109947. doi: 10.1016/J.CELLSIG.2021.109947

Tews, D., Brenner, R. E., Siebert, R., Debatin, K. M., Fischer-Posovszky, P., and Wabitsch, M. (2022). 20 Years with SGBS cells - a versatile in vitro model of human adipocyte biology. *Int J Obes* 46, 1939–1947. doi: 10.1038/s41366-022-01199-9

Tews, D., Fischer-Posovszky, P., Fromme, T., Klingenspor, M., Fischer, J., Rüther, U., et al. (2013). FTO Deficiency Induces UCP-1 Expression and Mitochondrial Uncoupling in Adipocytes. *Endocrinology* 154, 3141–3151. doi: 10.1210/EN.2012-1873

Tiulpakov, A., White, C. W., Abhayawardana, R. S., See, H. B., Chan, A. S., Seeber, R. M., et al. (2016). Mutations of Vasopressin Receptor 2 Including Novel L312S Have Differential Effects on Trafficking. *Molecular Endocrinology* 30, 889–904. doi: 10.1210/ME.2016-1002

Toktay, Y., Dayanc, B., and Senturk, S. (2022). Engineering and validation of a dual luciferase reporter system for quantitative and systematic assessment of regulatory sequences in Chinese hamster ovary cells. *Sci Rep* 12, 1–14. doi: 10.1038/S41598-022-09887-2

Torres Irizarry, V. C., Jiang, Y., He, Y., and Xu, P. (2022). Hypothalamic Estrogen Signaling and Adipose Tissue Metabolism in Energy Homeostasis. *Front Endocrinol (Lausanne)* 13, 898139. doi: 10.3389/FENDO.2022.898139

Trayhurn, P. (2013). Hypoxia and adipose tissue function and dysfunction in obesity. *Physiol Rev* 93, 1–21. doi: 10.1152/PHYSREV.00017.2012

Trayhurn, P., and Beattie, J. H. (2001). Physiological role of adipose tissue: white adipose tissue as an endocrine and secretory organ. *Proceedings of the Nutrition Society* 60, 329–339. doi: 10.1079/PNS200194

Triglia, R. P., and Linscott, W. D. (1980). Titers of nine complement components, conglutinin and C3b-inactivator in adult and fetal bovine sera. *Mol Immunol* 17, 741–748. doi: 10.1016/0161-5890(80)90144-3

Tsai, Y.-S., Huang, A., Lin, Y.-S., Kao, L.-Z., Tang, M.-J., and Tsai, P.-J. (2022). Adipose tissue stiffness in the development of metabolic diseases. *The FASEB Journal* 36. doi: 10.1096/FASEBJ.2022.36.S1.R5289

Tsalamandris, S., Antonopoulos, A. S., Oikonomou, E., Papamikroulis, G. A., Vogiatzi, G., Papaioannou, S., et al. (2019). The Role of Inflammation in Diabetes: Current Concepts and Future Perspectives. *European Cardiology Review* 14, 50. doi: 10.15420/ECR.2018.33.1

Tseng, H., Daquinag, A. C., Souza, G. R., and Kolonin, M. G. (2018). Three-dimensional magnetic levitation culture system simulating white adipose tissue. *Methods in Molecular Biology* 1773, 147–154. doi: 10.1007/978-1-4939-7799-4_12

Tsien, R. Y. (2006). Breeding and building molecules to spy on cells and tumors. *Keio J Med* 55, 127–140. doi: 10.2302/KJM.55.127

Tsigos, C., Kyrou, I., Chala, E., Tsapogas, P., Stavridis, J. C., Raptis, S. A., et al. (1999). Circulating tumor necrosis factor alpha concentrations are higher in abdominal versus peripheral obesity. *Metabolism* 48, 1332–1335. doi: 10.1016/S0026-0495(99)90277-9

Tsuchiya, S., Kobayashi, Y., Goto, Y., Okumura, H., Nakae, S., Konno, T., et al. (1982). Induction of Maturation in Cultured Human Monocytic Leukemia Cells by a Phorbol Diester. *Cancer Res* 42, 1530–1536. Available at: https://aacrjournals.org/cancerres/article/42/4/1530/486562/Induction-of-Maturation-in-Cultured-Human (Accessed September 25, 2025).

Tsuchiya, S., Yamabe, M., Yamaguchi, Y., Kobayashi, Y., Konno, T., and Tada, K. (1980). Establishment and characterization of a human acute monocytic leukemia cell line (THP-1). *Int J Cancer* 26, 171–176. doi: 10.1002/IJC.2910260208

Tsui, L. (2022). Adipocyte-based high throughput screening for anti-obesity drug discovery: Current status and future perspectives. *SLAS Discovery* 27, 375–383. doi: 10.1016/J.SLASD.2022.08.001

Tunaru, S., Kero, J., Schaub, A., Wufka, C., Blaukat, A., Pfeffer, K., et al. (2003). PUMA-G and HM74 are receptors for nicotinic acid and mediate its anti-lipolytic effect. *Nat Med* 9, 352–355. doi: 10.1038/nm824

Turer, A. T., and Scherer, P. E. (2012). Adiponectin: Mechanistic insights and clinical implications. *Diabetologia* 55, 2319–2326. doi: 10.1007/S00125-012-2598-X

Turner, P. A., Garrett, M. R., Didion, S. P., and Janorkar, A. V. (2018). Spheroid Culture System Confers Differentiated Transcriptome Profile and Functional Advantage to 3T3-L1 Adipocytes. *Ann Biomed Eng* 46, 772–787. doi: 10.1007/S10439-018-1993-Y

Turner, P. A., Gurumurthy, B., Bailey, J. L., Elks, C. M., and Janorkar, A. V. (2017). Adipogenic differentiation of human adipose-derived stem cells grown as spheroids. *Process Biochemistry* 59, 312–320. doi: 10.1016/J.PROCBIO.2017.02.003

Turner, P. A., Tang, Y., Weiss, S. J., and Janorkar, A. V. (2015). Three-Dimensional Spheroid Cell Model of In Vitro Adipocyte Inflammation. *Tissue Engineering - Part A: Research Advances* 21, 1837–1847. doi: 10.1089/TEN.TEA.2014.0531

Ueno, H., Ito, R., Abe, S. I., Ogino, H., Maruyama, M., Miyashita, H., et al. (2019). GPR40 full agonism exerts feeding suppression and weight loss through afferent vagal nerve. *PLoS One* 14. doi: 10.1371/journal.pone.0222653

Umetsu, A., Watanabe, M., Sato, T., Higashide, M., Nishikiori, N., Furuhashi, M., et al. (2024). TGF-β effects on adipogenesis of 3T3-L1 cells differ in 2D and 3D cell culture conditions. *FEBS Open Bio* 14, 2026–2037. doi: 10.1002/2211-5463.13890

Underwood, O., Haider, R. S., Sanchez, J., and Canals, M. (2025). Arrestin-centred interactions at the membrane and their conformational determinants. *Br J Pharmacol* 182, 3135–3150. doi: 10.1111/BPH.16331

Uno, M., Nishimura, S., Fukuchi, K., Kaneta, Y., Oda, Y., Komori, H., et al. (2012). Identification of physiologically active substances as novel ligands for MRGPRD. *J Biomed Biotechnol* 2012. doi: 10.1155/2012/816159

Vaidehi, N., Sadler, F., and Sivaramakrishnan, S. (2021). Dynamical Basis of GPCR-G Protein Coupling Selectivity and Promiscuity. *GPCRs as Therapeutic Targets* 1, 373–387. doi: 10.1002/9781119564782.CH11

Valentini, A., Dibnah, B., Ciba, M., Duncan, E. M., Manandhar, A., Strellis, B., et al. (2025). Multicolored sequential resonance energy transfer for detection of simultaneous ligand binding at G protein-coupled receptors. *Nat Commun* 16, 1–15. doi: 10.1038/s41467-025-61690-5

Valentini x, A., Dibnah, B., Ciba, M., Duncan, E. M., Manandhar, A., Strellis, B., et al. (2025). Multicolored sequential resonance energy transfer for detection of simultaneous ligand binding at G protein-coupled receptors. *Nature Communications 2025 16:1* 16, 1–15. doi: 10.1038/s41467-025-61690-5

Valk, J. van der, and Gstraunthaler, G. (2017). Fetal Bovine Serum (FBS) — A Pain in the Dish? *ATLA Alternatives to Laboratory Animals* 45, 329–332. doi: 10.1177/026119291704500611

Van De Parre, T. J. L., Martinet, W., Schrijvers, D. M., Herman, A. G., and De Meyer, G. R. Y. (2005). mRNA but not plasmid DNA is efficiently transfected in murine J774A.1 macrophages. *Biochem Biophys Res Commun* 327, 356–360. doi: 10.1016/J.BBRC.2004.12.027

van der Valk, J., Bieback, K., Buta, C., Cochrane, B., Dirks, W. G., Fu, J., et al. (2018). Fetal bovine serum (FBS): Past – present – future. *ALTEX - Alternatives to Animal Experimentation* 35, 99–118. doi: 10.14573/ALTEX.1705101

Van Senten, J. R., Bebelman, M. P., Fan, T. S., Heukers, R., Bergkamp, N. D., Van Gasselt, P., et al. (2019). The human cytomegalovirus-encoded G protein–coupled receptor UL33 exhibits oncomodulatory properties. *Journal of Biological Chemistry* 294, 16297–16308. doi: 10.1074/JBC.RA119.007796

Vassilatis, D. K., Hohmann, J. G., Zeng, H., Li, F., Ranchalis, J. E., Mortrud, M. T., et al. (2003). The G protein-coupled receptor repertoires of human and mouse. *Proc Natl Acad Sci U S A* 100, 4903. doi: 10.1073/PNAS.0230374100

Vilardaga, J. P., Bünemann, M., Krasell, C., Castro, M., and Lohse, M. J. (2003). Measurement of the millisecond activation switch of G protein–coupled receptors in living cells. *Nat Biotechnol* 21, 807–812. doi: 10.1038/nbt838

Violin, J. D., Zhang, J., Tsien, R. Y., and Newton, A. C. (2003). A genetically encoded fluorescent reporter reveals oscillatory phosphorylation by protein kinase C. *Journal of Cell Biology* 161, 899–909. doi: 10.1083/JCB.200302125

Viravaidya, K., and Shuler, M. L. (2004). Incorporation of 3T3-L1 cells to mimic bioaccumulation in a microscale cell culture analog device for toxicity studies. *Biotechnol Prog* 20, 590–597. doi: 10.1021/BP034238D

Viswanadha, S., and Londos, C. (2006). Optimized conditions for measuring lipolysis in murine primary adipocytes. *J Lipid Res* 47, 1859–1864. doi: 10.1194/JLR.D600005-JLR200

Vitacolonna, M., Bruch, R., Agaçi, A., Nürnberg, E., Cesetti, T., Keller, F., et al. (2024). A multiparametric analysis including single-cell and subcellular feature assessment reveals differential behavior of spheroid cultures on distinct ultra-low attachment plate types. *Front Bioeng Biotechnol* 12, 1422235. doi: 10.3389/FBIOE.2024.1422235

Wabitsch, M., Brenner, R., Melzner, I., Braun, M., Möller, P., Heinze, E., et al. (2001). Characterization of a human preadipocyte cell strain with high capacity for adipose differentiation. *Int J Obes* 25, 8–15. doi: 10.1038/SJ.IJO.0801520

Wabitsch, M., Brüderlein, S., Melzner, I., Braun, M., Mechtersheimer, G., and Möller, P. (2000). LiSa-2, a novel human liposarcoma cell line with a high capacity for terminal adipose differentiation. *Int. J. Cancer* 88, 889–894. doi: 10.1002/1097-0215(20001215)88:6

Wagner, A., Lautaoja-Kivipelto, J., Pehkonen, K., Hassinen, A., Kuusela, M., Röttger, L., et al. (2025). In vitro model of human subcutaneous adipocyte spheroids for studying mitochondrial dysfunction and mitochondria activating compounds. *bioRxiv*, 2025.04.16.649074. doi: 10.1101/2025.04.16.649074

Walters, R. W., Shukla, A. K., Kovacs, J. J., Violin, J. D., DeWire, S. M., Lam, C. M., et al. (2009). β-Arrestin1 mediates nicotinic acid–induced flushing, but not its antilipolytic effect, in mice. *J Clin Invest* 119, 1312–1321. doi: 10.1172/JCI36806

Wan, Q., Okashah, N., Inoue, A., Nehme, R., Carpenter, B., Tate, C. G., et al. (2018). Mini G protein probes for active G protein–coupled receptors (GPCRs) in live cells. *Journal of Biological Chemistry* 293, 7466–7473. doi: 10.1074/JBC.RA118.001975

Wang, C. Y., and Liao, J. K. (2012). A Mouse Model of Diet-Induced Obesity and Insulin Resistance. *Methods in Molecular Biology* 821, 421–433. doi: 10.1007/978-1-61779-430-8_27

Wang, J., Wen, Y., Zhao, W., Zhang, Y., Lin, F., Ouyang, C., et al. (2023). Hepatic conversion of acetyl-CoA to acetate plays crucial roles in energy stress. *Elife* 12, RP87419. doi: 10.7554/ELIFE.87419

Wang, Q. A., Scherer, P. E., and Gupta, R. K. (2014). Improved methodologies for the study of adipose biology: insights gained and opportunities ahead. *J Lipid Res* 55, 605. doi: 10.1194/JLR.R046441

Ward, R. J., Alvarez-Curto, E., and Milligan, G. (2011). Using the Flp-InTM T-RexTM System to Regulate GPCR Expression. *Methods in Molecular Biology* 746, 21–37. doi: 10.1007/978-1-61779-126-0_2

Watterson, K. R., Hansen, S. V. F., Hudson, B. D., Alvarez-Curto, E., Raihan, S. Z., Azevedo, C. M. G., et al. (2017). Probe-dependent negative allosteric modulators of the long-chain free fatty acid receptor FFA4. *Mol Pharmacol* 91, 630–641. doi: 10.1124/mol.116.107821

Weber, P., Schickinger, S., Wagner, M., Angres, B., Bruns, T., and Schneckenburger, H. (2015). Monitoring of Apoptosis in 3D Cell Cultures by FRET and Light Sheet Fluorescence Microscopy. *Int J Mol Sci* 16, 5375–5385. doi: 10.3390/IJMS16035375

Weber, T., Malakpour-Permlid, A., Chary, A., D'Alessandro, V., Haut, L., Seufert, S., et al. (2025). Fetal bovine serum: how to leave it behind in the pursuit of more reliable science. *Frontiers in Toxicology* 7, 1612903. doi: 10.3389/FTOX.2025.1612903

Wehr, M. C., and Rossner, M. J. (2016). Split protein biosensor assays in molecular pharmacological studies. *Drug Discov Today* 21, 415–429. doi: 10.1016/J.DRUDIS.2015.11.004

Weisberg, S. P., McCann, D., Desai, M., Rosenbaum, M., Leibel, R. L., and Ferrante, A. W. (2003). Obesity is associated with macrophage accumulation in adipose tissue. *J Clin Invest* 112, 1796–1808. doi: 10.1172/JCI19246

Wilding, J. (2006). Thiazolidinediones, insulin resistance and obesity: finding a balance. *Int J Clin Pract* 60, 1272–1280. doi: 10.1111/J.1742-1241.2006.01128.X

Williams, C. G., Lee, H. J., Asatsuma, T., Vento-Tormo, R., and Haque, A. (2022). An introduction to spatial transcriptomics for biomedical research. *Genome Med* 14, 68-. doi: 10.1186/S13073-022-01075-1

Willows, J. W., Blaszkiewicz, M., Lamore, A., Borer, S., Dubois, A. L., Garner, E., et al. (2021). Visualization and analysis of whole depot adipose tissue neural innervation. *iScience* 24, 103127. doi: 10.1016/J.ISCI.2021.103127

Wise, A., Foord, S. M., Fraser, N. J., Barnes, A. A., Elshourbagy, N., Eilert, M., et al. (2003). Molecular Identification of High and Low Affinity Receptors for Nicotinic Acid. *Journal of Biological Chemistry* 278, 9869–9874. doi: 10.1074/JBC.M210695200

Wolff, A., Frank, M., Staehlke, S., and Peters, K. (2022). A Comparative Study on the Adipogenic Differentiation of Mesenchymal Stem/Stromal Cells in 2D and 3D Culture. *Cells* 11, 1313. doi: 10.3390/CELLS11081313

World Health Organisation (2021). WHO Diabetes Fact Sheet. Available at: https://www.who.int/news-room/fact-sheets/detail/diabetes (Accessed December 8, 2021).

World Health Organisation (2025). Obesity and Overweight Fact Sheet. Available at: https://www.who.int/news-room/fact-sheets/detail/obesity-and-overweight (Accessed October 5, 2025).

World Obesity Federation (2025). World Obesity Atlas 2025. London. Available at: https://data.worldobesity.org/publications/?cat=23 (Accessed June 10, 2025).

Wright, S. C., Avet, C., Gaitonde, S. A., Muneta-Arrate, I., Le Gouill, C., Hogue, M., et al. (2024). Conformation- and activation-based BRET sensors differentially report on GPCR–G protein coupling. *Sci Signal* 17, 4747. doi: 10.1126/SCISIGNAL.ADI4747

Wright, S. C., Lukasheva, V., Gouill, C. Le, Kobayashi, H., Breton, B., Mailhot-Larouche, S., et al. (2021). BRET-based effector membrane translocation assay monitors GPCR-promoted and endocytosis-mediated Gqactivation at early endosomes. *Proc Natl Acad Sci U S A* 118. doi: 10.1073/PNAS.2025846118/-/DCSUPPLEMENTAL

Wrzesinski, K., Frandsen, H. S., Calitz, C., Gouws, C., Korzeniowska, B., and Fey, S. J. (2021). Clinostat 3D Cell Culture: Protocols for the Preparation and Functional Analysis of Highly Reproducible, Large, Uniform Spheroids and Organoids. *Methods in Molecular Biology* 2273, 17–62. doi: 10.1007/978-1-0716-1246-0_2

Wu, H., and Ballantyne, C. M. (2020). Metabolic Inflammation and Insulin Resistance in Obesity. *Circ Res*, 1549–1564. doi: 10.1161/CIRCRESAHA.119.315896

Wu, H., Pula, T., Tews, D., Amri, E. Z., Debatin, K. M., Wabitsch, M., et al. (2021). Microrna-27a-3p but not-5p is a crucial mediator of human adipogenesis. *Cells* 10, 3205. doi: 10.3390/CELLS10113205

Wu, J., Boström, P., Sparks, L. M., Ye, L., Choi, J. H., Giang, A. H., et al. (2012). Beige Adipocytes Are a Distinct Type of Thermogenic Fat Cell in Mouse and Human. *Cell* 150, 366–376. doi: 10.1016/J.CELL.2012.05.016

Xiong, Y., Miyamoto, N., Shibata, K., Valasek, M. A., Motoike, T., Kedzierski, R. M., et al. (2004). Short-chain fatty acids stimulate leptin production in adipocytes through the G protein-coupled receptor GPR41. *Proc Natl Acad Sci U S A* 101, 1045–1050. doi: 10.1073/PNAS.2637002100

Xu, H., Barnes, G. T., Yang, Q., Tan, G., Yang, D., Chou, C. J., et al. (2003). Chronic inflammation in fat plays a crucial role in the development of obesity-related insulin resistance. *J Clin Invest* 112, 1821–1830. doi: 10.1172/JCI19451

Xu, Y., Piston, D. W., and Johnson, C. H. (1999). A bioluminescence resonance energy transfer (BRET) system: Application to interacting circadian clock proteins. *Proc Natl Acad Sci U S A* 96, 151. doi: 10.1073/PNAS.96.1.151

Yadav, M. K., Sarma, P., Maharana, J., Ganguly, M., Mishra, S., Zaidi, N., et al. (2024). Structure-guided engineering of biased-agonism in the human niacin receptor via single amino acid substitution. *Nat Commun* 15, 1–16. doi: 10.1038/s41467-024-46239-2

Yamamoto, N., Ueda-Wakagi, M., Sato, T., Kawasaki, K., Sawada, K., Kawabata, K., et al. (2015). Measurement of Glucose Uptake in Cultured Cells. *Curr Protoc Pharmacol* 71, 12.14.1-12.14.26. doi: 10.1002/0471141755.PH1214S71

Yang, D., Zhou, Q., Labroska, V., Qin, S., Darbalaei, S., Wu, Y., et al. (2021). G protein-coupled receptors: structure- and function-based drug discovery. *Signal Transduct Target Ther* 6, 1–27. doi: 10.1038/s41392-020-00435-w

Yang, J., and Johnson, C. H. (2021). Bioluminescent Sensors for Ca++ Flux Imaging and the Introduction of a New Intensity-Based Ca++ Sensor. *Front Bioeng Biotechnol* 9, 773353. doi: 10.3389/FBIOE.2021.773353

Yang, X., Zhang, W., Wang, L., Zhao, Y., and Wei, W. (2024). Metabolite-sensing GPCRs in rheumatoid arthritis. *Trends Pharmacol Sci* 45, 118–133. doi: 10.1016/J.TIPS.2023.12.001

Yaribeygi, H., Farrokhi, F. R., Butler, A. E., and Sahebkar, A. (2019). Insulin resistance: Review of the underlying molecular mechanisms. *J Cell Physiol* 234, 8152–8161. doi: 10.1002/JCP.27603

Yarmo, M. N., Gagnon, A., and Sorisky, A. (2010). The anti-adipogenic effect of macrophage-conditioned medium requires the IKKβ/NF-κB pathway. *Hormone and Metabolic Research* 42, 831–836. doi: 10.1055/S-0030-1263124/BIB

Ye, J., Coulouris, G., Zaretskaya, I., Cutcutache, I., Rozen, S., and Madden, T. L. (2012). Primer-BLAST: A tool to design target-specific primers for polymerase chain reaction. *BMC Bioinformatics* 13, 134-. doi: 10.1186/1471-2105-13-134

Younossi, Z. M., Golabi, P., Paik, J. M., Henry, A., Van Dongen, C., and Henry, L. (2023). The global epidemiology of nonalcoholic fatty liver disease (NAFLD) and nonalcoholic steatohepatitis (NASH): a systematic review. *Hepatology* 77, 1335–1347. doi: 10.1097/HEP.0000000000000004

Younossi, Z. M., Stepanova, M., Al Shabeeb, R., Eberly, K. E., Shah, D., Nguyen, V., et al. (2024). The changing epidemiology of adult liver transplantation in the United States in 2013-2022: The dominance of metabolic dysfunction-associated steatotic liver disease and alcohol-associated liver disease. *Hepatol Commun* 8. doi: 10.1097/HC9.0000000000000352

Yu, J. H., Kim, J. H., Soung, N. K., Moon, E. Y., and Koo, J. H. (2023). Identification of the primary ciliary proteins IFT38 and IFT144 to enhance serum-mediated YAP activation and cell proliferation. *Biochem Biophys Res Commun* 681, 186–193. doi: 10.1016/j.bbrc.2023.09.082

Yudaeva, A., Kostyusheva, A., Kachanov, A., Brezgin, S., Ponomareva, N., Parodi, A., et al. (2024). Clinical and Translational Landscape of Viral Gene Therapies. *Cells* 13, 1916. doi: 10.3390/CELLS13221916

Zacharias, D. A., Violin, J. D., Newton, A. C., and Tsien, R. Y. (2002). Partitioning of lipid-modified monomeric GFPs into membrane microdomains of live cells. *Science (1979)* 296, 913–916. doi: 10.1126/SCIENCE.1068539

Zahorska-Markiewicz, B., Anowska, J., Olszanecka-Glinianowicz, M., and Zurakowski, A. (2000). Serum concentrations of TNF-α and soluble TNF-α receptors in obesity. *Int J Obes* 24, 1392–1395. doi: 10.1038/sj.ijo.0801398

Zaragosi, L.-E., Billon, N., Ailhaud, G., and Dani, C. (2007). Nucleofection Is a Valuable Transfection Method for Transient and Stable Transgene Expression in Adipose Tissue-Derived Stem Cells. *Stem Cells* 25, 790–797. doi: 10.1634/STEMCELLS.2006-0235

Zebisch, K., Voigt, V., Wabitsch, M., and Brandsch, M. (2012). Protocol for effective differentiation of 3T3-L1 cells to adipocytes. *Anal Biochem* 425, 88–90. doi: 10.1016/J.AB.2012.03.005

Zhang, J., Ma, Y., Taylor, S. S., and Tsien, R. Y. (2001). Genetically encoded reporters of protein kinase A activity reveal impact of substrate tethering. *Proc Natl Acad Sci U S A* 98, 14997–15002. doi: 10.1073/PNAS.211566798;SUBPAGE:STRING:FULL

Zhang, R., and Xie, X. (2012). Tools for GPCR drug discovery. *Acta Pharmacol Sin* 33, 372. doi: 10.1038/APS.2011.173

Zhang, Y., Proenca, R., Maffei, M., Barone, M., Leopold, L., and Friedman, J. M. (1994). Positional cloning of the mouse obese gene and its human homologue. *Nature* 372, 425–432. doi: 10.1038/372425A0

Zhang, Y., Schmidt, R. J., Foxworthy, P., Emkey, R., Oler, J. K., Large, T. H., et al. (2005). Niacin mediates lipolysis in adipose tissue through its G-protein coupled receptor HM74A. *Biochem Biophys Res Commun* 334, 729–732. doi: 10.1016/J.BBRC.2005.06.141

Zhao, H., Doyle, T. C., Coquoz, O., Kalish, F., Rice, B. W., and Contag, C. H. (2005). Emission spectra of bioluminescent reporters and interaction with mammalian tissue determine the sensitivity of detection in vivo. *J Biomed Opt* 10, 041210. doi: 10.1117/1.2032388

Zheng, C., Javitch, J. A., Lambert, N. A., Donthamsetti, P., and Gurevich, V. V. (2023). In-cell arrestin-receptor interaction assays. *Curr Protoc* 3, e890. doi: 10.1002/CPZ1.890

Zhu, X., Ricci-Tam, C., Hager, E. R., and Sgro, A. E. (2023). Self-cleaving peptides for expression of multiple genes in Dictyostelium discoideum. *PLoS One* 18, e0281211. doi: 10.1371/JOURNAL.PONE.0281211

Zilberfarb, V., Piétri-Rouxel, F., Jockers, R., Krief, S., Delouis, C., Issad, T., et al. (1997). Human immortalized brown adipocytes express functional ß3-adrenoceptor coupled to lipolysis. *J Cell Sci* 110, 801–807. doi: 10.1242/JCS.110.7.801